Scaffolding proteins in membrane trafficking: The role of ELKS

ISBN: 978-90-393-6322-5

Printed by Gildeprint-Enschede
Layout and cover design by MgA. Petra Mejstrikova

The research presented in this thesis was performed at the Department of Cell Biology, Erasmus Medical Center in Rotterdam and at the division of Cell Biology, Department of Biology, Faculty of Science, Utrecht University, the Netherlands.

This research was supported by Netherlands Organization for Scientific Research (NWO-ALW-VICI) and the Netherlands Organization for Health Research and Development (ZonMw-TOP) awarded to Prof. dr. Anna Akhmanova.

Scaffolding proteins in membrane trafficking: The role of ELKS

Verbindingseiwitten in het membraantransport: De rol van ELKS

(met een samenvatting in het Nederlands)

Proefschrift
ter verkrijging van de graad van doctor
aan de Universiteit Utrecht op gezag van de rector magnificus,
prof. dr. G. J. van der Zwaan,
ingevolge het besluit van het college voor promoties
in het openbaar te verdedigen
op woensdag 17 juni 2015 des middags te 2:30 uur

door

Ká Lou Yu

geboren op 14 oktober 1981
te Macau S.A.R.

Promotor: Prof. dr. A.S. Akhmanova

Contents

Outline of this thesis

In this thesis, we focus on the role of the multifunctional adaptor ELKS and some other scaffolding factors involved in the regulation of intracellular trafficking.

Chapter 1 gives an overview on the CAST/ELKS family of proteins and their known functions in different cellular pathways, such as microtubule organization, exocytosis and signaling in vertebrates and in invertebrates.

Chapter 2 describes the two pull-down methods that have been widely used as an approach to identify new protein binding partners in combination with mass spectrometry analysis in the later chapters. We also discuss how we use GFP-fusion proteins to validate the interactions using dual-color imaging in fixed and live cells.

Chapter 3 dissects the interaction of YIF1A with VAPB in the early secretory pathway and their biological roles in cultured hippocampal neurons.

Chapter 4 reveals how two Rab GTPases cooperate with monooxygenase enzyme MICAL-3 through the formation of a cortical complex containing ELKS in the docking and fusion of exocytotic vesicles with the plasma membrane.

Chapter 5 extends our understanding of MICAL family proteins. We first focus on the role of MICAL-1 on vesicular trafficking and actin reorganization using a knockout cell model. We then describe novel binding partners of MICAL-3 and highlight a potential role of MICAL-3 in cytokinesis.

Chapter 6 describes the generation of ELKS knock-out and GFP-ELKS knock-in mice. We show that while ELKS knockout is homozygously lethal, GFP-ELKS knock-in mice are viable and fertile, demonstrating that different cells and tissues derived from these mice can be used to study ELKS dynamics.

Chapter 7 addresses the recruitment and behavior of ELKS at the cell cortex using different cellular models including mouse embryonic fibroblasts and pancreatic islets.

Chapter 8 presents a general overview the experimental data presented in the previous chapters and discusses the potential new directions for future research.

Chapter 1

ELKS - a multifunctional adaptor protein involved in secretion, cytoskeletal regulation and signaling

Ka Lou Yu and Anna Akhmanova

Membrane trafficking in cells

All cells are enveloped by membranes, lipid bilayers, which provide a boundary between the cellular content and the outside world. *Prokaryotes* typically lack membrane-bound organelles, and therefore all their intracellular components are present in the common cytoplasm. *Eukaryotic* cells are much more complex, as they contain multiple intracellular membranes, which divide the cellular space into compartments where different biochemical processes take place. These include the cell nucleus, mitochondria (and chloroplasts in plants), the endoplasmic reticulum (ER), Golgi apparatus, lysosomes and peroxisomes. Due to their large size and complex architecture, eukaryotic cells require efficient transport systems to shuttle molecules between different compartments and export or import them to/from outside.

Intracellular transport includes three major mechanisms: transmembrane transport (transition of ions, as well as small and large molecules across the two sides of a membrane), gated transport (which refers to trafficking of macromolecular complexes through specialized structures, the nuclear pores) and vesicular trafficking, in which membrane-enclosed transport intermediates pinch off one cellular compartment and fuse with another one. Vesicular transport is involved in the delivery of molecules to and from the plasma membrane (exocytosis and endocytosis) (Fig. 1A) and the exchange of molecules between intracellular compartments of the secretory pathway.

The inward membrane trafficking route, endocytosis, starts with the invagination of the plasma membrane that subsequently pinches off and forms an endocytic vesicle, which is typically directed to intracellular compartments such as other endosomes, Golgi or lysosomes. The endocytic pathway can be divided into phagocytosis, pinocytosis and receptor-mediated endocytosis (Fig. 1B). Phagocytosis is the ingestion of macromolecules such as microorganisms or dead cells into vesicular structures called phagosomes (~250 nm in diameter). Pinocytosis, a process that takes place in most eukaryotic cells, is the ingestion of fluid and solutes into pinocytic vesicles (~100 nm in diameter). Receptor-mediated endocytosis is the internalization of receptor-ligand complexes from the plasma membrane, which is used to take up macromolecules like cholesterol-containing lipoproteins from the extracellular fluid and is also a means of recycling receptor proteins after ligand binding.

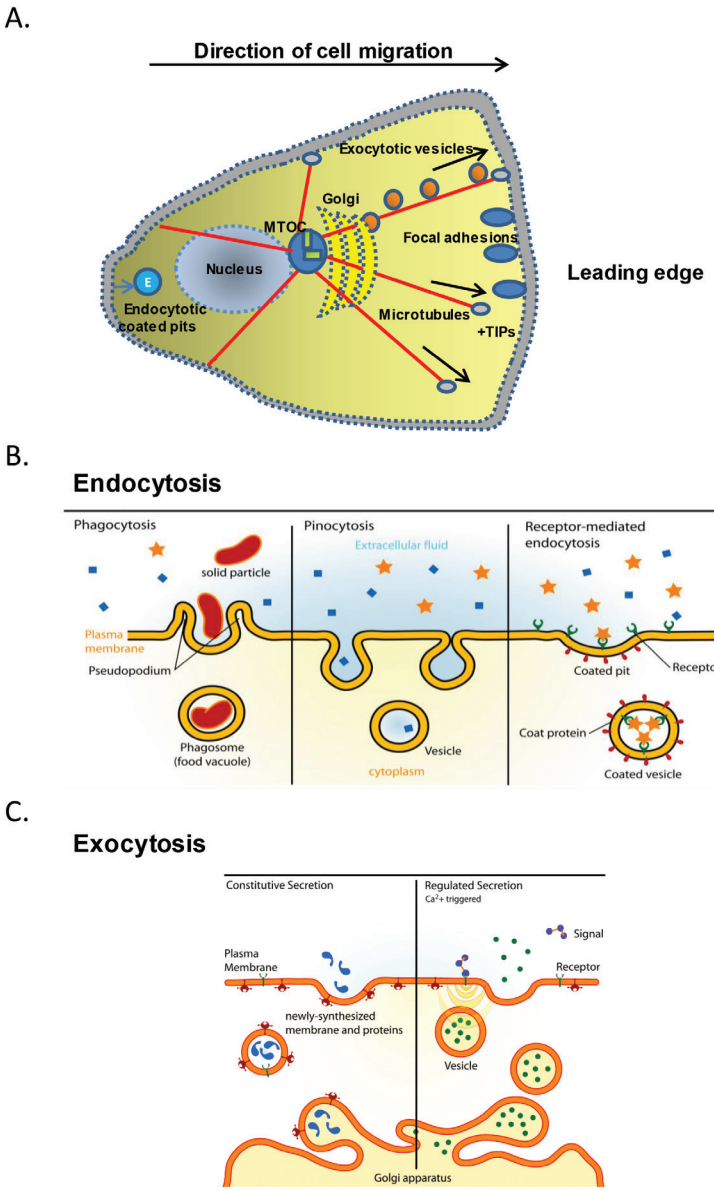

Figure 1. **The microtubule organization of a polarized cell and the intracellular membrane trafficking. (A)** A scheme of a migrating cell. Microtubules, dynamic cytoskeletal filaments, which can grow and shrink, radiate from the microtubule organizing center (MTOC). Growing microtubules, decorated by plus-end tracking proteins at their plus ends (+TIPs), can be stabilized and anchored by specific factors at the cell cortex. Exocytotic vesicles contain lipids, newly synthesized proteins and receptors bud from the Golgi apparatus and travel along microtubules towards the plasma membrane. Lipids, receptors and proteins can also recycle from the plasma membrane via the endocytotic pathway. **(B)** An illustration of different forms of endocytosis, including phagocytosis, pinocytosis and receptor-mediated endocytosis. (Adapted from http://en.wikipedia.org/wiki/Endocytosis) **(C)** An illustration of constitutive exocytosis and regulated exocytosis. Exocytosis can take place constitutively or upon receptor stimulation from an extracellular signal. (Adapted from http://commons.wikimedia.org/wiki/File:Exocytosis_types.svg)

The outward transport pathway, exocytosis, is responsible for the delivery of the components of the plasma membrane, extracellular matrix, signaling molecules and other secreted cargos (Fig. 1A,C). Exocytotic vesicles bud off the Golgi, travel along the cytoskeleton towards cell periphery, where they dock and fuse with the plasma membrane. This process can occur constitutively, to maintain cell homeostasis and adhesion to the surrounding matrix and other cells (constitutive exocytosis), but can also deliver specific cargos in differentiated cells, where it is often strongly controlled in time and space (regulated exocytosis). The latter process plays an important role in synaptic neurotransmission, endocrine and paracrine signaling (through the secretion of hormones such as insulin or growth factors), mucous secretion, or the release of enzymes by intestinal cells or neutrophils.

Importantly, all membrane compartments involved in endo- and exocytosis as well as the synthesis, maturation and degradation of different cargo molecules, including the ER, Golgi complex, endosomes, lysosomes and secretory carriers (which together form the secretory pathway) are interconnected by vesicular transport routes. Vesicular transport thus provides directional delivery of specific molecules and also insures the maintenance of the constant size of intracellular compartments by balancing membrane flows.

Major classes of molecules involved in vesicular trafficking

While the cargos transported by different vesicular trafficking pathways can be very diverse, the molecular mechanisms of generation, transport and fusion of membrane carriers utilize common principles and similar sets of molecular players. These include:

- Coat proteins (clathrin, COPI, COPII, retromer) and their adaptor proteins, which coordinate cargo sorting with membrane invagination and budding.

- Small GTPases: Sar1, Arf GTPases, Rabs, which regulate the formation of coats or recruit specific effectors such as cytoskeletal motors or vesicle docking and fusion machinery.

- Cargo receptors (KDEL receptor, mannose-6-phosphate receptor, etc), which concentrate specific molecules in carriers leaving one compart-

ment and release them in another compartment, providing a mechanism of directional delivery of molecules in the secretory pathway.

- Vesicle scission factors, which promote detachment of the already formed vesicles into the cytoplasm (e.g. dynamin, acting on endosomes) or in the opposite direction (ESCRT complexes in the biogenesis of multivesicular bodies, abscission or viral budding).

- Membrane docking and tethering complexes (CORVET, HOPS, Golgins), which establish physical connections between membrane compartments to direct and promote membrane fusion.

- Cytoskeletal motors, which are used to transport the vesicles and position membrane compartments within the cell.

- SNAREs (Soluble N-ethylmalimide-sensitive factor attachment protein receptors), molecules directly responsible for bringing two membranes together during a fusion event.

The rich protein machinery responsible for different steps in membrane transport includes transmembrane and peripheral membrane proteins, as well as soluble cytosolic factors. Many of them possess different enzymatic activities such as the ability to hydrolyze GTP or ATP. The energy derived from the nucleotide hydrolysis is used for conformational changes that can drive vesicle movement or scission, or promote the assembly and disassembly of large protein complexes, such as membrane coats. In addition to these enzymes, numerous scaffolding molecules, which do not possess any enzymatic activity, bridge different participating factors and by doing so perform an essential function to control intracellular architecture at different scales.

In this chapter, we focus on one evolutionarily conserved scaffolding protein, which is known as ELKS (named so due to the high content of glutamic acid (E), leucine (L), lysine (K) and serine (S) residues). This protein and its homologues in different animal species ranging from worms and flies to mammals have been described in various cellular contexts, including constitutive and regulated exocytosis, microtubule organization as well as signaling. We will provide

a systematic overview of the structure, binding partners and functions of ELKS and its homologues in different pathways and discuss how these functions connect to each other.

Discovery of the ELKS-encoding gene

The human ELKS-encoding gene (which is named *ERC1*, see below) was first identified in a papillary thyroid carcinoma, in which gene rearrangement via the translocation t(10;12) resulted in a fusion of the 5' prime end of the *ERC1* gene to the gene encoding the receptor-type tyrosine kinase RET/TRKA (Nakata et al., 1999). Full-length ELKS cDNA was subsequently cloned from a human brain cDNA library. This cDNA encoded a novel protein of 948-amino acids, which does not contain any conspicuous domains except for predicted coiled coils interspersed with hinge sequences. ELKS was found to be ubiquitously expressed: Northern blotting showed that ~9 kilobase (kb) transcripts were abundantly present in heart, thyroid, pancreas, testis and placenta, while shorter transcripts could also be detected in skeletal muscles. Almost at the same time, ELKS, also known as KIAA1081, was cloned from a human brain cDNA library, and expression profiling using RT-PCR showed highest expression in brain, including amygdala, thalamus, as well as heart, lung and ovary (Kikuno et al., 1999).

ELKS is encoded by a very large gene (more than 500 kb in humans) (Yokota et al., 2000). The point of fusion of the *ERC1* and *RET* genes in papillary thyroid carcinoma is localized in the intron 10 of the *ERC1* gene; the ELKS-RET fusion protein can be expected to contain the ~700 N-terminal amino acids of ELKS, and the coiled coil domains present in this protein fragment would be expected to drive constitutive di- or oligomerization of the RET kinase. This change in the oligomerization status can be expected to induce constitutive activation of this tyrosine kinase, which normally acts as a receptor of the glial cell line-derived neutrophic factor (GDNF) and is activated by ligand-mediated heterodimerization (Airaksinen et al., 1999). Some experimental evidence was found to support this view (Nakata et al., 2002).

ELKS has a close mammalian homologue, CAST (cytomatrix at the active zone (CAZ)-associated structural protein), which is encoded by a different gene. CAST was identified by biochemical methods as a component of the postsynaptic density (PSD) fraction of rat brain and demonstrated to associate with

the presynaptic structures (Ohtsuka et al., 2002). ELKS has thus been termed CAST2, as it is also present at the presynapse (Deguchi-Tawarada et al., 2004). Through a yeast two-hybrid screen, ELKS has been found to be a binding partner of the small GTPase Rab6, and was named Rab6 interacting protein 2 (Rab6IP2) (Monier et al., 2002) (Fig. 2A). Finally, using RIM1 (Rab3-interacting molecule 1), a synaptic active zone component in another yeast two-hybrid screen led to the identification of ELKS and CAST as binding partners of the conserved PDZ domain of RIM1 (Wang et al., 2002) (Fig.2B). To summarize these findings, it was proposed the name ELKS, which is sometimes also called ELKS1, ERC1 (ELKS/RAB6-interacting/CAST family member 1), while CAST was named ERC2 (or ELKS2) (Wang et al., 2002). While the names *ERC1* and *ERC2* are used for the corresponding genes, for the protein products the names ELKS and CAST are used more frequently, and we will keep this nomenclature in the remaining part of this thesis.

The mouse ELKS-encoding gene contains 22 exons, with a translation start in exon 3. An alternative promotor generates a transcript, the translation of which starts in exon 4 (Liu et al., 2014). CAST-encoding gene also contains an alternative transcription initiation site between exons 5 and 6 (Kaeser et al., 2009). However, the resulting shorter isoforms of ELKS and CAST are expressed only at low levels; in neurons, they account for less than 5% of the total ELKS/CAST pool (Liu et al., 2014). ELKS-encoding transcripts undergo extensive alternative splicing, including the generation of two alternative 3'-regions, which encode proteins with different C-termini. The shorter brain-specific ELKS isoform, which was termed ELKSα according to the nomenclature proposed by Nakata et al. (Nakata et al., 2002) (also named ELKS1αB in (Liu et al., 2014)), contains a C-terminal type II PDZ-binding motif (IWA) that binds to RIMs (Deguchi-Tawarada et al., 2004; Wang et al., 2002).

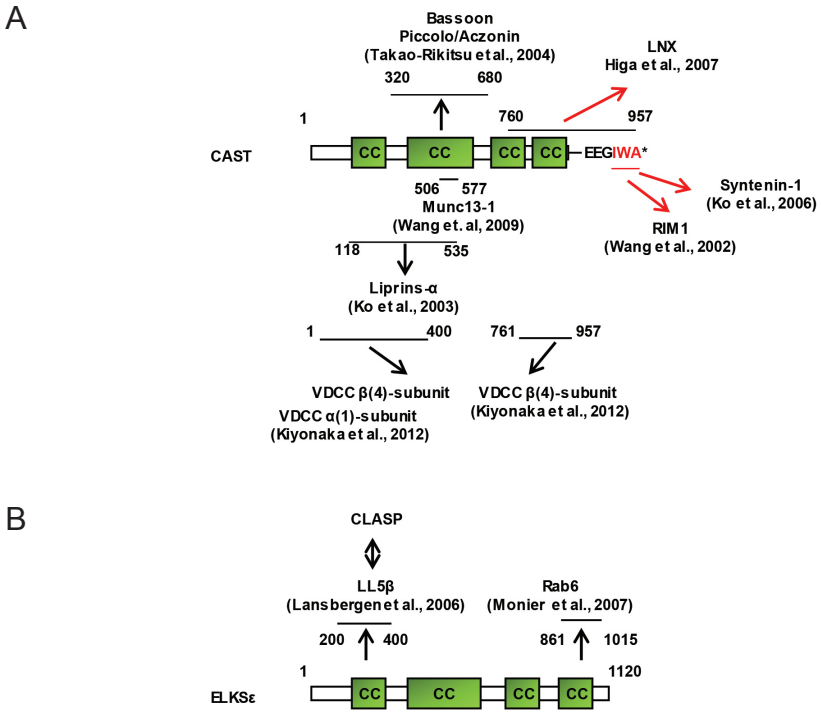

Figure 2. Schematic structure of CAST and ELKS proteins and the domains interacting with different partners in in HeLa cells (A) or at the synaptic active zone (B). The structural basis of the ELKS-RIM interaction has been investigated for RIM1α and ELKS1B using NMR spectroscopy; it was shown that the specificity of the interaction could be explained by an unusually deep narrow peptide-binding cavity in the PDZ domain of RIM1. The shape of the cavity is complementary to the four C-terminal residues of ELKS (Lu et al., 2005).

The longer ELKS ELKS isoforms (such as ELKSε/αELKS1B), which are expressed in non-neuronal tissues, do not contain this C-terminal PDZ domain-binding sequence (Fig. 2A). The major isoform of CAST, a protein predominantly expressed in the brain, also contains the C-terminal PDZ-binding motif interacting with RIM1 (Fig. 2B). An alternatively spliced longer version of CAST protein lacking this motif also exists (Kaeser et al., 2009). The potential functional redundancy between ELKS and CAST is mostly relevant in neurons, and will be discussed below.

ELKS is an evolutionarily conserved protein: ELKS homologues have been extensively characterized in two invertebrate model systems, *Caenorhabditis elegans* and *Drososphila melanogaster*, both of which contain a single ELKS homologue that has been strongly implicated in synaptic structure and function (see below).

The role of ELKS in microtubule organization and exocytosis in fibroblasts and cancer cells

As indicated above, ELKS is a ubiquitously expressed protein. In cultured mammalian cells, ELKS predominantly localizes to the cell cortex (Fig. 3). In non-motile HeLa cells, it specifically accumulates at the free cell edges that are not in contact with other cells (Lansbergen et al., 2006). In migrating cells, such as breast cancer cells and fibroblasts, ELKS concentrates at the leading or protruding edges (Astro et al., 2014; Lansbergen et al., 2006). Cortical localization of ELKS was initially discovered in a search for proteins that target the microtubule-stabilizing proteins CLASP1 and CLASP2 (CLIP-associating protein 1 and 2) to the cell cortex (Lansbergen et al., 2006). CLASPs are microtubule plus-end tracking proteins (+TIPs), which are recruited to the microtubule tips by EB1 and can specifically stabilize microtubule plus ends at the cell periphery (Akhmanova et al., 2001; Mimori-Kiyosue et al., 2005). A mass spectrometry-based screen identified ELKS as well as a phosphatidylinositol 3, 4, 5-trisphosphate (PIP3)-interacting protein LL5β as the binding partners of CLASP2 (Lansbergen et al., 2006). Detailed analysis showed that ELKS directly binds to LL5β (Figure 3), but not to the CLASPs, and that LL5β is required for the recruitment of ELKS and CLASPs to the cell cortex (Lansbergen et al., 2006). The peripheral localization of LL5β, which interacts with PIP3 via its pleckstrin homology (PH) domain (Paranavitane et al., 2003), is partly controlled by phosphatidylinositol-4,5-bisphosphate 3-kinase (PI3K), although this is not the only factor responsible for the recruitment of LL5β to the cortex. LL5β, CLASPs and ELKS thus form a PIP3-regulated cortical hub, which is responsible for the generation of stable and dense microtubule arrays (Akhmanova et al., 2001; Lansbergen et al., 2006; Mimori-Kiyosue et al., 2005) (Fig.3). Within this hub, LL5β is required for the targeting of CLASPs and ELKS to the cortex, while CLASPs directly bind and stabilize microtubules. The effect of ELKS depletion on the microtubule organization is relatively mild because ELKS does not bind to microtubules and is not essential for the cortical localization of LL5β or CLASPs but rather plays a scaffolding role, by concentrating cortical clusters of LL5β and CLASPs at the cell periphery (Lansbergen et al., 2006).

At the cortex, LL5β and ELKS are typically found in close proximity to focal adhesions, but never spatially overlap with them (Lansbergen et al. 2006). Such localization is likely to be important in polarized epithelia, where LL5β, its homologue LL5α and CLASPs are found at the basal side, in the proximity

of the basal membrane where activated integrins are located. This localization is controlled by the integrin activation through binding to laminin, and is important for regulating microtubule density at the basal cortex (Hotta et al., 2010). CLASP and LL5-mediated anchoring of microtubules to the basal cortex was shown to play a role during chicken development, where it prevents epithelial-mesenchymal transition of epiblast cells and thus promotes the maintenance of their epithelial status (Nakaya et al., 2013).

A search for additional components of the cortical LL5β-ELKS-CLASP complex identified liprin-α1, liprin-β1 KANK1, KANK2 and the microtubule growth-inhibiting kinesin-4 KIF21A (van der Vaart et al., 2013) (Fig. 3). The two liprins are required to increase microtubule density at the cortex, similar to LL5β, while KANK1 and its binding partner KIF21A inhibit microtubule elongation and thus prevent microtubule overgrowth at the cell margin (van der Vaart et al., 2013). Finding liprin-α1 was not surprising because liprin-α1 has already been reported to directly bind to CAST and ELKS (Ko et al., 2003) (Table I). The liprin family is composed of four liprin-α and two liprin-β proteins, which can interact directly and form homo- and heterodimers (de Curtis, 2011; Spangler and Hoogenraad, 2007). Liprin-α1, the most ubiquitously expressed member of the liprin-α protein family, has been shown to be required for efficient cell migration and invasion *in vitro* (Asperti et al., 2010). A recent report has shown that liprin-α1, LL5α, LL5β and ELKS localize to the protrusions of migrating human breast cancer cells MDA-231 (Astro et al., 2014). The efficient accumulation of ELKS at the front of the protrusions depended on both LL5s and liprin-α1, while ELKS depletion did not have a strong effect on the localization of LL5s and liprin-α1 (Astro et al., 2014). Depletion of all these proteins resulted in migratory defects in 2D and 3D environments and showed that these factors promote the stability of lamellipodia and regulate recycling of active β1 integrins from the cell surface (Astro et al., 2014).

The molecular function of the cortical complexes containing LL5s, ELKS, liprins and their partners goes beyond microtubule organization, because these complexes are also involved in controlling constitutive secretion (Fig. 3). ELKS appears to be a central player in this process (Grigoriev et al., 2007). ELKS directly interacts with all isoforms the small GTPase Rab6 (Rab6A, Rab6A' and Rab6B) (Monier et al., 2002). Ra6A is an abundantly expressed Rab GTPase, which strongly decorates the Golgi apparatus and cytoplasmic vesicles (Del Nery et al., 2006; Martinez et

al., 1997; Martinez et al., 1994). Although these vesicles were originally believed to be responsible for COPI-independent transport from ER to Golgi (Girod et al., 1999; White et al., 1999), detailed imaging studies demonstrated that these vesicles in fact predominantly fuse with the plasma membrane and thus represent carriers of constitutive secretion (Grigoriev et al., 2007).

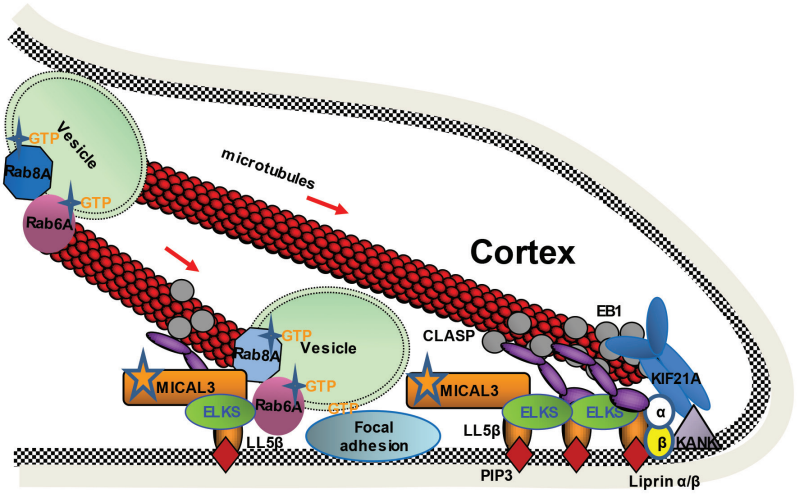

Figure 3. A hypothetical model illustrating ELKS-containing cortical complexes in HeLa cells and in breast cancer cells. LL5β is recruited to the cell cortex via the interaction with PIP3 at the plasma membrane. LL5β interacts with ELKS and CLASPs, attaching the plus-ends of microtubules to the cell cortex. LL5β is essential for the cortical accumulation of CLASPs and microtubule stabilization. Liprin-α1/β1 are upstream regulators of the cortical microtubule attachment complex. Liprin-β1 interacts with KANK1, which in turn recruits to the cortex the microtubule growth inhibitor KIF21A. Rab6-positive exocytotic vesicles bud from the Golgi apparatus. Rab6 recruits Rab8 GTPase, another Rab implicated in trafficking; Rab6/Rab8-positive vesicles travel along microtubules towards the plasma membrane. ELKS is a Rab6-interacting partner, which recruits Rab6-containing vesicles for docking and fusion with the plasma membrane. ELKS forms a complex with Rab8 via MICAL-3, an monooxygenase enzyme that regulates both the remodeling of the ELKS/Rab8-MICAL-3 complex and vesicle fusion. Rab8 interacts with the C terminus of MICAL-3.

Rab6A-positive vesicles immobilize and fuse at the cortical patches containing LL5β, and ELKS depletion causes strong accumulation of Rab6A-positive vesicles at the cell periphery because although the exit of exocytotic vesicles from the Golgi and their microtubule-based transport are not perturbed, their docking and fusion are inhibited (Grigoriev et al., 2007). Thus, although not essential for recruitment of either LL5s or liprin-α1 to the cortex, ELKS plays a crucial role in controlling exocytosis. In Chapter 4, we describe important molecular details of the underlying mechanism, which depends on the small GTPase Rab8 and the flavoprotein monooxynase MICAL-3 (Fig.3). ELKS-dependent exocytosis is likely to be important for regulating focal adhesions, because it was shown that

in migrating keratinocytes, LL5β and CLASPs accumulate around focal adhesions and promote their disassembly (Stehbens et al., 2014). The exact mechanism is not entirely clear but probably involves the targeting of the exocytotic vesicles containing matrix metalloprotease MT1-MMP (membrane-type 1 matrix metalloprotease) to the proximity of focal adhesions (Stehbens et al., 2014).

Table I. A summary of the interacting regions on CAST shared by different interacting partners at the presynaptic active zone.

CAST-interacting partners	CAST (amino acids)	References
Liprin-α	118-535	Ko et. al, 2003
VDCC-β(4) subunit	1-400; 761-957	Kiyonaka et al., 2012
VDCC-α(4) subunit	1-400	Kiyonaka et al., 2012
Bassoon Piccolo/Aczonin	320-680	Takao-Rikitsu et al., 2004
Munc13-1	506-577	Wang et. al, 2009
LNX	760-957	Higa et al, 2007
RIM-1	954-957	Wang et. al, 2009
Syntenin-1	954-957	Ko et. al, 2006

LL5β and ELKS were also shown to concentrate at podosomes, actin-rich dynamic structures, which can remodel the extracellular matrix (Proszynski and Sanes, 2013). Interestingly, podosome-like structures ("synaptic podosomes") are also formed at neuromuscular junctions (NMJ) undergoing remodeling during postnatal stages of development, and LL5β, which strongly localizes to regions of high density of acetylcholine receptors at the NMJ, has been implicated in this process (Kishi et al., 2005; Proszynski et al., 2009; Proszynski and Sanes, 2013). The "synaptic podosomes" in myotubes also contain ELKS, and the proper localization of ELKS in this system requires Amotl2, a member of the motin family of scaffolding proteins (Proszynski and Sanes, 2013). At the NMJ, the complexes of LL5β and CLASPs were shown to capture microtubule plus ends and in this way create a route for the delivery of vesicles containing acetylcholine receptors to the postsynaptic membrane (Basu et al., 2015; Basu et al., 2014; Schmidt et al., 2012). It is currently unknown whether ELKS participates in the regulation of the fusion of acetylcholine receptor-containing

carriers with the plasma membrane, but this possibility seems quite likely, given the involvement of ELKS in secretion and the observation that ELKS is present at the NMJ (Tokoro et al., 2007). The overall picture, which emerges from these studies, is that ELKS is a part of multicomponent cortical machinery, which can capture microtubules and promote the delivery to the plasma membrane of different exocytotic cargo. ELKS is not essential for the cortical recruitment of its partners but might be key for promoting site-specific secretion.

CAST and ELKS at the active zone in mammalian synapses

As discussed above, there are some indications that ELKS might play a role at the post-synaptic side of the NMJ; however, the major involvement of ELKS and its homologue CAST in neurotransmission has so far been documented at the presynaptic side, at the active zone (for review, see (Hida and Ohtsuka, 2010)). The active zone is the principal site of Ca^{2+}-dependent exocytosis of neurotransmitters (Fig. 4). It is a specialized region of the plasma membrane where tethering, docking and fusion of synaptic vesicles take place (Gundelfinger and Fejtova, 2012; Sudhof, 2012). Active zones also recruit trans-synaptic cell adhesion molecules that determine proper apposition of pre- and post-synaptic machinery. Finally, the organization and function of the active zone is also an important determinant of synaptic plasticity. Cytologically, the active zone appears as an electron-dense structure beneath the plasma membrane, where a network of multi-domain scaffolding proteins form the CAZ. The scaffolds localized at the CAZ can regulate the coupling of the calcium influx, which occurs through voltage-gated calcium channels, to rapid fusion of synaptic vesicles. The active zone thus ensures prompt release of the neurotransmitter into the synaptic cleft upon neuronal activation. In addition, the scaffolding function of CAZ components might confer long-term stability to the individual presynaptic sites (Gundelfinger and Fejtova, 2012; Sudhof, 2012).

ELKS and CAST are among the best-studied CAZ proteins (Fig. 4). Other major CAZ components are:

- RIMs, which are essential for synaptic vesicle docking and priming, Ca^{2+} channel recruitment to the active zone and plasticity
- RIM-BPs (RIM-binding proteins), which promote linking of Ca^{2+} channels to RIMs

- Munc13s, which through the interaction with SNAREs are involved in synaptic vesicle priming and synaptic plasticity
- Bassoon and Piccolo/Aczonin, very large vertebrate-specific proteins involved in binding and organizing synaptic vesicles at the synapse
- Liprin-as, which appear have a scaffolding function in the CAZ architecture
- CASK/Veli/Mint1, multivalent complexes which through PDZ domains and other interactions connect to various synaptic and cell adhesion molecules

It should be noted that the core fusion machinery, such as SNAREs, is also present at the active zone but is not enriched there (Gundelfinger and Fejtova, 2012; Sudhof, 2012).

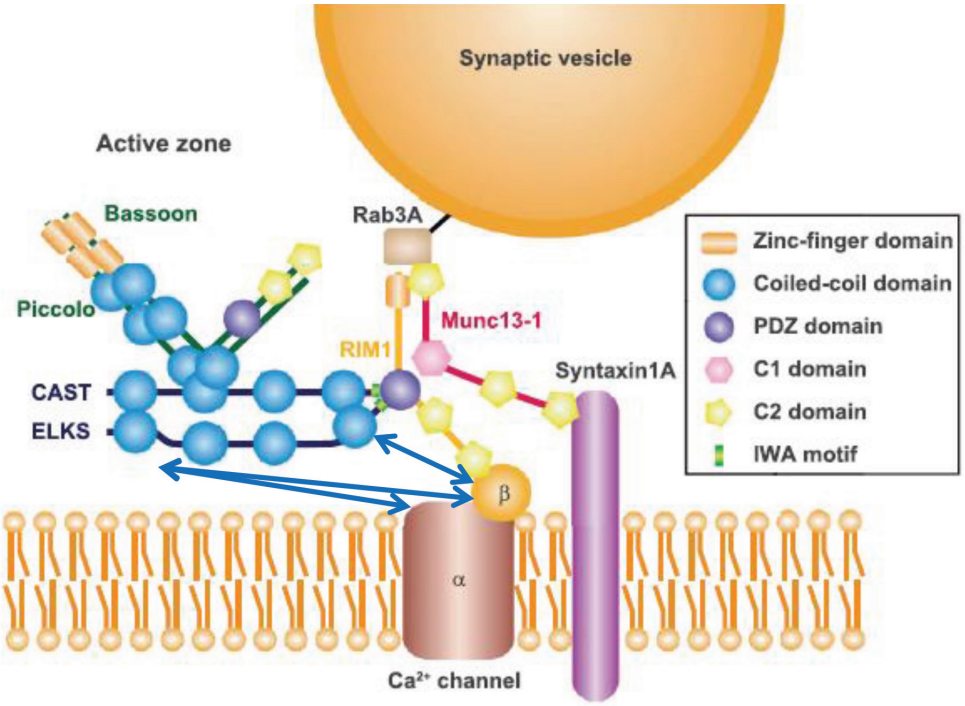

Figure 4. Schematic representation of the organization of the major players at the active zone. Active zone-specific proteins, ELKS, RIM1, Munc13-1, Bassoon and Piccolo form a hub to regulate neurotransmission of the synaptic vesicles at the presynaptic plasma membrane. ELKS directly binds to Piccolo and Bassoon via its second coiled coil region. The IWA motif at C terminus of CAST/ELKS is required for the interaction with RIM1 via the PDZ domain. RIM1 interacts with Rab3A and Munc13-1 via the zinc-finger domain at the N-terminus. The interactions of CAST with the α1 and β4 subunits of the Voltage-Dependent Calcium Channels (VDCCs) are also direct (marked with blue arrows). The interaction between CAST/ELKS and Munc13 is not indicated. Adapted from Hida and Ohtsuka, 2010.

Both CAST and ELKS directly associate with several CAZ components (Fig. 2B, Fig.4,5; Table I). As indicated above, both CAST and ELKS can interact with RIM1 through their C-terminal PDZ binding sequence IWA (Deguchi-Tawarada et al., 2004; Wang et al., 2002). For both proteins, alternatively spliced isoforms lacking these sequences also exist (ELKSε/ELKS1A and ELKS2A); however, RIM-binding CAST/ELKS isoforms (ELKSα/ELKS1B and CAST/ELKS2B) predominate in the brain (Kaeser et al., 2009; Liu et al., 2014). The expression of ELKS and CAST in the brain is similar, so that each protein accounts for ~50% of the total pool, although a particular isoform can be enriched in specific brain areas (Kaeser et al., 2009; Liu et al., 2014).

RIMs are evolutionarily conserved key players at the active zone, which act as molecular scaffolds that can interact with multiple synaptic proteins. RIMs encompass a zinc finger domain with surrounding α-helices at the N-terminus, a central PDZ domain and two C2 domains at the C-terminus (Fig. 5). RIM N-terminus binds to the N-terminus of Munc13 and to Rab3, and these interactions connect synaptic vesicles to the active zone (see Gundelfinger and Fejtova, 2012; Sudhof, 2012 and references therein). The PDZ domain of RIMs binds to CAST/ELKS and also to Ca^{2+} channels, an interaction required for the recruitment of the channels to the active zone (Kaeser et al., 2011). RIMs contain a proline-rich sequence that binds to the SH3 domain of RIM-BPs, which also contribute to recruitment of Ca^{2+} channels to the active zone (Hibino et al., 2002; Wang et al., 2000). The C-terminal C2 domains of RIMs bind to liprin-α proteins, synaptotagmin and possibly SNAREs and might regulate the function of Ca^{2+} channels (Coppola et al., 2001; Kaeser et al., 2011; Schoch et al., 2002). The function of the interaction between RIMs and CAST/ELKS is currently not completely clear; however, its significance is supported by the observation that RIM1α shows increased solubility in homogenates of brains of CAST knockout mice (Kaeser et al., 2009), and that CAST/ELKS solubility is increased in RIM1 knockout mice (Kaeser et al., 2008).

The other potential interacting partners of the PDZ-binding domain of CAST/ELKS are the Ligand-of-Numb protein X (LNX), an interactor of Numb with four PDZ domains (Higa et al., 2007), and the tandem PDZ protein syntenin-1, a factor known to associate with several synaptic components (Ko et al., 2006) (Fig. 2B, Fig.5, Table I). CAST was shown to co-localize with LNX in axons (Higa et al., 2007) and also to promote clustering of syntenin-1 (Ko et al., 2006),

but the physiological significance of these interactions requires further elucidation.

Through a coiled coil region in the middle of the molecule, CAST binds to the coiled coil domains of Bassoon and Piccolo/Aczonin (Takao-Rikitsu et al., 2004). The same region of CAST also bind to Munc13; in fact RIM1, Munc13, Bassoon, Piccolo/Aczonin and CAST form a complex interaction network which converges on the N-terminal part of Munc13 (Wang et al., 2009) (Fig.2B, Fig.4). Since the CAZ proteins are extensively interconnected through direct and indirect interactions, it is not possible to identify a clear hierarchy of their recruitment to presynaptic membrane. However, important players in such recruitment might be the liprin-α family members. Through its central coiled coil region, CAST binds to the second coiled coil in the N-terminal part of liprin-α1 (Ko et al., 2003) (Fig.2B, Fig.4, 5; Table I). An interaction between ELKS and liprin-α1 also exists, and, as described above, is relevant also in non-neuronal cells (Astro et al., 2014; van der Vaart et al., 2013). Studies in cultured hippocampal neurons demonstrated that the depletion of the most abundant hippocampal liprin-α isoform, liprin-α2, strongly affected presynaptic recruitment of several active zone proteins including CAST/ELKS, and caused a decrease in presynaptic efficacy (Spangler et al., 2013). Conversely, CAST/ELKS depletion had no significant effect on the recruitment of liprin-α2, suggesting that liprins act upstream of CAST/ELKS in protein targeting to the presynaptic membrane.

CAST and ELKS were also shown to bind to the β-subunits of voltage-gated Ca^{2+} channels (Billings et al., 2012; Chen et al., 2011; Kiyonaka et al., 2012); the interaction is direct and appears to involve both the N- and C-terminal parts of CAST, but does not involve either the middle part of the protein (which binds to Bassoon) or the RIM-binding C-terminal IWA sequence (Kiyonaka et al., 2012). This interaction is very likely to be functionally important, because the complete removal of both ELKS and CAST from cultured hippocampal neurons significantly reduced the action potential-triggered Ca^{2+}influx at inhibitory synapses (Liu et al., 2014). This effect appeared to be due to an altered regulation of the Ca^{2+} channels and not to the change in their localization at the active zone (Liu et al., 2014). CAST and ELKS might also bind to other transmembrane proteins, such as, for example, α7-containig nicotinic acetylcholine receptors, which can promote neurotransmitter release (Gomez-Varela and Berg, 2013).

The exact stoichiometry of the CAZ complexes is also not yet clear. Interestingly, staining of chemically fixed electron microscopy (EM) preparations of mammalian synapses with heavy metal ions revealed regularly spaced cone-shaped structures with a size of ~50 nm termed "dense projections". Whether these structures really exist or represent a fixation artifact is currently not clear, but they probably reflect in some way the modular structure of the CAZ (Gundelfinger and Fejtova, 2012; Limbach et al., 2011; Sudhof, 2012). EM-based mapping of the positions of different CAZ epitopes suggested that CAST and RIMs localize more closely to the plasma membrane than Piccolo/Aczonin (Limbach et al., 2011), which would fit with their respective roles in vesicle fusion/Ca2+ channel organization and vesicle guidance (Gundelfinger and Fejtova, 2012; Sudhof, 2012).

Initial studies of the function CAST and ELKS using protein overexpression and microinjection of CAST domains involved in binding to RIM1 and Bassoon suggested an essential role of these proteins in synaptic transmission (Takao-Rikitsu et al., 2004). The observation that ELKS overexpression increased stimulated exocytosis of the human growth hormone from PC12 cells supported the idea that ELKS is involved in RIM-Munc13-dependent secretion in neurons (Inoue et al., 2006). However, the subsequent well-controlled studies in knockout mice showed that the neuronal functions of CAST and ELKS might be more subtle. *CAST/ERC2/ELKS2* constitutive knockout mice are viable and fertile (Kaeser et al., 2009). Loss of CAST had no visible effect on the synapse ultrastructure or the number of docked vesicles, but increased the strength of inhibitory synaptic transmission and the size of the readily releasable pool of synaptic vesicles, possibly because CAST negatively affects vesicle priming through some yet unknown mechanisms (Kaeser et al., 2009).

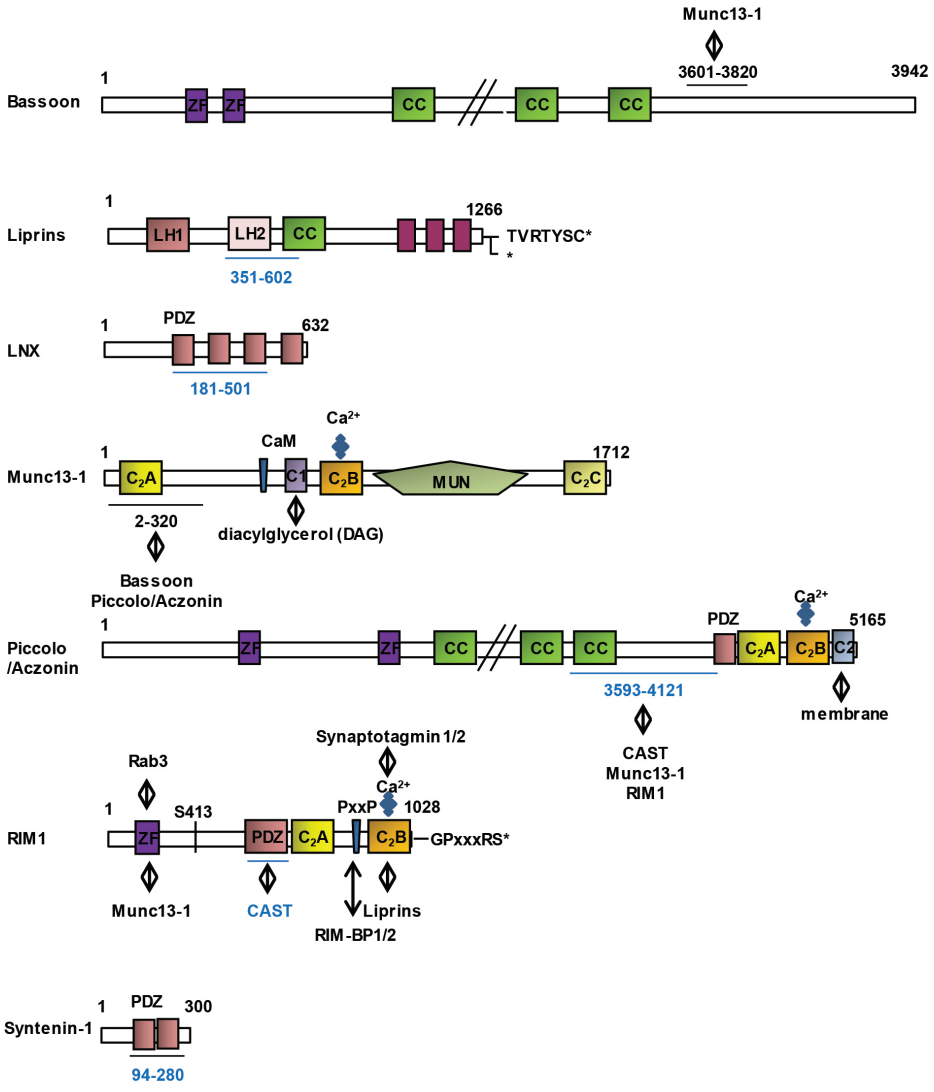

Figure 5. Domain structures of different CAST-interacting partners at the active zone. The amino acid positions of the domains responsible for the interactions with CAST are highlighted and indicated in blue. The schemes are not drawn exactly to scale.

The function of CAST has also been investigated in detail at the ribbon synapses, a unique type of chemical synapses present in photoreceptors in the retina (tom Dieck et al., 2005; tom Dieck et al., 2012). These synapses contain electron-dense bands extending from the sites of neurotransmitter release to the presynaptic cytoplasm. The structural integrity of these synapses depends on Bassoon, because in Bassoon knockout mice the ribbons containing the

specific synaptic component RIBEYE detach from the presynaptic membrane (Dick et al., 2003; tom Dieck et al., 2005). Bassoon interacts with RIBEYE, and this interaction is required for the assembly of the ribbon complex (tom Dieck et al., 2005). CAST is located close to the presynaptic membrane, together with RIM2, Munc13 and Ca^{2+} channels, and does not detach from the membrane together with RIBEYE in Bassoon mutants (tom Dieck et al., 2005). It should be noted that the functions of CAST and ELKS might be different at the ribbon synapse because while at the EM level CAST localizes at the base of the ribbon, ELKS seems to be located around the ribbons (Deguchi-Tawarada et al., 2006). In CAST knockout mice, the size of the active zones in rod receptors was reduced, leading to impaired visual processing, but the synaptic architecture was not altered (tom Dieck et al., 2012). ELKS was significantly (~1.7 times) upregulated in the retina of CAST knockout mice, and could potentially compensate to some extent for the loss of CAST function (tom Dieck et al., 2012).

The functional redundancy between CAST and ELKS was directly addressed by simultaneous acute deletion of CAST and ELKS (Liu et al., 2014). ELKS knockout mice die before day 14 of embryonic development, a phenotype that is unlikely to be caused by defects in synaptic function. Simultaneous disruption of the CAST and ELKS-encoding genes by expressing Cre recombinase in a double conditional knockout cultured hippocampal neurons had no dramatic effect on the neuronal morphology or number and structure of synapses. However, neurotransmitter release at inhibitory synapses was reduced by ~50%. Consistently, action potential-triggered Ca^{2+} influx was reduced, although the levels of presynaptic Ca^{2+} channels were not affected, suggesting that CAST and ELKS somehow modulate the Ca^{2+} channel function. The size of the readily releasable vesicle pool was unchanged, which is surprising, because an increase in this pool was observed in the single CAST knockout (Kaeser et al., 2009). This might be explained by the assumption that ELKS and CAST affect the readily releasable pool in opposite ways (Liu et al., 2014). Additional mouse studies using single and combined conditional deletions of CAST and ELKS in different types of neurons and specific synapses would be needed to understand the common, the non-redundant and the potentially opposing functions of these proteins.

Neuronal functions of the ELKS homologues in invertebrates

C. elegans has a single ELKS homologue, which is localized at the active zone and interacts with RIM; however, the worm ELKS and RIM do not depend on each other for the synaptic localization, and *elks* mutants display no defects in behavior or synaptic physiology (Deken et al., 2005). Similar to the mammalian system, the function of worm ELKS is strongly linked to that of liprin-α (SYD-2 in worm) (Dai et al., 2006). Loss of SYD-2 affected the size of presynaptic structures and disrupted the accumulation of synaptic vesicles, while a gain-of-function mutation in SYD-2 rescued the phenotype caused by the loss of another important synaptic protein, the Rho GAP SYD-1. This SYD-2 gain-of-function point mutation increased the binding of SYD-2 to ELKS, and ELKS was needed to the SYD-2-mediated rescue of the SYD-1 phenotype (Dai et al., 2006). The gain-of-function mutation in SYD-2 is located in the N-terminal coiled coil region of the protein which does not overlap with the mammalian liprin-α1 fragment reported to interact with ELKS (Dai et al., 2006; Ko et al., 2003). This mutation was shown to promote di- or oligomerization of SYD-2, and it has been proposed that the dimers or multimers of SYD-2 through their increased affinity for ELKS increase the recruitment of ELKS to the active zone and the size of the associated electron-dense projections (Kittelmann et al., 2013).Taken together, studies in worms suggest that ELKS contributes to the assembly of active zone, but its function might be redundant with other pathways.

In flies, the structure of the ELKS homologue strongly deviates from its worm and mammalian counterparts: the protein, which is called Bruchpilot, is significantly longer than ELKS, because an N-terminal ELKS-like domain is fused to an unrelated C-terminal domain with extensive coiled coil regions, which have no clear homology to any vertebrate proteins (Wagh et al., 2006). The name Bruchpilot (BRP) is derived from German for "crash pilot", due to unstable flight of the flies, in which the expression of the protein was reduced by RNA interference (Wagh et al., 2006).

In flies, prominent electron-dense projections are present at the presynaptic active zones; these projections, called T-bars, have table-like appearance that can be visible as T-like cross-sections in electron microscopy (Wichmann and Sigrist, 2010). The T-bars were absent from the photoreceptor terminals and NMJ of flies depleted of BRP (Wagh et al., 2006). Subsequent detailed studies

showed that null *brp* mutants are not viable but can survive up to larval stage (Kittel et al., 2006). This work confirmed the essential role of BRP in synaptic function and formation of T-bars, and demonstrated BRP involvement in recruitment of Ca^{2+} channels to the docking sites of synaptic vesicles (Kittel et al., 2006). Analysis of the localization of N- and C-terminal epitopes of BRP using a combination of stimulated emission depletion (STED) microscopy with confocal microscopy and electron microscopy showed that BRP proteins are direct T-bar components. BRP forms complexes that adopt a funnel-like organization, with the N-terminal ends (the CAST/ELKS-homologous part) located close to the plasma membrane and the C-terminal parts splaying out into a donut-shaped structure (Fouquet et al., 2009; Kittel et al., 2006). Ca^{2+} channels bind to the BRP N-terminus (Fouquet et al., 2009), while the C-terminal 17 amino acids are required for tethering of synaptic vesicles, as their deletion led to normally shaped electron-dense bodies that were devoid of vesicles, a phenotype associated with synaptic depression (Hallermann et al., 2010). BRP does not appear to be required for the initial recruitment of Ca^{2+} channels to the active zone but might be more important for the maintenance of channel clustering (Wichmann and Sigrist, 2010). Further work showed that BRP is expressed as two isoforms differing at their N-termini; the isoform-specific mutations affected basal synaptic transmission and detailed analysis showed that the combined function of the two isoforms, which together form BRP filaments, regulates the readily releasable pool of synaptic vesicles (Matkovic et al., 2013). During active zone assembly, BRP acts downstream of the fly homologue of SYD-1, with which it interacts, as it arrives to the presynaptic membrane relatively late, after Syd-1 and liprin-α (Fouquet et al., 2009; Owald et al., 2010). These results are consistent with the data obtained in worms and mammals demonstrating that liprins can promote ELKS recruitment to the presynaptic membrane. Importantly, due to the large C-terminal extension, BRP appears to combine the functions of ELKS and Bassoon/Piccolo, acting in both the regulation of Ca^{2+} influx and synaptic vesicle binding (Wichmann and Sigrist, 2010).

The role of ELKS in secretion in pancreatic β cells and mast cells

In addition to neurons, our body contains many other cell types that secrete specific molecules in response to stimuli. Well-studied examples of such secretory cells are pancreatic β cells, which produce insulin when stimulated with glucose

in order to maintain glucose homeostasis, and mast cells, immune cells that secrete inflammatory mediators. Most secretory cells share some of the components of the exocytotic machinery with the neurons and, not surprisingly, the ubiquitously expressed ELKS protein appears to play a role in regulated exocytosis in these cell types.

In pancreatic β cells, insulin secretion is stimulated by the elevation of the levels of extracellular glucose, which is rapidly taken up and metabolized, resulting in an increase in the ATP:ADP ratio (MacDonald, 2011; Meglasson and Matschinsky, 1986; Wang and Thurmond, 2009). This leads to cell depolarization and Ca^{2+} influx, which triggers the exocytosis of insulin granules. Additional pathways, which include receptor-mediated generation of cyclic AMP (cAMP) and other signaling mediators, are involved in enhancing insulin secretion by promoting insulin granule recruitment and priming at the plasma membrane (MacDonald, 2011; Wang and Thurmond, 2009). Insulin secretion is biphasic, with a first rapid phase of 5-10 min, which is probably accounted for by the readily releasable pool of pre-docked insulin granules, and the second phase, which can be sustained for several hours when glucose levels remain elevated. Several components characteristic for the neuronal CAZ and SNARE accessory factors, such as RIM2, Piccolo, Munc13 and Munc18, are present in pancreatic β cells (MacDonald, 2011; Wang and Thurmond, 2009). While CAST is not expressed in the pancreas, ELKS is abundantly present (Fujimoto et al., 2002; Ohara-Imaizumi et al., 2005). In clonal insulin-producing cell line MIN6 ELKS localizes as clusters at the cell cortex (Ohara-Imaizumi et al., 2005). These clusters often coincide with the sites of docking and fusion of insulin granules, and consistent with this observation, ELKS clusters show significant overlap with the clusters of the SNARE syntaxin 1 (Ohara-Imaizumi et al., 2005). ELKS also colocalises with Bassoon, and Bassoon-binding ELKS fragment introduced in β cells, as well as partial ELKS depletion, caused inhibition of insulin exocytosis (Ohara-Imaizumi et al., 2005). Insulin secretion might be regulated by the interactions of ELKS with RIM2 and Bassoon, but the underlying mechanism requires further elucidation.

ELKS was also found to be expressed in the rat basophilic leukemia cells (RBL-2H3, a cell culture model of mast cells), together with other CAZ components such as Munc13-1, liprin-α1 and RIM (Nomura et al., 2009; Nomura et al., 2011). ELKS depletion reduced degranulation when cells were stimulated with a specific antigen; however, the increase of Ca^{2+} concentration after antigen

stimulation was not affected, suggesting that in this cell type ELKS acts downstream of Ca^{2+} influx (Nomura et al., 2009). A fluorescent fusion of ELKS was found in the cytosol, and its translocation towards plasma membrane was observed upon stimulation (Nomura et al., 2009). Liprin-α1, the binding partner of ELKS, was also found to be involved in exocytosis as well as spreading of mast cells, suggesting that the two proteins are likely to act in concert (Nomura et al., 2011). Taken together, these data suggests the existence of conserved machinery responsible for regulated exocytosis in multiple different cell types, with ELKS being a ubiquitous component.

The role of ELKS in NF-κB signaling

A separate line of studies identified ELKS as a player in the NF-kappaB signaling pathway (Ducut Sigala et al., 2004). NF-κB regulates cell survival and proliferation during inflammation, immune response, infection, stress or cancer (Ghosh and Karin, 2002; Karin et al., 2004; Li and Verma, 2002). In the classical NF-kappaB pathway, the transcription factors of NF-κB family are kept inactive in the cytoplasm through the interaction with their inhibitors (IκB) (Ghosh and Karin, 2002; Hayden and Ghosh, 2004; Li and Verma, 2002). When IκB is phosphorylated by IκB kinase (IKK), it is targeted for degradation by proteasome machinery (Fig. 6). As a result, NF-κB dimers are released into the nucleus where they activate transcription of various genes important for protection against apoptosis, cell growth, proliferation and morphogenesis. IKK consists of two catalytic subunits, IKK1 (alpha) and IKK2 (beta), and a regulatory factor NEMO (also known as IKK gamma). IKK can be activated by multiple upstream factors, such as tumour necrosis factor (TNF), B- and T-cell receptors with their associated proteins, or the nuclear ataxia telangiectasia mutated (ATM) in response to DNA damage (Kovalenko and Wallach, 2006; Weil and Israel, 2004; Wu et al., 2006). ELKS was identified as an essential regulator of IKK, necessary for efficient NF-κB activation by different stimuli (Ducut Sigala et al., 2004; Wu et al., 2006). It was initially shown that ELKS interacts with IKK subunits as well as with IκB in cells where NF-κB signaling is induced by TNF-α treatment (Ducut Sigala et al., 2004).

A subsequent study focused on the role of ELKS in the induction of NF-κB signaling by genotoxic stress and showed that ELKS functioned downstream of ATM but upstream of IKK in DNA damage-induced NF-κB activation (Wu et al., 2006). When DNA double-strand breaks are induced (Fig. 6), a small frac-

tion of ATM exits nucleus and associates with IKK catalytic subunits through interaction with NEMO and ELKS (Wu et al., 2006).

The underlying mechanism appears to be complex: in response to genotoxic stimulation ELKS is modified by the addition of K63-ubiquitin chains, a process which is facilitated by the ubiquitin ligase XIAP (X-linked inhibitor of apoptosis) (Wu et al., 2010). K63-linked polyubiquitination of ELKS promotes the formation of a complex between ELKS, the IKKs and TGFβ-activated kinase (TAK1), which is also required for the activation of NF-κB signaling (Wu et al., 2010) (Fig.6). In this work, the authors generated ELKS knockout mice using a gene trap insertion between exons 5 and 6 of the *ERC1* gene and found that ELKS knockout mouse embryonic fibroblasts were defective in the activation of TAK1, IKK and NF-κB upon treatment with genotoxic agents. Mice heterozygous for the *ERC1* knockout allele were more sensitive to ionizing radiation compared to wild type counterparts, supporting the view that ELKS plays an important role in physiological responses to genotoxic agents (Wu et al., 2010). In a follow-up study, the same authors provided evidence indicating that a cytosolic pool of ELKS with K63-linked polyubiquitin chains forms a platform to recruit NEMO and the E3 ligase linear ubiquitin chain assembly complex (LUBAC) that promotes linear ubiquitination of NEMO, which in turn is needed for genotoxic stress-induced activation of NF-κB (Niu et al., 2011). It is currently unclear whether the ELKS-mediated assembly of the signaling complexes occurs at the cell cortex or in the cytosol. It would be interesting to know whether the scaffolding roles of ELKS in NF-κB signaling and secretion are functionally related.

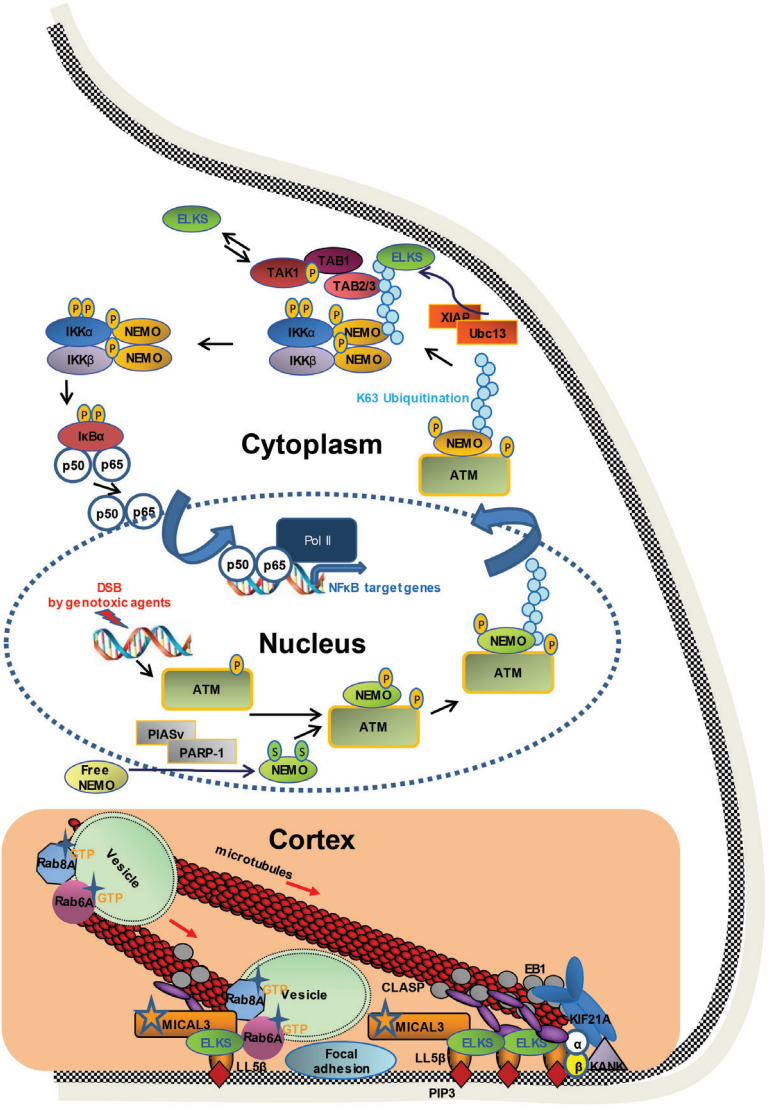

Figure 6. The role of ELKS in the NF-κB signaling pathway and the cortical pathway. Transcription factors of the NF-κB family, p50 and p65 heterodimers are kept inactive in the cytoplasm by interacting with IκB. In response to DNA damage caused by genotoxic agents, the NF-κB pathway is activated in a manner dependent on NEMO and ELKS. Induction of double-stranded breaks activates ATM, and free NEMO enters the nucleus with participation of some accessory factors. NEMO forms a complex with activated ATM, exits the nucleus and promotes K63-polyubiquitination of ELKS in the cytoplasm by XIAP and Ubc13. This leads to the formation of ELKS/TAK1/TAB2/TAB3 complex, which is required for the activation of the downstream NF-κB signaling, as it activates the IKK complex composed of IKKα and IKKβ and NEMO. Activation of the IKK complex leads to phosphorylation of IκB; the phosphorylated IκB releases p50 and p65 and is targeted for proteasome degradation. Active p50/p65 are then transported into nucleus to regulate downstream gene transcription. These regulatory events associated with ELKS take place in cytoplasm, where ELKS also participates in the regulation of microtubule anchoring and exocytosis (depicted at the bottom of the image), but it is currently unclear whether and how the two pathways intersect. Adapted from Wu et al., 2010 and Hadian and Krappmann, 2011.

Involvement of ELKS in human disease

ELKS-encoding gene *ERC1* was suggested to be an interesting candidate gene for the autism spectrum disorder, based on studies of a patient with a 1.5 Mb-large 12p13.33 deletion which removed 13 genes including *ERC1* (Silva et al., 2014). In another study, analysis of 9 patients with a speech delay revealed 12p13.33 subtelomeric or interstitial rearrangements; all these patients had an overlapping deletion in *ERC1*, which suggests that ELKS might be a candidate gene for this disability (Thevenon et al., 2013). Furthermore, ELKS was also identified as a new and rare antigen present in the sera of patients with Lambert-Eaton myasthenic syndrome, a condition characterized by fluctuating muscle weakness and autonomic dysfunction (Huijbers et al., 2013). It should be noted that in none of these cases the functional involvement of ELKS has been properly established, and more studies will be needed to dissect the importance of ELKS in these human syndromes.

Conclusion

The overview of the literature shows that ELKS is a mutifunctional adaptor protein involved in a very diverse set of pathways including cytoskeletal organization, vesicle trafficking and signaling. ELKS is a coiled coil-containing scaffolding factor, which participates in all these pathways by forming binding platforms for other proteins.

References

Airaksinen, M.S., A. Titievsky, and M. Saarma. 1999. GDNF family neurotrophic factor signaling: four masters, one servant? *Mol Cell Neurosci*. 13:313-25.

Akhmanova, A., C.C. Hoogenraad, K. Drabek, T. Stepanova, B. Dortland, T. Verkerk, W. Vermeulen, B.M. Burgering, C.I. De Zeeuw, F. Grosveld, and N. Galjart. 2001. Clasps are CLIP-115 and -170 associating proteins involved in the regional regulation of microtubule dynamics in motile fibroblasts. *Cell*. 104:923-35.

Asperti, C., E. Pettinato, and I. de Curtis. 2010. Liprin-alpha1 affects the distribution of low-affinity beta1 integrins and stabilizes their permanence at the cell surface. *Exp Cell Res*. 316:915-26.

Astro, V., S. Chiaretti, E. Magistrati, M. Fivaz, and I. de Curtis. 2014. Liprin-alpha1, ERC1 and LL5 define polarized and dynamic structures that are implicated in cell migration. *J Cell Sci*. 127:3862-76.

Basu, S., S. Sladecek, Y.V.I. Martinez de la Pena, M. Akaaboune, I. Smal, K. Martin, N. Galjart, and H.R. Brenner. 2015. CLASP2-dependent microtubule capture at the neuromuscular junction membrane requires LL5beta and actin for focal delivery of acetylcholine receptor vesicles. *Mol Biol Cell*.

Basu, S., S. Sladecek, H. Pemble, T. Wittmann, J.A. Slotman, W. van Cappellen, H.R. Brenner, and N. Galjart. 2014. Acetylcholine receptor (AChR) clustering is regulated both by glycogen synthase kinase 3beta (GSK-3beta)-dependent phosphorylation and the level of CLIP-associated protein 2 (CLASP2) mediating the capture of microtubule plus-ends. *J Biol Chem*. 289:30857-67.

Billings, S.E., G.L. Clarke, and H. Nishimune. 2012. ELKS1 and Ca(2+) channel subunit beta4 interact and colocalize at cerebellar synapses. *Neuroreport*. 23:49-54.

Chen, J., S.E. Billings, and H. Nishimune. 2011. Calcium channels link the muscle-derived synapse organizer laminin beta2 to Bassoon and CAST/Erc2 to organize presynaptic active zones. *J Neurosci*. 31:512-25.

Coppola, T., S. Magnin-Luthi, V. Perret-Menoud, S. Gattesco, G. Schiavo, and R. Regazzi. 2001. Direct interaction of the Rab3 effector RIM with Ca2+ channels, SNAP-25, and synaptotagmin. *J Biol Chem*. 276:32756-62.

Dai, Y., H. Taru, S.L. Deken, B. Grill, B. Ackley, M.L. Nonet, and Y. Jin. 2006. SYD-2 Liprin-alpha organizes presynaptic active zone formation through ELKS. *Nat Neurosci*. 9:1479-1487.

de Curtis, I. 2011. Function of liprins in cell motility. *Exp Cell Res*. 317:1-8.

Deguchi-Tawarada, M., E. Inoue, E. Takao-Rikitsu, M. Inoue, I. Kitajima, T. Ohtsuka, and Y. Takai. 2006. Active zone protein CAST is a component of conventional and ribbon synapses in mouse retina. *J Comp Neurol*. 495:480-96.

Deguchi-Tawarada, M., E. Inoue, E. Takao-Rikitsu, M. Inoue, T. Ohtsuka, and Y. Takai. 2004. CAST2: identification and characterization of a protein structurally related to the presynaptic cytomatrix protein CAST. *Genes Cells*. 9:15-23.

Deken, S.L., R. Vincent, G. Hadwiger, Q. Liu, Z.W. Wang, and M.L. Nonet. 2005. Redundant localization mechanisms of RIM and ELKS in Caenorhabditis elegans. *J Neurosci*. 25:5975-83.

Del Nery, E., S. Miserey-Lenkei, T. Falguieres, C. Nizak, L. Johannes, F. Perez, and B. Goud. 2006. Rab6A and Rab6A' GTPases play non-overlapping roles in membrane trafficking. *Traffic*. 7:394-407.

Dick, O., S. tom Dieck, W.D. Altrock, J. Ammermuller, R. Weiler, C.C. Garner, E.D. Gundelfinger, and J.H. Brandstatter. 2003. The presynaptic active zone protein bassoon is essential for photoreceptor ribbon synapse formation in the retina. *Neuron*. 37:775-86.

Ducut Sigala, J.L., V. Bottero, D.B. Young, A. Shevchenko, F. Mercurio, and I.M. Verma. 2004. Activation of transcription factor NF-kappaB requires ELKS, an IkappaB kinase regulatory subunit. *Science*. 304:1963-7.

Fouquet, W., D. Owald, C. Wichmann, S. Mertel, H. Depner, M. Dyba, S. Hallermann, R.J. Kittel, S. Eimer, and S.J. Sigrist. 2009. Maturation of active zone assembly by Drosophila Bruchpilot. *J Cell Biol*. 186:129-45.

Fujimoto, K., T. Shibasaki, N. Yokoi, Y. Kashima, M. Matsumoto, T. Sasaki, N. Tajima, T. Iwanaga, and S. Seino. 2002. Piccolo, a Ca2+ sensor in pancreatic beta-cells. Involvement of cAMP-GEFII.Rim2. Piccolo complex in cAMP-dependent exocytosis. *J Biol Chem*. 277:50497-502.

Ghosh, S., and M. Karin. 2002. Missing pieces in the NF-kappaB puzzle. *Cell*. 109 Suppl:S81-96.

Girod, A., B. Storrie, J.C. Simpson, L. Johannes, B. Goud, L.M. Roberts, J.M. Lord, T. Nilsson, and R. Pepperkok. 1999. Evidence for a COP-I-in-

dependent transport route from the Golgi complex to the endoplasmic reticulum. *Nat Cell Biol*. 1:423-30.

Gomez-Varela, D., and D.K. Berg. 2013. Lateral mobility of presynaptic alpha7-containing nicotinic receptors and its relevance for glutamate release. *J Neurosci*. 33:17062-71.

Grigoriev, I., D. Splinter, N. Keijzer, P.S. Wulf, J. Demmers, T. Ohtsuka, M. Modesti, I.V. Maly, F. Grosveld, C.C. Hoogenraad, and A. Akhmanova. 2007. Rab6 regulates transport and targeting of exocytotic carriers. *Dev Cell*. 13:305-14.

Gundelfinger, E.D., and A. Fejtova. 2012. Molecular organization and plasticity of the cytomatrix at the active zone. *Curr Opin Neurobiol*. 22:423-30.

Hadian, K., and D. Krappmann. 2011. Signals from the nucleus: activation of NF-kappaB by cytosolic ATM in the DNA damage response. Sci Signal. 4:pe2.

Hallermann, S., R.J. Kittel, C. Wichmann, A. Weyhersmuller, W. Fouquet, S. Mertel, D. Owald, S. Eimer, H. Depner, M. Schwarzel, S.J. Sigrist, and M. Heckmann. 2010. Naked dense bodies provoke depression. *J Neurosci*. 30:14340-5.

Hayden, M.S., and S. Ghosh. 2004. Signaling to NF-kappaB. *Genes Dev*. 18:2195-224.

Hibino, H., R. Pironkova, O. Onwumere, M. Vologodskaia, A.J. Hudspeth, and F. Lesage. 2002. RIM binding proteins (RBPs) couple Rab3-interacting molecules (RIMs) to *voltage*-gated Ca(2+) channels. *Neuron*. 34:411-23.

Hida, Y., and T. Ohtsuka. 2010. CAST and ELKS proteins: structural and functional determinants of the presynaptic active zone. *J Biochem*. 148:131-7.

Higa, S., T. Tokoro, E. Inoue, I. Kitajima, and T. Ohtsuka. 2007. The active zone protein CAST directly associates with Ligand-of-Numb protein X. *Biochem Biophys Res Commun*. 354:686-92.

Hotta, A., T. Kawakatsu, T. Nakatani, T. Sato, C. Matsui, T. Sukezane, T. Akagi, T. Hamaji, I. Grigoriev, A. Akhmanova, Y. Takai, and Y. Mimori-Kiyosue. 2010. Laminin-based cell adhesion anchors microtubule plus ends to the epithelial cell basal cortex through LL5alpha/beta. *J Cell Biol*. 189:901-17.

Huijbers, M.G., A.F. Lipka, M. Potman, P.J. Hensbergen, M.J. Titulaer, E.H. Niks, S.M. van der Maarel, R. Klooster, and J.J. Verschuuren. 2013. Antibodies to active zone protein ERC1 in Lambert-Eaton myasthenic syn-

drome. *Hum Immunol*. 74:849-51.

Inoue, E., M. Deguchi-Tawarada, E. Takao-Rikitsu, M. Inoue, I. Kitajima, T. Ohtsuka, and Y. Takai. 2006. ELKS, a protein structurally related to the active zone protein CAST, is involved in Ca2+-dependent exocytosis from PC12 cells. *Genes Cells*. 11:659-72.

Kaeser, P.S., L. Deng, A.E. Chavez, X. Liu, P.E. Castillo, and T.C. Sudhof. 2009. ELKS2alpha/CAST deletion selectively increases neurotransmitter release at inhibitory synapses. *Neuron*. 64:227-39.

Kaeser, P.S., L. Deng, Y. Wang, I. Dulubova, X. Liu, J. Rizo, and T.C. Sudhof. 2011. RIM proteins tether Ca2+ channels to presynaptic active zones via a direct PDZ-domain interaction. *Cell*. 144:282-95.

Kaeser, P.S., H.B. Kwon, C.Q. Chiu, L. Deng, P.E. Castillo, and T.C. Sudhof. 2008. RIM1alpha and RIM1beta are synthesized from distinct promoters of the RIM1 gene to mediate differential but overlapping synaptic functions. *J Neurosci*. 28:13435-47.

Karin, M., Y. Yamamoto, and Q.M. Wang. 2004. The IKK NF-kappa B system: a treasure trove for drug development. *Nat Rev Drug Discov*. 3:17-26.

Kikuno, R., T. Nagase, K. Ishikawa, M. Hirosawa, N. Miyajima, A. Tanaka, H. Kotani, N. Nomura, and O. Ohara. 1999. Prediction of the coding sequences of unidentified human genes. XIV. The complete sequences of 100 new cDNA clones from brain which code for large proteins in vitro. *DNA Res*. 6:197-205.

Kishi, M., T.T. Kummer, S.J. Eglen, and J.R. Sanes. 2005. LL5beta: a regulator of postsynaptic differentiation identified in a screen for synaptically enriched transcripts at the neuromuscular junction. *J Cell Biol*. 169:355-66.

Kittel, R.J., C. Wichmann, T.M. Rasse, W. Fouquet, M. Schmidt, A. Schmid, D.A. Wagh, C. Pawlu, R.R. Kellner, K.I. Willig, S.W. Hell, E. Buchner, M. Heckmann, and S.J. Sigrist. 2006. Bruchpilot promotes active zone assembly, Ca2+ channel clustering, and vesicle release. *Science*. 312:1051-4.

Kittelmann, M., J. Hegermann, A. Goncharov, H. Taru, M.H. Ellisman, J.E. Richmond, Y. Jin, and S. Eimer. 2013. Liprin-alpha/SYD-2 determines the size of dense projections in presynaptic active zones in C. elegans. *J Cell Biol*. 203:849-63.

Kiyonaka, S., H. Nakajima, Y. Takada, Y. Hida, T. Yoshioka, A. Hagiwara, I. Kitajima, Y. Mori, and T. Ohtsuka. 2012. Physical and functional inter-

action of the active zone protein CAST/ERC2 and the beta-subunit of the voltage-dependent Ca(2+) channel. *J Biochem*. 152:149-59.

Ko, J., M. Na, S. Kim, J.R. Lee, and E. Kim. 2003. Interaction of the ERC family of RIM-binding proteins with the liprin-alpha family of multidomain proteins. *J Biol Chem*. 278:42377-85.

Ko, J., C. Yoon, G. Piccoli, H.S. Chung, K. Kim, J.R. Lee, H.W. Lee, H. Kim, C. Sala, and E. Kim. 2006. Organization of the presynaptic active zone by ERC2/CAST1-dependent clustering of the tandem PDZ protein syntenin-1. *J Neurosci*. 26:963-70.

Kovalenko, A., and D. Wallach. 2006. If the prophet does not come to the mountain: dynamics of signaling complexes in NF-kappaB activation. *Mol Cell*. 22:433-6.

Lansbergen, G., I. Grigoriev, Y. Mimori-Kiyosue, T. Ohtsuka, S. Higa, I. Kitajima, J. Demmers, N. Galjart, A.B. Houtsmuller, F. Grosveld, and A. Akhmanova. 2006. CLASPs attach microtubule plus ends to the cell cortex through a complex with LL5beta. *Dev Cell*. 11:21-32.

Li, Q., and I.M. Verma. 2002. NF-kappaB regulation in the immune system. *Nat Rev Immunol*. 2:725-34.

Limbach, C., M.M. Laue, X. Wang, B. Hu, N. Thiede, G. Hultqvist, and M.W. Kilimann. 2011. Molecular in situ topology of Aczonin/Piccolo and associated proteins at the mammalian neurotransmitter release site. *Proc Natl Acad Sci U S A*. 108:E392-401.

Liu, C., L.S. Bickford, R.G. Held, H. Nyitrai, T.C. Sudhof, and P.S. Kaeser. 2014. The active zone protein family ELKS supports Ca2+ influx at nerve terminals of inhibitory hippocampal neurons. *J Neurosci*. 34:12289-303.

Lu, J., H. Li, Y. Wang, T.C. Sudhof, and J. Rizo. 2005. Solution structure of the RIM1alpha PDZ domain in complex with an ELKS1b C-terminal peptide. *J Mol Biol*. 352:455-66.

MacDonald, P.E. 2011. Signal integration at the level of ion channel and exocytotic function in pancreatic beta-cells. *Am J Physiol Endocrinol Metab*. 301:E1065-9.

Martinez, O., C. Antony, G. Pehau-Arnaudet, E.G. Berger, J. Salamero, and B. Goud. 1997. GTP-bound forms of rab6 induce the redistribution of Golgi proteins into the endoplasmic reticulum. *Proc Natl Acad Sci U S A*. 94:1828-33.

Martinez, O., A. Schmidt, J. Salamero, B. Hoflack, M. Roa, and B. Goud. 1994.

The small GTP-binding protein rab6 functions in intra-Golgi transport. *J Cell Biol*. 127:1575-88.

Matkovic, T., M. Siebert, E. Knoche, H. Depner, S. Mertel, D. Owald, M. Schmidt, U. Thomas, A. Sickmann, D. Kamin, S.W. Hell, J. Burger, C. Hollmann, T. Mielke, C. Wichmann, and S.J. Sigrist. 2013. The Bruchpilot cytomatrix determines the size of the readily releasable pool of synaptic vesicles. *J Cell Biol*. 202:667-83.

Meglasson, M.D., and F.M. Matschinsky. 1986. Pancreatic islet glucose metabolism and regulation of insulin secretion. *Diabetes Metab Rev*. 2:163-214.

Mimori-Kiyosue, Y., I. Grigoriev, G. Lansbergen, H. Sasaki, C. Matsui, F. Severin, N. Galjart, F. Grosveld, I. Vorobjev, S. Tsukita, and A. Akhmanova. 2005. CLASP1 and CLASP2 bind to EB1 and regulate microtubule plus-end dynamics at the cell cortex. *J Cell Biol*. 168:141-53.

Monier, S., F. Jollivet, I. Janoueix-Lerosey, L. Johannes, and B. Goud. 2002. Characterization of novel Rab6-interacting proteins involved in endosome-to-TGN transport. *Traffic*. 3:289-97.

Nakata, T., Y. Kitamura, K. Shimizu, S. Tanaka, M. Fujimori, S. Yokoyama, K. Ito, and M. Emi. 1999. Fusion of a novel gene, ELKS, to RET due to translocation t(10;12)(q11;p13) in a papillary thyroid carcinoma. *Genes Chromosomes Cancer*. 25:97-103.

Nakata, T., T. Yokota, M. Emi, and S. Minami. 2002. Differential expression of multiple isoforms of the ELKS mRNAs involved in a papillary thyroid carcinoma. *Genes Chromosomes Cancer*. 35:30-7.

Nakaya, Y., E.W. Sukowati, and G. Sheng. 2013. Epiblast integrity requires CLASP and Dystroglycan-mediated microtubule anchoring to the basal cortex. *J Cell Biol*. 202:637-51.

Niu, J., Y. Shi, K. Iwai, and Z.H. Wu. 2011. LUBAC regulates NF-kappaB activation upon genotoxic stress by promoting linear ubiquitination of NEMO. *EMBO J*. 30:3741-53.

Nomura, H., T. Ohtsuka, S. Tadokoro, M. Tanaka, and N. Hirashima. 2009. Involvement of ELKS, an active zone protein, in exocytotic release from RBL-2H3 cells. *Cell Immunol*. 258:204-11.

Nomura, H., S. Tadokoro, and N. Hirashima. 2011. Liprin-alpha is involved in exocytosis and cell spreading in mast cells. *Immunol Lett*. 139:110-6.

Ohara-Imaizumi, M., T. Ohtsuka, S. Matsushima, Y. Akimoto, C. Nishiwaki, Y. Nakamichi, T. Kikuta, S. Nagai, H. Kawakami, T. Watanabe, and

S. Nagamatsu. 2005. ELKS, a protein structurally related to the active zone-associated protein CAST, is expressed in pancreatic beta cells and functions in insulin exocytosis: interaction of ELKS with exocytotic machinery analyzed by total internal reflection fluorescence microscopy. *Mol Biol Cell*. 16:3289-300.

Ohtsuka, T., E. Takao-Rikitsu, E. Inoue, M. Inoue, M. Takeuchi, K. Matsubara, M. Deguchi-Tawarada, K. Satoh, K. Morimoto, H. Nakanishi, and Y. Takai. 2002. Cast: a novel protein of the cytomatrix at the active zone of synapses that forms a ternary complex with RIM1 and munc13-1. *J Cell Biol*. 158:577-90.

Owald, D., W. Fouquet, M. Schmidt, C. Wichmann, S. Mertel, H. Depner, F. Christiansen, C. Zube, C. Quentin, J. Korner, H. Urlaub, K. Mechtler, and S.J. Sigrist. 2010. A Syd-1 homologue regulates pre- and postsynaptic maturation in Drosophila. *J Cell Biol*. 188:565-79.

Paranavitane, V., W.J. Coadwell, A. Eguinoa, P.T. Hawkins, and L. Stephens. 2003. LL5beta is a phosphatidylinositol (3,4,5)-trisphosphate sensor that can bind the cytoskeletal adaptor, gamma-filamin. *J Biol Chem*. 278:1328-35.

Proszynski, T.J., J. Gingras, G. Valdez, K. Krzewski, and J.R. Sanes. 2009. Podosomes are present in a postsynaptic apparatus and participate in its maturation. *Proc Natl Acad Sci U S A*. 106:18373-8.

Proszynski, T.J., and J.R. Sanes. 2013. Amotl2 interacts with LL5beta, localizes to podosomes and regulates postsynaptic differentiation in muscle. *J Cell Sci*. 126:2225-35.

Schmidt, N., S. Basu, S. Sladecek, S. Gatti, J. van Haren, S. Treves, J. Pielage, N. Galjart, and H.R. Brenner. 2012. Agrin regulates CLASP2-mediated capture of microtubules at the neuromuscular junction synaptic membrane. *J Cell Biol*. 198:421-37.

Schoch, S., P.E. Castillo, T. Jo, K. Mukherjee, M. Geppert, Y. Wang, F. Schmitz, R.C. Malenka, and T.C. Sudhof. 2002. RIM1alpha forms a protein scaffold for regulating neurotransmitter release at the active zone. *Nature*. 415:321-6.

Silva, I.M., J. Rosenfeld, S.A. Antoniuk, S. Raskin, and V.S. Sotomaior. 2014. A 1.5Mb terminal deletion of 12p associated with autism spectrum disorder. *Gene*. 542:83-6.

Spangler, S.A., and C.C. Hoogenraad. 2007. Liprin-alpha proteins: scaffold

molecules for synapse maturation. *Biochem Soc Trans*. 35:1278-82.

Spangler, S.A., S.K. Schmitz, J.T. Kevenaar, E. de Graaff, H. de Wit, J. Demmers, R.F. Toonen, and C.C. Hoogenraad. 2013. Liprin-alpha2 promotes the presynaptic recruitment and turnover of RIM1/CASK to facilitate synaptic transmission. *J Cell Biol*. 201:915-28.

Stehbens, S.J., M. Paszek, H. Pemble, A. Ettinger, S. Gierke, and T. Wittmann. 2014. CLASPs link focal-adhesion-associated microtubule capture to localized exocytosis and adhesion site turnover. *Nat Cell Biol*. 16:561-73.

Sudhof, T.C. 2012. The presynaptic active zone. *Neuron*. 75:11-25.

Takao-Rikitsu, E., S. Mochida, E. Inoue, M. Deguchi-Tawarada, M. Inoue, T. Ohtsuka, and Y. Takai. 2004. Physical and functional interaction of the active zone proteins, CAST, RIM1, and Bassoon, in neurotransmitter release. *J Cell Biol*. 164:301-11.

Thevenon, J., P. Callier, J. Andrieux, B. Delobel, A. David, S. Sukno, D. Minot, L. Mosca Anne, N. Marle, D. Sanlaville, M. Bonnet, A. Masurel-Paulet, F. Levy, L. Gaunt, S. Farrell, C. Le Caignec, A. Toutain, V. Carmignac, F. Mugneret, J. Clayton-Smith, C. Thauvin-Robinet, and L. Faivre. 2013. 12p13.33 microdeletion including ELKS/ERC1, a new locus associated with childhood apraxia of speech. *Eur J Hum Genet*. 21:82-8.

Tokoro, T., S. Higa, M. Deguchi-Tawarada, E. Inoue, I. Kitajima, and T. Ohtsuka. 2007. Localization of the active zone proteins CAST, ELKS, and Piccolo at neuromuscular junctions. *Neuroreport*. 18:313-6.

tom Dieck, S., W.D. Altrock, M.M. Kessels, B. Qualmann, H. Regus, D. Brauner, A. Fejtova, O. Bracko, E.D. Gundelfinger, and J.H. Brandstatter. 2005. Molecular dissection of the photoreceptor ribbon synapse: physical interaction of Bassoon and RIBEYE is essential for the assembly of the ribbon complex. *J Cell Biol*. 168:825-36.

tom Dieck, S., D. Specht, N. Strenzke, Y. Hida, V. Krishnamoorthy, K.F. Schmidt, E. Inoue, H. Ishizaki, M. Tanaka-Okamoto, J. Miyoshi, A. Hagiwara, J.H. Brandstatter, S. Lowel, T. Gollisch, T. Ohtsuka, and T. Moser. 2012. Deletion of the presynaptic scaffold CAST reduces active zone size in rod photoreceptors and impairs visual processing. *J Neurosci*. 32:12192-203.

van der Vaart, B., W.E. van Riel, H. Doodhi, J.T. Kevenaar, E.A. Katrukha, L. Gumy, B.P. Bouchet, I. Grigoriev, S.A. Spangler, K.L. Yu, P.S. Wulf, J. Wu, G. Lansbergen, E.Y. van Battum, R.J. Pasterkamp, Y. Mimori-Ki-

yosue, J. Demmers, N. Olieric, I.V. Maly, C.C. Hoogenraad, and A. Akhmanova. 2013. CFEOM1-associated kinesin KIF21A is a cortical microtubule growth inhibitor. *Dev Cell*. 27:145-60.

Wagh, D.A., T.M. Rasse, E. Asan, A. Hofbauer, I. Schwenkert, H. Durrbeck, S. Buchner, M.C. Dabauvalle, M. Schmidt, G. Qin, C. Wichmann, R. Kittel, S.J. Sigrist, and E. Buchner. 2006. Bruchpilot, a protein with homology to ELKS/CAST, is required for structural integrity and function of synaptic active zones in Drosophila. *Neuron*. 49:833-44.

Wang, X., B. Hu, A. Zieba, N.G. Neumann, M. Kasper-Sonnenberg, A. Honsbein, G. Hultqvist, T. Conze, W. Witt, C. Limbach, M. Geitmann, H. Danielson, R. Kolarow, G. Niemann, V. Lessmann, and M.W. Kilimann. 2009. A protein interaction node at the neurotransmitter release site: domains of Aczonin/Piccolo, Bassoon, CAST, and rim converge on the N-terminal domain of Munc13-1. *J Neurosci*. 29:12584-96.

Wang, Y., X. Liu, T. Biederer, and T.C. Sudhof. 2002. A family of RIM-binding proteins regulated by alternative splicing: Implications for the genesis of synaptic active zones. *Proc Natl Acad Sci U S A*. 99:14464-9.

Wang, Y., S. Sugita, and T.C. Sudhof. 2000. The RIM/NIM family of neuronal C2 domain proteins. Interactions with Rab3 and a new class of Src homology 3 domain proteins. *J Biol Chem*. 275:20033-44.

Wang, Z., and D.C. Thurmond. 2009. Mechanisms of biphasic insulin-granule exocytosis - roles of the cytoskeleton, small GTPases and SNARE proteins. *J Cell Sci*. 122:893-903.

Weil, R., and A. Israel. 2004. T-cell-receptor- and B-cell-receptor-mediated activation of NF-kappaB in lymphocytes. *Curr Opin Immunol*. 16:374-81.

White, J., L. Johannes, F. Mallard, A. Girod, S. Grill, S. Reinsch, P. Keller, B. Tzschaschel, A. Echard, B. Goud, and E.H. Stelzer. 1999. Rab6 coordinates a novel Golgi to ER retrograde transport pathway in live cells. *J Cell Biol*. 147:743-60.

Wichmann, C., and S.J. Sigrist. 2010. The active zone T-bar--a plasticity module? *J Neurogenet*. 24:133-45.

Wu, Z.H., Y. Shi, R.S. Tibbetts, and S. Miyamoto. 2006. Molecular linkage between the kinase ATM and NF-kappaB signaling in response to genotoxic stimuli. *Science*. 311:1141-6.

Wu, Z.H., E.T. Wong, Y. Shi, J. Niu, Z. Chen, S. Miyamoto, and V. Tergaonkar. 2010. ATM- and NEMO-dependent ELKS ubiquitination coordinates

TAK1-mediated IKK activation in response to genotoxic stress. *Mol Cell*. 40:75-86.

Yokota, T., T. Nakata, S. Minami, J. Inazawa, and M. Emi. 2000. Genomic organization and chromosomal mapping of ELKS, a gene rearranged in a papillary thyroid carcinoma. *J Hum Genet*. 45:6-11.

Chapter 2

Isolation of Novel +TIPs and Their Binding Partners Using Affinity Purification Techniques

Ka Lou Yu, Nanda Keijzer, Casper C. Hoogenraad, and Anna Akhmanova

Chapter 21

Isolation of Novel +TIPs and Their Binding Partners Using Affinity Purification Techniques

Ka Lou Yu, Nanda Keijzer, Casper C. Hoogenraad, and Anna Akhmanova

Abstract

Microtubule organization and dynamics are controlled by a large set of cellular factors. An important group of microtubule regulators is microtubule plus-end-tracking proteins (+TIPs), which accumulate specifically at the growing microtubule ends, affect different phases of dynamic instability, and link microtubules to various cellular structures. +TIPs include a very diverse set of proteins with widely different structural properties. One of the most conserved and ubiquitous +TIP families are end-binding (EB) proteins, which can track growing microtubule ends autonomously in the absence of any other factors. In contrast, the majority of other known +TIPs cannot recognize the growing microtubule plus ends on their own; instead, they "hitchhike" to the plus ends by interacting with one of the members of the EB family. Therefore, the association with EBs and the ability to track growing microtubule ends are tightly linked, and binding to the EBs can be used to identify new +TIPs. In this chapter, we describe two affinity purification techniques, glutathione S-transferase and biotinylation tag-based pull-down assays that proved to be very useful for the identification of new EB-interacting +TIPs and their binding partners by mass spectrometry. We also discuss cytological techniques that can be applied to confirm plus-end localization of newly identified proteins.

Key words: Microtubule dynamics, EB1, GST, Biotinylation, Mass spectrometry

1. Introduction

Microtubules (MTs) grow and disassemble from their ends, and numerous microtubule end-binding (EB) proteins regulate different aspects of microtubule function (1, 2). Microtubule plus-end-tracking proteins (+TIPs) are defined by their specific comet-like accumulation at the ends of growing MTs (3, 4). +TIPs include a wide variety of proteins that form a complex interaction network. Recent studies showed that the core of this network is

Anne Straube (ed.), *Microtubule Dynamics: Methods and Protocols*, Methods in Molecular Biology, vol. 777,
DOI 10.1007/978-1-61779-252-6_21, © Springer Science+Business Media, LLC 2011

formed by small (~30 kDa) and highly conserved EB proteins, which are represented in mammals by three homologues, EB1, EB2, and EB3 (4–6). The N-terminal part of the EBs consists of a Calponin Homology domain that binds to MTs (7) while the C-terminal part includes a coiled coil domain that ends with a four-helix bundle and an acidic tail that resembles the tail of α-tubulin (8–11). EB C-terminus binds to two major types of partners: CAP-Gly domain proteins, such as the CLIPs (12), and various structurally unrelated proteins with basic and serine-rich regions harboring a short linear motif SxIP (13). Both types of interactions show affinities in a low micromolar range and are relatively unstable, allowing +TIP complexes to remodel and exchange rapidly at the MT tips (4, 13–15). Because +TIP interactions are relatively weak and transient, the EBs are usually difficult to co-precipitate together with their partners from cell extracts unless they are overexpressed. On the other hand, complexes of EBs with other +TIPs easily form in vitro. Furthermore, unlike many other +TIPs, EB proteins with different tags can be readily purified from bacteria in their native form. Therefore, glutathione S-transferase (GST) pull-down assays are ideally suited for the identification of new EB partners: recombinant GST–EB fusions can be easily prepared and used to capture different EB partners in cell extracts. Numerous studies employed this approach to confirm the interactions between EBs with other proteins (13, 16–21). In combination with mass spectrometry, this technique was successfully used to identify new +TIPs, such as RhoGEF2, transmembrane ER-resident protein STIM1, and a neuronal adaptor p140Cap (22–24).

While GST pull-down assays proved very successful for identifying EB interaction partners, the success of their application to other proteins is variable because it strongly depends on the possibility to purify intact and properly folded proteins from *Escherichia coli*, and also because many protein complexes do not assemble easily in cell extracts. Overexpression of tagged proteins and their immunoprecipitation is a common alternative approach. In this chapter, we describe the use of the biotinylation tag, ~20 amino acid polypeptide, which contains a lysine residue that can be very specifically biotinylated by the bacterial biotin ligase BirA (25, 26). Coexpression of BirA together with the tagged protein of interest results in its efficient biotinylation in eukaryotic cells. Biotinylated proteins can be purified by a one-step procedure through their binding to streptavidin (27–29). Since the affinity of biotin to streptavidin is very high ($K_d = 10^{-15}$ M, which is several orders of magnitude higher than a typical antibody), purification is efficient even when the protein of interest is expressed at low levels. The procedure permits use of different cell lysis buffers,

and can be applied to cross-linked materials (30). Since the binding is fast, unstable proteins and transient protein complexes can be readily purified. Furthermore, since no antibodies are used, their presence does not complicate mass spectrometry analysis. It is also important to note that biotin is a covalently attached cofactor of some metabolic enzymes, but their number is small (31) and their presence among the isolated proteins does not pose significant problems with identification of the relevant partners. However, streptavidin beads generally show higher levels of unspecific protein binding compared to glutathione sepharose. Therefore, proper controls, such as pull downs from cells expressing BirA alone or in combination with irrelevant biotinylation-tagged protein, like GFP, should be carried out. Because of high reproducibility of biotinylation-tag affinity purification assays, it is possible to assemble lists of common background proteins in specific cell types and use them as a reference.

Here, we describe the preparation of samples for GST-EB and biotinylation tag-based pull downs that can be used for mass spectrometry analysis. We provide lists for the most common background proteins frequently observed in these assays (Tables 1–3). Finally, we also briefly describe the most important cytological validation techniques, which are based on making GFP fusions of the newly identified proteins and the dual-color imaging in fixed and live cells.

Table 1
Common background proteins in GST pull-down assays from HeLa cells

Description	Entrez gene	Acc./id
Carbonyl reductase 1 [Homo sapiens]	CBR1	gi|75061940
Eukaryotic translation elongation factor 1 [Homo sapiens]	EEF1A1	gi|48734733
Glutathione S-transferase [Homo sapiens]	GSTM3	gi|14250650
Heat shock 70 kDa protein [Homo sapiens]	HSPA	gi|5123454
Keratin [Homo sapiens]	KRT1 KRT2 KRT6A KRT9 KRT14	gi|11935049 gi|47132620 gi|5031839 gi|55956899 gi|119581149

A list of proteins observed in several GST pull downs using GST alone and Triton-X100 extracts of HeLa cells. Only proteins that showed a Mascot Score higher than 300 were included

Table 2
Common background proteins in pull-down assays with strepatividin beads from HeLa cells

Description	Entrezgene			Acc./id		
Acetyl-CoA carboxylase [Homo sapiens]	ACACB	ACACA		gi|94963132	gi|38679960	
Actin, alpha [Homo sapiens]	ACTA1			gi|4501881		
Actin, beta [Homo sapiens]	ACTB	ACTBL2		gi|4501885	gi|63055057	
Actin, gamma [Homo sapiens]	ACTG1			gi|4501887		
Actinin, alpha [Homo sapiens]	ACTN1	ACTN4		gi|4501891	gi|2804273	
AHNAK nucleoprotein isoform 1 [Homo sapiens]	AHNAK			gi|535177		
Serum albumin [Homo sapiens]	ALB			gi|28592		
Annexin A2 [Homo sapiens]	ANXA2			gi|18645167		
ATP synthase beta subunit [Homo sapiens]	ATP5B			gi|32189394		
Hypothetical protein LOC126353 [Homo sapiens]	C19orf21			gi|27735067		
Carbamoyl-phosphate synthetase AD protein [Homo sapiens]	CAD			gi|18105007		
F-actin capping protein [Homo sapiens]	CAPZA1	CAPZB		gi|5453597	gi|4826659	
Chaperonin containing TCP1 [Homo sapiens]	CCT2 CCT5	CCT3 CCT6A	CCT4 CCT8	gi|5453603 gi|24307939	gi|58761484 gi|62089036	gi|38455427 gi|48762932
CD55 antigen [Homo sapiens]	CD55			gi|119613891	gi|1857867	
Clathrin heavy chain 1 [Homo sapiens]	CLTC			gi|4758012	gi|119614803	
Coronin, actin-binding protein 1C [Homo sapiens]	CORO1C			gi|7656991		
Amplaxin [Homo sapiens]	CTTN			gi|182087		
Drebrin 1 [Homo sapiens]	DBN1			gi|18426913		
DEAD (Asp-Glu-Ala-Asp) box polypeptide 5 [Homo sapiens]	DDX5			gi|4758138		
Desmoglein 2 [Homo sapiens]	DSG2			gi|416178		

Eukaryotic translation elongation factor [Homo sapiens]	EEF1A1	EEF1AL3	EEF2	gi|4503471	gi|74746925	gi|4503483
Eukaryotic translation initiation factor 4A [Homo sapiens]	EIF4A1			gi|4503529		
Enolase 1 [Homo sapiens]	ENO1			gi|4503571		
Epiplakin [Homo sapiens]	EPPK1			gi|37196760		
Glutamyl-prolyl tRNA synthetase [Homo sapiens]	EPRS			gi|62241042		
Hypothetical protein LOC222584 [Homo sapiens]	FAM83B			gi|61676089		
Family with sequence similarity FAM83H [Homo sapiens]	FAM83H			gi|157311635		
Fatty acid synthase [Homo sapiens]	FASN			gi|41872631		
Flightless-I homolog [Homo sapiens]	FLII			gi|440177		
Filamin [Homo sapiens]	FLNA	FLNB		gi|116063573	gi|3282771	
Flotillin 1 [Homo sapiens]	FLOT1			gi|5031699		
Fascin 1 [Homo sapiens]	FSCN1			gi|4507115		
Fragile X mental retardation syndrome-related protein 1	FXR1			gi|114590562		
Guanine nucleotide-binding protein alpha polypeptide 3 [Homo sapiens]	GNAI3			gi|5729850		
Heat shock 90 kDa protein [Homo sapiens]	HSP90AA1	HSP90AB1	HSP90B1	gi|62914009	gi|306891	gi|62088648
Heat shock 70 kDa protein [Homo sapiens]	HSPA1A HSPA8	HSPA1B HSPA9	HSPA5	gi|4529893 gi|5729877	gi|4529892 gi|292059	gi|16507237
Heat shock protein 27 [Homo sapiens]	HSPB1	HSPD1		gi|662841	gi|31542947	
Mitofilin [Homo sapiens]	IMMT			gi|8131894		
Plakoglobin [Homo sapiens]	JUP			gi|762885		
Phostensin [Homo sapiens]	KIAA1949			gi|145386517		

(continued)

Table 2
(continued)

Description	Entrezgene			Acc./id		
Keratin [Homo sapiens]	KRT1 KRT9 KRT7 KRT6A KRT14	KRT2 KRT10 KRT8 KRT6B KRT16	KRT5 KRT13 KRT17 KRT18	gi|11935049 gi|55956899 gi|12803727 gi|46812692 gi|12803709	gi|386849 gi|21961605 gi|4504919 gi|386849 gi|24430192	gi|18999435 gi|158261511 gi|4557701 gi|4557888
LIMA1 protein [Homo sapiens]	LIMA1			gi|7705373		
LIM and calponin homology domains-containing protein 1 [Homo sapiens]	LIMCH1			gi|163310741		
Lamin A protein [Homo sapiens]	LMNA			gi|386856		
LIM domain only 7 [Homo sapiens]	LMO7			gi|119600955		
LUZP1 protein [Homo sapiens]	LUZP1			gi|30354561		
3-methylcrotonyl-CoA carboxylase [Homo sapiens]	MCCC1	MCCC2		gi|12276066	gi|11545863	
Myosin phosphatase-Rho interacting protein isoform 1 [Homo sapiens]	MPRIP			gi|50980307		
Myosin heavy chain nonmuscle [Homo sapiens]	MYH10	MYH9		gi|641958	gi|12667788	
Myosin [Homo sapiens]	MYO10 MYO1B MYO1G	MYO6 MYO1C	MYO18A MYO1E	gi|9910111 gi|56204015 gi|54873627	gi|27529702 gi|68533085	gi|24660442 gi|55956916
Polyadenylate-binding protein [Homo sapiens]	PABPC1	PABPC4		gi|693937	gi|4504715	
Poly (ADP-ribose) polymerase [Homo sapiens]	PARP1			gi|22902366		
Pyruvate carboxylase precursor [Homo sapiens]	PC			gi|106049292		
Propionyl-Coenzyme A carboxylase [Homo sapiens]	PCCA	PCCB		gi|65506442	gi|62087598	
Plectin [Homo sapiens]	PLEC1			gi|41322916		

Plastin 3 [Homo sapiens]	PLS3			gi|7549809		
Protein phosphatase 1, regulatory (inhibitor) subunit 12A [Homo sapiens]	PPP1R12A			gi|4505317		
Tumor necrosis factor type 1 receptor-associated protein [Homo sapiens]	PSMD2			gi|687239		
Novel retinal pigment epithelial cell protein [Homo sapiens]	RAI14			gi|7274242		
Raichu404X [Homo sapiens]	RAP1A			gi|14595132		
RNA-binding motif protein 14 [Homo sapiens]	RBM14			gi|5454064		
Replication protein A1, 70 kDa [Homo sapiens]	RPA1			gi|4506583		
S3 ribosomal protein [Homo sapiens]	RPS3			gi|7765076		
Structure protein NSP5a3b [Homo sapiens]	SPECC1			gi|56789962		
Spectrin, alpha (alpha-fodrin) [Homo sapiens]	SPTAN1			gi|31565122		
Spectrin, beta [Homo sapiens]	SPTBN1			gi|62089082		
Sperm-specific antigen 2 [Homo sapiens]	SSFA2			gi|134047924		
Stomatin peptide [Homo sapiens]	STOM			gi|181184		
Tropomodulin 3 [Homo sapiens]	TMOD3			gi|6934244		
Tropomyosin [Homo sapiens]	TPM1	TPM4	TPM4ALK	gi|29792232	gi|4507651	gi|13274400
Alpha-tubulin [Homo sapiens]	TUBA1A	TUBA1B		gi|37492	gi|340021	
Beta-tubulin [Homo sapiens]	TUBB	TUBB2C	TUBB3	gi|338695	gi|5174735	gi|62897639
Vimentin [Homo sapiens]	VIM			gi|62414289		
WDR1 protein [Homo sapiens]	WDR1			gi|9257257		
Kaiso [Homo sapiens]	ZBTB33			gi|5803229		

A list of proteins observed in several streptavidin bead pull downs using HeLa cells expressing BirA in combination with biotinylation-tagged GFP. Only proteins that showed a Mascot Score higher than 300 were included

Table 3
Common background proteins in pull-down assays with strepatividin beads from HEK293T cells

Description	Entrezgene			Acc./id		
Acetyl-Coenzyme A carboxylase alpha isoform 2 [Homo sapiens]	ACACA			gi|38679967		
Actin, gamma 1 [Homo sapiens]	ACTG1			gi|4501887		
Serum albumin [Homo sapiens]	ALB			gi|4502027		
Ataxin-2-related domain protein [Homo sapiens]	ATXN2L			gi|18071115		
GPI-anchored membrane protein 1 [Homo sapiens]	CAPRIN1			gi|42558250		
Chaperonin containing TCP1 [Homo sapiens]	CCT2 CCT6A	CCT3 CCT7	CCT4 CCT8	gi|5453603 gi|4502643	gi|14124984 gi|5453607	gi|38455427 gi|1136741
Desmoplakin I [Homo sapiens]	DSP			gi|58530840	gi|1147813	
Eukaryotic translation elongation factor [Homo sapiens]	EEF1A1	EEF1AL3	EEF2	gi|4503471	gi|55665593	gi|4503483
Eukaryotic translation initiation factor 4A isoform 1 [Homo sapiens]	EIF4A1			gi|4503529		
Enolase 1 [Homo sapiens]	ENO1			gi|693933		
Fatty acid synthase [Homo sapiens]	FASN			gi|41872631		
Filamin A [Homo sapiens]	FLNA			gi|53791219		
Ras-GAP SH3-binding protein [Homo sapiens]	G3BP1	G3BP2		gi|5031703	gi|3098601	
Heterogeneous nuclear ribonucleoprotein [Homo sapiens]	HNRNPF HNRNPM	HNRNPH1 HNRNPU	HNRNPK HNRNPUL1	gi|4826760 gi|187281	gi|5031753 gi|32358	gi|14165437 gi|12803479

Heat shock 90 kDa protein [Homo sapiens]	HSP90AA1		gi|62914009	gi|17865490	gi|83699649	
	HSP90AB1		gi|306891			
Heat shock 70 kDa protein [Homo sapiens]	HSPA1A HSPA8	HSPA1B	HSPA5	gi|386785 gi|5729877	gi|4885431	gi|16507237
Heat shock protein beta-1 [Homo sapiens]	HSPB1	HSPD1		gi|4504517	gi|31542947	
Keratin [Homo sapiens]	KRT1	KRT2	KRT5	gi|11935049	gi|47132620	gi|18999435
	KRT7	KRT8	KRT9	gi|12803727	gi|181400	gi|55956899
	KRT10	KRT13	KRT14	gi|21961605	gi|131412225	gi|12803709
	KRT15	KRT16	KRT17	gi|24430190	gi|1195531	gi|4557701
	KRT18	KRT19	KRT6A	gi|4557888	gi|7594734	gi|908801
	KRT73 KRT77	KRT75	KRT77	gi|28173564 gi|113414871	gi|3901030	gi|119617049
Methylcrotonoyl-Coenzyme A carboxylase [Homo sapiens]	MCCC1	MCCC2		gi|12276066	gi|11545863	
Non-POU domain containing [Homo sapiens]	NONO			gi|34932414		
Pyruvate carboxylase [Homo sapiens]	PC			gi|106049292		
Plectin [Homo sapiens]	PLEC1			gi|1477646		
Peroxiredoxin [Homo sapiens]	PRDX1	PRDX4		gi|4505591	gi|5453549	
Siah-binding protein 1 [Homo sapiens]	PUF60			gi|1809248		
Raichu404X [Homo sapiens]	RAP1A			gi|14595132		
S3 ribosomal protein [Homo sapiens]	RPS3			gi|7765076		
Splicing factor proline/glutamine rich [Homo sapiens]	SFPQ			gi|4826998		
Solute carrier family 25 [Homo sapiens]	SLC25A3	SLC25A5	SLC25A6	gi|4505775	gi|45829841	gi|15928608

(continued)

Table 3
(continued)

Description	Entrezgene			Acc./id		
Sjogren syndrome/scleroderma autoantigen 1 [Homo sapiens]	SSSCA1			gi|5453838		
Stomatin peptide [Homo sapiens]	STOM			gi|181184		
Alpha-tubulin [Homo sapiens]	TUBA1A	TUBA1B	TUBA1C	gi|37492	gi|158259731	gi|193786502
Tubulin, beta [Homo sapiens]	TUBB TUBB4	TUBB2C TUBB6	TUBB3	gi|18088719 gi|21361322	gi|5174735 gi|194388028	gi|50592996
Vimentin [Homo sapiens]	VIM			gi|340219	gi|62414289	

A list of proteins observed in several streptavidin bead pull downs using HeLa and HEK293 cells expressing BirA in combination with biotinylation-tagged GFP. Only proteins that showed a Mascot Score higher than 300 were included

2. Materials

2.1. Equipment

1. Incubator shaker for growing bacteria (Innova 4300, New Brunswick Scientific).
2. Spectrophotometer (Ultrospec III, Pharmacia).
3. Centrifuges:

   Eppendorf microcentrifuge 5415R for 1.5/2-ml Eppendorf tubes

   Eppendorf centrifuge 5810R for 15- and 50-ml Falcon tubes

   High-speed centrifuge RC5C, equipped with SLA-1500 and SS-34 rotors (Sorvall Instruments)
4. Tissue culture incubator (37°C, 5% CO_2) (Sanyo).
5. Laminar flow cabinet for tissue culture.
6. Ultrasonic disintegrator Soniprep 150 (MSE).
7. Rotating wheel.
8. Dynal MPC-S magnet.
9. Microscope suitable for imaging fixed and/or live cells, equipped with a high NA 100× objective. Description of microscopy equipment goes beyond the scope of this chapter.
10. The description of mass spectrometry methods and equipment is beyond the scope of this chapter. Most of our analyses are currently performed with NanoLC-MS/MS on a 1100 series capillary LC system (Agilent Technologies) coupled to an LTQ ion trap mass spectrometer (Thermo) operating in positive mode and equipped with a nanospray source.

2.2. Preparation of GST Proteins from E. coli

1. GST fusions of EB1, EB2, and EB3: EB1, EB2, and EB3 open reading frames were generated by PCR and cloned into *Bam*HI and *Eco*RI sites of the pGEX-3× vector (18, 32).
2. LB Broth EZMix Powder, dust-free, fast-dissolving fermentation medium (Sigma).
3. Ampicillin (working concentration: 100–200 μg/ml).
4. Isopropyl β-d-1-thiogalactopyranoside (IPTG; working concentration: 0.8–1.6 mM; stock solution prepared in water).
5. *E. coli* strain BL21 competent cells: An overnight culture of BL21 *E. coli* is used to inoculate a fresh culture (dilution 1:40) and grown for 1.5–3 h at 37°C with agitation. Cells are collected by centrifugation, washed in ice-cold 0.1 M $CaCl_2$ (10 ml per 250 ml culture), resuspended in ice-cold 0.1 M $CaCl_2$ solution containing 15% glycerol (5 ml per 250 ml culture), aliquoted, and stored at −80°C.

6. Glutathione Sepharose 4B (GE Healthcare).
7. Bacteria lysis buffer: 1% Triton X-100 in phosphate-buffered saline (PBS), supplemented with the complete protease inhibitor cocktail (Roche). Prepare fresh and keep ice cold.
8. Washing buffer: 0.1% Triton in PBS. Prepare fresh and keep ice cold.
9. High-salt washing buffer: 0.1% Triton in PBS, 500 mM NaCl. Prepare fresh and keep ice cold.

2.3. Pull-Down Assays with GST-EB Fusion Proteins from Cell Extracts

1. Dulbecco's Phosphate-Buffered Saline (DPBS) without calcium and magnesium (BioWhittaker, Lonza).
2. Cell culture medium: 45% Dulbecco's modified Eagle's medium (DMEM) with ultraglutamine and 4.5 g/l glucose (BioWhittaker, Lonza), 45% Ham's F10 without thymidine and with ultraglutamine (BioWhittaker, Lonza), 10% fetal calf serum (FCS; Lonza), supplemented with penicillin and streptomycin (PS, 100× stock; Lonza).
3. Cell lysis buffer: 1% Triton X-100 in PBS supplemented with the complete protease inhibitor cocktail (Roche). Prepare fresh and keep ice cold.
4. Washing buffer: 20 mM Tris–HCl, pH 8.0, 150 mM NaCl, 0.05% Triton, 1 mM DTT. Prepare fresh and keep ice cold.
5. NuPAGE Novex precast gels and buffers (Invitrogen).
6. Colloidal Blue staining kit (Invitrogen).

2.4. Biotinylation Tag-Based Pull-Down Experiments from Transfected Cells

1. Biotinylation tag fusion of the protein of interest: We most frequently use an N-terminal biotinylation tag with the sequence MASGLNDIFEAQKIEWHEGGG; the lysine residue (underlined) can be biotinylated by BirA and the three glycines serve as flexible linkers. The sequence can be inserted in the plasmid of interest as a synthetic oligonucleotide linker.
2. The expression construct for biotin ligase BirA under the CMV promoter (33).
3. Cell culture medium: 45% DMEM with ultraglutamine and 4.5 g/l glucose (BioWhittaker, Lonza), 45% Ham's F10 without thymidine and with ultraglutamine (BioWhittaker, Lonza), 10% FCS (Lonza), supplemented with penicillin and streptomycin (PS, 100× stock; Lonza).
4. DPBS without calcium and magnesium (BioWhittaker, Lonza).
5. Polyethylenimine (PEI) "Max" (nominally Mw 40,000) – High-Potency Linear PEI (Equivalent to Mw 25,000 in Free Base Form; Polysciences).
6. Dynabeads M-280 Streptavidin (Invitrogen).
7. Dynabead blocking buffer: 20 mM HEPES, pH 7.5, 150 mM KCl, 0.1% Triton X-100, 20% glycerol, 0.2 μg/μl albumin

from chicken egg white (Grade V, minimum 98% agarose gel electrophoresis; Sigma). Albumin from chicken egg white should be added freshly to the blocking buffer. Prepare a 20 mg/ml stock in PBS and store at −20°C.

8. Cell lysis buffer: 20 mM HEPES, pH 7.5, 150 mM KCl, 1% Triton X-100 supplemented with complete protease inhibitor cocktail (Roche). Prepare fresh and keep ice cold.
9. Washing buffer: 20 mM HEPES, pH 7.5, 150 mM KCl, 0.1% Triton X-100. Prepare fresh and keep on ice.

2.5. Immunofluorescent Staining for +TIPs and Adaptor Proteins

1. Cell culture medium: 45% DMEM with ultraglutamine and 4.5 g/l glucose (BioWhittaker, Lonza), 45% Ham's F10 without thymidine and with ultraglutamine (BioWhittaker, Lonza), 10% FCS (Lonza), supplemented with penicillin and streptomycin (PS, 100× stock; Lonza).
2. Trypsin–EDTA (0.25% Trypsin in EDTA; Lonza).
3. Labtek Chamber Slides (Thermo Scientific Nunc; 4-well glass slides).
4. Ham's F10 without thymidine and with ultraglutamine (BioWhittaker, Lonza).
5. Polyfect Transfection Reagent (Qiagen).
6. Paraformaldehyde (PFA; Sigma Aldrich). Prepare 4% PFA solution in PBS prior to the experiment. Dissolve 4 g of PFA in 100 ml PBS at 65°C and cool to room temperature.
7. Blocking buffer: 1% albumin from bovine serum (Fraction V; Sigma)/0.1% Tween 20/PBS. Prepare fresh and keep on ice.
8. Washing buffer: 0.1% Tween-20 in PBS.
9. Secondary Alexa 350- and 594-conjugated goat antibodies against mouse IgG and rabbit IgG antibodies (Molecular Probes, Invitrogen). Store at −20°C.
10. Vectashield (with DAPI, H-1200, or without DAPI, H-1000, Vector laboratories).
11. Coverslips 24 × 60 mm (Menzel-Gläser).

2.6. +TIP Imaging in Cultured Cells

1. 25-mm diameter round coverslips (N1, Menzel-Glaser).
2. Cell culture medium: 45% DMEM with ultraglutamine and 4.5 g/l glucose (BioWhittaker, Lonza), 45% Ham's F10 without thymidine and with ultraglutamine (BioWhittaker, Lonza), 10% FCS (Lonza), supplemented with penicillin and streptomycin (PS, 100× stock; Lonza).
3. Ham's F10 without thymidine and with ultraglutamine (BioWhittaker, Lonza).
4. Polyfect Transfection Reagent (Qiagen).
5. Attofluor cell chamber (A-7816, Molecular Probes).

3. Methods

3.1. Preparation of GST Proteins from E. coli

1. Transform GST, GST-EB1, GST-EB2, and GST-EB3 plasmids into competent BL21 *E. coli* cells by heat shock at 42°C, plate on LB agar plates with ampicillin, and grow overnight at 37°C.
2. Inoculate individual colonies in 10-ml LB liquid medium with ampicillin and grow overnight at 37°C (see Note 1).
3. Transfer 10 ml of the overnight bacterial culture to a 1-l Erlenmeyer flask with 250-ml LB medium with ampicillin.
4. Grow the cultures at 37°C for 3 h with agitation. Take 1 ml of culture and measure the optical density (OD) at 600 nm. Use 1 ml of LB medium as a blank.
5. When OD 600 is 0.6–0.8, induce protein expression by adding IPTG to a final concentration of 0.8–1.6 mM. Continue growing for 4 h at 37°C with agitation.
6. Transfer bacterial cultures to centrifuge buckets (Sorvall SLA-1500 rotor) and centrifuge at 2,000 × *g* for 30 min at 4°C. Discard the supernatant and store the pellets at –20°C or proceed with purification.
7. Resuspend bacterial pellets in 4 ml of freshly prepared ice-cold lysis buffer.
8. Sonicate the lysates on ice eight times for 10 s with 30 s intervals while keeping the tubes on ice. At this stage, the lysates should become semitransparent; additional cycles of sonication can be performed if necessary.
9. Preclear the lysates by centrifuging for 10 min at 20,000 × *g* at 4°C (using the Sorvall SS-34 rotor).
10. Take a 1.5 ml aliquot of glutathione sepharose beads (50% slurry); add 1 ml ice-cold lysis buffer, mix, centrifuge briefly at 800 × *g* in a 15-ml Falcon tube at 4°C, and discard the supernatant; repeat the procedure 2–3 times.
11. Transfer the precleared bacterial lysate to the tube with the washed glutathione sepharose beads (bead volume ~0.75 ml) and incubate for 2 h at 4°C on a rotating wheel (see Note 2).
12. After a 2-h incubation, centrifuge the beads for 3 min at 800 × *g* in a 15-ml Falcon tube at 4°C and remove the supernatants. Wash the beads three times with the ice-cold washing buffer (5 ml per wash), three times with ice-cold high-salt washing buffer (5 ml per wash), and then again three times with the ice-cold washing buffer (5 ml per wash). For each washing step, mix the beads with the buffer, centrifuge for 3 min at 800 × *g* at 4°C, and aspirate the supernatant (see Note 3).

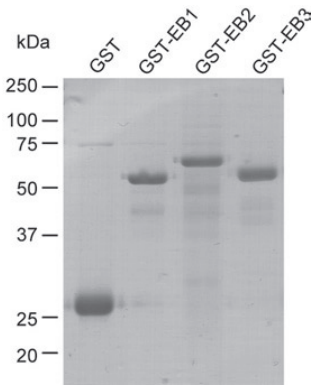

Fig. 1. Characterization of the GST fusion proteins. GST alone, GST-EB1, GST-EB2, and GST-EB3 were purified from *E. coli* and analyzed on a Coomassie-stained gel. Note that due to the presence of ~40 amino acid N-terminal extension, EB2 is longer than EB1 and EB3. Image courtesy of S. Montenegro Gouveia (Erasmus MC, Rotterdam).

13. Resuspend the beads as 2× slurry in ice-cold PBS, 0.1% Triton, and 10% glycerol. Keep 20 µl of the beads apart for running SDS PAGE. The rest of the beads (~1.5 ml of 2× slurry) can be aliquoted, snap-frozen in liquid nitrogen, and stored at −80°C.
14. Run the proteins on 12% SDS PAGE, fix in 25% methanol, 10% acetic acid, and stain with Coomassie blue staining solution. Destain the gel in 25% methanol (Fig. 1) (see Note 4).

3.2. Pull-Down Assays with GST-EB Fusion Proteins from Cell Extracts

1. Prepare two 100-mm tissue culture dishes with cells (>80% confluence) for each GST pull-down assay. Scrape the cells in DPBS (10 ml/dish) with a plastic disposable scrapper and transfer into a 50-ml Falcon tube. Centrifuge at 200 × *g* for 5 min at 4°C, aspirate the supernatant, and lyse the cell pellet in 150–200 µl ice-cold cell lysis buffer per dish. Incubate the lysate on ice for 10 min and preclear by centrifuging in a microcentrifuge for 10 min at 16,100 × *g* at 4°C.
2. Thaw on ice purified GST fusion proteins bound to glutathione sepharose beads that were stored at −80°C.
3. Prepare 200 µl aliquots of each purified GST protein (2× slurry) in 1.5-ml Eppendorf tubes and wash once with 1 ml fresh ice-cold lysis buffer; centrifuge at 400 × *g* in a microcentrifuge at 4°C, discard the supernatant, add the precleared cell lysate (~300 µl per tube), and incubate for 2 h at 4°C on a rotating wheel.
4. Centrifuge the beads for 3 min at 400 × *g* at 4°C and aspirate the supernatants. Wash the beads four times with 1 ml ice-cold washing buffer (20 mM Tris–HCl, pH 8.0, 150 mM NaCl, 0.05% Triton, 1 mM DTT) (see Note 5).

5. Resuspend the beads together with the bound proteins in 100 µl 1× NuPAGE LDS sample buffer supplemented with 1 mM DTT, boil and run on NuPAGE Novex T precast polyacrylamide gel, stain with the Colloidal Blue staining kit (Invitrogen), and send for mass spectrometry analysis (see Note 6). Alternatively, analyze the bound proteins by Western blotting.

3.3. Biotinylation Tag-Based Pull-Down Experiments from Transfected Cells

1. Prepare three 100-mm tissue culture dishes of HEK293T cells for each individual pull down. One day before transfection, passage 100% confluent (1×10^7 cells per dish) by thorough resuspension with a glass pipette. Seed 2.5×10^6 cells per 100-mm dish for transfecting them the next day or 1×10^6 cells if you intend to perform transfection after 2 days.
2. On the day of transfection, HEK293T cells should reach 70–85% confluence. Transfect the biotinylated-tagged fusion construct (i.e., Bio-GFP-CLASP2α) together with a plasmid-expressing BirA ligase using PEI transfection reagent. For each 100-mm dish, incubate a mixture of the two plasmids (2.5 µg each) and 15 µl PEI transfection reagent in two separate tubes containing 0.5 ml DPBS for 5 min at room temperature. Next, mix gently the DNA/DPBS and PEI/DPBS solutions and incubate for another 20 min at room temperature. Add 5-ml cell culture medium to the transfection mixture and transfer to the dish of HEK293T cells. Incubate the cells together with the transfection medium at 37°C, 5% CO_2 for 24–48 h (see Notes 7–9).
3. One hour before starting cell lysis and pull-down experiment, resuspend the Dynabeads in the original vial by vortexing. For each pull down, make a 50 µl aliquot of Dynabead suspension in a 1.5-ml Eppendorf tube (see Note 10).
4. Place the tube into the Dynal MPC-S magnet and remove the supernatant. Incubate the Dynabeads with 250 µl ice-cold blocking buffer for 1 h at 4°C on a rotating wheel.
5. Remove the medium from the dishes of transfected HEK293T cells, resuspend the cells by vigorous pipetting in 5 ml of DPBS per dish, transfer to 50-ml Falcon tubes, centrifuge at $200 \times g$ for 5 min at 4°C, and aspirate the supernatant. For strongly adherent cell lines, scrape the cells in DPBS (10 ml/dish) with a plastic disposable scrapper, transfer into a 50-ml Falcon tube, centrifuge, and aspirate as described above.
6. Resuspend the cell pellet thoroughly in ice-cold cell lysis buffer (300 µl per 100-mm dish) (see Note 11). Centrifuge the lysate in a microcentrifuge at $16{,}100 \times g$ for 10 min at 4°C. Collect 50 µl lysate and mix with 2× SDS sample buffer as the input fraction for analysis on SDS PAGE and Western blotting.

Use the rest of the cell lysate as input for the pull-down experiment.

7. Place the tubes with Dynabeads in the blocking buffer in the magnet for 1 min and aspirate the supernatant.
8. Add the cell lysate to the Dynabeads and incubate the mixture for 1 h at 4°C on a rotating wheel.
9. Place the tubes in the magnet for 1 min and remove the supernatant. Wash the Dynabeads 4–6 times with ice-cold washing buffer (1 ml per wash). For each washing step, remove the tubes from the magnet and mix by inverting them several times, place back onto the magnet, and aspirate the supernatant (see Note 5).
10. After the last washing step, remove the supernatant, resuspend the bound Dynabeads in 50 µl 1× NuPAGE sample buffer, and boil for 10 min at 100°C.
11. Use 5 µl of the bound Dynabeads samples for running SDS PAGE and stain with Coomassie or perform Western blotting (Fig. 2). The remaining Dynabeads can be used to run an NuPAGE Novex precast polyacrylamide gel. Stain the gel with the Colloidal Blue staining kit and send for mass spectrometry analysis (see Note 6).

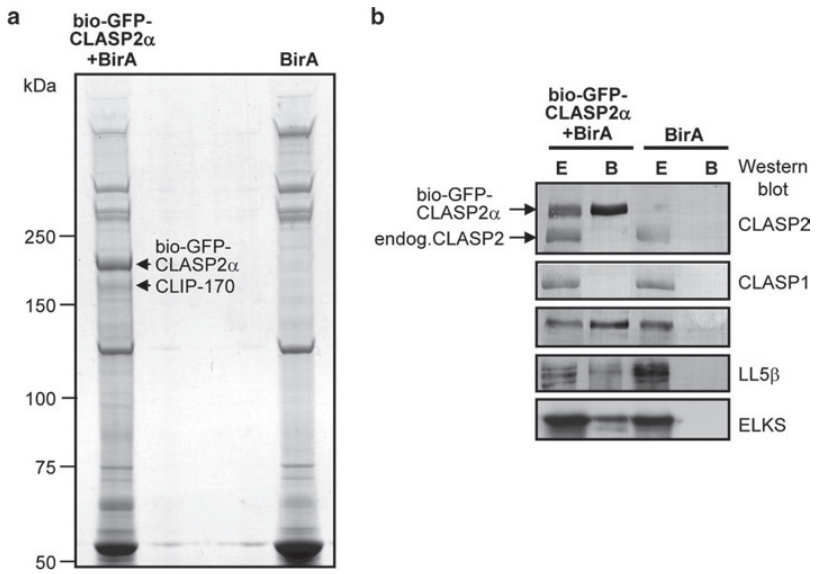

Fig. 2. Identification of CLASP binding partners by pull-down assays using biotinylation tag. Pull-down assays with streptavidin beads were performed with lysates of HeLa cells, coexpressing bio-GFP-CLASP2α together with BirA or BirA alone. Proteins bound to streptavidin beads were analyzed on a Coomassie-stained gel (**a**) or by Western blotting with the indicated antibodies (**b**). In panel (**a**), only the fraction bound to the beads was loaded. In panel (**b**), the extract before the pull down (lanes marked "E") and proteins bound to the beads (lanes marked "B") are shown. Lanes marked "E" correspond to 25% of the extract, used to obtain lanes marked "B" reproduced from (34) with permission from Elsevier.

3.4. Immunofluorescent Staining for +TIPs and Adaptor Proteins

1. One day before transfection, split a 100-mm dish of confluent HeLa cells (1×10^7 cells per dish). Trypsinize cells with 1 ml of trypsin–EDTA and resuspend in 9 ml of cell culture medium. Prepare HeLa cells in a dilution of 1:40. Seed 1 ml of cell suspension into one well of a four-well Labtek chamber slide; incubate the cells overnight with normal medium at 37°C in a humidified incubator with 5% CO_2.
2. Prewarm the cell culture media at 37°C and centrifuge all plasmid DNA for 3 min at 16,100 × *g* in a microcentrifuge. Prepare transfection mixture: for one well of a four-well Labtek Chamber slide, add 30 µl of Ham's F10 medium, 0.5 µl of plasmid DNA (1 µg/µl), and 3 µl Polyfect transfection reagent. Incubate for 15 min at room temperature (see Note 12).
3. Add 300 µl cell culture medium (50% DMEM/50% Ham's F10/10% FCS/PS) to the transfection mixture, mix, and add to the chamber with cells after removing the culture medium. Place the cells back into incubator and incubate for 16–24 h at 37°C with 5% CO_2.
4. Aspirate the transfection medium and add fresh medium (1 ml/chamber); incubate for 1.5 h at 37°C with 5% CO_2.
5. Aspirate the medium from Labtek chamber slides, wash the cells with DPBS (1 ml/chamber), and detach the plastic disposable chamber.
6. Fix the cells for 10 min by inserting the slide into a Hellendahl staining jar containing 100% methanol precooled to –20°C. Transfer immediately to 4% PFA maintained at room temperature for another 10 min (see Notes 13 and 14).
7. Wash the cells in a Hellendahl staining jar with 1.5% Trition X-100 in PBS for 10 min with gentle agitation on a shaker at room temperature.
8. Pipet blocking buffer onto the glass slides (~100 µl per chamber) and incubate for 30 min at room temperature in a humidified and light-protected chamber.
9. Thaw on ice primary antibodies and centrifuge for 3 min at 16,100 × *g* at 4°C. Prepare antibody dilutions in the blocking buffer (50 µl antibody mixture/chamber). Typically, commercial monoclonal antibodies are diluted 1:100–1:300, and crude polyclonal antibodies 1:300–1:400.
10. Carefully remove the blocking buffer from the slides by absorbing it with a tissue paper (avoid touching the cells). Apply 50 µl of diluted primary antibodies per well and incubate for 1 h at room temperature in a humidified and light-protected chamber.
11. Carefully remove the primary antibody solution from the slides with a tissue paper (avoid touching the cells). Wash the

slides three times with 0.1% Tween-20 in PBS in a Hellendahl staining jar.

12. Thaw on ice secondary antibodies and centrifuge for 3 min at 16,100 × *g* at 4°C. Prepare antibody dilutions in the blocking buffer (50 µl antibody mixture/chamber). Typically, commercial secondary antibodies are diluted 1:300–1:500.
13. Apply 50 µl of diluted secondary antibodies per well and incubate for 45 min at room temperature in a humidified and light-protected chamber.
14. Carefully remove the secondary antibody solution from the slides with a tissue paper (avoid touching the cells). Wash the slides three times with 0.1% Tween-20 in PBS in a Hellendahl staining jar.
15. Remove the gelatin frames from the slides using sharp forceps or a knife. Rinse the slides in 70% ethanol and then 100% ethanol, air-dry, mount in Vectashield (with or without DAPI), and cover with glass coverslips. Slides can be stored indefinitely in a slide holder at −20°C in dark.
16. Use an appropriate fluorescent microscope for taking images (Fig. 3).

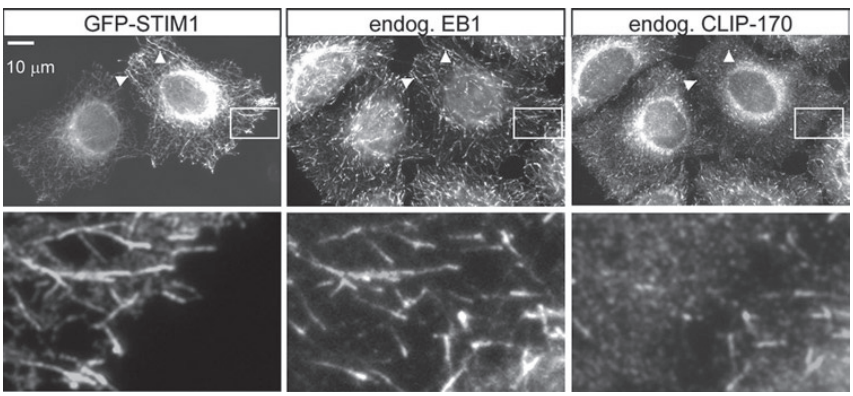

Fig. 3. Detection of GFP fusion protein at the MT plus ends by immunofluorescent cell staining. STIM1, an ER-resident protein essential for store-operated calcium entry, was identified as binding partner of EB1 by GST pull-down assays from extracts of B16F1 melanoma cells (24). To test if STIM1 associates with MT ends, HeLa cells were transfected with GFP-STIM1, fixed, and stained for the endogenous +TIPs. Antibodies against EB1 (monoclonal mouse EB1 antibody, dilution 1:200, BD Biosciences) and CLIP-170 (polyclonal rabbit CLIP-170 antibodies #2221 and #2360 (37), dilution 1:400) were used. Images were obtained with a Leica DMRBE microscope with a PL Fluotar 100× 1.3 NA objective, equipped with a Hamamatsu CCD camera (C4880) and processed in Adobe Photoshop. Insets show enlargements of the boxed areas. Note that in the cell with a higher GFP-STIM1 expression, CLIP-170 signal on GFP-STIM1-positive MT tips is reduced (*arrowheads*) because of competition between GFP-STIM1 and CLIP-170 for the binding sites on EB1 C-terminus. When performing these experiments, it is thus important to stain for endogenous EB proteins and not for any other +TIPs, which might be affected even by mild expression of exogenous plus-end-binding proteins due to competition for the binding to the EBs.

3.5. +TIP Imaging in Live Cultured Cells

1. Plate cells onto coverslips at the appropriate density (see Note 15). Different coverslips can be used depending on the observation chamber, including glass bottom Petri dishes. 25-mm diameter round coverslips are placed into six-well cell culture plates. Typically, cells should be at 25–30% confluence on the day of transfection and 50–75% confluence during imaging.
2. Prewarm the cell culture media at 37°C and centrifuge all plasmid DNA for 3 min at 16,100 × *g* in a microcentrifuge. Prepare transfection mixture: for one well of a six-well cell culture plate, add 100 µl of Ham's F10 medium, 1.5–2 µl of plasmid DNA (1 µg/µl), and 10 µl Polyfect transfection reagent. Incubate for 15 min at room temperature (see Note 12).
3. Add 1.5-ml cell culture medium (50% DMEM/50% Ham's F10/10% FCS/PS) to the transfection mixture, mix, and add to the well with cells after removing the culture medium. Place the cells back into incubator and incubate for 16–24 h at 37°C with 5% CO_2.
4. Aspirate the transfection mixture and add fresh culture medium (50% DMEM/50% Ham's F10/10% FCS/PS) before imaging. Mount the coverslip with cells into the observation chamber. Never allow the cells to dry during any preparation steps.
5. For a typical inverted microscope setup, which is most convenient for imaging live mammalian cells, add immersion oil on top of the lens. Use a 63× or a 100× objective.
6. Insert the chamber with cells into the heating incubator or onto the stage (this depends on the microscope configuration). Cells should be maintained at 37°C during imaging.
7. Collect live cell images. Imaging at 1–2 frames per second gives optimal results, but one frame per 2–3 s is sufficient (see Note 16). Collect 50–100 frames.
8. Watch the movie or generate a maximum intensity projection of consecutive frames; this helps to detect +TIP comets if the signal-to-noise ratio is low (Fig. 4).

4. Notes

1. Frozen stocks of BL21 cells transformed with GST constructs can be stored at −80°C and used for inoculating overnight cultures.
2. 1 ml of glutathione sepharose bead volume binds approximately 5 mg of GST protein.

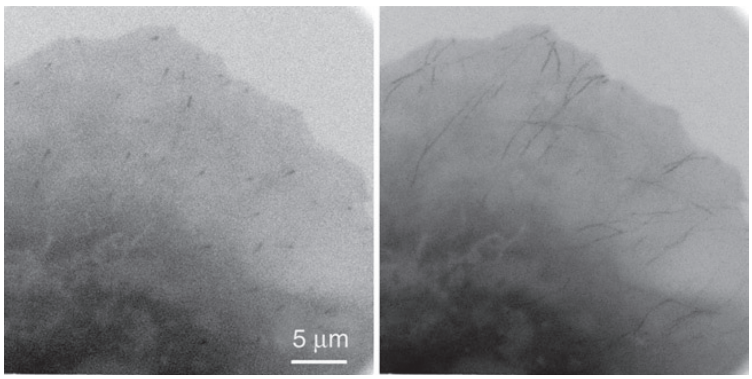

Fig. 4. Detection of MT plus-end tracking of a GFP fusion protein by live cell imaging. Images of a COS-7 cell transiently expressing a GFP fusion of the C-terminal fragment of MACF2 (13). Wide-field time-lapse imaging was performed on an inverted research Nikon Eclipse TE2000E (Nikon) microscope with a CFI Apo TIRF 100× 1.49 NA oil objective (Nikon). The microscope was equipped with a QuantEM EMCCD camera (Roper Scientific) and controlled by the MetaMorph 7.1 software package (Molecular Devices). For excitation, we used HBO 103 W/2 Mercury Short Arc Lamp (Osram) and Chroma ET-GFP filter cube. 16-bit images were projected onto the CCD chip at a magnification of 0.067 µm/pixel, with intermediate magnification of 2.5×. Images were collected with 500 ms exposure without delay between frames. A single frame is shown on the left, and maximum intensity projection of 100 consecutive frames is shown on the right. Note that although the GFP-labeled microtubule plus ends might be difficult to distinguish in individual frames due to high cytoplasmic background, they become apparent as characteristic linear tracks in maximum intensity projections of several frames. Image courtesy of I. Grigoriev (Erasmus MC, Rotterdam).

3. High-salt washing buffer reduces unspecific protein binding to the glutathione sepharose beads during purification.
4. The yield of GST-EB2 is lower than GST-EB1 or EB3, and its purity is typically less good.
5. Increasing salt concentration in the washing buffer can help to reduce unspecific binding during pull-down assays with cell lysates.
6. During preparation of samples and gels for mass spectrometry analysis, keratin contaminations should be avoided as much as possible: use clean tubes and glassware and wear gloves at all times.
7. For cell transfection, column-purified plasmid DNA always works better. We use QIAGEN QIAfilter DNA purification kits.
8. Transfection with Lipofectamine 2000 (Invitrogen) also works well for HEK293T cells. Although more expensive, it is preferable when large proteins (>150 kDa) need to be expressed.
9. Keep in mind that while some tissue culture media contain biotin (for example, Ham's F10), other media do not (for example, DMEM). If the culture medium contains no

biotin, exogenous biotin should be added to achieve efficient biotinylation. The medium described in Subheading 2.3 can be used for culturing all cell lines mentioned in this chapter.

10. The binding capacity of the Dynabeads (6.7×10^8 beads/ml, 10 mg/ml) is approximately 200 pmol biotinylated peptides per 1 mg. The actual protein yield observed in these experiments is ~2–10 μg protein per 50 μl beads. Protein binding can depend on protein size because of the sterical hindrance.
11. Biotinylation tag-based pull-down assays work in different buffers, including those with ionic detergents (for example, radioimmunoprecipitation assay (RIPA) buffer with 1% NP-40, 1% Deoxycholate, and 0.05% SDS).
12. When several plasmid DNAs are cotransfected, add DNA to the transfection mixture first, and only then add the transfection reagent to insure efficient cotransfection. Numerous other transfection reagents are commercially available; for example, Fugene 6 (Roche) is a good alternative to Polyfect.
13. Make sure that PFA solution has neutral pH and is at room temperature; otherwise, certain protein epitopes and direct GFP fluorescence may be negatively affected.
14. Combined cold methanol/PFA fixation is optimal for labeling EB and CLIP comets. Cold methanol insures very quick fixation and optimal preservation of microtubule cytoskeleton, but destroys membrane structures, such as vesicles. Postfixation with PFA prevents protein extraction after fixation; when it is omitted, staining for EBs and CLIPs still works but the signal is weaker. However, in some cases, like, for example, when staining for CLASPs or LL5β (34), PFA postfixation blocks epitope accessibility and inhibits labeling. Finally, the classic fixation with 4% PFA alone at room temperature is good for preserving membrane compartments, but cannot be used for visualizing microtubule plus ends because +TIPs rapidly dissociate from microtubule ends during fixation. Alternative protocols suitable for +TIP fixation are available (35, 36). For new proteins and epitopes, different fixation conditions should be tested and optimized.
15. Different cell types can be used, but cells that are easy to transfect, are flat and have relatively sparse microtubule cytoskeleton, such as COS-7 monkey kidney cells or MRC5 human lung fibroblasts, are preferable.
16. Keep in mind that in mammalian cells cultured at 37°C, microtubules grow with a velocity of 0.1–0.5 μm/s.

Acknowledgments

This work was supported by the Netherlands Organisation for Scientific Research grants ZonMW-VIDI and CW-ECHO to C.C.H and ALW-VICI and ZonMW-TOP to A.A. We thank Susana Montenegro Gouveia and Daniël Splinter for their contribution to establishing affinity purification protocols, Ilya Grigoriev for establishing live cell imaging protocols, and Jeroen Demmers for mass spectrometry analysis.

References

1. Desai, A., and Mitchison, T. J. (1997) Microtubule polymerization dynamics. *Annu Rev Cell Dev Biol 13*, 83–117.
2. Howard, J., and Hyman, A. A. (2003) Dynamics and mechanics of the microtubule plus end. *Nature 422*, 753–758.
3. Schuyler, S. C., and Pellman, D. (2001) Microtubule "plus-end-tracking proteins": The end is just the beginning. *Cell 105*, 421–424.
4. Akhmanova, A., and Steinmetz, M. O. (2008) Tracking the ends: a dynamic protein network controls the fate of microtubule tips. *Nat Rev Mol Cell Biol 9*, 309–322.
5. Su, L. K., and Qi, Y. (2001) Characterization of human MAPRE genes and their proteins. *Genomics 71*, 142–149.
6. Juwana, J. P., Henderikx, P., Mischo, A., Wadle, A., Fadle, N., Gerlach, K., Arends, J. W., Hoogenboom, H., Pfreundschuh, M., and Renner, C. (1999) EB/RP gene family encodes tubulin binding proteins. *Int J Cancer 81*, 275–284.
7. Hayashi, I., and Ikura, M. (2003) Crystal structure of the amino-terminal microtubule-binding domain of end-binding protein 1 (EB1). *J Biol Chem 278*, 36430–36434.
8. Slep, K. C., Rogers, S. L., Elliott, S. L., Ohkura, H., Kolodziej, P. A., and Vale, R. D. (2005) Structural determinants for EB1-mediated recruitment of APC and spectraplakins to the microtubule plus end. *J Cell Biol 168*, 587–598.
9. Honnappa, S., John, C. M., Kostrewa, D., Winkler, F. K., and Steinmetz, M. O. (2005) Structural insights into the EB1-APC interaction. *Embo J 24*, 261–269.
10. Honnappa, S., Okhrimenko, O., Jaussi, R., Jawhari, H., Jelesarov, I., Winkler, F. K., and Steinmetz, M. O. (2006) Key interaction modes of dynamic +TIP networks. *Mol Cell 23*, 663–671.
11. Hayashi, I., Wilde, A., Mal, T. K., and Ikura, M. (2005) Structural basis for the activation of microtubule assembly by the EB1 and p150Glued complex. *Mol Cell 19*, 449–460.
12. Steinmetz, M. O., and Akhmanova, A. (2008) Capturing protein tails by CAP-Gly domains. *Trends Biochem Sci 33*, 535–545.
13. Honnappa, S., Gouveia, S. M., Weisbrich, A., Damberger, F. F., Bhavesh, N. S., Jawhari, H., Grigoriev, I., van Rijssel, F. J., Buey, R. M., Lawera, A., Jelesarov, I., Winkler, F. K., Wuthrich, K., Akhmanova, A., and Steinmetz, M. O. (2009) An EB1-binding motif acts as a microtubule tip localization signal. *Cell 138*, 366–376.
14. Bieling, P., Kandels-Lewis, S., Telley, I. A., van Dijk, J., Janke, C., and Surrey, T. (2008) CLIP-170 tracks growing microtubule ends by dynamically recognizing composite EB1/tubulin-binding sites. *J Cell Biol 183*, 1223–1233.
15. Dragestein, K. A., van Cappellen, W. A., van Haren, J., Tsibidis, G. D., Akhmanova, A., Knoch, T. A., Grosveld, F., and Galjart, N. (2008) Dynamic behavior of GFP-CLIP-170 reveals fast protein turnover on microtubule plus ends. *J Cell Biol 180*, 729–737.
16. Berrueta, L., Tirnauer, J. S., Schuyler, S. C., Pellman, D., and Bierer, B. E. (1999) The APC-associated protein EB1 associates with components of the dynactin complex and cytoplasmic dynein intermediate chain. *Curr Biol 9*, 425–428.
17. Bu, W., and Su, L. K. (2003) Characterization of functional domains of human EB1 family proteins. *J Biol Chem 278*, 49721–49731.
18. Komarova, Y., Lansbergen, G., Galjart, N., Grosveld, F., Borisy, G. G., and Akhmanova, A. (2005) EB1 and EB3 control CLIP dissociation from the ends of growing microtubules. *Mol Biol Cell 16*, 5334–5345.

19. Mimori-Kiyosue, Y., Grigoriev, I., Lansbergen, G., Sasaki, H., Matsui, C., Severin, F., Galjart, N., Grosveld, F., Vorobjev, I., Tsukita, S., and Akhmanova, A. (2005) CLASP1 and CLASP2 bind to EB1 and regulate microtubule plus-end dynamics at the cell cortex. *J Cell Biol 168*, 141–153.
20. Lee, T., Langford, K. J., Askham, J. M., Bruning-Richardson, A., and Morrison, E. E. (2008) MCAK associates with EB1. *Oncogene 27*, 2494–2500.
21. Jiang, K., Wang, J., Liu, J., Ward, T., Wordeman, L., Davidson, A., Wang, F., and Yao, X. (2009) TIP150 interacts with and targets MCAK at the microtubule plus ends. *EMBO Rep 10*, 857–865.
22. Rogers, S. L., Wiedemann, U., Hacker, U., Turck, C., and Vale, R. D. (2004) Drosophila RhoGEF2 Associates with Microtubule Plus Ends in an EB1-Dependent Manner. *Curr Biol 14*, 1827–1833.
23. Jaworski, J., Kapitein, L. C., Gouveia, S. M., Dortland, B. R., Wulf, P. S., Grigoriev, I., Camera, P., Spangler, S. A., Di Stefano, P., Demmers, J., Krugers, H., Defilippi, P., Akhmanova, A., and Hoogenraad, C. C. (2009) Dynamic microtubules regulate dendritic spine morphology and synaptic plasticity. *Neuron 61*, 85–100.
24. Grigoriev, I., Gouveia, S. M., van der Vaart, B., Demmers, J., Smyth, J. T., Honnappa, S., Splinter, D., Steinmetz, M. O., Putney, J. W., Jr., Hoogenraad, C. C., and Akhmanova, A. (2008) STIM1 is a MT-plus-end-tracking protein involved in remodeling of the ER. *Curr Biol 18*, 177–182.
25. Smith, P. A., Tripp, B. C., DiBlasio-Smith, E. A., Lu, Z., LaVallie, E. R., and McCoy, J. M. (1998) A plasmid expression system for quantitative in vivo biotinylation of thioredoxin fusion proteins in Escherichia coli. *Nucleic Acids Res 26*, 1414–1420.
26. Beckett, D., Kovaleva, E., and Schatz, P. J. (1999) A minimal peptide substrate in biotin holoenzyme synthetase-catalyzed biotinylation. *Protein Sci 8*, 921–929.
27. de Boer, E., Rodriguez, P., Bonte, E., Krijgsveld, J., Katsantoni, E., Heck, A., Grosveld, F., and Strouboulis, J. (2003) Efficient biotinylation and single-step purification of tagged transcription factors in mammalian cells and transgenic mice. *Proc Natl Acad Sci USA 100*, 7480–7485.
28. Grosveld, F., Rodriguez, P., Meier, N., Krpic, S., Pourfarzad, F., Papadopoulos, P., Kolodziej, K., Patrinos, G. P., Hostert, A., and Strouboulis, J. (2005) Isolation and characterization of hematopoietic transcription factor complexes by in vivo biotinylation tagging and mass spectrometry. *Ann N Y Acad Sci 1054*, 55–67.
29. Rodriguez, P., Braun, H., Kolodziej, K. E., de Boer, E., Campbell, J., Bonte, E., Grosveld, F., Philipsen, S., and Strouboulis, J. (2006) Isolation of transcription factor complexes by in vivo biotinylation tagging and direct binding to streptavidin beads. *Methods Mol Biol 338*, 305–323.
30. Kolodziej, K. E., Pourfarzad, F., de Boer, E., Krpic, S., Grosveld, F., and Strouboulis, J. (2009) Optimal use of tandem biotin and V5 tags in ChIP assays. *BMC Mol Biol 10*, 6.
31. Chapman-Smith, A., and Cronan, J. E., Jr. (1999) The enzymatic biotinylation of proteins: a post-translational modification of exceptional specificity. *Trends Biochem Sci 24*, 359–363.
32. Stepanova, T., Slemmer, J., Hoogenraad, C. C., Lansbergen, G., Dortland, B., De Zeeuw, C. I., Grosveld, F., van Cappellen, G., Akhmanova, A., and Galjart, N. (2003) Visualization of microtubule growth in cultured neurons via the use of EB3-GFP (end-binding protein 3-green fluorescent protein). *J Neurosci 23*, 2655–2664.
33. Driegen, S., Ferreira, R., van Zon, A., Strouboulis, J., Jaegle, M., Grosveld, F., Philipsen, S., and Meijer, D. (2005) A generic tool for biotinylation of tagged proteins in transgenic mice. *Transgenic Res 14*, 477–482.
34. Lansbergen, G., Grigoriev, I., Mimori-Kiyosue, Y., Ohtsuka, T., Higa, S., Kitajima, I., Demmers, J., Galjart, N., Houtsmuller, A. B., Grosveld, F., and Akhmanova, A. (2006) CLASPs attach microtubule plus ends to the cell cortex through a complex with LL5beta. *Dev Cell 11*, 21–32.
35. Maney, T., Hunter, A. W., Wagenbach, M., and Wordeman, L. (1998) Mitotic centromere-associated kinesin is important for anaphase chromosome segregation. *J Cell Biol 142*, 787–801.
36. Rogers, S. L., Rogers, G. C., Sharp, D. J., and Vale, R. D. (2002) Drosophila EB1 is important for proper assembly, dynamics, and positioning of the mitotic spindle. *J Cell Biol 158*, 873–884.
37. Coquelle, F. M., Caspi, M., Cordelieres, F. P., Dompierre, J. P., Dujardin, D. L., Koifman, C., Martin, P., Hoogenraad, C. C., Akhmanova, A., Galjart, N., De Mey, J. R., and Reiner, O. (2002) LIS1, CLIP-170's key to the dynein/dynactin pathway. *Mol Cell Biol 22*, 3089–3102.

Chapter 3

The ALS8 protein VAPB interacts with the ER–Golgi recycling protein YIF1A and regulates membrane delivery into dendrites

Marijn Kuijpers[1,2], Ka Lou Yu[1,2],
Eva Teuling[2], Anna Akhmanova[1],
Dick Jaarsma[2]
and Casper C Hoogenraad[1,2,*]

[1]Division of Cell Biology, Department of Biology,
Faculty of Science, Utrecht University, Utrecht, The Netherlands
and [2]Department of Neuroscience, Erasmus Medical Center, Rotterdam, The Netherlands

The EMBO Journal (2013) 32, 2056–2072
www.embojournal.org

TRANSPARENT PROCESS

THE EMBO JOURNAL

The ALS8 protein VAPB interacts with the ER–Golgi recycling protein YIF1A and regulates membrane delivery into dendrites

Marijn Kuijpers[1,2], Ka Lou Yu[1,2], Eva Teuling[2], Anna Akhmanova[1], Dick Jaarsma[2] and Casper C Hoogenraad[1,2,*]

[1]Division of Cell Biology, Department of Biology, Faculty of Science, Utrecht University, Utrecht, The Netherlands and [2]Department of Neuroscience, Erasmus Medical Center, Rotterdam, The Netherlands

The vesicle-associated membrane protein (VAMP) associated protein B (VAPB) is an integral membrane protein localized to the endoplasmic reticulum (ER). The P56S mutation in VAPB has been linked to motor neuron degeneration in amyotrophic lateral sclerosis type 8 (ALS8) and forms ER-like inclusions in various model systems. However, the role of wild-type and mutant VAPB in neurons is poorly understood. Here, we identified Yip1-interacting factor homologue A (YIF1A) as a new VAPB binding partner and important component in the early secretory pathway. YIF1A interacts with VAPB via its transmembrane regions, recycles between the ER and Golgi and is mainly localized to the ER–Golgi intermediate compartments (ERGICs) in rat hippocampal neurons. VAPB strongly affects the distribution of YIF1A and is required for intracellular membrane trafficking into dendrites and normal dendritic morphology. When VAPB-P56S is present, YIF1A is recruited to the VAPB-P56S clusters and loses its ERGIC localization. These data suggest that both VAPB and YIF1A are important for ER-to-Golgi transport and that missorting of YIF1A may contribute to VAPB-associated motor neuron disease.

The EMBO Journal (2013) **32,** 2056–2072. doi:10.1038/emboj.2013.131; Published online 4 June 2013
Subject Categories: membranes & transport; neuroscience
Keywords: amyotrophic lateral sclerosis (ALS); dendrite morphology; secretory pathway; VAMP-associated protein (VAP); Yip1 interacting factor (YIF1)

Introduction

The secretory pathway is responsible for the delivery of a variety of protein and lipid cargo, such as ion channels, receptors and lipid membranes, to their proper location. In the early secretory pathway, newly synthesized proteins that pass the quality control of the endoplasmic reticulum (ER) concentrate at specialized ER subdomains called the ER exit sites (ERES) (Lee *et al*, 2004; Dancourt and Barlowe, 2010). From here, cargo leaves the ER and is transported to the Golgi compartments to undergo further processing, sorting and subsequent delivery to the plasma membrane or other cellular organelles. ER-derived vesicles deliver their cargo either directly to the cis-Golgi membrane or pass a specialized membrane compartment called the ER–Golgi intermediate compartment (ERGIC) (Watson and Stephens, 2005; Appenzeller-Herzog and Hauri, 2006; Saraste *et al*, 2009; Lorente-Rodriguez and Barlowe, 2011). Whereas the early secretory pathway and its organization is well studied in a variety of cellular model systems such as yeast and fibroblasts, little information is available about this trafficking pathway in neuronal cells. A number of studies have demonstrated the presence of ER-to-Golgi transport components in neurons (Krijnse-Locker *et al*, 1995; Pierce *et al*, 2001; Horton and Ehlers, 2003) and indicated the importance of the early secretory trafficking for neuronal development and morphogenesis (Hanus and Ehlers, 2008; Tang, 2008; Aridor and Fish, 2009; Jan and Jan, 2010).

Members of the highly conserved VAP family, including the mammalian vesicle-associated membrane protein associated protein A (VAPA) and VAPB proteins, are present in the ER and have been proposed to play a role in maintaining Golgi complex identity, ER morphology, lipid transfer and in regulating ER and Golgi transport (Soussan *et al*, 1999; Skehel *et al*, 2000; Pennetta *et al*, 2002; Amarilio *et al*, 2005; Teuling *et al*, 2007; Lev *et al*, 2008; Peretti *et al*, 2008; Tsuda *et al*, 2008; Han *et al*, 2012). VAP proteins contain an N-terminal domain, which is highly homologous to the nematode major sperm protein (MSP), a central domain that forms a coiled-coil structure and the C-terminal transmembrane tail domain (Nishimura *et al*, 1999; Kaiser *et al*, 2005). Interest in VAP proteins has greatly increased after the discovery of a dominant missense mutation P56S in the MSP domain of VAPB, which causes a familial motor neuron disease, designated amyotrophic lateral sclerosis type 8 (ALS8) (Nishimura *et al*, 2004). P56S mutant VAPB accumulates in inclusions that contain abnormal organized ER (Teuling *et al*, 2007; Papiani *et al*, 2012) and recruit wild-type VAPA/B in these inclusions, suggesting that VAPB-P56S could have a dominant-negative effect on VAP function (Teuling *et al*, 2007). Indeed, a loss-of-function mechanism has been observed in several model systems (Chai *et al*, 2008; Ratnaparkhi *et al*, 2008; Tsuda *et al*, 2008; Suzuki *et al*, 2009; Forrest *et al*, 2013). Moreover, a reduction in VAP protein levels has been described in sporadic ALS patients, SOD1 mutant mice as well as ALS-derived motor neurons (Teuling *et al*, 2007; Anagnostou *et al*, 2010; Mitne-Neto *et al*, 2011). However, mechanisms leading to VAPB-linked motor neuron degeneration are still poorly understood.

To gain more insight into the role of VAPB in neurons, we searched for new binding partners of VAPB. We identified Yip1-interacting factor homologue A (YIF1A) as a new VAPB

*Corresponding author. Cell Biology, Faculty of Science, Utrecht University, Padualaan 8, 3584 CH Utrecht, The Netherlands. Tel.: +31 30 2534585; Fax: +31 30 2532837; E-mail c.hoogenraad@uu.nl

Received: 2 November 2012; accepted: 7 May 2013; published online: 4 June 2013

binding partner that interacts with both wild-type VAPB and mutant VAPB-P56S. YIF1A is the human orthologue of the budding yeast Yif1p, a transmembrane protein that plays an important role in early secretory transport in yeast and mammalian cells (Matern *et al*, 2000; Barrowman *et al*, 2003; Jin *et al*, 2005; Yoshida *et al*, 2008). We find that YIF1A recycles between the ER and Golgi and is mainly localized to the ERGIC in hippocampal neurons. Both VAPB and YIF1A are required for membrane trafficking to dendrites and proper dendrite morphology. In addition, we show that ALS8 mutant VAPB-P56S strongly disrupts the localization of YIF1A to ERGIC. Our data suggest an important role for YIF1A and VAPB in the early secretory pathway and we propose that the missorting of YIF1A plays a role in VAPB-associated motor neuron disease. These findings advance the knowledge of fundamental trafficking processes in neuronal cells and have important implications for our understanding of neuronal degeneration.

Results

YIF1A interacts with both wild-type and mutant VAPB

To identify new VAPB interacting proteins, we performed pull-down assays combined with mass spectrometry. Biotinylated and GFP-tagged VAPB (bio-GFP-VAPB) and control bio-GFP constructs were transiently co-expressed in HeLa cells together with the protein-biotin ligase BirA, isolated with streptavidin beads and the proteins were analysed by mass spectrometry. Bio-GFP-VAPB bound to several previously identified VAPB binding partners, such as the FFAT-motif containing proteins NIR2, OSBPL3, OSBPL6 and OSBPL9 (Wyles and Ridgway, 2004; Amarilio *et al*, 2005; Lehto *et al*, 2005; Teuling *et al*, 2007) (Figure 1A). In addition, a novel potential VAPB binding partner was identified, YIF1A, a transmembrane protein of 293 amino acids and mammalian orthologue of the *Saccharomyces cerevisiae* protein Yif1p (Yip1p-interacting factor 1) (Matern *et al*, 2000). YIF1A and its close homologue YIF1B are members of a large protein family, named FinGERs, which share a common structure with an N-terminal hydrophilic region, followed by conserved transmembrane regions (Shakoori *et al*, 2003; Pfeffer and Aivazian, 2004).

The interaction of VAPB and YIF1A was confirmed by biotin pull-down experiments using extracts of HEK293T cells overexpressing GFP-YIF1A and bio-HA-VAPB (Figure 1B). Pull-down experiments also revealed binding between YIF1B and VAPB (Figure 1B) and between VAPA and both YIF homologues (Figure 1C). To further confirm the interaction between VAPB and YIF1A, we performed immunofluorescence experiments in COS-7 cells. HA-YIF1A co-localized with both endogenous VAPB and co-transfected myc-VAPB, which as previously demonstrated localize to the ER (Nishimura *et al*, 2004; Kanekura *et al*, 2006; Teuling *et al*, 2007; Kim *et al*, 2010; Papiani *et al*, 2012) (Figure 1D and E). Significantly, HA-YIF1A also co-distributes with ALS-linked mutant VAPB-P56S and VAPA-P56S (Figure 1F and H), which accumulates in small spherical inclusions (Nishimura *et al*, 2004; Kanekura *et al*, 2006; Teuling *et al*, 2007; Kim *et al*, 2010; Papiani *et al*, 2012). Likewise also YIF1B was recruited to mutant VAPA/B inclusion (Figure 1G and I). Together, these results show that YIF1A/B interacts with VAPA/B family proteins.

The transmembrane domains of both VAPB and YIF1A are required for their interaction

Secondary structure predictions indicate that YIF1A contains four transmembrane domains at the C-terminus (Figure 2A) (Altschul *et al*, 1997; Hirokawa *et al*, 1998), while the N-terminus of the yeast homologue Yif1p has been shown to face the cytosol (Matern *et al*, 2000). To confirm that the N-terminus of YIF1A faces the cytosol, we generated a YIF1A construct with a biotinylation tag at the N-terminus (Figure 2B). Pull-down experiments showed that this construct was biotinylated when the biotinylating enzyme BirA was localized in the cytoplasm, but not by a variant BirA that is localized in the ER lumen (Figure 2B).

To identify the regions through which VAPB interacts with YIF1A, we first made truncated GFP-YIF1A constructs encoding either the N-terminus (1–131) or the C-terminal transmembrane region (131–293) of YIF1A (Figure 2A). Pull-down experiments using HEK293T cells co-expressing HA-VAPB and the YIF1A deletion constructs showed that VAPB only co-precipitates with YIF1A construct that contained the transmembrane region (Figure 2C and D). These data were confirmed by a glutathione S-transferase (GST) pull-down assay with cell lysates expressing truncated YIF1A constructs using VAPB and VAPB-P56S immobilized on GST beads. The C-terminal part, but not the N-terminal part of YIF1A co-precipitated with VAPB and VAPB-P56S (Figure 2E). To characterize in more detail the YIF1A domain that binds VAPB, we made additional truncated YIF1A constructs, which contain only the first two transmembrane domains (131–198), the last two transmembrane domains (198–298) or the N-terminal cytosolic domain with the first two transmembrane domains (1–198) (Figure 2A). Pull-down experiments with biotinylated VAPB showed that all transmembrane containing YIF1A constructs co-precipitated with VAPB (Figure 2F). However, VAPB brings down considerable higher amounts of truncated GFP-YIF1A proteins that contain the first and second transmembrane domain (131–198) (Figure 2F), indicating that the VAPB interaction is strongest with this region. The marked difference between binding of the first two transmembrane domains compared to the last two transmembrane domains suggests a specific interaction between YIF1A and VAPB. GFP-YIF1A (131–198) also efficiently co-precipitated with VAPB-P56S (Figure 2G). Moreover, the GFP-tagged single transmembrane domain of VAPB co-immunoprecipitates with YIF1A, suggesting that the transmembrane domain of VAPB is important for binding YIF1A (Figure 2H). To further explore the binding of YIF1A with VAPB, we mutated two GxxxG motifs that are present in the first and third transmembrane domain of YIF1A (Figure 2A). GxxxG motifs are known to facilitate interactions between transmembrane helices and mediate the assembly of the transmembrane helices in VAPB (Kim *et al*, 2010). However, disruption of these motifs in YIF1A did not interfere with VAPB binding (Figure 2I). These data were confirmed by immunofluorescence in COS-7 cells (Figure 2J–L; Supplementary Figure S1). The results show that the first two transmembrane domains of YIF1A are important for VAPB binding but that this binding does not depend on GxxxG motifs. Together, these data indicate that the transmembrane domains of both VAPB and YIF1A are important for their interaction.

YIF1A recycles between the Golgi and ER and localizes to the ERGIC in hippocampal neurons

Next, we investigated the function of the VAPB–YIF1A interaction using primary cultured rat hippocampal neurons as a model system. VAPB is mainly localized to the ER in neuronal cells (Teuling *et al*, 2007), whereas the distribution of YIF1A in neurons is not clear. Immunofluorescent stainings of HA-YIF1A expressing neurons at 16 days *in vitro* (DIV16) showed that YIF1A is present in a reticular network throughout the neuron and localizes to discrete puncta in the cell body (Figure 3A). The reticular YIF1A staining partially co-localizes with endogenous VAPB and the ER marker protein disulphide

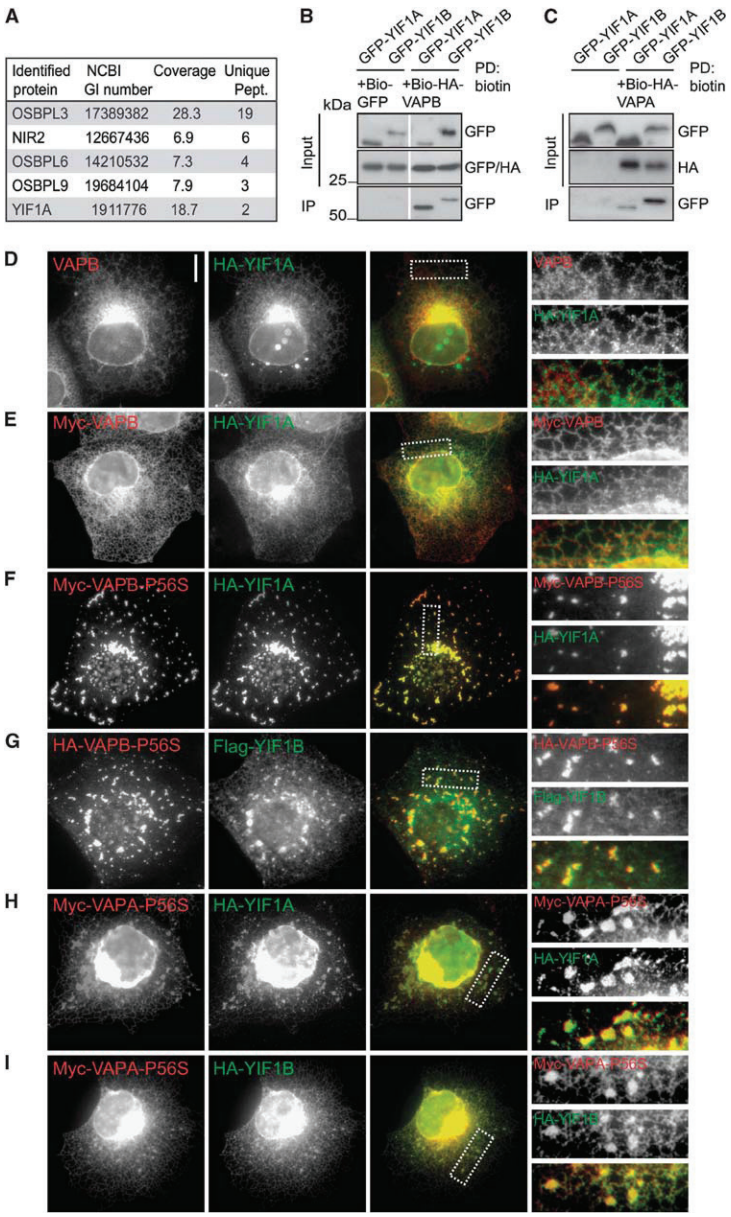

isomerase (PDI) (Figure 3B and C). Double labelling with the ERGIC marker ERGIC53/p58 showed partial co-localization in the cell body, indicating that the YIF1A-positive puncta coincide with the ERGIC (Figure 3D). In contrast, the endosome marker early endosomal autoantigen 1 (EEA1) showed no co-localization with HA-YIF1A (Figure 3E).

To further verify the co-localization of YIF1A with the ERGIC, we blocked vesicular trafficking between ER and Golgi using brefeldin A (BFA). Co-stainings with cis-Golgi marker GM130 and ERGIC marker ERGIC53/p58 show respectively little and moderate co-localization with YIF1A in control neurons (Figure 4A, C and E). However, after blocking vesicular trafficking using BFA, YIF1A accumulates in the perinuclear region of the cell body where it strongly co-localizes with Golgi and ERGIC markers (Figure 4B and D). Analysis of the Pearson's correlation coefficients of fluorescent signals confirmed that BFA treatment significantly increases the co-localization of YIF1A with Golgi and ERGIC (Figure 4E). In contrast, VAPB is present in the ER, not localized to Golgi and ERGIC structures and its localization is unaffected by BFA treatment (Figure 4F, G and E). These results indicate that while VAPB is restricted to the ER, YIF1A recycles between the Golgi and ER and is predominantly present in the ERGIC.

VAPB retains YIF1A in the ER and inhibits its recycling into ERGIC and Golgi

We next determined whether the specific distribution of YIF1A and VAPB depends on each other's subcellular localization. We generated YIF1A, YIF1B, VAPA and VAPB shRNAs based on the previously published siRNA sequences to perform knockdown experiments in neurons (Teuling *et al*, 2007; Carrel *et al*, 2008). Both VAPA and VAPB shRNAs showed a significant reduction in immunostaining for the respective VAP, indicating an effective knockdown for all VAP-shRNA constructs (Supplementary Figure S2). First, we tested if the VAPB localization in the ER depends on YIF1. In DIV16 neurons, absence of YIF1A/B did not affect the localization of VAPB. Second, we tested if YIF localization depends on VAP using VAPA and VAPB shRNAs. The VAPA/B-shRNA expressing neurons at DIV16 showed a consistent change in YIF1A localization. Whereas control cells have a widespread reticular and punctate YIF1A staining (Figure 5A), VAPA/B knockdown neurons displayed a strong accumulation of YIF1A in the perinuclear region of the cell body (Figure 5B) and a marked co-distribution of YIF1A with cis-Golgi marker GM130 and ERGIC marker ERGIC53/p58. Quantification revealed that the co-localization of YIF1A with GM130 and ERGIC53/p58 is strongly increased in the absence of VAP (Figure 5C–G). These data indicate that knockdown of VAP in neurons leads to a translocation of YIF1A in post-ER structures.

The above data imply that VAPB is important to retain YIF1A in the ER and might control the recycling of YIF1A from the ER to the ERGIC and Golgi. To test this hypothesis, we overexpressed myc-VAPB together with HA-YIF1A. Indeed, YIF1A shows a strong reticular distribution throughout the neuron and loses its characteristic ERGIC localization (Figure 6A, B and D). Next, we tested whether a previously characterized interacting partner of YIF1A, YIP1, also retains YIF1A in the ER. YIP1 has been shown to localize to ER and Golgi membranes as well as coat protein complex II (COPII) transport vesicles in yeast (Yang *et al*, 1998; Matern *et al*, 2000; Heidtman *et al*, 2005; Jin *et al*, 2005). In hippocampal neurons, Flag-YIP1A has moderate Golgi and a pronounced ERGIC localization (Figure 6C). In contrast to VAPB, Flag-YIP1A overexpression increased YIF1A in the Golgi and ERGIC, while reducing its ER localization, thus having the opposite effect of VAPB (Figure 6C and D). Next, we used fluorescence recovery after photobleaching (FRAP) to examine the mobility of GFP-YIF1A molecules under the influence of increased VAPB levels. A 3-by-3 μm region of the cell soma was bleached by high laser power and fluorescence intensity was measured over a period of ~5 min (Figure 6E). GFP-YIF1A fluorescence recovered rapidly in control neurons and reached a maximal recovery of ~90% within this time frame. In neurons co-expressing myc-VAPB the maximal recovery of GFP-YIF1A is decreased to ~70% (Figure 6E and F), indicating an increase in the immobile fraction of YIF1A molecules in the ER. Taken together, these data suggest that the ER-resident protein VAPB indeed binds YIF1A in the ER and thereby inhibits its recycling to the ERGIC and Golgi.

YIF and VAP are required for normal dendrite morphology

Studies in *Drosophila* neurons and recently in zebrafish suggest that VAPB has an important role in the transport of proteins to the axon (Yang *et al*, 2012; Forrest *et al*, 2013) and that loss of VAP proteins affects neuron morphology (Pennetta *et al*, 2002; Tsuda *et al*, 2008; Forrest *et al*, 2013). To assess the morphological effects of depleting YIF1, YIP1 and VAP proteins, we analysed the length of axons and dendrites in hippocampal neurons transfected at DIV1 with VAPA/B-shRNAs, YIF1A/B-shRNAs or YIP1A-shRNA, together with β-galactosidase to visualize neuron morphology (Figure 7A). Neurons were fixed at DIV5 and immunofluorescent staining with antibody against tau was used to distinguish the axon from the dendrites (Figure 7B). Depletion of YIF1 and VAP, but not YIP1, caused a significant decrease in axonal length (Figure 7C). Previous data showed

Figure 1 Interaction of YIF1A with wild-type and mutant VAPB. (**A**) Identification of wild-type VAPB binding partners by mass spectrometry in HeLa cell extract. The table shows proteins identified with a significant Mascot score in the pull-down with streptavidin beads from an extract of HeLa cells co-expressing Bio-GFP-VAPB and biotin ligase BirA. The list is corrected for background proteins, which were identified in a control pull-down from HeLa cells expressing bio-GFP. Abbreviations used in the table to indicate the identified proteins: OSBPL, oxysterol binding protein-like; NIR, N-terminal domain-interacting receptor. (**B**) Biotin pull-downs (PD) from HEK293T extract transfected with Bio-HA-VAPB and GFP-YIF1A, GFP-YIF1B or control bio-GFP and probed for GFP and HA. (**C**) Biotin pull-downs from HEK293T extract transfected with Bio-HA-VAPA and GFP-YIF1A or GFP-YIF1B and probed for GFP and HA. The ratio input/pellet is 2–5% for all pull-down and immunoprecipitation experiments. (**D**) COS-7 cells transfected with HA-YIF1A and stained with anti-HA (green) and anti-VAPB (red) antibodies. (**E**, **F**) COS-7 cells double transfected with HA-YIF1A and myc-VAPB (**D**) or myc-VAPB-P56S (**E**) stained with anti-HA (green) and anti-myc (red) antibodies. (**G**) COS-7 cells double transfected with HA-VAPB-P56S and Flag-YIF1B, fixed and stained with anti-HA (green) and anti-Flag (red) antibodies. (**H**, **I**) COS-7 cells double transfected with myc-VAPA-P56S and HA-YIF1A (**H**) or HA-YIF1B (**I**) stained with anti-HA (green) and anti-myc (red) antibodies. Panels on the right side show enlargements of the boxed regions. Scale bar, 10 μm.

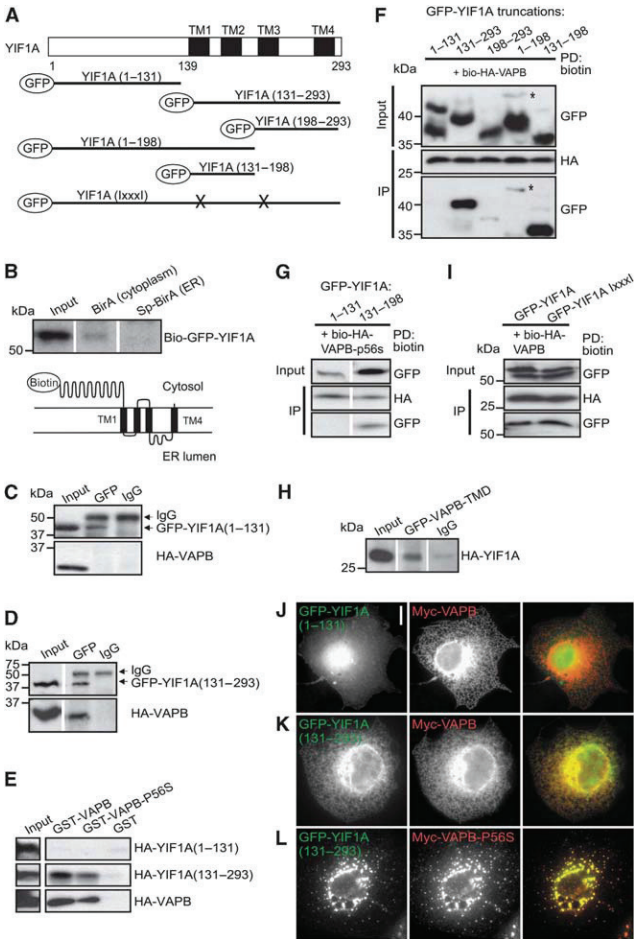

Figure 2 The transmembrane domain of YIF1A interacts with VAPB. (**A**) YIF1A deletion constructs were made containing amino acids 1–131 of YIF1A, amino acids 131–293, 198–293, 1–198 and amino acids 131–198. GxxxG motifs in transmembrane domain one and three were mutated by replacing the glycine residues with isoleucine. The predicted transmembrane domains are labelled with TM. (**B**) Biotin pull-down to determine the topology of YIF1A using HEK293T extracts transfected with bio-GFP-YIF1A and BirA (cytoplasm) or SP-BirA (ER lumen). Bio-GFP-YIF1A binds to streptavidin beads in the presence of cytoplasmic BirA but not in the presence of luminal BirA. Samples were immunoblotted using anti-GFP antibodies. (**C**, **D**) Analysis of YIF1A binding domain by co-immunoprecipitation. HEK293T cells co-transfected with (**C**) GFP-YIF1A(1–131) or (**D**) GFP-YIF1A(131-293) and HA-VAPB were immunoprecipitated with anti-GFP or IgG (control) antibodies. (**E**) Binding domain analysis by GST pull-down assay using lysates of HEK293T cells expressing HA-YIF1A truncated constructs and GST-VAPB or GST-VAPB-P56S. Samples were immunoblotted using anti-HA antibodies. (**F**) Biotin pull-downs (PD) from HEK293T extracts transfected with GFP-YIF1A truncated constructs and bio-HA-VAPB. Probed for GFP and HA. The asterisk denotes a band corresponding to the YIF1A (1–198) protein. (**G**) Biotin pull-down (PD) from HEK293T extracts transfected with GFP-YIF1A truncated constructs and bio-HA-VAPB-P56S and probed for GFP and HA. (**H**) Immunoprecipitation from extract of HEK293T cells co-expressing GFP-VAPB-TMD and HA-YIF1A. Immunoblot is probed for HA. (**I**) Biotin pull-down from HEK293T extracts transfected with GFP-YIF1A IxxxI and bio-HA-VAPB and probed for GFP and HA. The ratio input/pellet is 2–5% for all pull-down and immunoprecipitation experiments. (**J**–**L**) COS-7 cells double transfected with myc-VAPB (**J**, **K**) or myc-VAPB-P56S (**L**) and GFP-YIF1A truncation constructs, fixed and stained with anti-myc (red) antibodies. Scale bar, 10 μm.

that ER-to-Golgi transport is particularly important for dendrite morphology (Ye *et al*, 2007). Since YIF1, YIP1 and VAP proteins localize to the early secretory pathway in hippocampal neurons we wondered whether depletion of these proteins had any effect on dendrite morphology. Indeed, DIV5 neurons showed a significant decrease in dendritic length when transfected with VAPA/B-shRNAs, YIF1A/B-shRNAs and YIP1A-shRNA (Figure 7D). Because in DIV5 neurons dendrites are short and hardly branched we used mature neurons to examine more closely the effect of

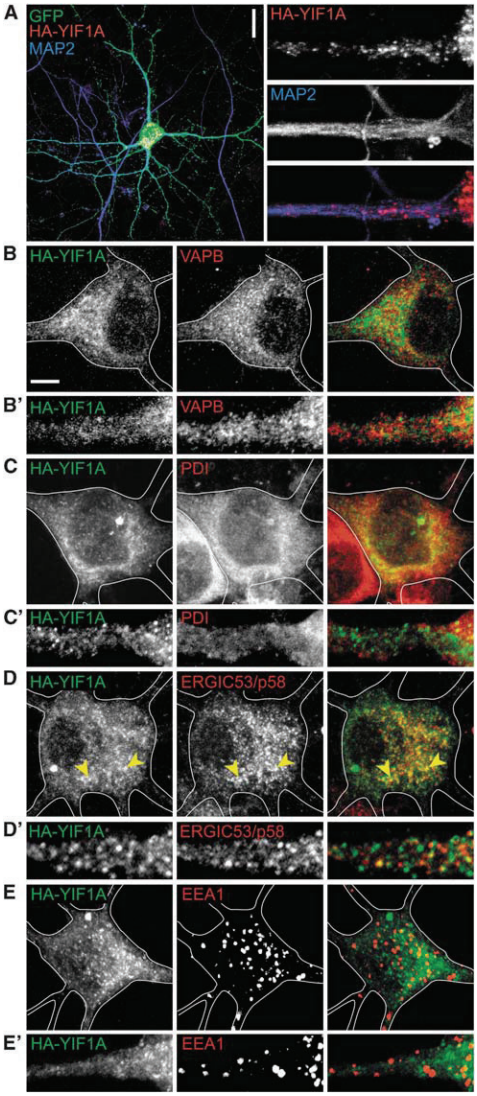

Figure 3 YIF1A localization in cultured hippocampal neurons. (**A**) Representative images of rat hippocampal neurons (DIV16) co-transfected with HA-YIF1A and GFP to visualize morphology and labelled with anti-HA (red) and anti-MAP2 (blue) antibodies. Scale bar, 20 μm. In the right panel, a dendritic segment is enlarged to show the presence of HA-YIF1A in proximal dendrites. (**B**–**E**) Representative images of rat hippocampal neurons transfected with HA-YIF1A and labelled with anti-HA (green) and anti-VAPB (red in **B**), anti-PDI (red in **C**), anti-ERGIC53/p58 (red in **D**) or anti-EEA1 (red in **E**). Solid lines indicate the cell edge and arrows show co-localization. Scale bars represent 20 μm in (**A**) and 5 μm in (**B**). (B'–E') Enlargement of dendritic segments to show localization of endogenous proteins and overexpressed YIF1A.

VAP, YIF1 and YIP1 depletion on dendrite morphology. At DIV19, VAPA/B-shRNAs, YIF1A/B-shRNAs and YIP1A-shRNA transfected neurons showed a striking dendritic phenotype (Figure 7E). Quantitative analysis of the pattern of dendritic branching by Sholl analysis (Sholl, 1953) revealed a simplified dendritic tree with reduced branching in proximal dendrites in neurons transfected with VAPA/B-shRNAs, YIF1A/B-shRNAs and YIP1A-shRNA (Figure 7F). The reduced dendritic complexity in the VAPA/B, YIF1A/B and YIP1A knock-down neurons was also revealed by measuring the total dendritic length, counting the number of primary dendrites directly emanating from the soma, and analysing the total number of dendritic tips (Figure 7G–I). Similar results were obtained with independent VAPA, VAPB, YIF1A and YIF1B shRNA sequences (Supplementary Figure S3). In summary, the early secretory pathway components VAPA/B, YIF1A/B and YIP1A are required for normal dendrite morphology in early and later stages of dendrite development.

YIF and VAP are required for intracellular membrane delivery into dendrites

The trafficking of new membrane proteins is essential for normal dendritic growth and morphology (Lecuit and Pilot, 2003). We next determined whether YIF1 and VAP proteins play a role in the delivery of vesicles or cellular material to dendrites. Recent papers show that YIF1B mediates the transport of the serotonin G-coupled receptor (5-HT1A) to dendrites (Carrel *et al*, 2008; Al Awabdh *et al*, 2012), however after transfection with VAPA/B-shRNAs or YIF1A/B-shRNAs we do not find changes in YFP-5HT1A receptor localization to mature dendrites (Supplementary Figure S4). Previous studies showed that the small GTPase Sar1, a critical regulator of ER-to-Golgi transport, controls dendritic growth through the delivery of membrane vesicles to dendrites (Ye *et al*, 2007). We therefore hypothesized that the observed morphological phenotype is caused by a decrease in membrane supply to the dendrites. To see whether VAP and YIF knockdown affect membrane trafficking in primary hippocampal neurons, we employed FRAP experiments. To examine the membrane supply from the soma to the dendrites, we marked membrane with the fluorescent transmembrane protein CD8-GFP (Hoogenraad *et al*, 2005; Ye *et al*, 2007). After photo-bleaching one entire dendrite the fluorescence recovery in the same dendrite was monitored immediately over a time period of 20 or 30 min. The fluorescence recovery, due to supply from the soma, in the proximal dendrite (35 μm from the soma) was used for quantifications. In control neurons, CD8-GFP fluorescence recovered to ~70% (Figure 8A, C and D; Supplementary Figure S5). The recovery could be fit with a double exponent (f) with 2 time constants (τ) of 36 ± 5 s and 476 ± 15 s (Supplementary Figure S5). To determine the source of GFP-CD8 recovery, we conducted several control experiments that indicate that the majority of GFP-CD8 recovery depends on intracellular trafficking in the secretory pathway but not on surface diffusion or local protein synthesis (Supplementary Figure S5). Next, we depleted VAP, YIF1 or SAR1 to test whether there is an effect on membrane delivery to dendrites. Sar1-shRNA as well as VAPA/B and YIF1A/B-shRNAs significantly reduced the delivery of CD8-GFP from the soma to the dendrites to ~40–60%, as evident from the recovery curve (Figure 8B and C) as well as the maximal recovery (Figure 8D). These results show that

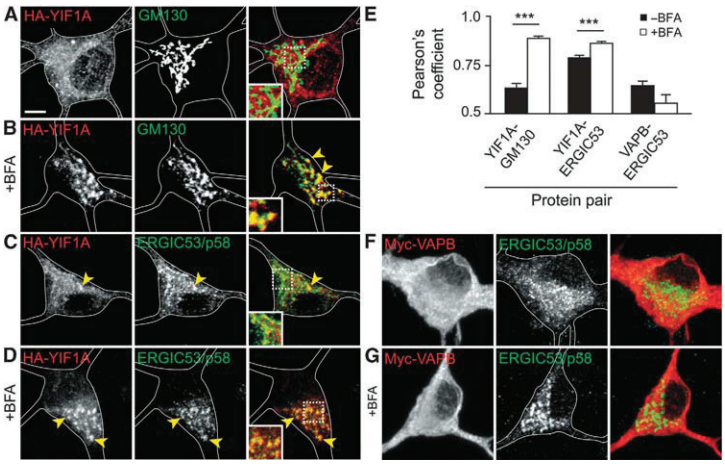

Figure 4 YIF1A localizes to the ER–Golgi intermediate compartment (ERGIC). (**A**) Image of the cell body of a hippocampal neuron transfected with HA-YIF1A and stained with anti-HA (red) and anti-GM130 (green) antibodies. (**B**) Redistribution of HA-YIF1A by BFA treatment. Neurons were transfected with HA-YIF1A, treated with BFA (5 μg/ml) for 15 min fixed and labelled with anti-HA (red) and anti-GM130 (green). (**C**) Representative image of the cell body of a hippocampal neuron transfected with HA-YIF1A and labelled with anti-HA (red) and anti-ERGIC (green). Redistribution of HA-YIF1A after BFA treatment is shown in (**D**). (**E**) Summary of co-localization experiments. Pearson's coefficient (r_p) for YIF1A versus ERGIC53/p58, YIF1A versus GM130 and VAPB versus ERGIC53/p58 in control (black bars) and BFA-treated cells (white bars). Twenty-three to twenty-five ROIs were analysed for each condition. Error bars indicate s.e.m., $***P<0.001$. (**F**, **G**) Images of cell bodies of hippocampal neurons transfected with myc-VAPB and labelled with anti-myc (red) and anti-ERGIC53/p58 (green). BFA treatment has no effect on myc-VAPB distribution (**G**). Solid lines indicate the cell edges; the insets show magnifications of boxed areas and arrows indicate co-localization. Scale bar, 5 μm.

VAP and YIF are required for the intracellular delivery of membrane, labelled by CD8-GFP, from soma to dendrites.

VAPB-P56S traps YIF1A in aggregates and thereby affects its localization

The P56S mutant form of VAPB is associated with motor neuron disorder ALS8. VAPB-P56S proteins aggregate and form multiple spherical inclusions in cellular and invertebrate model systems. As in COS-7 cells (Figure 1F), HA-YIF1A is recruited to the myc-VAPB-P56S inclusions in neurons (Figure 9A). Consistent with the data that the interaction depends on the transmembrane domain of VAPB-P56S, replacement of this region with a different, unrelated transmembrane domain prevents YIF1A recruitment to VAPB inclusions (Figure 9B). In cells transfected with wild-type VAPB, YIF1A strongly co-localized to the ERGIC after BFA treatment (Figures 4D and 9C). Interestingly, in VAPB-P56S expressing cells, YIF1A is absent from the ERGIC structures even after BFA treatment (Figure 9D). These data suggest that when VAPBP-P56S is present, YIF1A loses its localization to the ERGIC. In contrast, the YIF1A binding protein Flag-YIP1A and YPF-ERGIC53/p58 do not co-localize with these VAPB-P56S/YIF1A-positive aggregates (Figure 9E–H).

The MSP domain in VAP proteins binds to the 'two phenylalanines in an acid tract', or 'FFAT' motif found in several cytoplasmic lipid-binding proteins, including OSBPL9 and NIR2 (Kaiser *et al*, 2005; Loewen and Levine, 2005; Teuling *et al*, 2007). In this way, VAP proteins may act as docking sites for cytoplasmic factors to interact with the ER, coordinate lipid transfer between ER and Golgi apparatus or maintain the structure of the ER by interacting with the cytoskeleton (Amarilio *et al*, 2005; Peretti *et al*, 2008; Ngo and Ridgway, 2009). It was recently shown that the P56S substitution in VAPB induces conformational changes within the MSP domain and perturbs FFAT-motif binding (Teuling *et al*, 2007; Kim *et al*, 2010). Consistent with these results, FFAT-motif containing proteins OSBPL9 and NIR2 are absent from YIF1A-positive VAPB-P56S aggregates in neurons (Supplementary Figure S6). Together, these results suggest that both perturbation of FFAT-dependent association with the ER and mislocalization of YIF1A could contribute to the pathological mechanisms observed in ALS8.

Discussion

In this study, we identified YIF1A as a new VAPB binding partner and we showed that, in contrast to other VAPB interaction partners, YIFIA does not bind to the MSP domain of VAPB, but via its transmembrane domain interacts with the transmembrane domain of VAPB. In hippocampal neurons, we showed that VAPB–YIF1A interaction controls the shuttling of YIF1A between the ERGIC and the ER and plays an important role in early secretory events in neurons, promoting membrane trafficking and normal dendritic growth. In addition, we show that YIF1A in contrast to other VAPB interaction partners also binds ALS8-mutant VAPB and co-accumulates in abnormal ER-derived structures. We propose that the mislocalization of YIF1A into VAPB-P56S aggregates could contribute to pathological mechanisms observed in VAPB-associated motor neuron diseases.

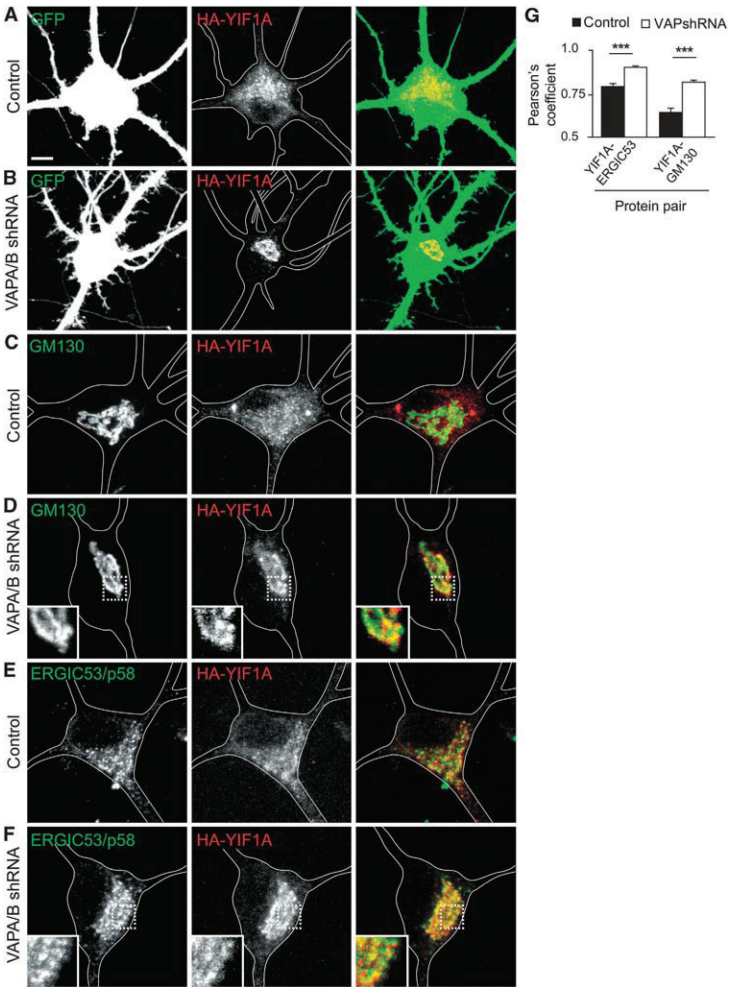

Figure 5 Effect of VAP knockdown on YIF1A localization in cultured hippocampal neurons. (**A**, **B**) Representative images of cell bodies of hippocampal neurons co-transfected at DIV16 for 4 days with HA-YIF1A (red), GFP and pSuper control vector (**A**) or pSuper-VAPA and pSuper-VAPB shRNAs (**B**). VAP knockdown results in relocalization of HA-YIF1A. (**C**–**F**) Cell bodies of neurons co-transfected with HA-YIF1A (red) and pSuper control vector (**C**, **E**) or pSuper-VAPA and pSuper-VAPB shRNAs (**D**, **F**). Neurons were stained for either GM130 (**C**, **D**) or ERGIC53/p58 (**E**, **F**). Solid lines indicate the cell edges. Scale bar, 5 μm. (**G**) Summary of co-localization experiments. Pearson's coefficient (r_p) for YIF1A versus ERGIC53/p58 and GM130 in control (black bars) and VAP knockdown neurons (white bars). Seventeen to twenty-three ROIs were analysed for each condition. Error bars indicate s.e.m., $***P<0.001$.

YIF1A interacts with VAPB in the early secretory pathway

VAPB has been implicated in multiple cellular functions, either as a conserved ER anchoring protein or as a secreted signalling molecule in invertebrates (Lev *et al*, 2008; Han *et al*, 2012). Proteins with an FFAT or an FFAT-like motif that can bind the FFAT-motif binding site in the MSP domain of VAPA and VAPB represent a major group of VAPB interacting proteins. FFAT-motif proteins include oxysterol binding proteins (OSBPs), OSBP-related proteins (ORPs) and NIR proteins (Wyles and Ridgway, 2004; Amarilio *et al*, 2005; Loewen and Levine, 2005; Kawano *et al*, 2006) and have been shown to play a role in ER structure (Wyles *et al*, 2002; Amarilio *et al*, 2005; Lehto *et al*, 2005) and the transport of membrane lipids (Kawano *et al*, 2006; Peretti *et al*, 2008). Other proteins with FFAT-like motifs include for instance PKA anchoring proteins that could play a role in cAMP signalling on the ER (Mikitova and Levine, 2012). In addition, an outer mitochondrial membrane protein (PTPIP51) was shown to interact with VAPB (De Vos *et al*, 2012) putatively via FFAT-

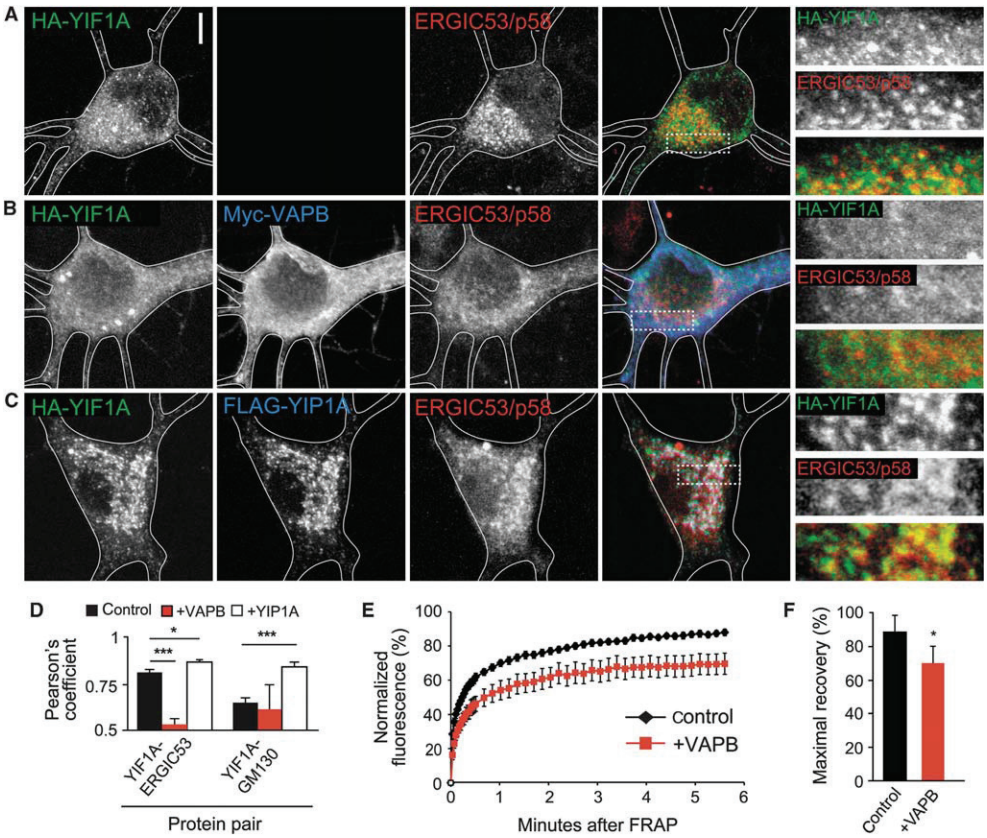

Figure 6 VAPB overexpression relocalizes YIF1A. (**A**–**C**) Hippocampal neurons transfected with HA-YIF1A and stained with anti-HA (green) and anti-ERGIC53/p58 (blue). Co-transfection with either myc-VAPB (**B**) or FLAG-YIP1A (**C**) results in relocalization of HA-YIF1A. Solid lines indicate the cell edges and panels on the right side show enlargements of the boxed regions. Scale bar, 5 μm. (**D**) Summary of co-localization experiments. Pearson's coefficient (r_p) for YIF1A versus ERGIC53/p58 and GM130 in control (black bars), VAPB overexpressing (red bars) and YIP1A overexpressing neurons (white bars). Thirteen to twenty-three ROIs were analysed for each condition. (**E**) Fluorescent recovery plots showing the rates of GFP-YIF1A recovery in cell bodies of control neurons and neurons overexpressing VAPB. Fluorescent intensity was normalized to intensity before bleaching. $P = 0.008$; repeated measures ANOVA. (**F**) Histogram representing the maximal recovery of fluorescence (estimated mobile fraction) in hippocampal neurons expressing GFP-YIF1A with ($n = 11$) or without VAPB overexpression ($n = 10$). Data are presented as means ± s.e.m., $^*P < 0.05$, $^{***}P < 0.001$.

like motifs, although the basis for this interaction was not studied (Mikitova and Levine, 2012). In contrast to the previously described VAP binding partners, the interaction with YIF1 occurs via the transmembrane domain, although we cannot fully exclude a role for the cytosolic VAPB domain. During submission of this paper, another study reported a similar transmembrane mediated interaction between *Drosophila* VAP and Sac1, a phosphoinositide phosphatase (Forrest *et al*, 2013). YIF1A and YIF1B in mammals are homologous to Yif1p in yeast. Yif1p is located to the Golgi membrane and COPII vesicles, forms a tight complex with its family member Yip1p and plays an important role in early secretory transport in yeast (Entian *et al*, 1999; Matern *et al*, 2000; Otte *et al*, 2001). Cell-free assays and thermosensitive yeast strains demonstrated that Yif1p and Yip1p play a critical role in the biogenesis of ER-derived COPII transport vesicles (Barrowman *et al*, 2003; Heidtman *et al*, 2005). Recent genome-wide RNA interference screens in *Drosophila* S2 and HeLa cells found that depletion of YIF1 or YIP1 inhibits secretion, indicating that YIF1/YIP1 are functionally conserved components of the secretory pathway (Wendler *et al*, 2010; Simpson *et al*, 2012). We find that YIF1A is predominantly localized to the ERGIC and recycles between the ER and Golgi in hippocampal neurons. In agreement with these results, proteomics analysis identified YIF1A in ERGIC-enriched membranes (Breuza *et al*, 2004) and BFA treatment of HeLa cells results in YIF1A accumulations in the ERGIC (Yoshida *et al*, 2008). Our data indicate that both VAPB and YIF1A are needed for an efficient transition of membrane cargo through the early secretory pathway in neurons.

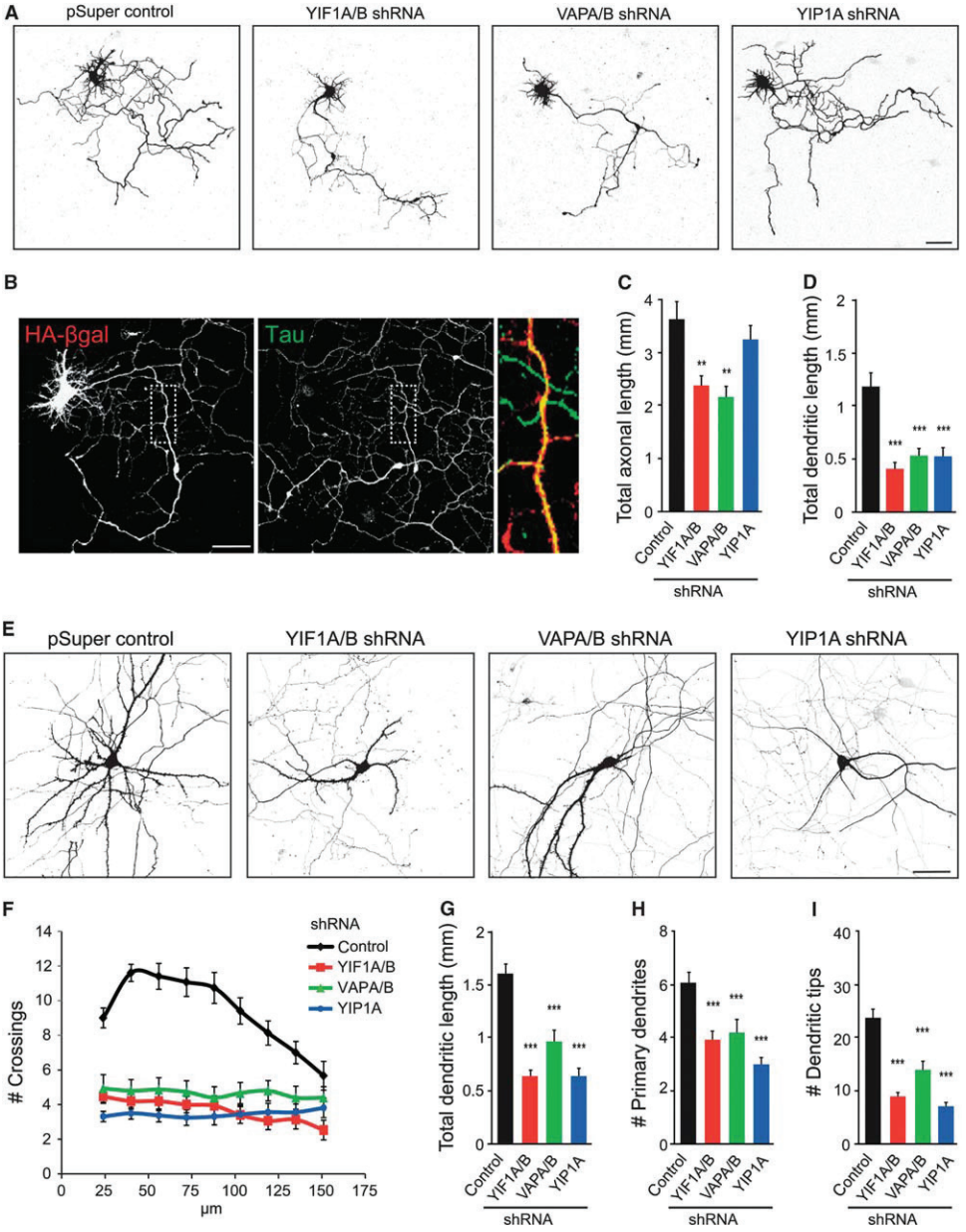

Figure 7 YIF1 and VAP are required for normal dendrite morphology. (**A**) Hippocampal neurons co-transfected at DIV1 with indicated constructs and β-galactosidase to visualize morphology. (**B**) Representative image of a hippocampal neurons (DIV5) co-transfected with empty pSuper and β-galactosidase and co-stained with Tau (green) to highlight the axon. (**C**, **D**) Quantification of total axonal length and dendritic length after 4 days overexpression of knockdown constructs or empty pSuper as control (14–16 cells were analysed for each condition). (**E**) Hippocampal neurons co-transfected at DIV15 with indicated constructs and β-galactosidase to visualize morphology. (**F**) Sholl analysis and quantification of the total dendritic length (**G**), number of primary dendrites (**H**) and dendritic tips (**I**) after 4 days overexpression of knockdown constructs or empty pSuper as control (15–17 cells were analysed for each condition). Error bars indicate s.e.m., $^{**}P<0.01$, $^{***}P<0.001$. Scale bars represent 50 μm.

Furthermore, we show that, while YIF1A is cycling between ER and Golgi, VAPB is restricted to the ER and is not present in ERGIC or Golgi, indicating that YIF1A-VAPB binding is most likely to occur in the ER membrane (Supplementary Figure S7). We hypothesize that YIF1A is retained in the ER membrane by its interaction with VAPB which subsequently allows specific membrane lipids and/or cargo proteins to concentrate at ERES before budding off in carriers destined for further transport towards the ERGIC and cis-Golgi membrane (Gurkan *et al*, 2006; Jensen and Schekman, 2011).

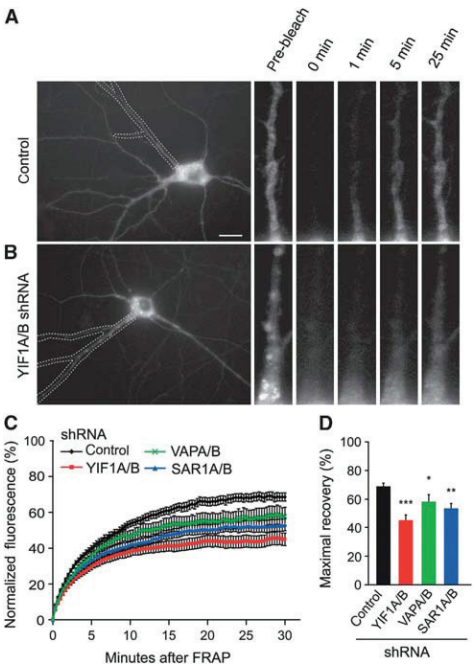

Figure 8 YIF1 and VAP play a role in membrane trafficking in primary hippocampal neurons. (**A**, **B**) Representative images of membrane-bound GFP (CD8-GFP) moving from soma into dendrites in hippocampal neurons (DIV16–19) co-expressing CD8-GFP with either empty pSuper control vector (**A**) or YIF1A and YIF1B shRNAs (**B**). Boxed area indicates photobleached dendritic region. In the right panel, proximal part of photobleached dendrite is shown. Scale bar, 20 μm. (**C**) Fluorescent recovery plots showing the rates of CD8-GFP recovery in photobleached dendrites of control and knockdown neurons. Fluorescent intensity was normalized to intensity before bleaching. $P<0.001$ for YIF1A/B versus control, $P=0.033$ for VAPA/B versus control and $P=0.008$ for SAR1A/B versus control (repeated measures ANOVA followed by Tukey's *post hoc* test). (**D**) Maximal fluorescence recovery. Nine to fifteen cells were analysed for each condition. Data are presented as means ± s.e.m., $*P<0.05$, $**P<0.01$, $***P<0.001$; one-way ANOVA, Tukey's *post hoc* test.

Moreover, interactome analyses in yeast revealed that the Yip1p/Yif1p family proteins associate with a large range of gene products that function in the vesicular transport pathway, including SNAREs, Rab GTPases, ARFGAP and sorting nexins (Ito *et al*, 2000; Uetz *et al*, 2000). Future studies using cell-free assays driven by purified proteins that recapitulate protein transport between the ER and the Golgi complex will help to elucidate the mechanisms regulating the interplay between VAPB, YIF1A and the other components of the ER-to-Golgi trafficking pathway and advance our understanding of the biogenesis of transport carriers in the early secretory transport.

YIF and VAP are required for intracellular membrane delivery into dendrites

The early secretory pathway is fundamentally important for neuronal development and function (Hanus and Ehlers, 2008; Tang, 2008; Aridor and Fish, 2009; Jan and Jan, 2010), and some lines of evidence suggest that the organization of secretory trafficking in neurons differs in several ways from the pathways in non-neuronal cells (Nelson and Yeaman, 2001; Stephens and Pepperkok, 2001; Tang, 2008). In particular components of the ER, ERGIC and Golgi have been identified in dendrites, specifically localizing at branch points and close to dendritic spines (Krijnse-Locker *et al*, 1995; Pierce *et al*, 2001; Horton *et al*, 2005; Appenzeller-Herzog and Hauri, 2006). Here, we identify VAPB and YIF1A as early secretory trafficking components that are required for membrane transport and important for normal dendrite morphology. First, we showed that VAPB is able to retain YIF1A in the ER thereby regulating its recycling to ERGIC and Golgi. Depletion of VAP proteins results in a relocalization of ERGIC protein YIF1A to the Golgi, indicating that VAPB regulates trafficking of YIF1A through the ERGIC. Recent studies showed that disruption of VAPB affects ER-to-Golgi transport and anterograde VSVG trafficking in HeLa cells (Peretti *et al*, 2008; Rao *et al*, 2012). Second, depletion of VAP, YIF1 as well as YIP1 affects dendrite morphology. This is consistent with the observed dendritic phenotype in secretory trafficking deficient *Drosophila* mutants (Ye *et al*, 2007). Third, we show that both VAPA/B and YIF are required for a normal membrane supply to dendrites, indicating that the observed effect on dendrite morphology is caused by a defect in early secretory trafficking. The fact that other proteins of the ER-to-Golgi trafficking pathway, such as Sar1, also affect dendritic growth and membrane trafficking (Ye *et al*, 2007) strengthens the model that VAPB and YIF1A have an important role in the secretory transport. Interestingly, YIF1B has been shown to play a role in the neuronal ER–Golgi trafficking machinery by specific targeting the serotonin G-coupled receptor (5-HT1A) to dendrites (Carrel *et al*, 2008). A recent follow-up study proposed that YIF1B acts as a scaffolding complex that recruits 5-HT1A together with Yip1A and Rab6 in dendritic transport vesicles (Al Awabdh *et al*, 2012). These results imply that at least YIF1B and

Figure 9 Mutant VAPB expression results in recruitment of YIF1A to clusters. (**A**) Co-transfection of hippocampal neurons with HA-YIF1A (red) and myc-VAPB-P56S (green) shows that YIF1A is recruited to the VAPB-P56S clusters. The far right panel shows enlargement of a dendrite. (**B**) Hippocampal neuron co-transfected with VAPB-P56S-CD8TM (green) and HA-YIF1A (red). (**C**, **D**) Images show that in the presence of overexpressed wild-type VAPB, HA-YIF1A localizes to ERGIC after BFA treatment. However, when VAPBP-P56S is expressed YIF1A loses its localization to the ERGIC. (**E**–**G**) Neurons co-transfected with HA-YIF1A (green) and Flag-YIP1A (**D**), myc-VAPB-P56S (**E**) or both (**F**). (**H**) Hippocampal neuron co-transfected with myc-VAPB-P56S (blue), YFP-ERGIC (green) and HA-YIF1A (red). Scale bar, 5 μm.

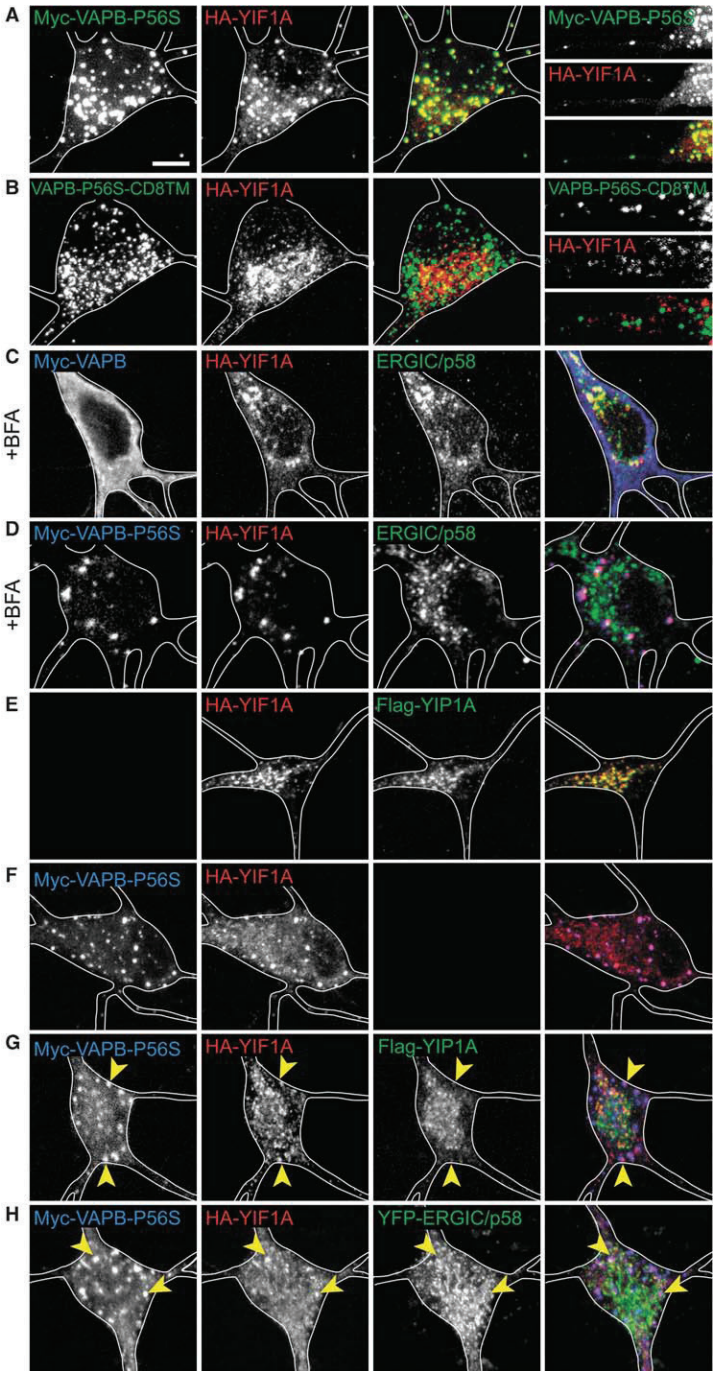

possibly other Yip1p/Yif1p family proteins play a role in the anterograde transport of a limited subset of cargo molecules from the ER to the Golgi. Although in our study we do not find evidence that YIF1 or VAP plays a role in the transport of the serotonin receptor we believe that defects in the transport of specific proteins under the influence of VAP or YIF impairments are difficult to measure as other, unconventionally, transport routes can be used as default (Grieve and Rabouille, 2011).

YIF1A and ALS8

The P56S mutation in the gene encoding VAPB causes ALS8 and some other related forms of motor neuron disease (Nishimura *et al*, 2004). Several studies already showed that VAPB-P56S induces the formation of abnormal ER-derived inclusions, perturbs ER–Golgi trafficking and triggers ER stress (Nishimura *et al*, 2004; Teuling *et al*, 2007; Tsuda *et al*, 2008; Suzuki *et al*, 2009; Chen *et al*, 2010; Fasana *et al*, 2010; Moumen *et al*, 2011). Ubiquitin (Moumen *et al*, 2011) and BAP31 (Fasana *et al*, 2010) have been described to accumulate in the VAPB-P56S clusters, suggesting that mutant VAPB-induced aggregation is part of the ER-associated degradation pathway. Mutant VAPB-P56S also induces the co-aggregation of wild-type VAPB, suggesting a dominant-negative mode of pathogenesis (Teuling *et al*, 2007). Disruption of ER and Golgi structure and function has previously been suggested as a possible pathological mechanism for neurodegenerative diseases (Mourelatos *et al*, 1996; Lehotsky *et al*, 2003; Paschen and Mengesdorf, 2005; Vlug *et al*, 2005; Yoshida, 2007). How VAPB-P56S disrupts protein trafficking between the ER and Golgi and how this may lead to the pathogenesis of ALS8 is not yet understood. The identification of the VAPB–YIF1A interaction and its role in early secretory transport raises the possibility that YIF1A might be involved in the development of neurodegenerative diseases. Both YIF1A and YIF1B are ubiquitously expressed in the CNS (Carrel *et al*, 2008) and a microarray analysis showed downregulation of YIF1A in motor neurons isolated from the spinal cord of SOD1-G93A transgenic mice, a model for familial ALS (Ferraiuolo *et al*, 2007). This suggests that YIF1A could be a potential factor involved in the multi-factorial causes leading to ALS. Although the relevance of our observations to heterozygous patients remains uncertain (as our observations are under overexpression conditions), our model suggests that mislocalization of YIF1A to aggregates leads to a defect in secretory trafficking and a subsequent inhibition of dendritic growth and maintenance. Defects in neuronal secretory trafficking already have been shown to affect dendritic growth (Horton *et al*, 2005; Ye *et al*, 2007). Dendritic alterations have been documented in mouse models for motor neuron dysfunction (Wiggins *et al*, 2012) and in ALS-affected patients (Liu *et al*, 2011). In patients, dendrites in anterior horn cells are shorter and thinner, or are lost (Kato *et al*, 1987; Sasaki and Iwata, 1996). Moreover, loss and atrophy of dendrites was found in motor neurons in the spinal cord (Karpati *et al*, 1988). Similarly, in pre-symptomatic SOD1-G93A transgenic mice dendrites in the motor cortex show signs of degeneration and in the prefrontal cortex a reduction in the length of basal dendrites and branch points was observed (Sgobio *et al*, 2008; Jara *et al*, 2012). Changes in dendritic architecture are indicative of defects in neuronal function and connectivity, and could be contributing to the development of sites of degeneration. Though there is overwhelming evidence for axonal transport dysfunctions in the pathogenesis of ALS (Chevalier-Larsen and Holzbaur, 2006; Sau *et al*, 2011), our study indicates that alterations in dendritic structure and trafficking may also play an important role in neurodegeneration. A recent study has reported mild late onset motor deficits in VAPB-deficient mice in the absence of axonal and neuromuscular junction abnormalities (Forrest *et al*, 2013). Whether these mice develop dendritic abnormalities and the degree of compensation of VAPB deficiency by VAPA in these mice requires further investigation.

In conclusion, we have identified YIF1A as a novel binding partner of VAPB and established a key role for these proteins in the neuronal early secretory pathway. We found that both VAP and YIF1 proteins are important for proper membrane trafficking and normal dendrite growth. Moreover, the ALS-linked mutant VAPB-P56S recruits YIF1A to aggregates and disrupts its normal localization to ERGICs. Understanding the cellular function of VAPB may indicate what molecular and cellular events are associated with the disease process of ALS8. Our current findings provide new molecular targets to investigate VAPB-linked neurodegeneration. It is likely that this information will be of relevance to both the inherited condition and the more common sporadic forms of disease.

Materials and methods

Expression constructs and shRNA

The following mammalian expression plasmids have been described previously: bio-HA-VAPB, GFP-VAPB-TMD, GFP-VAPB, HA- and myc-tagged VAPA, VAPB and VAPA/B-P56S constructs (Teuling *et al*, 2007), protein-biotin ligase BirA (Lansbergen *et al*, 2006), flag-YIF1B (Carrel *et al*, 2008), flag-YIP1A (Dykstra *et al*, 2010), ERGIC/p58-YFP (Ward *et al*, 2001) and CD8-GFP (Hoogenraad *et al*, 2005). Bio-GFP-VAPB, Bio-HA-VAPB-P56S and Bio-HA-VAPA were generated by incorporating a biotinylation-tag (MSGLNDIFEAQKIEWHE) before the GFP- or HA-tagged mutant or wild-type VAPA/B construct. VAPB-P56S-CD8TM was made by removing the transmembrane domain of VAPB-P56S and adding the transmembrane domain of CD8 with a PCR-based strategy using HA-VAPB-P56S and GFP-CD8 as a template and subcloned into a pβactin expression vector. Full-length and truncated human YIF1A constructs were generated by PCR using IMAGE clone 3451489 as template and cloned into HA- and GFP-tagged pGW1-expression vectors. For bio-GFP-YIF1A, a biotinylation tag was inserted in front of the pEGFP-C2 (Clontech) and the YIF1A openreading frame subsequently subcloned in the biotin-tag-GFP vector. GFP-YIF1A IxxxI was generated from GFP-YIF1A by introducing G154I, G158I, G222I and G226I mutations using a PCR-based strategy. GFP-YIF1B was generated by a PCR-based strategy using flag-YIF1B and subcloned into a GFP-tagged pGW1-expression vector. Sp-BirA was made by incorporating the Ig kappa light chain leader sequence (METDTLLLWLLLLWVPGSTG) at the N-terminus of BirA and myc tag at its C-terminus in a pSCT expression vector. The following shRNA sequences were used in this study: VAPA#1 and #2 and VAPB#1 shRNA constructs (Teuling *et al*, 2007) and rat VAPB#2 (5′-GTTTATGGTTCAGTCTATG-3′), YIF1A#1 (5′-CCATGGCCTTCATCACATA-3′), rat YIF1B#1 (5′-gtactcatg tactggctca-3′), rat YIF1B#2 (5′-GCCATGGCTTTCATAACCT-3′), rat SAR1A (5′-AACCACTCTTCTTCACAT-3′) and rat SAR1B (5′-AACTA CCTTCCTGCTATCA-3′) sequences were designed based on previously published sequences (Kanekura *et al*, 2006; Ye *et al*, 2007; Carrel *et al*, 2008). The targeting sequences for rat YIP1A (5′-GCAGTATGCTGGCTGTGAG-3′) and YIF1A#2 (5′-gaagctaggg ctattggtc-3′) were designed by using the siRNA selection program at the Whitehead Institute for Biomedical Research (http://jura.wi.mit.edu/bioc/siRNAext/home.php) (Yuan *et al*, 2004). The

complementary oligonucleotides were annealed and inserted into a pSuper vector (Brummelkamp *et al*, 2002). Unless otherwise specified, all VAP and YIF shRNAs presented in the paper refer to shRNAs#1.

Antibodies and reagents

The following antibodies were used for immunocytochemistry: rabbit-anti-VAPB and rabbit-anti-VAPA (1:500) (Teuling *et al*, 2007); NIR2 (1:500) (Litvak *et al*, 2004), OSBPL9 (1:600) (Ngo and Ridgway, 2009); human-anti-EEA1 (1:500) (Selak *et al*, 2000). The following antibodies were obtained from commercial sources: mouse-anti-tau (1:500, Chemicon); mouse-anti-disulphide isomerase (PDI; 1:300, Affinity BioReagents); mouse-anti-GM130 (1:1000, BD Biosciences); mouse-anti-HA (1:500, Roche); mouse-anti-MAP2 (1:2000, Sigma); mouse-anti-myc (1:200, Santa Cruz Biotechnology); mouse-anti-flag (1:2000, Sigma); rabbit-anti-ERGIC53/p58 (1:200, Sigma); rabbit-anti-HA (1:500; Santa Cruz Biotechnology); rabbit-anti-flag (1:2000, Sigma); rabbit-anti-myc (1:200; Cell Signaling Technology); rabbit-anti-β-galactosidase (1:2000, MP Biomedicals); rat-anti-HA (1:200, Roche); mouse-anti-CD8 (1:20, Mabtech); Alexa Fluor 488-, Alexa Fluor 598-, and Alexa Fluor 633-conjugated secondary antibodies (1:400, Invitrogen) and Cy5-conjugated secondary antibody (1:400, Jackson ImmunoResearch Labs). The following antibodies were used for western blot analysis: rabbit anti-GFP (1:1000, Abcam); rabbit anti-HA (1:500, Santa Cruz); mouse anti-HA (1:500, Covance) and HRP-conjugated secondary antibodies (1:5000, Dako). BFA and cycloheximide were obtained from Sigma.

Transfection and immunofluorescence of cultured COS-7 cells

COS-7 cells were cultured in DMEM/Ham's F10 (50/50%) medium containing 10% FCS and 1% penicillin/streptomycin. Two days before transfection, cells were plated at 1:30 in Lab-tek chamber slides (Nunc). Cells were transfected with Fugene6 (Roche) according to manufacturer's protocol and incubated overnight. Cells were fixed in 4% paraformaldehyde for 10 min at room temperature followed by 5 min in 0.1% Triton X-100 in PBS. Slides were blocked in 0.5% BSA/0.02% glycine in PBS and labelled with primary antibody for 2 h at room temperature. Slides were washed three times with 0.05% Tween-20 in PBS, labelled with secondary antibodies for 1 h at room temperature, washed three times with 0.05% Tween-20 in PBS and mounted using Vectashield mounting medium (Vector laboratories). Images were acquired using a Leica DMRBE microscope equipped with $\times 40$ and $\times 100$ oil objectives.

Animals

All animal experiments were performed in compliance with the guidelines for the welfare of experimental animals issued by the Federal Government of The Netherlands. All animal experiments were approved by the Animal Ethical Review Committee (DEC) of the Erasmus Medical Center and Utrecht University.

Hippocampal neuron cultures, transfection and immunohistochemistry

Primary hippocampal cultures were prepared from embryonic day 18 (E18) rat brains (Banker and Goslin, 1988; Kapitein *et al*, 2010). Cells were plated on coverslips coated with poly-L-lysine (35 μg/ml) and laminin (5 μg/ml) at a density of 75 000/well. Hippocampal cultures were grown in Neurobasal medium (NB) supplemented with B27, 0.5 mM glutamine, 12.5 μM glutamate and penicillin/streptomycin. Hippocampal neurons were transfected using Lipofectamine 2000 (Invitrogen). Briefly, DNA (3.6 μg/well) was mixed with 3 μl of Lipofectamine 2000 in 200 μl of NB, incubated for 30 min, and then added to the neurons in NB at 37°C in 5% CO_2 for 45 min. Next, neurons were washed with NB and transferred in the original medium at 37°C in 5% CO_2. After 2–4 days of transfection, neurons were fixed with 4% paraformaldehyde/4% sucrose in PBS, washed three times in PBS for 10 min and incubated with the indicated primary antibodies in GDB buffer (0.2% BSA, 0.8 M NaCl, 0.5% Triton X-100, 30 mM phosphate buffer, pH 7.4) overnight at 4°C. Neurons were then washed three times in PBS for 30 min, incubated with secondary antibodies in GDB for 1 h at room temperature and washed three times in PBS for 30 min. Slides were mounted using Vectashield mounting medium (Vector Laboratories). Images for co-localization measurements were acquired using a Nikon microscope equipped with a $\times 100$ oil objective. Confocal images were acquired using a LSM510 confocal microscope (Zeiss) with a $\times 40$ or $\times 63$ oil objective.

Immunoprecipitation

HEK293T cells were cultured in DMEM/Hams-F10 (50/50%) medium containing 10% FCS and 1% penicillin/streptomycin and were transfected using Lipofectamine2000 (Invitrogen). Cells were harvested 24 h after transfection, by scraping the cells in ice-cold PBS and lysing cell pellets in lysis buffer (50 mM Tris–HCl, 100 mM NaCl, 1.0% Triton X-100 and protease inhibitors (Roche). Supernatant and pellet fractions were separated by centrifugation at 13 200 r.p.m. for 5 min. Supernatants were mixed with an equal amount of lysis buffer, protein-A-agarose beads (GE Healthcare), and 3 μg of rabbit anti-GFP, mouse anti-HA or control IgG (Sigma). Samples were incubated 4 h while rotating at 4°C, centrifuged at 2000 r.p.m. and pellets were washed three times with lysis buffer. Samples were mixed with 4 × Sample Buffer (8% SDS, 25% Glycerol, 0.05 M Tris pH 6.8, 200 mM DTT, 40 mg/l Bromophenol Blue) and boiled. Equal amounts of protein were loaded onto SDS–PAGE gels and subjected to western blotting on polyvinylidene difluoride membrane. Blots were blocked with 2% bovine serum albumin/0.05% Tween-20 in PBS and incubated with primary antibodies at 4°C overnight. Blots were washed with 0.05% Tween-20 in PBS three times for 10 min at room temperature and incubated with secondary antibodies conjugated to horseradish peroxidase (Dako). Blots were developed with enhanced chemiluminescent Western blotting substrate (Pierce).

GST pull-down

Full-length wild-type and mutant VAPB GST fusion proteins were obtained as described earlier (Teuling *et al*, 2007). HEK293T cells were transfected as described before with HA-YIF1A, HA-YIF1A (1–131), HA-YIF1A (131–193) and HA-YIF1A (198–293) and lysed in 50 mm Tris–HCl, 100 mm NaCl, and 1% Triton X-100 containing protease inhibitors (Roche). Lysates were incubated with GST beads (GE Healthcare Bio-Sciences) for 2 h at 4°C, washed four times with lysis buffer, and analysed by SDS–PAGE and western blotting as described before.

Biotin-streptavidin pull-down and mass spectrometry

For biotin-streptavidin pull-down assays, HeLa or HEK293T cells were transfected with biotin-tagged VAPB using Lipofectamine-2000 (Invitrogen) transfection reagent according to manufacturer's instructions. Cells were lysed 16 h later in 20 mm Tris–HCl, pH 8.0, 150 mm KCl, 1% Triton X-100, and protease inhibitors (Roche). To increase the solubility of VAPB-P56S, transfected cells were incubated for 2 h at 20°C before lysis. Cell lysates were centrifuged at 13 000 r.p.m. for 15 min and the supernatants were incubated with Dynabeads M-280 streptavidin (Dynal; Invitrogen) for 45 min. Beads were separated by using a magnet (Dynal; Invitrogen) and washed five times in lysis buffer. For protein elution, the beads were boiled in NuPAGE LDS 4 sample buffer (Invitrogen), separated, and supernatants were run on a 10% NuPAGE Bis-Tris gel (Invitrogen). The gel was stained with the Colloidal Blue staining kit (Invitrogen) and analysed by western blotting. Mass spectrometry was performed as described previously (Lansbergen *et al*, 2006). The Mascot score cutoff value for a positive protein hit was set to 100. Individual peptide tandem mass spectrometry spectra with Mascot scores below 100 were checked manually and either interpreted as valid identifications or discarded. Proteins present in the negative controls (pull-down assays with bio-GFP alone) were regarded as background.

Photobleaching experiments

For quantitative FRAP experiments, neurons were transfected as described before, and imaged on a Nikon Eclipse TE2000E (Nikon) equipped with an incubation chamber (INUG2-ZILCS-H2; Tokai Hit) mounted on a motorized stage (Prior) (Jaworski *et al*, 2009). Coverslips (24 mm) were mounted in metal rings and maintained at 37°C and 5% CO_2. A dendrite or a 3×3 μm regions of interest (ROI) in the cell body was photobleached with high laser power. Immediately after photobleaching, images of GFP fluorescence were acquired using a $\times 40$ objective (Nikon) and a Coolsnap HQ camera (Photometrics). Intensity of GFP signal in dendrites was measured over a length of 30 μm from the soma with MetaMorph image analysis software (Universal Imaging). Background intensity was subtracted and fluorescence intensity after photobleaching was calculated relative to the intensity before bleaching. Sigmaplot 12.3 software was used to perform curve fitting.

Image analysis and quantification

Measurement of neurite outgrowth. To measure neurite length, we used β-galactosidase as an unbiased cell-fill. Hippocampal neurons were transfected with the indicated constructs, fixed at the appropriate time point and subjected to immunofluorescent staining. Confocal images were obtained at 1024 × 1024 pixel resolution using a LSM510 confocal microscope (Zeiss) with a ×40 oil objective (0.7 digital zoom). Each image was a z-series of images; the obtained stack was 'flattened' into a single image using maximum projection. Morphometric analysis and quantification were performed using MetaMorph image analysis software (Universal Imaging). For measurement of total dendrite or axonal length, all dendrites or axons of individual neurons were traced. All non-axonal protrusions initiating from the cell soma longer than 10 μm were defined as primary dendrites. For dendrite tip number, tips of all non-axonal protrusions longer than 10 μm were counted. For Sholl analysis, concentric circles with 16 μm differences in diameter were automatically drawn around the cell body, and the number of dendrites crossing each circle was counted.

Co-localization of two fluorescent signals. Co-localization of two fluorescent signals was indicated by the Pearson's coefficient (r_p), determined using the JACoP plugin (Bolte and Cordelieres, 2006) for ImageJ. For each cell, three ROIs were selected; *n* was defined as the number of ROIs.

Statistical analyses

Statistical analyses were performed with MS Excel or SPSS software. Data were averaged over multiple cells and statistical analysis was performed with Student's *t*-test, one-way ANOVA or repeated measures ANOVA and Tukey's *post hoc* test. $P<0.05$ was considered as significant.

Supplementary data

Supplementary data are available at *The EMBO Journal* Online (http://www.embojournal.org).

Acknowledgements

We thank Dr N Ridgway for the OSBP9 antibody, Dr S Lev for the NIR2 antibody, Dr T Lee for the Flag-YIP1A construct, Dr M Darmon for the Flag-YIF1B and YFP-5HT1A plasmid, Dr. JF Presley for the p58-YFP construct and Jeroen Demmers and Karel Bezstarosti for help with mass spectrometry analyses. This work was supported by Het Prinses Beatrix Spierfonds grant (DJ and CCH), Netherlands Organization for Scientific Research (NWO-ALW-VICI, AA and CCH), the Netherlands Organization for Health Research and Development (ZonMW-TOP, CCH), the European Science Foundation (EURYI, CCH), EMBO Young Investigators Program (YIP, CCH) and the Human Frontier Science Program (HFSP-CDA, CCH).

Author contributions: MK, DJ, AA and CCH designed research; MK, KLY and ET performed research; MK analysed the data; MK and CCH wrote the paper; CCH supervised the project.

Conflict of interest

The authors declare that they have no conflict of interest.

References

Al Awabdh S, Miserey-Lenkei S, Bouceba T, Masson J, Kano F, Marinach-Patrice C, Hamon M, Emerit MB, Darmon M (2012) A new vesicular scaffolding complex mediates the G-protein-coupled 5-HT1A receptor targeting to neuronal dendrites. *J Neurosci* **32:** 14227–14241

Altschul SF, Madden TL, Schaffer AA, Zhang J, Zhang Z, Miller W, Lipman DJ (1997) Gapped BLAST and PSI-BLAST: a new generation of protein database search programs. *Nucleic Acids Res* **25:** 3389–3402

Amarilio R, Ramachandran S, Sabanay H, Lev S (2005) Differential regulation of endoplasmic reticulum structure through VAP-Nir protein interaction. *J Biol Chem* **280:** 5934–5944

Anagnostou G, Akbar MT, Paul P, Angelinetta C, Steiner TJ, de Belleroche J (2010) Vesicle associated membrane protein B (VAPB) is decreased in ALS spinal cord. *Neurobiol Aging* **31:** 969–985

Appenzeller-Herzog C, Hauri HP (2006) The ER-Golgi intermediate compartment (ERGIC): in search of its identity and function. *J Cell Sci* **119:** 2173–2183

Aridor M, Fish KN (2009) Selective targeting of ER exit sites supports axon development. *Traffic* **10:** 1669–1684

Banker G, Goslin K (1988) Developments in neuronal cell culture. *Nature* **336:** 185–186

Barrowman J, Wang W, Zhang Y, Ferro-Novick S (2003) The Yip1p.Yif1p complex is required for the fusion competence of endoplasmic reticulum-derived vesicles. *J Biol Chem* **278:** 19878–19884

Bolte S, Cordelieres FP (2006) A guided tour into subcellular colocalization analysis in light microscopy. *J Microsc* **224:** 213–232

Breuza L, Halbeisen R, Jeno P, Otte S, Barlowe C, Hong W, Hauri HP (2004) Proteomics of endoplasmic reticulum-Golgi intermediate compartment (ERGIC) membranes from brefeldin A-treated HepG2 cells identifies ERGIC-32, a new cycling protein that interacts with human Erv46. *J Biol Chem* **279:** 47242–47253

Brummelkamp TR, Bernards R, Agami R (2002) A system for stable expression of short interfering RNAs in mammalian cells. *Science* **296:** 550–553

Carrel D, Masson J, Al Awabdh S, Capra CB, Lenkei Z, Hamon M, Emerit MB, Darmon M (2008) Targeting of the 5-HT1A serotonin receptor to neuronal dendrites is mediated by Yif1B. *J Neurosci* **28:** 8063–8073

Chai A, Withers J, Koh YH, Parry K, Bao H, Zhang B, Budnik V, Pennetta G (2008) hVAPB, the causative gene of a heterogeneous group of motor neuron diseases in humans, is functionally interchangeable with its Drosophila homologue DVAP-33A at the neuromuscular junction. *Hum Mol Genet* **17:** 266–280

Chen HJ, Anagnostou G, Chai A, Withers J, Morris A, Adhikaree J, Pennetta G, de Belleroche JS (2010) Characterization of the properties of a novel mutation in VAPB in familial amyotrophic lateral sclerosis. *J Biol Chem* **285:** 40266–40281

Chevalier-Larsen E, Holzbaur EL (2006) Axonal transport and neurodegenerative disease. *Biochim Biophys Acta* **1762:** 1094–1108

Dancourt J, Barlowe C (2010) Protein sorting receptors in the early secretory pathway. *Annu Rev Biochem* **79:** 777–802

De Vos KJ, Morotz GM, Stoica R, Tudor EL, Lau KF, Ackerley S, Warley A, Shaw CE, Miller CC (2012) VAPB interacts with the mitochondrial protein PTPIP51 to regulate calcium homeostasis. *Hum Mol Genet* **21:** 1299–1311

Dykstra KM, Pokusa JE, Suhan J, Lee TH (2010) Yip1A structures the mammalian endoplasmic reticulum. *Mol Biol Cell* **21:** 1556–1568

Entian KD, Schuster T, Hegemann JH, Becher D, Feldmann H, Guldener U, Gotz R, Hansen M, Hollenberg CP, Jansen G, Kramer W, Klein S, Kotter P, Kricke J, Launhardt H, Mannhaupt G, Maierl A, Meyer P, Mewes W, Munder T *et al.* (1999) Functional analysis of 150 deletion mutants in Saccharomyces cerevisiae by a systematic approach. *Mol Gen Genet* **262:** 683–702

Fasana E, Fossati M, Ruggiano A, Brambillasca S, Hoogenraad CC, Navone F, Francolini M, Borgese N (2010) A VAPB mutant l inked to amyotrophic lateral sclerosis generates a novel form of organized smooth endoplasmic reticulum. *FASEB J* **24:** 1419–1430

Ferraiuolo L, Heath PR, Holden H, Kasher P, Kirby J, Shaw PJ (2007) Microarray analysis of the cellular pathways involved in the adaptation to and progression of motor neuron injury in the SOD1 G93A mouse model of familial ALS. *J Neurosci* **27:** 9201–9219

Forrest S, Chai A, Sanhueza M, Marescotti M, Parry K, Georgiev A, Sahota V, Mendez-Castro R, Pennetta G (2013) Increased levels of phosphoinositides cause neurodegeneration in a Drosophila model of amyotrophic lateral sclerosis. *Hum Mol Genet* (advance online publication, 29 March 2013; doi:10.1093/hmg/ddt118)

Grieve AG, Rabouille C (2011) Golgi bypass: skirting around the heart of classical secretion. *Cold Spring Harb Perspect Biol* **3:** a005298

Gurkan C, Stagg SM, Lapointe P, Balch WE (2006) The COPII cage: unifying principles of vesicle coat assembly. *Nat Rev Mol Cell Biol* **7:** 727–738

Han SM, Tsuda H, Yang Y, Vibbert J, Cottee P, Lee SJ, Winek J, Haueter C, Bellen HJ, Miller MA (2012) Secreted VAPB/ALS8 major sperm protein domains modulate mitochondrial localization and morphology via growth cone guidance receptors. *Dev Cell* **22:** 348–362

Hanus C, Ehlers MD (2008) Secretory outposts for the local processing of membrane cargo in neuronal dendrites. *Traffic* **9:** 1437–1445

Heidtman M, Chen CZ, Collins RN, Barlowe C (2005) Yos1p is a novel subunit of the Yip1p-Yif1p complex and is required for transport between the endoplasmic reticulum and the Golgi complex. *Mol Biol Cell* **16:** 1673–1683

Hirokawa T, Boon-Chieng S, Mitaku S (1998) SOSUI: classification and secondary structure prediction system for membrane proteins. *Bioinformatics* **14:** 378–379

Hoogenraad CC, Milstein AD, Ethell IM, Henkemeyer M, Sheng M (2005) GRIP1 controls dendrite morphogenesis by regulating EphB receptor trafficking. *Nat Neurosci* **8:** 906–915

Horton AC, Ehlers MD (2003) Dual modes of endoplasmic reticulum-to-Golgi transport in dendrites revealed by live-cell imaging. *J Neurosci* **23:** 6188–6199

Horton AC, Racz B, Monson EE, Lin AL, Weinberg RJ, Ehlers MD (2005) Polarized secretory trafficking directs cargo for asymmetric dendrite growth and morphogenesis. *Neuron* **48:** 757–771

Ito T, Tashiro K, Muta S, Ozawa R, Chiba T, Nishizawa M, Yamamoto K, Kuhara S, Sakaki Y (2000) Toward a protein-protein interaction map of the budding yeast: A comprehensive system to examine two-hybrid interactions in all possible combinations between the yeast proteins. *Proc Natl Acad Sci USA* **97:** 1143–1147

Jan YN, Jan LY (2010) Branching out: mechanisms of dendritic arborization. *Nat Rev Neurosci* **11:** 316–328

Jara JH, Villa SR, Khan NA, Bohn MC, Ozdinler PH (2012) AAV2 mediated retrograde transduction of corticospinal motor neurons reveals initial and selective apical dendrite degeneration in ALS. *Neurobiol Dis* **47:** 174–183

Jaworski J, Kapitein LC, Gouveia SM, Dortland BR, Wulf PS, Grigoriev I, Camera P, Spangler SA, Di Stefano P, Demmers J, Krugers H, Defilippi P, Akhmanova A, Hoogenraad CC (2009) Dynamic microtubules regulate dendritic spine morphology and synaptic plasticity. *Neuron* **61:** 85–100

Jensen D, Schekman R (2011) COPII-mediated vesicle formation at a glance. *J Cell Sci* **124:** 1–4

Jin C, Zhang Y, Zhu H, Ahmed K, Fu C, Yao X (2005) Human Yip1A specifies the localization of Yif1 to the Golgi apparatus. *Biochem Biophys Res Commun* **334:** 16–22

Kaiser SE, Brickner JH, Reilein AR, Fenn TD, Walter P, Brunger AT (2005) Structural basis of FFAT motif-mediated ER targeting. *Structure* **13:** 1035–1045

Kanekura K, Nishimoto I, Aiso S, Matsuoka M (2006) Characterization of amyotrophic lateral sclerosis-linked P56S mutation of vesicle-associated membrane protein-associated protein B (VAPB/ALS8). *J Biol Chem* **281:** 30223–30233

Kapitein LC, Yau KW, Hoogenraad CC (2010) Microtubule dynamics in dendritic spines. *Methods Cell Biol* **97:** 111–132

Karpati G, Carpenter S, Durham H (1988) A hypothesis for the pathogenesis of amyotrophic lateral sclerosis. *Rev Neurol (Paris)* **144:** 672–675

Kato T, Hirano A, Donnenfeld H (1987) A Golgi study of the large anterior horn cells of the lumbar cords in normal spinal cords and in amyotrophic lateral sclerosis. *Acta Neuropathol* **75:** 34–40

Kawano M, Kumagai K, Nishijima M, Hanada K (2006) Efficient trafficking of ceramide from the endoplasmic reticulum to the Golgi apparatus requires a VAMP-associated protein-interacting FFAT motif of CERT. *J Biol Chem* **281:** 30279–30288

Kim S, Leal SS, Ben Halevy D, Gomes CM, Lev S (2010) Structural requirements for VAP-B oligomerization and their implication in amyotrophic lateral sclerosis-associated VAP-B(P56S) neurotoxicity. *J Biol Chem* **285:** 13839–13849

Krijnse-Locker J, Parton RG, Fuller SD, Griffiths G, Dotti CG (1995) The organization of the endoplasmic reticulum and the intermediate compartment in cultured rat hippocampal neurons. *Mol Biol Cell* **6:** 1315–1332

Lansbergen G, Grigoriev I, Mimori-Kiyosue Y, Ohtsuka T, Higa S, Kitajima I, Demmers J, Galjart N, Houtsmuller AB, Grosveld F, Akhmanova A (2006) CLASPs attach microtubule plus ends to the cell cortex through a complex with LL5beta. *Dev Cell* **11:** 21–32

Lecuit T, Pilot F (2003) Developmental control of cell morphogenesis: a focus on membrane growth. *Nat Cell Biol* **5:** 103–108

Lee MC, Miller EA, Goldberg J, Orci L, Schekman R (2004) Bidirectional protein transport between the ER and Golgi. *Annu Rev Cell Dev Biol* **20:** 87–123

Lehotsky J, Kaplan P, Babusikova E, Strapkova A, Murin R (2003) Molecular pathways of endoplasmic reticulum dysfunctions: possible cause of cell death in the nervous system. *Physiol Res* **52:** 269–274

Lehto M, Hynynen R, Karjalainen K, Kuismanen E, Hyvarinen K, Olkkonen VM (2005) Targeting of OSBP-related protein 3 (ORP3) to endoplasmic reticulum and plasma membrane is controlled by multiple determinants. *Exp Cell Res* **310:** 445–462

Lev S, Ben Halevy D, Peretti D, Dahan N (2008) The VAP protein family: from cellular functions to motor neuron disease. *Trends Cell Biol* **18:** 282–290

Litvak V, Argov R, Dahan N, Ramachandran S, Amarilio R, Shainskaya A, Lev S (2004) Mitotic phosphorylation of the peripheral Golgi protein Nir2 by Cdk1 provides a docking mechanism for Plk1 and affects cytokinesis completion. *Mol Cell* **14:** 319–330

Liu M, Duggan J, Salt TE, Cordeiro MF (2011) Dendritic changes in visual pathways in glaucoma and other neurodegenerative conditions. *Exp Eye Res* **92:** 244–250

Loewen CJ, Levine TP (2005) A highly conserved binding site in vesicle-associated membrane protein-associated protein (VAP) for the FFAT motif of lipid-binding proteins. *J Biol Chem* **280:** 14097–14104

Lorente-Rodriguez A, Barlowe C (2011) Entry and exit mechanisms at the cis-face of the Golgi complex. *Cold Spring Harb perspect Biol* **3:** a005207

Matern H, Yang X, Andrulis E, Sternglanz R, Trepte HH, Gallwitz D (2000) A novel Golgi membrane protein is part of a GTPase-binding protein complex involved in vesicle targeting. *EMBO J* **19:** 4485–4492

Mikitova V, Levine TP (2012) Analysis of the key elements of FFAT-like motifs identifies new proteins that potentially bind VAP on the ER, including two AKAPs and FAPP2. *PLoS One* **7:** e30455

Mitne-Neto M, Machado-Costa M, Marchetto MC, Bengtson MH, Joazeiro CA, Tsuda H, Bellen HJ, Silva HC, Oliveira AS, Lazar M, Muotri AR, Zatz M (2011) Downregulation of VAPB expression in motor neurons derived from induced pluripotent stem cells of ALS8 patients. *Hum Mol Genet* **20:** 3642–3652

Moumen A, Virard I, Raoul C (2011) Accumulation of wildtype and ALS-linked mutated VAPB impairs activity of the proteasome. *PLoS ONE* **6:** e26066

Mourelatos Z, Gonatas NK, Stieber A, Gurney ME, Dal Canto MC (1996) The Golgi apparatus of spinal cord motor neurons in transgenic mice expressing mutant Cu,Zn superoxide dismutase becomes fragmented in early, preclinical stages of the disease. *Proc Natl Acad Sci USA* **93:** 5472–5477

Nelson WJ, Yeaman C (2001) Protein trafficking in the exocytic pathway of polarized epithelial cells. *Trends Cell Biol* **11:** 483–486

Ngo M, Ridgway ND (2009) Oxysterol binding protein-related Protein 9 (ORP9) is a cholesterol transfer protein that regulates Golgi structure and function. *Mol Biol Cell* **20:** 1388–1399

Nishimura AL, Mitne-Neto M, Silva HC, Richieri-Costa A, Middleton S, Cascio D, Kok F, Oliveira JR, Gillingwater T, Webb J, Skehel P, Zatz M (2004) A mutation in the vesicle-trafficking protein VAPB causes late-onset spinal muscular atrophy and amyotrophic lateral sclerosis. *Am J Hum Genet* **75:** 822–831

Nishimura Y, Hayashi M, Inada H, Tanaka T (1999) Molecular cloning and characterization of mammalian homologues of vesicle-associated membrane protein-associated (VAMP-associated) proteins. *Biochem Biophys Res Commun* **254:** 21–26

Otte S, Belden WJ, Heidtman M, Liu J, Jensen ON, Barlowe C (2001) Erv41p and Erv46p: new components of COPII vesicles involved in transport between the ER and Golgi complex. *J Cell Biol* **152:** 503–518

Papiani G, Ruggiano A, Fossati M, Raimondi A, Bertoni G, Francolini M, Benfante R, Navone F, Borgese N (2012) Restructured endoplasmic reticulum generated by mutant amyotrophic lateral sclerosis-linked VAPB is cleared by the proteasome. *J Cell Sci* **125:** 3601–3611

Paschen W, Mengesdorf T (2005) Cellular abnormalities linked to endoplasmic reticulum dysfunction in cerebrovascular disease–therapeutic potential. *Pharmacol Ther* **108:** 362–375

Pennetta G, Hiesinger PR, Fabian-Fine R, Meinertzhagen IA, Bellen HJ (2002) Drosophila VAP-33A directs bouton formation at neuromuscular junctions in a dosage-dependent manner. *Neuron* **35:** 291–306

Peretti D, Dahan N, Shimoni E, Hirschberg K, Lev S (2008) Coordinated lipid transfer between the endoplasmic reticulum and the Golgi complex requires the VAP proteins and is essential for Golgi-mediated transport. *Mol Biol Cell* **19:** 3871–3884

Pfeffer S, Aivazian D (2004) Targeting Rab GTPases to distinct membrane compartments. *Nat Rev Mol Cell Biol* **5:** 886–896

Pierce JP, Mayer T, McCarthy JB (2001) Evidence for a satellite secretory pathway in neuronal dendritic spines. *Curr Biol* **11:** 351–355

Rao M, Song W, Jiang A, Shyr Y, Lev S, Greenstein D, Brantley-Sieders D, Chen J (2012) VAMP-Associated Protein B (VAPB) promotes breast tumor growth by modulation of Akt Activity. *PLoS One* **7:** e46281

Ratnaparkhi A, Lawless GM, Schweizer FE, Golshani P, Jackson GR (2008) A Drosophila model of ALS: human ALS-associated mutation in VAP33A suggests a dominant negative mechanism. *PloS One* **3:** e2334

Saraste J, Dale HA, Bazzocco S, Marie M (2009) Emerging new roles of the pre-Golgi intermediate compartment in biosynthetic-secretory trafficking. *FEBS Lett* **583:** 3804–3810

Sasaki S, Iwata M (1996) Dendritic synapses of anterior horn neurons in amyotrophic lateral sclerosis: an ultrastructural study. *Acta Neuropathol* **91:** 278–283

Sau D, Rusmini P, Crippa V, Onesto E, Bolzoni E, Ratti A, Poletti A (2011) Dysregulation of axonal transport and motorneuron diseases. *Biol Cell* **103:** 87–107

Selak S, Woodman RC, Fritzler MJ (2000) Autoantibodies to early endosome antigen (EEA1) produce a staining pattern resembling cytoplasmic anti-neutrophil cytoplasmic antibodies (C-ANCA). *Clin Exp Immunol* **122:** 493–498

Sgobio C, Trabalza A, Spalloni A, Zona C, Carunchio I, Longone P, Ammassari-Teule M (2008) Abnormal medial prefrontal cortex connectivity and defective fear extinction in the presymptomatic G93A SOD1 mouse model of ALS. *Genes Brain Behav* **7:** 427–434

Shakoori A, Fujii G, Yoshimura S, Kitamura M, Nakayama K, Ito T, Ohno H, Nakamura N (2003) Identification of a five-pass transmembrane protein family localizing in the Golgi apparatus and the ER. *Biochem Biophys Res Commun* **312:** 850–857

Sholl DA (1953) Dendritic organization in the neurons of the visual and motor cortices of the cat. *J Anat* **87:** 387–406

Simpson JC, Joggerst B, Laketa V, Verissimo F, Cetin C, Erfle H, Bexiga MG, Singan VR, Heriche JK, Neumann B, Mateos A, Blake J, Bechtel S, Benes V, Wiemann S, Ellenberg J, Pepperkok R (2012) Genome-wide RNAi screening identifies human proteins with a regulatory function in the early secretory pathway. *Nat Cell Biol* **14:** 764–774

Skehel PA, Fabian-Fine R, Kandel ER (2000) Mouse VAP33 is associated with the endoplasmic reticulum and microtubules. *Proc Natl Acad Sci USA* **97:** 1101–1106

Soussan L, Burakov D, Daniels MP, Toister-Achituv M, Porat A, Yarden Y, Elazar Z (1999) ERG30, a VAP-33-related protein, functions in protein transport mediated by COPI vesicles. *J Cell Biol* **146:** 301–311

Stephens DJ, Pepperkok R (2001) Illuminating the secretory pathway: when do we need vesicles? *J Cell Sci* **114:** 1053–1059

Suzuki H, Kanekura K, Levine TP, Kohno K, Olkkonen VM, Aiso S, Matsuoka M (2009) ALS-linked P56S-VAPB, an aggregated loss-of-function mutant of VAPB, predisposes motor neurons to ER stress-related death by inducing aggregation of co-expressed wild-type VAPB. *J Neurochem* **108:** 973–985

Tang BL (2008) Emerging aspects of membrane traffic in neuronal dendrite growth. *Biochim Biophys Acta* **1783:** 169–176

Teuling E, Ahmed S, Haasdijk E, Demmers J, Steinmetz MO, Akhmanova A, Jaarsma D, Hoogenraad CC (2007) Motor neuron disease-associated mutant vesicle-associated membrane protein-associated protein (VAP) B recruits wild-type VAPs into endoplasmic reticulum-derived tubular aggregates. *J Neurosci* **27:** 9801–9815

Tsuda H, Han SM, Yang Y, Tong C, Lin YQ, Mohan K, Haueter C, Zoghbi A, Harati Y, Kwan J, Miller MA, Bellen HJ (2008) The amyotrophic lateral sclerosis 8 protein VAPB is cleaved, secreted, and acts as a ligand for Eph receptors. *Cell* **133:** 963–977

Uetz P, Giot L, Cagney G, Mansfield TA, Judson RS, Knight JR, Lockshon D, Narayan V, Srinivasan M, Pochart P, Qureshi-Emili A, Li Y, Godwin B, Conover D, Kalbfleisch T, Vijayadamodar G, Yang M, Johnston M, Fields S, Rothberg JM (2000) A comprehensive analysis of protein-protein interactions in Saccharomyces cerevisiae. *Nature* **403:** 623–627

Vlug AS, Teuling E, Haasdijk ED, French P, Hoogenraad CC, Jaarsma D (2005) ATF3 expression precedes death of spinal motoneurons in amyotrophic lateral sclerosis-SOD1 transgenic mice and correlates with c-Jun phosphorylation, CHOP expression, somato-dendritic ubiquitination and Golgi fragmentation. *Eur J Neurosci* **22:** 1881–1894

Ward TH, Polishchuk RS, Caplan S, Hirschberg K, Lippincott-Schwartz J (2001) Maintenance of Golgi structure and function depends on the integrity of ER export. *J Cell Biol* **155:** 557–570

Watson P, Stephens DJ (2005) ER-to-Golgi transport: form and formation of vesicular and tubular carriers. *Biochim Biophys Acta* **1744:** 304–315

Wendler F, Gillingham AK, Sinka R, Rosa-Ferreira C, Gordon DE, Franch-Marro X, Peden AA, Vincent JP, Munro S (2010) A genome-wide RNA interference screen identifies two novel components of the metazoan secretory pathway. *EMBO J* **29:** 304–314

Wiggins LM, Kuta A, Stevens JC, Fisher EM, von Bartheld CS (2012) A novel phenotype for the dynein heavy chain mutation Loa: Altered dendritic morphology, organelle density, and reduced numbers of trigeminal motoneurons. *J Comp Neurol* **520:** 2757–2773

Wyles JP, McMaster CR, Ridgway ND (2002) Vesicle-associated membrane protein-associated protein-A (VAP-A) interacts with the oxysterol-binding protein to modify export from the endoplasmic reticulum. *J Biol Chem* **277:** 29908–29918

Wyles JP, Ridgway ND (2004) VAMP-associated protein-A regulates partitioning of oxysterol-binding protein-related protein-9 between the endoplasmic reticulum and Golgi apparatus. *Exp Cell Res* **297:** 533–547

Yang X, Matern HT, Gallwitz D (1998) Specific binding to a novel and essential Golgi membrane protein (Yip1p) functionally links the transport GTPases Ypt1p and Ypt31p. *EMBO J* **17:** 4954–4963

Yang Z, Huh SU, Drennan JM, Kathuria H, Martinez JS, Tsuda H, Hall MC, Clemens JC (2012) Drosophila Vap-33 is required for axonal localization of Dscam isoforms. *J Neurosci* **32:** 17241–17250

Ye B, Zhang Y, Song W, Younger SH, Jan LY, Jan YN (2007) Growing dendrites and axons differ in their reliance on the secretory pathway. *Cell* **130:** 717–729

Yoshida H (2007) ER stress and diseases. *FEBS J* **274:** 630–658

Yoshida Y, Suzuki K, Yamamoto A, Sakai N, Bando M, Tanimoto K, Yamaguchi Y, Sakaguchi T, Akhter H, Fujii G, Yoshimura S, Ogata S, Sohda M, Misumi Y, Nakamura N (2008) YIPF5 and YIF1A recycle between the ER and the Golgi apparatus and are involved in the maintenance of the Golgi structure. *Exp Cell Res* **314:** 3427–3443

Yuan B, Latek R, Hossbach M, Tuschl T, Lewitter F (2004) siRNA Selection Server: an automated siRNA oligonucleotide prediction server. *Nucleic Acids Res* **32:** W130–W134

SUPPLEMENTARY INFORMATION

Manuscript: **"The amyotrophic lateral sclerosis 8 protein VAPB interacts with the ER-Golgi recycling protein YIF1A and regulates membrane delivery into dendrites"** by Kuijpers et al.

SUPPLEMENTAL FIGURE LEGENDS

Figure S1. The transmembrane domains of YIF1A and VAPB are important for binding
(A) COS-7 cells double transfected with GFP-YIF1A(1-131) (red) and myc-VAPB-P56S (green) and stained with anti-myc antibody.
(B, C) COS-7 cells double transfected with GFP-VAPB-TMD (green) and HA-YIF1A(131-293) or HA-YIF1A(189-293) with anti-HA (red) antibodies. Scalebar, 10 μm.

Figure S2. shRNA knockdown of VAPA and VAPB in primary hippocampal neurons
(A,B) Representative images of primary neurons co-expressing GFP and pSuper or VAPA-shRNA or VAPB-shRNA for 4 days and stained for endogenous VAPA (A) or VAPB (B).
(C) Quantification of VAPA and VAPB-levels in dendrites of knockdown neurons. Per shRNA-construct 9-11 images were measured. Data are presented as means ± SEM, ***P<0.001. Scalebar, 5 μm

Figure S3. shRNA#2 knockdown of VAPA and VAPB in primary hippocampal neurons
(A) Hippocampal neurons co-transfected at DIV 15 with indicated constructs and β-galactosidase to visualize morphology.
(B) Sholl analysis and quantification of total dendritic length (C) the number of primary dendrites (D) and dendritic tips (E) after 4 days overexpression of knockdown constructs or empty pSuper as control (12–19 cells were analyzed for each condition). Error bars indicate SEM, *P<0.05, ***P<0.001. Scale bars represent 50 μm.

Figure S4. No evidence for a role of YIF1 and VAP in 5HT serotonin receptor localization to dendrites
(A,B,C) Representative images of hippocampal neurons co-transfected with 5-HT1A receptor (5HTR; green) and β-galactosidase (red) (A) together with YIF1A/B-shRNA (B) or VAPA/B shRNA (C).

(D) Quantification of the ratio of 5HT-receptor intensities in the distal (first 100 μm) versus the proximal dendrite (second 100 μm). Data are presented as means ± SEM. Scale bar, 20 μm.

Figure S5. Fluorescence recovery after photobleaching (FRAP) of membrane-bound GFP (CD8-GFP) in neurons

(A) Fluorescent recovery plot showing the rate of CD8-GFP recovery in photobleached dendrites of control neurons (DIV 20, 10 cells were measured). Fluorescent intensity was normalized to intensity before bleaching. The recovery could be fit with a double exponent with 2 time constants (τ) of 36 ± 5 s and 476 ± 15 s.

(B) Fluorescent recovery plots showing the rate of CD8-GFP recovery for total and surface GFP-CD8. Surface recovery was measured by labeling the extracellular GFP-CD8 with a rhodamine tagged anti-hCD8 antibody. Subsequently, both GFP (total CD8) and rhodamine (surface CD8) were photobleached simultaneously and recovery was monitored (5 cells were measured). In the right panel a representative image is shown of a neuron with GFP-CD8 and surface rhodamine-CD8 labeling. On the far right the proximal part of the photobleached dendrite is shown. Boxed area indicates photobleached dendritic region.

(C) Quantification of the level of surface versus total GFP-CD8 in hippocampal neurons. Cells were transfected at DIV 20 with GFP-CD8 and treated with or without Triton X-100 to respectively label total or surface GFP-CD8 with rhodamine-hCD8 antibody. The ratio GFP versus total antibody staining was set to 1. Seven (total) or 10 cells (surface) were measured. Images on the right show examples of fixed and stained neurons.

(D) Fluorescent recovery plots showing CD8-GFP recovery after treatment of BFA or cycloheximide (5-10 cells analyzed). BFA treatment (20 μM) severely inhibited the GFP-CD8 recovery while cycloheximide (70 μM) treatment did not, indicating that ER-Golgi trafficking but not local protein synthesis plays a role in GFP-CD8 recovery. Data are presented as means ± SEM. Scale bars, 20 μm.

Figure S6. VAPB-P56S aggregates do not recruit FFAT-motif containing proteins OSBPL9 and NIR2

(A) Representative image of hippocampal neuron transfected with myc-VAPB-P56S (blue) shows no recruitment of VAPB binding partner OSBPL9 (green) to mutant aggregates.

(B) Neuron expressing HA-YIF1A (red) and OSBPL9 (green).

(C, D) Neurons co-expressing VAPB-P56S (blue) and YIF1A (red) stained for VAPB binding partners OSBPL9 (C) or NIR2 (D). Arrows indicate co-localization of VAPB with YIF1A.
(E) Summary of co-localization experiments, expressed as Pearson's coefficients. Pearson's coefficient (r_p) for VAPB-P56S vs. YIF1A (r_p=0.9), OSBPL9 (r_p=0.2), or NIR2 (r_p =0.2). Error bars indicate SEM, ***P<0.001 statistically significant from VAPBP56S/YIF1A.

Figure S7. Schematic model showing the VAPB and YIF1A interaction.
Schematic model showing VAPB and YIF1A interaction. Under normal circumstances YIF1A is retained in the ER membrane by its interaction with VAPB, trafficking to ERGIC however can still take place. We hypothesize that the formation of the YIF1A-VAPB complex allows specific membrane lipids and/or cargo proteins to concentrate, thus facilitating protein enrichment at the ER exit sites and further transport of cargo to the ERGIC. When VAPB is mutated, YIF1A is trapped in aggregates, preventing its transfer to the ERGIC and Golgi. Other ERGIC components such as YIP1A and ERGIC53 are not affected by aggregation and are still present in the ERGIC.

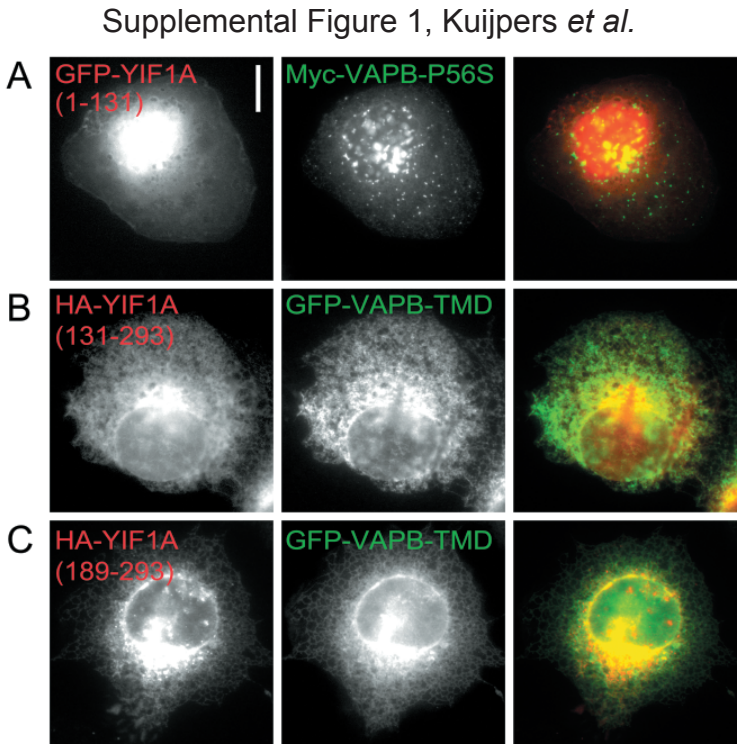

Supplemental Figure 2, Kuijpers *et al.*

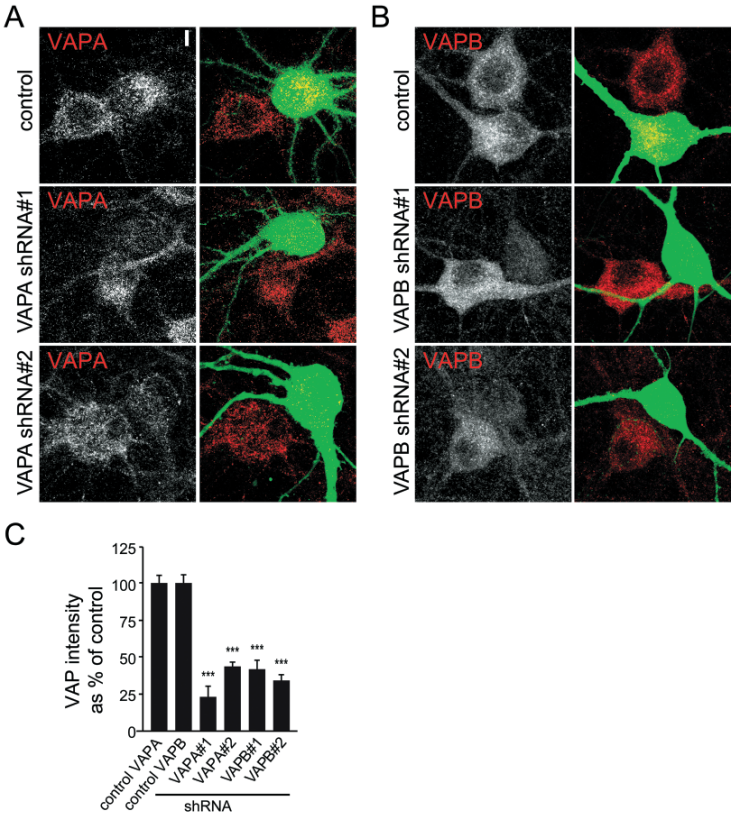

Supplemental Figure 3, Kuijpers *et al.*

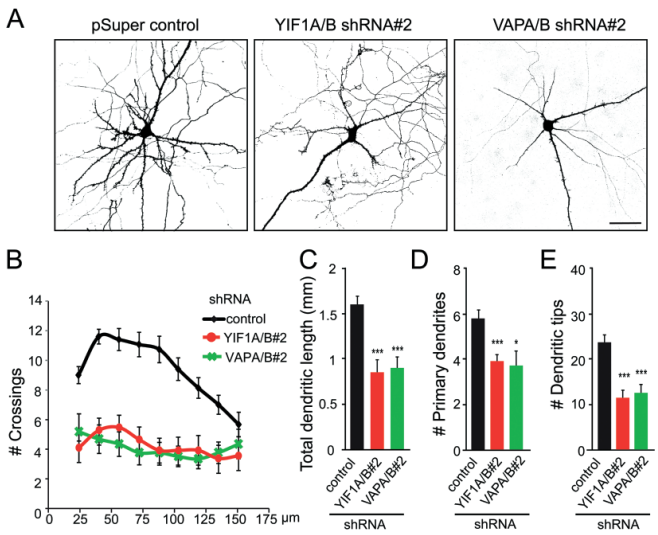

Supplemental Figure 4, Kuijpers *et al.*

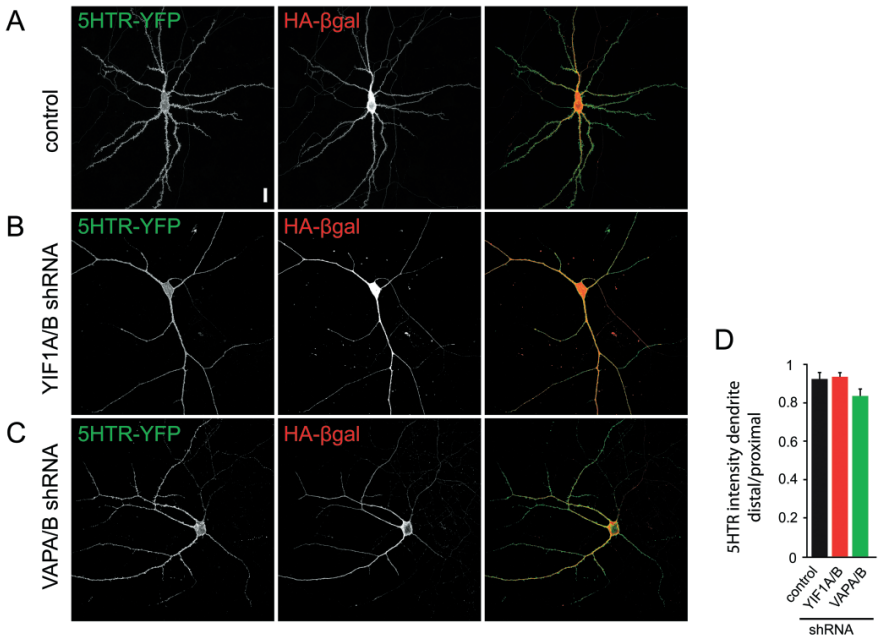

Supplemental Figure 5, Kuijpers *et al.*

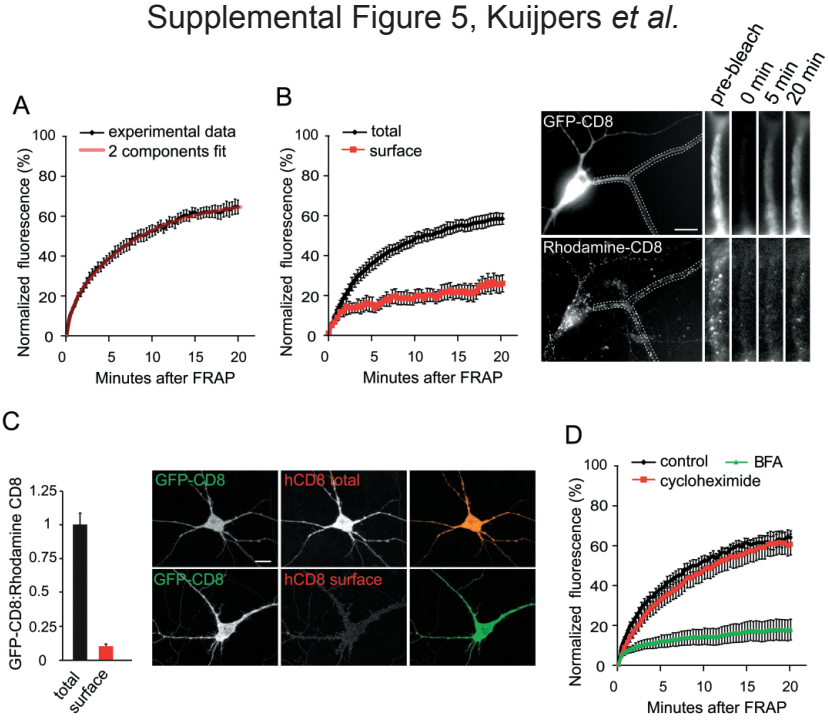

Supplemental Figure 6, Kuijpers *et al.*

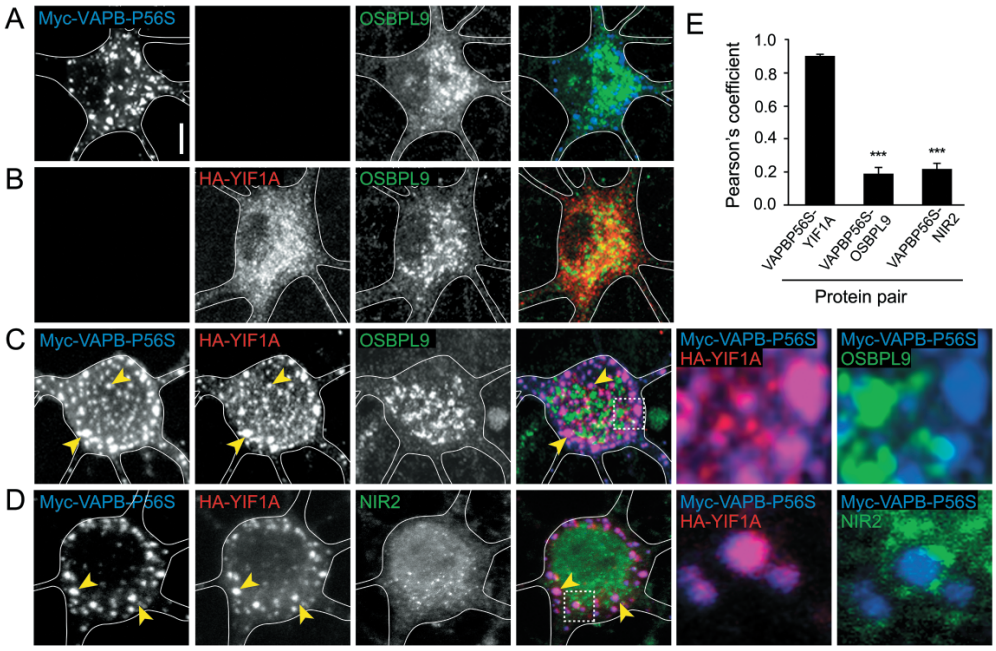

Supplemental Figure 7, Kuijpers *et al.*

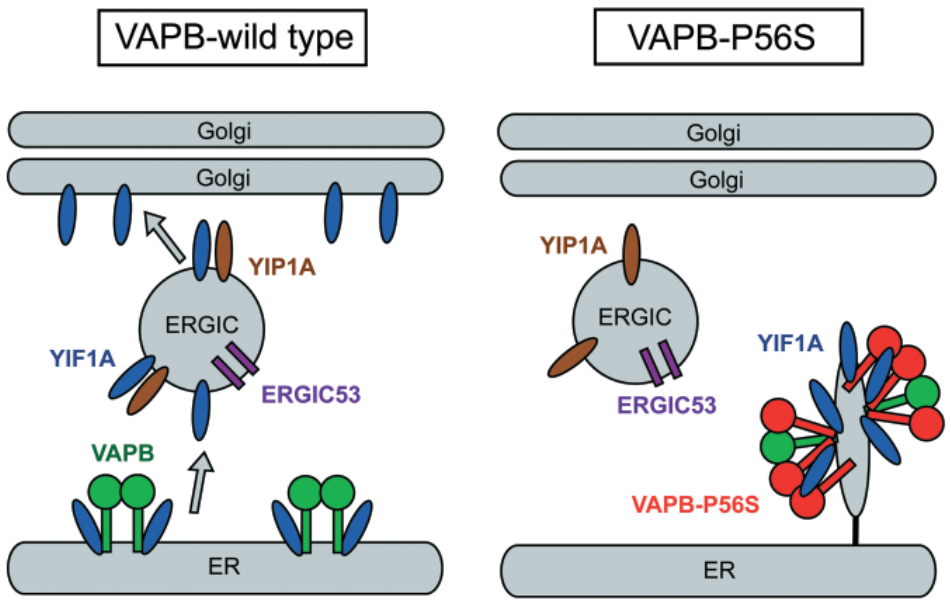

Chapter 4

Rab6, Rab8, and MICAL3 Cooperate in Controlling Docking and Fusion of Exocytotic Carriers

Ilya Grigoriev,[1,8,9] Ka Lou Yu,[1,8] Emma Martinez-Sanchez,[2,8] Andrea Serra-Marques,[1,9] Ihor Smal,[3] Erik Meijering,[3] Jeroen Demmers,[4] Johan Peränen,[5] R. Jeroen Pasterkamp,[6] Peter van der Sluijs,[2] Casper C. Hoogenraad,[7,9] and Anna Akhmanova[1,9,*]

[1]Department of Cell Biology, Erasmus Medical Center, PO Box 2040, 3000 CA Rotterdam, The Netherlands,[2]Department of Cell Biology, University Medical Center Utrecht, 3584 CX Utrecht, The Netherlands, [3]Biomedical Imaging Group Rotterdam, Department of Medical Informatics and Radiology, Erasmus Medical Center, PO Box 2040, 3000 CA Rotterdam, The Netherlands, [4]Proteomics Center, Erasmus Medical Center, 3015 GE Rotterdam, The Netherlands, [5]Institute of Biotechnology, University of Helsinki, PO Box 56, Viikinkaari 9, FIN-00014, Finland, [6]Department of Neuroscience and Pharmacology, Rudolf Magnus Institute of Neuroscience, University Medical Center Utrecht, 3584 CG Utrecht, The Netherlands, [7]Department of Neuroscience, Erasmus Medical Center, 3015 GE Rotterdam, The Netherlands, [8]These authors contributed equally to this work [9]Present address: Division of Cell Biology, Faculty of Science, Utrecht University, Padualaan 8, 3584 CH Utrecht, The Netherlands
*Correspondence: a.akhmanova@uu.nl

Current Biology *21*, 967–974, June 7, 2011 DOI 10.1016/j.cub.2011.04.030

Report

Rab6, Rab8, and MICAL3 Cooperate in Controlling Docking and Fusion of Exocytotic Carriers

Ilya Grigoriev,[1,8,9] Ka Lou Yu,[1,8] Emma Martinez-Sanchez,[2,8] Andrea Serra-Marques,[1,9] Ihor Smal,[3] Erik Meijering,[3] Jeroen Demmers,[4] Johan Peränen,[5] R. Jeroen Pasterkamp,[6] Peter van der Sluijs,[2] Casper C. Hoogenraad,[7,9] and Anna Akhmanova[1,9,*]

[1]Department of Cell Biology, Erasmus Medical Center, PO Box 2040, 3000 CA Rotterdam, The Netherlands
[2]Department of Cell Biology, University Medical Center Utrecht, 3584 CX Utrecht, The Netherlands
[3]Biomedical Imaging Group Rotterdam, Department of Medical Informatics and Radiology, Erasmus Medical Center, PO Box 2040, 3000 CA Rotterdam, The Netherlands
[4]Proteomics Center, Erasmus Medical Center, 3015 GE Rotterdam, The Netherlands
[5]Institute of Biotechnology, University of Helsinki, PO Box 56, Viikinkaari 9, FIN-00014, Finland
[6]Department of Neuroscience and Pharmacology, Rudolf Magnus Institute of Neuroscience, University Medical Center Utrecht, 3584 CG Utrecht, The Netherlands
[7]Department of Neuroscience, Erasmus Medical Center, 3015 GE Rotterdam, The Netherlands

Summary

Rab6 is a conserved small GTPase that localizes to the Golgi apparatus and cytoplasmic vesicles and controls transport and fusion of secretory carriers [1]. Another Rab implicated in trafficking from the trans-Golgi to the plasma membrane is Rab8 [2–5]. Here we show that Rab8A stably associates with exocytotic vesicles in a Rab6-dependent manner. Rab8A function is not needed for budding or motility of exocytotic carriers but is required for their docking and fusion. These processes also depend on the Rab6-interacting cortical factor ELKS [1], suggesting that Rab8A and ELKS act in the same pathway. We show that Rab8A and ELKS can be linked by MICAL3, a member of the MICAL family of flavoprotein monooxygenases [6]. Expression of a MICAL3 mutant with an inactive monooxygenase domain resulted in a strong accumulation of secretory vesicles that were docked at the cell cortex but failed to fuse with the plasma membrane, an effect that correlated with the strongly reduced mobility of MICAL3. We propose that the monooxygenase activity of MICAL3 is required to regulate its own turnover and the concomitant remodeling of vesicle-docking protein complexes in which it is engaged. Taken together, the results of our study illustrate cooperation of two Rab proteins in constitutive exocytosis and implicates a redox enzyme in this process.

Results and Discussion

Small GTPase Rab6 is associated with the Golgi complex and cytoplasmic vesicles; it is represented in mammals by Rab6A and Rab6A′, which are ubiquitously expressed and will be collectively called Rab6 here when referring to the endogenous protein, and the neuronal isoform Rab6B [7–10]. In nonpolarized cells such as HeLa, the majority of Rab6 vesicles are constitutive secretion carriers [1]. Because Rab8 has also been implicated in secretory traffic [2–5], we tested whether endogenous Rab6 and Rab8A colocalize on the same vesicles and found that this was indeed the case (Figures 1A and 1B). Rab8A-positive vesicles are exocytotic carriers because they contain the secretion marker neuropeptide Y (NPY)-Venus [1, 11] (Figure 1C). In addition, antibodies against Rab8A weakly stain the Golgi region and strongly decorate tubules, which show strong variability in size and abundance and likely represent an endosomal compartment [5, 12]. These tubules were devoid of endogenous Rab6 or NPY-Venus (arrows in Figures 1A and 1L; Figure 2E).

Next, we analyzed Rab6A-Rab8A colocalization by live imaging and found a high degree of overlap between the two markers on vesicles (Figures 1D and 1E). Colocalization of the two Rabs on moving vesicles was observed from the moment the vesicles left the Golgi area (Figure 1H; see also Figures S1A and S1B available online). Similar results were obtained in other cell lines, such as MRC5-SV (data not shown) and hTert-RPE1 (Figures S1C and S1D). Importantly, in serum-starved hTert-RPE1 cells, mStrawberry-Rab8A strongly accumulated in the primary cilia, in line with the published data [13], whereas GFP-Rab6 was not enriched in cilia (Figure S1C).

To investigate at which point Rab8A was recruited to secretory vesicles, we used Rab8A fused to photoactivatable GFP [14] (PAGFP-Rab8A) in combination with the Golgi marker mCherry-galactosyl transferase (GT) or mStrawberry-Rab6A. When PAGFP-Rab8A was photoactivated in the Golgi area, we observed weak fluorescence of the Golgi stacks and bright vesicles that rapidly moved away from the Golgi membranes to the cell periphery (Figures 1F and 1G; Movie S1). These vesicles were positive for mStrawberry-Rab6 (data not shown). Photoactivation of other cell regions visualized PAGFP-Rab8A-labeled vesicles that moved to the cell periphery where they disappeared (Movie S2). PAGFP-Rab8A-positive but Rab6A-negative tubular structures were also present in some cells (Movie S2); importantly, we never observed fusion of such structures to Rab6A-positive vesicles.

Using *f*luorescence *r*ecovery *a*fter *p*hotobleaching (FRAP) assay, we have shown that Rab6A does not significantly exchange on exocytotic vesicles [1], and we found that the same was true for Rab8A (Figure S1E and S1F). In line with this result, when PAGFP-Rab8A was photoactivated on vesicles, no significant fluorescence loss was observed within 30 s (Figures 1I and 1J), which is approximately one-third of the ~100 s duration of the exocytotic vesicle life cycle.

Next, we examined Rab8A behavior in the vicinity of the plasma membrane by using dual-color live *t*otal *i*nternal *r*eflection *f*luorescence *m*icroscopy (TIRFM). Before PAGFP-Rab8A/mStrawberry-Rab6A double-positive vesicles disappeared, they displayed a simultaneous increase of the green and red fluorescence followed by lateral diffusion of the two markers, as expected for a plasma membrane fusion event [15] (Figures 1I and 1K; Movie S2). Taken together, our data show that

[8]These authors contributed equally to this work
[9]Present address: Division of Cell Biology, Faculty of Science, Utrecht University, Padualaan 8, 3584 CH Utrecht, The Netherlands
*Correspondence: a.akhmanova@uu.nl

Current Biology Vol 21 No 11
968

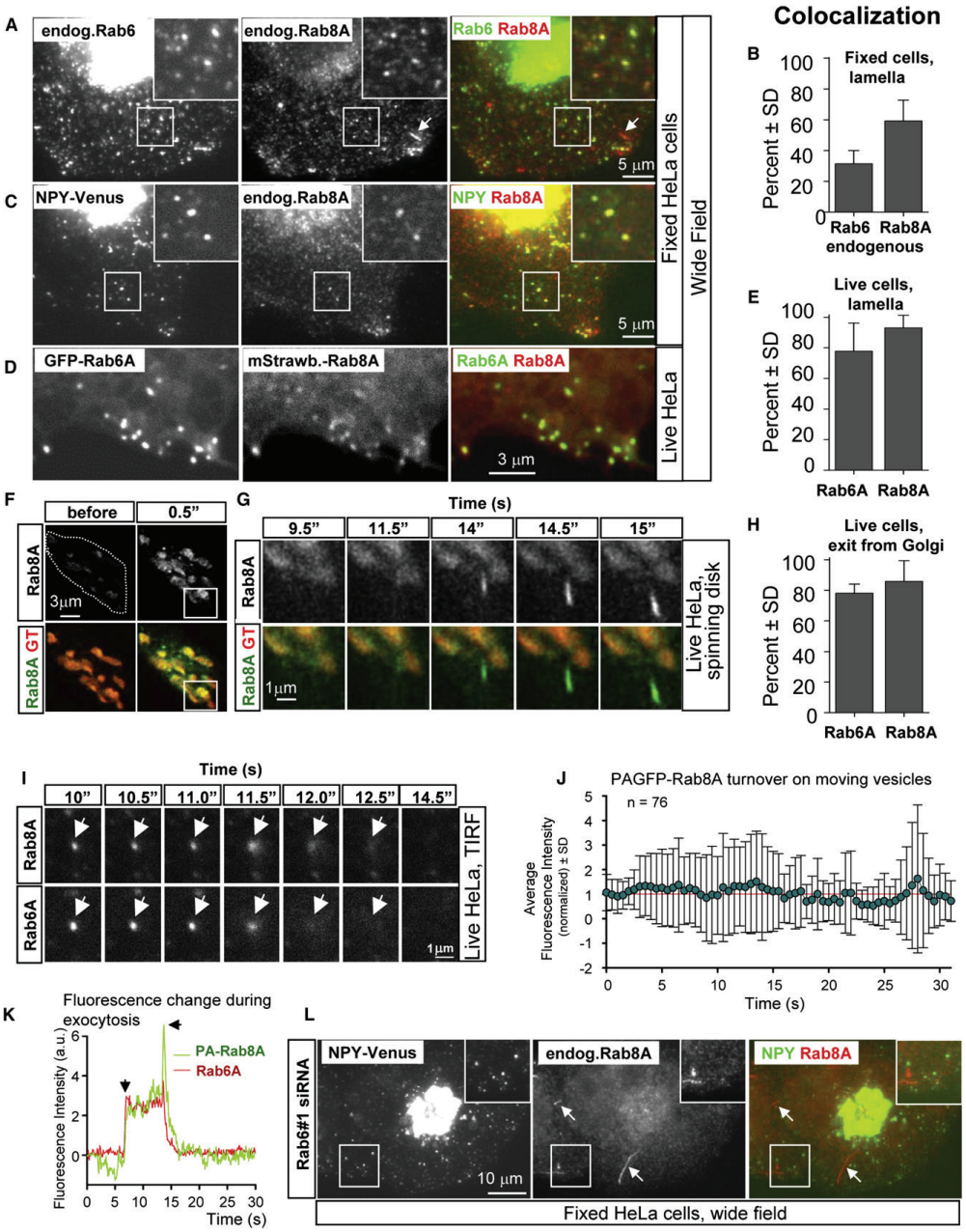

Figure 1. Rab8A Binds to Exocytotic Carriers in a Rab6-Dependent Manner

(A) HeLa cells were stained for endogenous Rab6 and Rab8A.

(B, E, and H) Quantification of colocalization of Rab6 and Rab8A in HeLa cells. (B) Colocalization of endogenous Rab6 and Rab8; note that because of the relatively high cytosolic Rab8A background, it was difficult to distinguish weak vesicular Rab8A staining, and the numbers for the endogenous proteins likely represent an underestimate. (E and H) Colocalization of Rab6A and Rab8A in live-cell images on vesicles in cell lamella or exiting the Golgi, respectively.

Rab8A is present on Rab6-negative membrane compartments, such as cytoplasmic tubules and cilia, and Rab6-positive exocytotic vesicles. Rab8A is loaded on these vesicles during or soon after their exit from the Golgi and displays little turnover until the vesicles fuse with the plasma membrane.

Rab6 depletion alters the behavior of exocytotic carriers but does not prevent their formation [1]. Interestingly, although Rab6 knockdown had no effect on Rab8A expression (Figure S1G), it caused a complete loss of both endogenous and fluorescently tagged Rab8A from NPY-Venus-positive exocytotic vesicles (Figure 1L; Figure S1H). We conclude that Rab6 is required for Rab8A recruitment to the secretory vesicle membrane. We have tested whether this was due to a direct interaction between Rab6 and Rab8 GEFs Rabin3/Rabin8 and Rabin3-like/GRAB [16, 17] but found no evidence supporting this idea (data not shown).

Next, we investigated whether the interference with Rab8A function by expressing Rab8 mutants would affect the behavior of Rab6 vesicles. Whereas overexpression of the GTP-bound Rab8A-Q67L caused a slight decrease in the number of endogenous Rab6 vesicles, the expression of GDP-bound Rab8A-T22N caused a strong increase in vesicle number at the cell margin (Figures 2A–2C and 2G). A small interfering RNA (siRNA)-mediated depletion of Rab8A also caused an increase in the number of vesicles (Figures 2D and 2G) without affecting Rab6 expression (Figure S1G). Peripherally accumulated Rab6 vesicles contained exocytotic marker NPY-Venus (Figure 2D), indicating that Rab6 recruitment to secretory vesicles is Rab8A independent. The specificity of the effect of Rab8 depletion could be confirmed by rescue with low-level expression of the GFP-Rab8A insensitive to the siRNAs used (Figure S2A).

To confirm the involvement of Rab8A in constitutive secretion, we used a flow cytometry-based assay [18], which employs a secreted GFP-tagged reporter protein that is aggregated and retained in the endoplasmic reticulum (ER) but becomes soluble and is rapidly secreted when a cell-permeable ligand is added. Using this assay, we observed a relatively mild but significant secretion delay in Rab8A-depleted cells and a stronger secretion defect in Rab6-depleted cells (Figure 2F). The latter was possibly due to defects in Golgi function and/or vesicle fission [19].

Using HeLa cells stably expressing GFP-Rab6A [1], we found that interference with Rab8A function had no significant effect on the frequency of emergence of GFP-Rab6A vesicles from the Golgi, or on their movement (Figures S2B–S2D). In contrast, whereas in control cells, Rab6 vesicles underwent rapid docking followed by fusion with the plasma membrane, which occurred within ~30 s after initial immobilization, in Rab8A-depleted cells, GFP-Rab6A vesicles underwent diffusive movements at the cell margin, and the duration of the pause between final immobilization and actual fusion with plasma membrane (terminal pause) was strongly increased (Figure 2H; Figures S2E, S2F, and S2H). Previously, we observed a similar defect in docking and fusion of Rab6 vesicles in cells depleted of the cortical Rab6-interacting coiled-coil protein ELKS (also known as ERC1, CAST2, or Rab6IP2) [1, 20]. Using ELKS siRNA, we showed that ELKS is not required for Rab8A recruitment to Rab6 vesicles (Figure 2E). Furthermore, we confirmed our previous results showing that ELKS had no effect on Rab6 vesicle emergence from the Golgi or their microtubule-based movement (Figures S2B–S2D) but was needed for their proper docking and fusion (Figure 2H; Figures S2F and S2H) and caused a reduction in secretion efficiency similar to Rab8A depletion (Figure 2F).

Our results suggest that Rab8A and ELKS might work in the same pathway. We could detect no significant pool of ELKS on the vesicles (data not shown). Instead, ELKS localized to patches at the cell cortex, and these patches served as sites for preferential docking and fusion of Rab6 vesicles [1, 21]. In Rab8A-depleted cells, Rab6 vesicles preferentially accumulated in regions devoid of cortical ELKS (Figure S2I), indicating that Rab8A might contribute to vesicle interaction with ELKS-positive sites at the plasma membrane. However, we could find no strong evidence for a direct binding between Rab8A and ELKS (data not shown).

To search for proteins that could link Rab8A and ELKS, we performed pull-down assays with biotinylation and GFP-tagged (BioGFP) ELKS (Figure S3A) and analyzed the resulting proteins by mass spectrometry. One of the most significant hits was MICAL3 (Figures S3B and S3C), a member of the MICAL family of flavoprotein monooxygenases implicated in axon guidance and actin remodeling [6, 22, 23]. MICALs, encoded in mammals by three genes, are large proteins, which, in addition to the monooxygenase enzymatic domain, include an actin-binding calponin homology (CH) domain, a LIM domain, and several predicted coiled coils (Figure 3A). There are also two MICAL-like proteins, which lack the monooxygenase domain [24]. The C-terminal domains of MICAL1, MICAL2 (MICAL-cl), and MICAL-L1/L2 were shown to interact with Rab8A as well as some other Rabs [24, 25]. We confirmed the Rab8A-MICAL1 binding and showed that MICAL3 also interacts with Rab8A through its C terminus (Figure 3B), an interaction that was previously overlooked because an incomplete MICAL3 cDNA was tested [24].

We raised antibodies against MICAL3 and showed that the full-length protein is expressed in HeLa cells (Figure S3D).

Left bar, Rab6 vesicles showing strong Rab8A labeling; right bar, Rab8A vesicles showing strong Rab6 labeling. Numbers of counted vesicles: endogenous Rab6/Rab8A, 1234 vesicles in 15 cells; Rab6A/Rab8A vesicles in lamella, 739 vesicles in 6 cells; Rab6A/Rab8A vesicles exiting the Golgi, 259 vesicles in 7 cells.

(C) HeLa cells, stably expressing NPY-Venus, were stained for endogenous Rab8A.

(D) Representative frames of a simultaneous two-color movie, showing the periphery of a HeLa cell expressing GFP-Rab6A and mStrawberry-Rab8A.

(F and G) Frames from a simultaneous two-color movie, showing the Golgi area of a HeLa cell expressing PAGFP-Rab8A (green) and mCherry-GT (red). The area indicated with a stippled line was photoactivated using a 408 nm laser. Images of the whole area (F) and enlargements of the boxed area (G) taken at different time points after photoactivation are shown. See also Movie S1.

(I) Frames from a TIRFM movie showing the behavior of a single PAGFP-Rab8A and mStrawberry-Rab6A-positive vesicle immediately before and during fusion. Time after photoactivation (performed in peripheral cytoplasm using a 407 nm laser) is indicated. See also Movie S2.

(J) Plot of the average fluorescent intensity of moving PAGFP-Rab8A vesicles after photoactivation in the Golgi area. Imaging was performed with a spinning disk microscope. Linescan (line thickness 0.32 μm) was applied to measure pixel intensities along the vesicle path in the kymographs of individual vesicles.

(K) Plot of average fluorescence intensity of a single PAGFP-Rab8A- and mStrawberry-Rab6A-positive vesicle (a circle with a diameter of 0.65 μm) over time. Vesicle appearance in the focal plane is indicated by a vertical arrow. The horizontal arrow points to the peak of fluorescence intensity, corresponding to vesicle fusion with the plasma membrane.

(L) HeLa cells stably expressing NPY-Venus were transfected with the indicated siRNA, fixed, and stained for the endogenous Rab8A 3 days after siRNA transfection. In (A), (B), and (L), insets show enlargements of the boxed areas. Rab8A-positive tubules are indicated by arrows.

Current Biology Vol 21 No 11
970

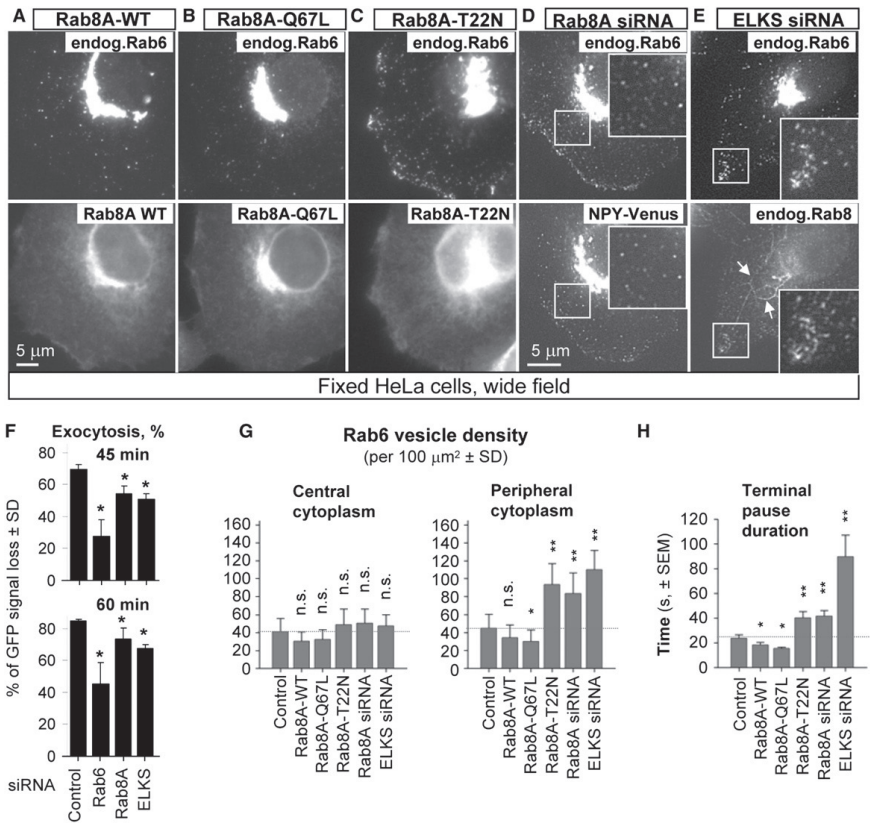

Figure 2. Rab8A Is Required for Docking and Fusion of Rab6 Vesicles

(A–C) HeLa cells were transfected with the indicated GFP-Rab8A fusions and stained for endogenous Rab6.

(D) HeLa cells stably expressing NPY-Venus were transfected with Rab8A siRNA, fixed 3 days later, and stained for endogenous Rab6.

(E) HeLa cells were transfected with ELKS siRNA, fixed 3 days later, and stained for endogenous Rab6 and Rab8A. Tubules positive for Rab8A and negative for Rab6 are indicated by arrowheads. In (D) and (E), insets show enlargements of the boxed areas.

(F) Cells stably expressing the secretion reporter SS-GFP-FM4-FCS-hGH [18] were transfected with different siRNAs; 3 days later, secretion was stimulated by the addition of 1 μM AP21998, and the average intracellular fluorescence was measured using flow cytometry at 45 and 60 min after ligand addition. The percentage of fluorescent signal loss at 45 and 60 min compared to control (no ligand added) was determined in four independent samples for each siRNA and each time point.

(G) Quantification of vesicles positive for endogenous Rab6 in HeLa cells fixed and stained as described for (A)–(E). At least 200 vesicles were analyzed in ~6 cells for each condition.

(H) HeLa cells stably expressing GFP-Rab6A and transfected with the indicated mStrawberry-Rab8A fusions or siRNAs were imaged using wide-field epifluorescence microscopy, and the duration of the pause between vesicle immobilization at the cell periphery and its disappearance was measured. One hundred vesicles in five cells were analyzed for each condition. In (F)–(H), values significantly different from control are indicated by asterisks (*$p < 0.05$; **$p < 0.01$; Mann-Whitney U test).

Using this antibody, we confirmed the interaction between endogenous MICAL3 and ELKS (Figure 3C). In contrast, we observed no strong interaction between ELKS and MICAL1, a conclusion supported by pull-downs of BioGFP-MICAL1 and BioGFP-MICAL3 (Figure S3E). Furthermore, using pull-down assays from cells expressing BioGFP-ELKS together with different MICAL3 fragments, we mapped the ELKS-interacting domain to the C-terminal portion of MICAL3 (MICAL3-C2) that is distinct from Rab8A-binding region MICAL3-CC (Figures 3A and 3D; Figure S3F). Using ELKS deletion mutants, we found that MICAL3- and Rab6-interacting regions on ELKS are also distinct: the sequence between amino acids 950 and 1015 of ELKS is required for Rab6, but not for MICAL3 binding (Figures 3E and 3G; Figure S3G).

Next, we investigated whether Rab8A, ELKS, and MICAL3 could form a triple complex in transfected cells and found that FLAG-tagged Rab8A coprecipitated GFP-ELKS more efficiently when it was coexpressed together with GFP-MICAL3 (Figure 3F). Coprecipitation was specific for Rab8A, because it was not observed with Rab7 (Figure S3H). We conclude

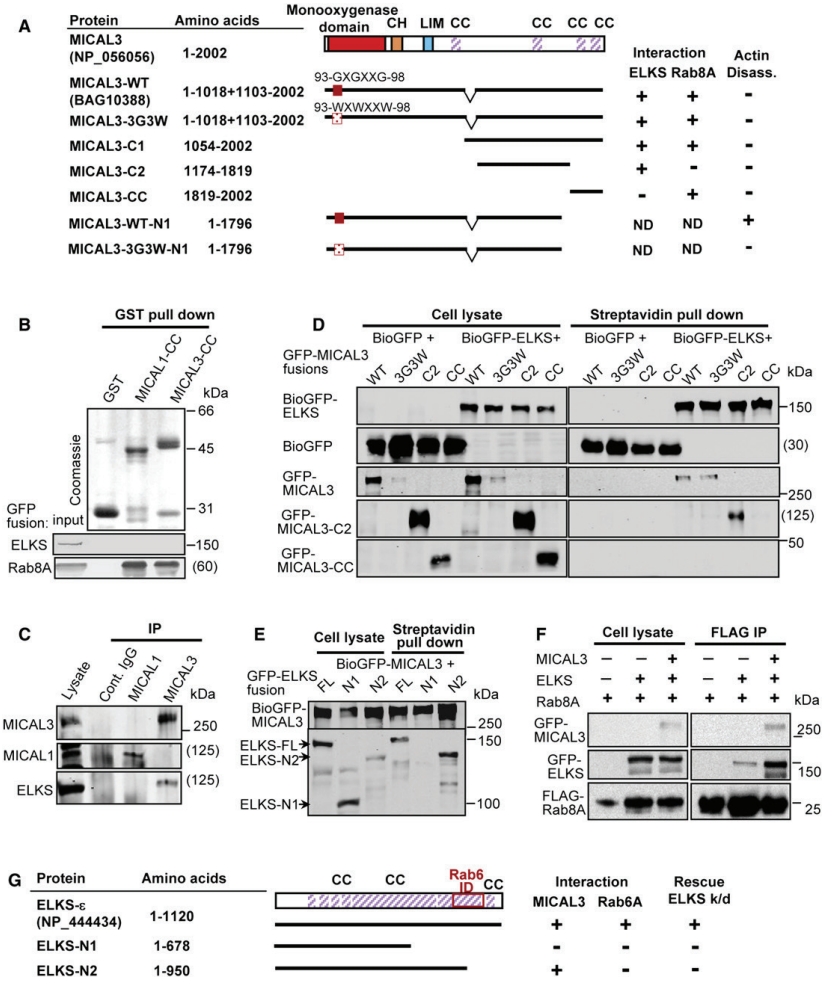

Figure 3. MICAL3 Binds to Rab8A and ELKS

(A) A scheme of MICAL3 protein and the constructs used in this study and a summary of identified interactions (ND, not determined). The accession numbers of the protein sequences used are indicated. The numbering is based on MICAL3 isoform 1 (NCBI protein NP_056056); compared to this sequence, the full-length clone used in this study contains a short internal deletion that does not affect any of the conserved domains. Abbreviations for protein domains: CH, calponin homology domain; LIM, Lin11, Isl-1, and Mec-3 domain (zinc binding); CC, predicted coiled coil. Actin disassembly was determined by phalloidin staining in transfected cells; see Figure S4F.

(B) GST pull-down assays were performed with the indicated GST fusions and lysates of cells expressing GFP-ELKS or GFP-Rab8A. Coomassie-stained gels are shown for GST fusions and western blots with anti-GFP antibodies for GFP fusions. Calculated molecular mass is indicated in parentheses in cases where it is not possible to show the marker position.

(C) Immunoprecipitations (IPs) from HeLa cell extracts with control rabbit IgG or antibodies against MICAL1 or MICAL3 were analyzed by western blotting with the indicated antibodies.

(D and E) Streptavidin pull-down assays from extracts of HEK293T cells coexpressing BirA, BioGFP, or BioGFP-ELKS and the indicated GFP-MICAL3 fusions (D) or BioGFP-MICAL3 and the indicated GFP-ELKS fusions (E). In (D), all proteins were detected with anti-GFP antibodies; in (E), BioGFP-MICAL3 was detected with anti-GFP antibodies and ELKS fusions with the antibodies against ELKS N terminus. In experiments shown in (B)–(E), 2% of the input and 10% of the precipitate was loaded on gel.

(F) IPs from HEK293T cells coexpressing the indicated constructs using anti-FLAG antibodies. Western blotting was performed with antibodies against GFP or the FLAG tag. For the blots with anti-GFP antibodies, 7% of the input and 40% of the precipitate was loaded on gel; for blots with anti-FLAG antibodies, 7% of input and precipitate was loaded.

(G) A scheme of ELKS protein and the constructs used in this study and a summary of their functional properties. CC, coiled coil; Rab6 ID, Rab6 interaction domain [20]; rescue ELKS k/d, reversal of Rab6 vesicle accumulation in ELKS-depleted cells [1].

Current Biology Vol 21 No 11
972

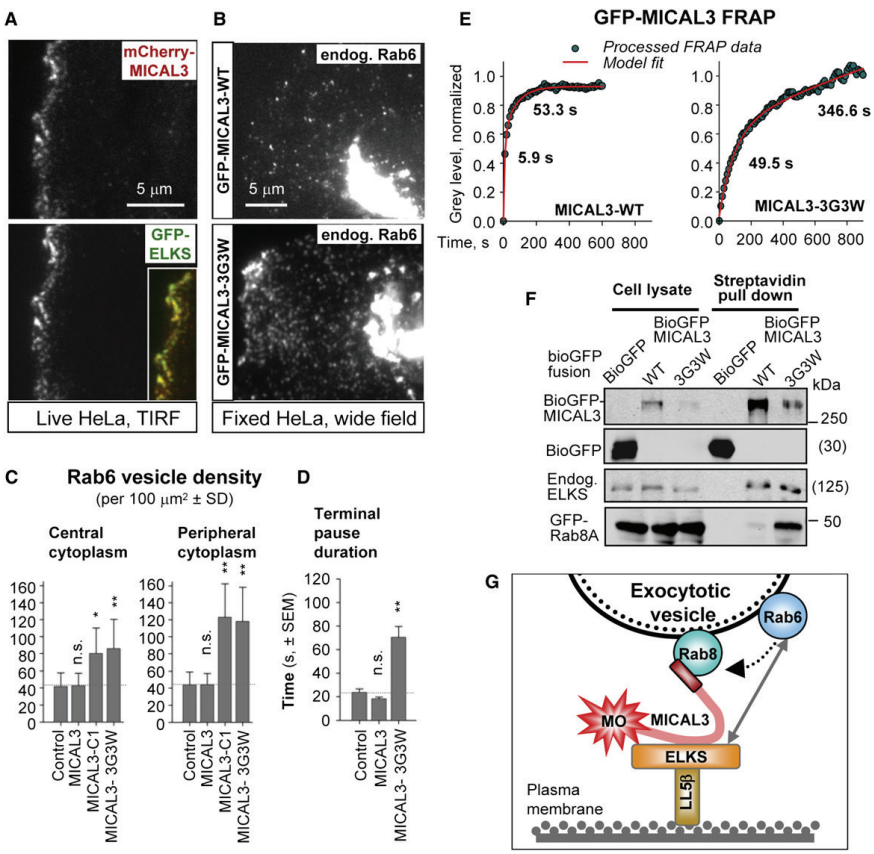

Figure 4. MICAL3 Is Involved in Rab6 Vesicle Fusion with the Plasma Membrane

(A) Analysis of colocalization of mCherry-MICAL3 with the indicated GFP fusions at low expression levels in live HeLa cells using TIRFM. Insets show overlays of the two channels, with GFP signal in green and mCherry in red.

(B) HeLa cells expressing the indicated GFP-MICAL3 fusions were fixed and stained for endogenous Rab6.

(C) Quantification of vesicles positive for endogenous Rab6 in HeLa cells as described for Figure 2G.

(D) Duration of the pause between vesicle immobilization at the cell periphery and its disappearance measured in HeLa cells stably expressing GFP-Rab6A and transiently transfected with mCherry-MICAL3-3G3W. Analysis was performed as described for Figure 2H. In (C) and (D), values significantly different from control are indicated by asterisks (*$p < 0.05$; **$p < 0.01$; Mann-Whitney U test).

(E) Analysis of GFP-MICAL3 and GFP-MICAL3-3G3W turnover by FRAP. The plots show processed FRAP data (green dots) and their fitting to a two-exponential model (red lines); see Supplemental Experimental Procedures and Table S1 for details. Eleven or twelve cells were analyzed in three experiments. The recovery half-times for the two components are indicated.

(F) Streptavidin pull-down assays from extracts of HEK293T cells coexpressing GFP-Rab8A, BirA, BioGFP, or the indicated BioGFP-MICAL3 fusions. All GFP proteins were detected with anti-GFP antibodies and endogenous ELKS with antibodies against ELKS C terminus. Two percent of the input and 10% of the precipitate was loaded on gel. Calculated molecular mass is indicated in parentheses in cases where it is not possible to show the marker position.

(G) A model for cooperative action of Rab6 and Rab8A in exocytosis. Rab6 promotes recruitment of Rab8A to the vesicles. Rab8A interacts with ELKS-positive cortical sites through MICAL3, which binds to ELKS. Rab6 also contributes to vesicle interactions with the cortex through direct binding to ELKS. Redox activity of MICAL3 promotes the docking-complex remodeling and vesicle fusion.

that MICAL3 can promote the interaction between Rab8A and ELKS. Importantly, the ELKS-N2 mutant, which can bind to MICAL3 but not to Rab6 (Figure 3G), cannot rescue the phenotype of ELKS depletion [1], indicating that the direct ELKS-Rab6 interaction appears functionally important in spite of the existence of an additional link between ELKS and the secretory vesicles provided by the MICAL3-Rab8 complex.

Fluorescently tagged MICAL3 localized to the nucleus and cytoplasm; it could be found on Rab8A-positive tubules, the size and number of which increased when both MICAL3 and Rab8A were highly overexpressed (Figure S4A). Using TIRFM in live cells, we could clearly detect MICAL3 in ELKS-positive patches at the cell cortex (Figure 4A). Endogenous MICAL3 was also found at the cortical patches where ELKS and its

cortical partner LL5β were accumulated (Figure S4B). We observed frequent immobilization and fusion of Rab6A- and Rab8A-labeled vesicles at the sites of cortical accumulation of MICAL3 (Figure S4C and data not shown).

We were unable to fully deplete MICAL3 (Figure S3D), and partial MICAL3 knockdown had no clear effect on Rab6 vesicle behavior. As an alternative, we generated a dominant-negative MICAL3 mutant, in which the three glycines in the FAD binding motif GXGXXG were mutated to tryptophans (the 3G3W mutant, Figure 3A). This triple mutation was shown to abrogate the function of *Drosophila* Mical in axon guidance and actin disassembly [22, 23]. Expression of MICAL3-3G3W, but not the wild-type MICAL3, dramatically increased the number of secretory vesicles positive for Rab6 and NPY-Venus (Figures 4B and 4C; Figure S4D). Live-cell imaging showed that these vesicles underwent rapid docking and became immobilized but failed to fuse with the plasma membrane for long time periods (Figure 4D; Figures S2G and S4E), suggesting that MICAL3 helps to attach Rab8-bound vesicles to the cortex, but, without the monooxygenase activity, subsequent fusion steps are inhibited.

The monooxygenase activity of *Drosophila* Mical is used to disassemble actin filaments [23]. We overexpressed the N-terminal part of MICAL3 and found that it strongly reduced the amount of filamentous actin in cells, an effect that was dependent on the intact monooxygenase domain (Figure S4F). The expression of the full-length protein showed no strong effect on actin, possibly as a result of autoinhibition by the C-terminal domain [26]. It is therefore possible that during vesicle fusion, activated MICAL3 promotes disassembly of the cortical actin. In line with this view, MICAL3-3G3W overexpression caused appearance of an actin pool with slow turnover (Figure S4G; Table S1). However, actin disassembly by latrunculin B did not prevent vesicle accumulation induced by the expression of MICAL3-3G3W (data not shown). Moreover, expression of MICAL3-C1, which lacks not only the monooxygenase activity but also the actin-binding CH domain (Figure 3A), caused a strong vesicle accumulation similar to that caused by MICAL3-3G3W (Figure 4C).

To explain these observations, we hypothesized that the redox function of MICAL3 might be needed to destabilize protein complexes in which it is engaged. In line with this view, we found that the turnover of MICAL3 at the cell cortex was much slower for the monooxygenase-deficient MICAL3-3G3W mutant as compared to the wild-type protein (Figure 4E; Table S1). Furthermore, although MICAL3-3G3W showed lower expression and was more difficult to precipitate than MICAL3-WT, it pulled down the same amount of ELKS and a larger amount of Rab8A than the wild-type protein, suggesting that its interaction with the binding partners is increased (Figure 4F). We propose that the redox activity of MICAL3 promotes vesicle fusion by remodeling vesicle-docking complexes in which it is engaged.

In this study, we showed that representatives of two highly conserved Rab families, Rab6 and Rab8, cooperate in control of exocytotic vesicle behavior. Crosstalk between different Rabs in regulation of adjacent trafficking stages was previously demonstrated for exocytosis as well as for endosomal Rabs [27, 28]. Here we provide an example of when two Rabs act simultaneously on the same vesicle, but have different functions: Rab6 controls Rab8A recruitment, vesicle transport, and the choice of fusion sites [1], while Rab8A promotes efficient vesicle docking and fusion, in agreement with the role of Rab8 homolog in yeast [27]. It is possible that a system dependent on two Rabs has evolved by convergence of two initially separate pathways, one controlling plasma membrane fusion (Rab8) and the other regulating the emergence and movement of Golgi-derived carriers (Rab6).

Participation of Rab8A in vesicle fusion with the plasma membrane might represent its general function, which might require interactions with actin-based motors [12, 29] or components of vesicle tethering and fusion machinery, such as the exocyst or SNAREs [27]. We provide evidence that this function is also associated with binding to the MICAL-family proteins (Figure 4G). The two mammalian MICAL-like (MICAL-L1/L2) family members, which lack the redox activity, were already implicated in vesicle trafficking [24, 30], and the *Mical* fly gene was found as a hit in a screen for secretory pathway components [31]. Our results suggest that the enzymatically active MICAL proteins can participate in vesicle tethering and fusion, most likely by monooxygenase-dependent disassembly of protein complexes.

Supplemental Information

Supplemental Information includes four figures, one table, Supplemental Experimental Procedures, and two movies and can be found with this article online at doi:10.1016/j.cub.2011.04.030.

Acknowledgments

We are grateful to A. Peden, A. Barnekow, I. Kaverina, J. Sanes, R. Tsien, A. Miyawaki, F. Melchior, and I. Mellman for the gift of materials and to G. Schaaf, R. van der Linden, and E. Dzierzak for the use of fluorescence-activated cell sorting (FACS) equipment. This work was supported by a Netherlands Organization for Health Research (ZonMW) TOP grant and the Netherlands Organization for Scientific Research (NWO) ALW-VICI grants to A.A.; by a Fundação para a Ciência e a Tecnologia fellowship to A.S.-M.; by NWO-ALW, NWO-CW, and ZonMW-VIDI grants and a ESF-EURYI award to C.C.H.; the ZonMW-VIDI and the Human Frontier Science Program (Career Development Awards) to R.J.P.; and a NWO-CW ECHO grant to P.v.d.S.

Received: October 10, 2010
Revised: March 16, 2011
Accepted: April 18, 2011
Published online: May 19, 2011

References

1. Grigoriev, I., Splinter, D., Keijzer, N., Wulf, P.S., Demmers, J., Ohtsuka, T., Modesti, M., Maly, I.V., Grosveld, F., Hoogenraad, C.C., and Akhmanova, A. (2007). Rab6 regulates transport and targeting of exocytotic carriers. Dev. Cell *13*, 305–314.
2. Ang, A.L., Folsch, H., Koivisto, U.M., Pypaert, M., and Mellman, I. (2003). The Rab8 GTPase selectively regulates AP-1B-dependent basolateral transport in polarized Madin-Darby canine kidney cells. J. Cell Biol. *163*, 339–350.
3. Huber, L.A., Pimplikar, S., Parton, R.G., Virta, H., Zerial, M., and Simons, K. (1993). Rab8, a small GTPase involved in vesicular traffic between the TGN and the basolateral plasma membrane. J. Cell Biol. *123*, 35–45.
4. Sato, T., Mushiake, S., Kato, Y., Sato, K., Sato, M., Takeda, N., Ozono, K., Miki, K., Kubo, Y., Tsuji, A., et al. (2007). The Rab8 GTPase regulates apical protein localization in intestinal cells. Nature *448*, 366–369.
5. Hattula, K., Furuhjelm, J., Tikkanen, J., Tanhuanpaa, K., Laakkonen, P., and Peranen, J. (2006). Characterization of the Rab8-specific membrane traffic route linked to protrusion formation. J. Cell Sci. *119*, 4866–4877.
6. Kolk, S.M., and Pasterkamp, R.J. (2007). MICAL flavoprotein monooxygenases: Structure, function and role in semaphorin signaling. Adv. Exp. Med. Biol. *600*, 38–51.
7. Martinez, O., Schmidt, A., Salamero, J., Hoflack, B., Roa, M., and Goud, B. (1994). The small GTP-binding protein rab6 functions in intra-Golgi transport. J. Cell Biol. *127*, 1575–1588.

Current Biology Vol 21 No 11
974

8. White, J., Johannes, L., Mallard, F., Girod, A., Grill, S., Reinsch, S., Keller, P., Tzschaschel, B., Echard, A., Goud, B., and Stelzer, E.H. (1999). Rab6 coordinates a novel Golgi to ER retrograde transport pathway in live cells. J. Cell Biol. *147*, 743–760.
9. Del Nery, E., Miserey-Lenkei, S., Falguieres, T., Nizak, C., Johannes, L., Perez, F., and Goud, B. (2006). Rab6A and Rab6A′ GTPases play non-overlapping roles in membrane trafficking. Traffic *7*, 394–407.
10. Opdam, F.J., Echard, A., Croes, H.J., van den Hurk, J.A., van de Vorstenbosch, R.A., Ginsel, L.A., Goud, B., and Fransen, J.A. (2000). The small GTPase Rab6B, a novel Rab6 subfamily member, is cell-type specifically expressed and localised to the Golgi apparatus. J. Cell Sci. *113*, 2725–2735.
11. Nagai, T., Ibata, K., Park, E.S., Kubota, M., Mikoshiba, K., and Miyawaki, A. (2002). A variant of yellow fluorescent protein with fast and efficient maturation for cell-biological applications. Nat. Biotechnol. *20*, 87–90.
12. Roland, J.T., Kenworthy, A.K., Peranen, J., Caplan, S., and Goldenring, J.R. (2007). Myosin Vb interacts with Rab8a on a tubular network containing EHD1 and EHD3. Mol. Biol. Cell *18*, 2828–2837.
13. Nachury, M.V., Loktev, A.V., Zhang, Q., Westlake, C.J., Peranen, J., Merdes, A., Slusarski, D.C., Scheller, R.H., Bazan, J.F., Sheffield, V.C., and Jackson, P.K. (2007). A core complex of BBS proteins cooperates with the GTPase Rab8 to promote ciliary membrane biogenesis. Cell *129*, 1201–1213.
14. Patterson, G.H., and Lippincott-Schwartz, J. (2002). A photoactivatable GFP for selective photolabeling of proteins and cells. Science *297*, 1873–1877.
15. Toomre, D., Steyer, J.A., Keller, P., Almers, W., and Simons, K. (2000). Fusion of constitutive membrane traffic with the cell surface observed by evanescent wave microscopy. J. Cell Biol. *149*, 33–40.
16. Hattula, K., Furuhjelm, J., Arffman, A., and Peranen, J. (2002). A Rab8-specific GDP/GTP exchange factor is involved in actin remodeling and polarized membrane transport. Mol. Biol. Cell *13*, 3268–3280.
17. Luo, H.R., Saiardi, A., Nagata, E., Ye, K., Yu, H., Jung, T.S., Luo, X., Jain, S., Sawa, A., and Snyder, S.H. (2001). GRAB: A physiologic guanine nucleotide exchange factor for Rab3A, which interacts with inositol hexakisphosphate kinase. Neuron *31*, 439–451.
18. Gordon, D.E., Bond, L.M., Sahlender, D.A., and Peden, A.A. (2010). A targeted siRNA screen to identify SNAREs required for constitutive secretion in mammalian cells. Traffic *11*, 1191–1204.
19. Miserey-Lenkei, S., Chalancon, G., Bardin, S., Formstecher, E., Goud, B., and Echard, A. (2010). Rab and actomyosin-dependent fission of transport vesicles at the Golgi complex. Nat. Cell Biol. *12*, 645–654.
20. Monier, S., Jollivet, F., Janoueix-Lerosey, I., Johannes, L., and Goud, B. (2002). Characterization of novel Rab6-interacting proteins involved in endosome-to-TGN transport. Traffic *3*, 289–297.
21. Lansbergen, G., Grigoriev, I., Mimori-Kiyosue, Y., Ohtsuka, T., Higa, S., Kitajima, I., Demmers, J., Galjart, N., Houtsmuller, A.B., Grosveld, F., and Akhmanova, A. (2006). CLASPs attach microtubule plus ends to the cell cortex through a complex with LL5beta. Dev. Cell *11*, 21–32.
22. Terman, J.R., Mao, T., Pasterkamp, R.J., Yu, H.H., and Kolodkin, A.L. (2002). MICALs, a family of conserved flavoprotein oxidoreductases, function in plexin-mediated axonal repulsion. Cell *109*, 887–900.
23. Hung, R.J., Yazdani, U., Yoon, J., Wu, H., Yang, T., Gupta, N., Huang, Z., van Berkel, W.J., and Terman, J.R. (2010). Mical links semaphorins to F-actin disassembly. Nature *463*, 823–827.
24. Yamamura, R., Nishimura, N., Nakatsuji, H., Arase, S., and Sasaki, T. (2008). The interaction of JRAB/MICAL-L2 with Rab8 and Rab13 coordinates the assembly of tight junctions and adherens junctions. Mol. Biol. Cell *19*, 971–983.
25. Fukuda, M., Kanno, E., Ishibashi, K., and Itoh, T. (2008). Large scale screening for novel rab effectors reveals unexpected broad Rab binding specificity. Mol. Cell. Proteomics *7*, 1031–1042.
26. Schmidt, E.F., Shim, S.O., and Strittmatter, S.M. (2008). Release of MICAL autoinhibition by semaphorin-plexin signaling promotes interaction with collapsin response mediator protein. J. Neurosci. *28*, 2287–2297.
27. Novick, P., Medkova, M., Dong, G., Hutagalung, A., Reinisch, K., and Grosshans, B. (2006). Interactions between Rabs, tethers, SNAREs and their regulators in exocytosis. Biochem. Soc. Trans. *34*, 683–686.
28. Rink, J., Ghigo, E., Kalaidzidis, Y., and Zerial, M. (2005). Rab conversion as a mechanism of progression from early to late endosomes. Cell *122*, 735–749.
29. Sahlender, D.A., Roberts, R.C., Arden, S.D., Spudich, G., Taylor, M.J., Luzio, J.P., Kendrick-Jones, J., and Buss, F. (2005). Optineurin links myosin VI to the Golgi complex and is involved in Golgi organization and exocytosis. J. Cell Biol. *169*, 285–295.
30. Sharma, M., Giridharan, S.S., Rahajeng, J., Naslavsky, N., and Caplan, S. (2009). MICAL-L1 links EHD1 to tubular recycling endosomes and regulates receptor recycling. Mol. Biol. Cell *20*, 5181–5194.
31. Wendler, F., Gillingham, A.K., Sinka, R., Rosa-Ferreira, C., Gordon, D.E., Franch-Marro, X., Peden, A.A., Vincent, J.P., and Munro, S. (2010). A genome-wide RNA interference screen identifies two novel components of the metazoan secretory pathway. EMBO J. *29*, 304–314.

Current Biology, Volume *21*

Supplemental Information

Rab6, Rab8, and MICAL3 Cooperate in Controlling Docking and Fusion of Exocytotic Carriers

Ilya Grigoriev, Ka Lou Yu, Emma Martinez-Sanchez, Andrea Serra-Marques, Ihor Smal, Erik Meijering, Jeroen Demmers, Johan Peränen, R. Jeroen Pasterkamp, Peter van der Sluijs, Casper C. Hoogenraad, and Anna Akhmanova

Inventory of Supplemental Information

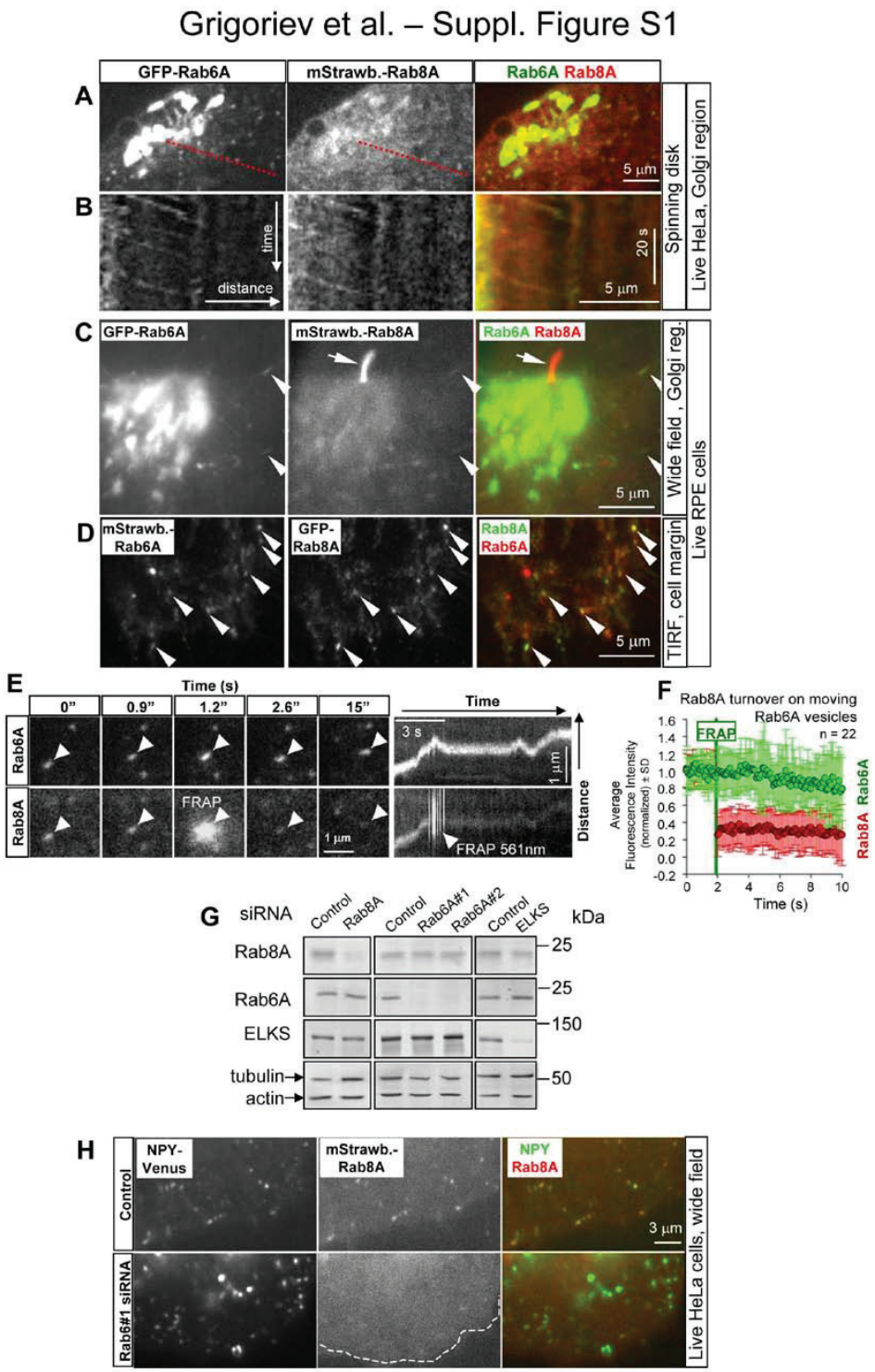
Grigoriev et al. – Suppl. Figure S1
A
GFP-Rab6A
mStrawb.-Rab8A
Rab6A Rab8A
5 µm
B
time
distance
20 s
5 µm
Spinning disk
Live HeLa, Golgi region
C
GFP-Rab6A
mStrawb.-Rab8A
Rab6A Rab8A
5 µm
Wide field , Golgi reg.
D
mStrawb.-Rab6A
GFP-Rab8A
Rab8A Rab6A
5 µm
TIRF, cell margin
Live RPE cells
E
Time (s)
0"
0.9"
1.2"
2.6"
15"
Rab6A
Rab8A
FRAP
1 µm
Time
3 s
1 µm
FRAP 561nm
Distance
F
Rab8A turnover on moving Rab6A vesicles
n = 22
FRAP
Average Fluorescence Intensity (normalized) ± SD
Time (s)
Rab6A
Rab8A
G
siRNA
Control
Rab8A
Control
Rab6A#1
Rab6A#2
Control
ELKS
kDa
Rab8A
Rab6A
ELKS
tubulin
actin
25
25
150
50
H
Control
Rab6#1 siRNA
NPY-Venus
mStrawb.-Rab8A
NPY Rab8A
3 µm
Live HeLa cells, wide field

Figure S1. Analysis of colocalization between Rab6 and Rab8A (Related to Figure 1)

(A) Representative frames of a simultaneous two-color movie, showing the Golgi area of a HeLa cell expressing GFP-Rab6A and mStrawberry-Rab8A.

(B) Kymograph drawn along the line indicated in red in the panel A, showing colocalization of GFP-Rab6A and mStrawberry-Rab8A on the vesicles that exit the Golgi.

(C and D) Rab6A and Rab8A colocalize on vesicles but not in the primary cilia. hTert-RPE1 cells were cotransfected with fluorescently tagged Rab6A and Rab8A, serum starved for two days and analyzed by simultaneous dual-color live cell imaging. Note the absence of colocalization of the two markers in the cilium (C, wide-field epi-fluorescence microscopy) but abundant colocalization on vesicles at the cell periphery (D, TIRFM). Vesicles positive for Rab6A and Rab8A are indicated by arrowheads.

(E) Frames from a two-color movie of a single vesicle double positive for GFP-Rab6A and mStrawberry-Rab8A are shown on the left. In the third shown frame the mStrawberry signal was bleached specifically on the vesicle using the 561 nm laser. Panels on the right show kymographs of the same vesicle throughout the movie in both channels.

(F) Quantification of the FRAP data obtained as in (E). Mean averaged fluorescence intensity (normalized for the first value) of GFP-Rab6A and mStrawberry-Rab8A on single vesicles. Linescan (line thickness 0.32 μm) was applied to measure pixel intensities along the vesicle path in the kymographs of individual vesicles.

(G) Western blots showing depletion of Rab8A, Rab6A and ELKS in HeLa cells three days after siRNA transfection. Actin and tubulin serve as loading controls.

(H) HeLa cells stably expressing NPY-Venus were transfected with the indicated siRNAs and with mStrawberry-Rab8A. Cells were analyzed by live cell imaging three days after siRNA transfection. Note complete absence of Rab8A signal from NPY-Venus labeled vesicles after Rab6 knockdown.

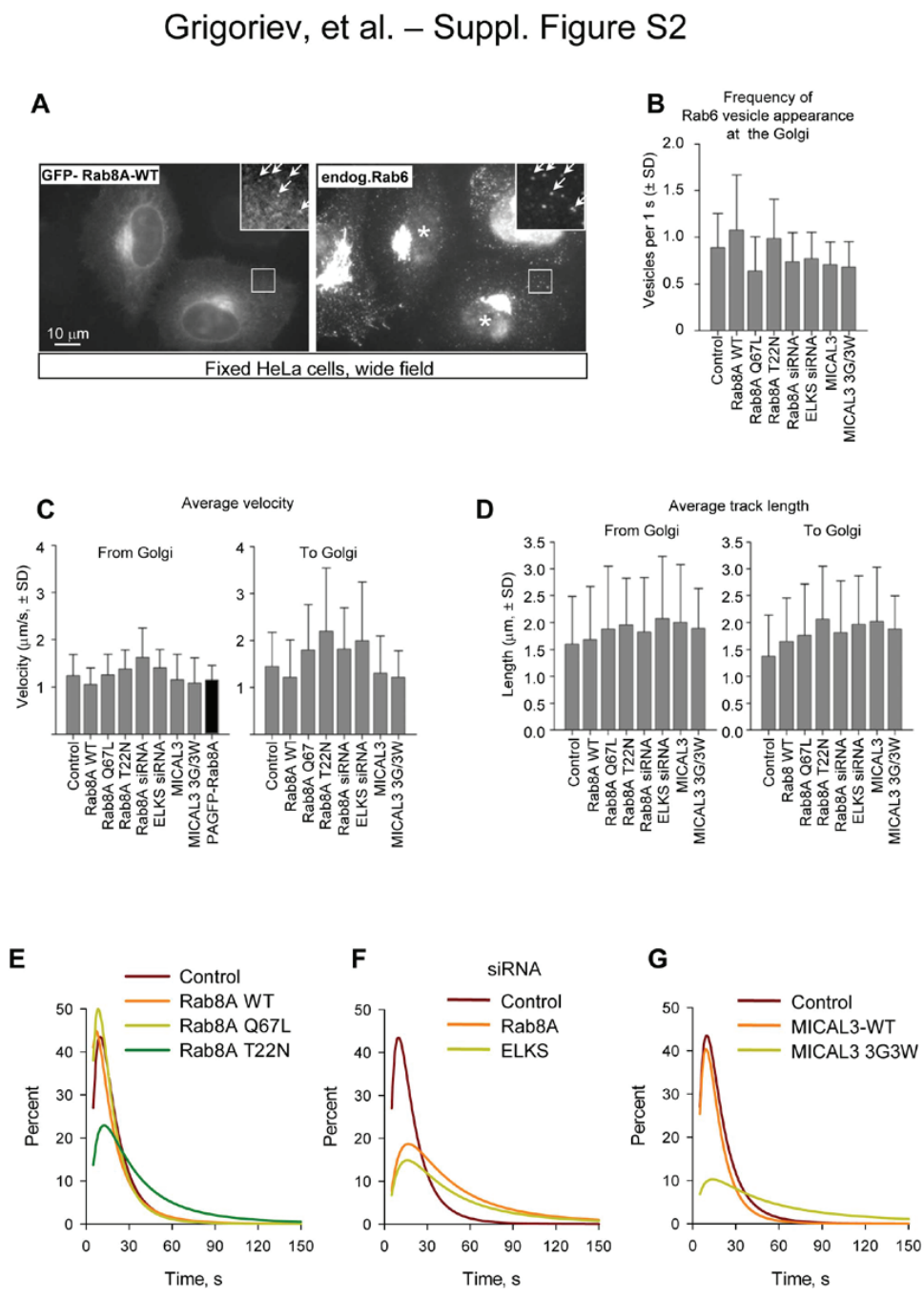
Grigoriev, et al. – Suppl. Figure S2
A
GFP- Rab8A-WT
endog.Rab6
10 μm
Fixed HeLa cells, wide field
B
Frequency of Rab6 vesicle appearance at the Golgi
Vesicles per 1 s (± SD)
Control
Rab8A WT
Rab8A Q67L
Rab8A T22N
Rab8A siRNA
ELKS siRNA
MICAL3
MICAL3 3G/3W
C
Average velocity
From Golgi
To Golgi
Velocity (μm/s, ± SD)
PAGFP-Rab8A
D
Average track length
From Golgi
To Golgi
Length (μm, ± SD)
E
Control
Rab8A WT
Rab8A Q67L
Rab8A T22N
Percent
Time, s
F
siRNA
Control
Rab8A
ELKS
G
Control
MICAL3-WT
MICAL3 3G3W

Grigoriev, et al. – Suppl. Figure S2

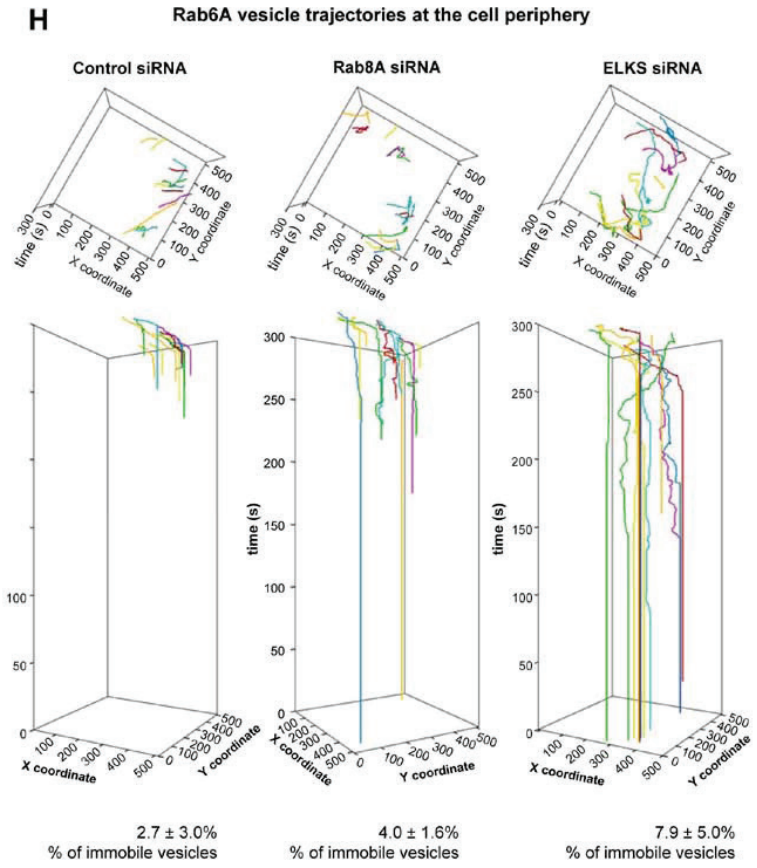

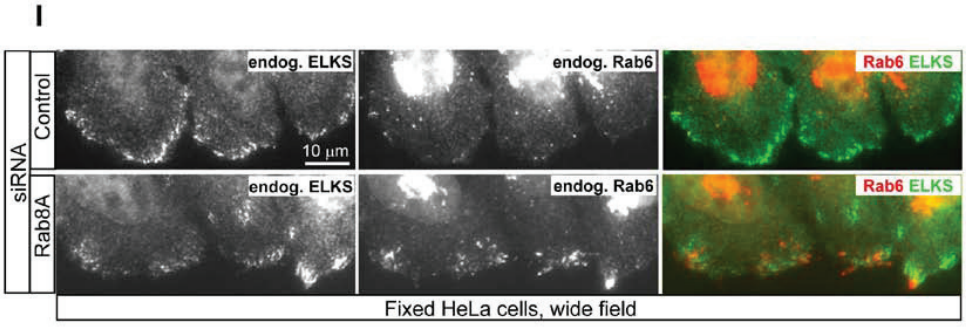

Figure S2. Behavior and localization of GFP-Rab6A vesicles after different treatments (Related to Figure 2)

(A) HeLa cells were transfected with Rab8A siRNA; two days later cells were transfected with GFP-Rab8A-WT; after one more day in culture cells were fixed and stained for endogenous Rab6. Insets show enlargements of the boxed areas. Individual vesicles positive for GFP-Rab8A and endogenous Rab6 are indicated by arrows.

(B–D) HeLa cells stably expressing GFP-Rab6A, transfected with the indicated fusion constructs or siRNAs were imaged using wide-field epi-fluorescence microscopy and the frequency of vesicle appearance at the Golgi (B), velocity of vesicle movement towards the cell periphery or to the cell center (C), and the lengths of movement tracks (D) were measured. Kymographs were used to measure the vesicle velocities, which were calculated as the tangent of the angle of the vesicle trajectory slope. For measurements of vesicle track length the same kymographs were used; tracks were defined as a part of the whole vesicle trajectory with a constant slope. The length of the track was measured as the sinus of the angle of the vesicle trajectory slope multiplied by the length of the measured segment. The left graph in panel (C) includes average velocity of movement of PAGFP-Rab8A vesicles after photoactivation (black bar). At least 50 vesicles in 10 cells were analyzed for each condition.

(E–G) Lognormal fits of distributions of the terminal pause duration times shown in Fig. 2H and 4D.

(H) Two-dimensional kymographs (X and Y displacements of vesicles over time shown on the Z-axis), illustrating the behavior of individual GFP-Rab6A vesicles (shown by different colors) at the cell periphery in cells transfected with the control, Rab8A or ELKS siRNAs. Straight vertical lines represent the terminal pauses between vesicle docking and fusion. Percentage of vesicles that were immobile throughout the movie (300 s) is indicated.

(I) HeLa cells were transfected with the indicated siRNAs, fixed three days later and stained for endogenous Rab6 and ELKS.

Grigoriev, et al. – Suppl. Figure S3

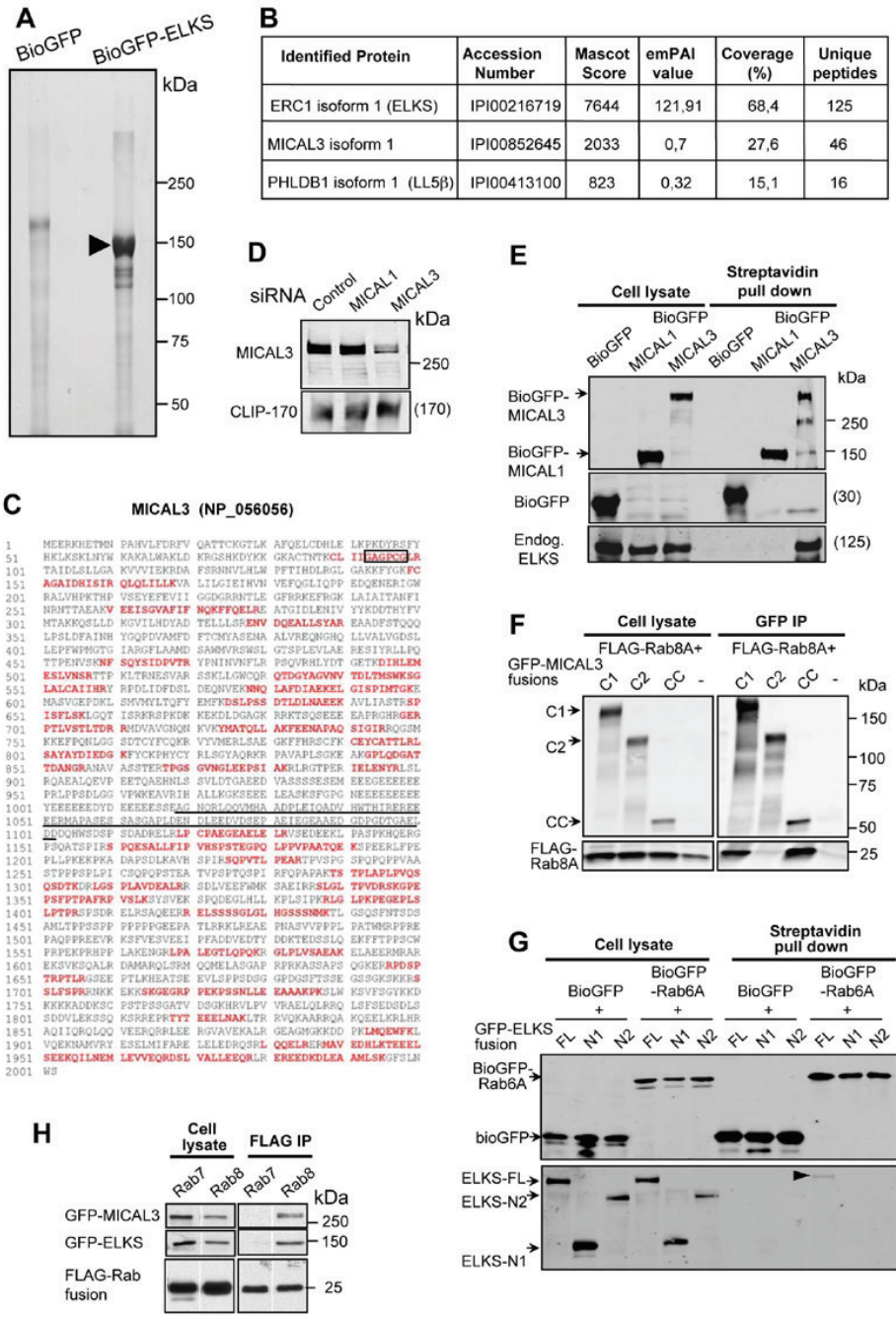

Identified Protein	Accession Number	Mascot Score	emPAI value	Coverage (%)	Unique peptides
ERC1 isoform 1 (ELKS)	IPI00216719	7644	121,91	68,4	125
MICAL3 isoform 1	IPI00852645	2033	0,7	27,6	46
PHLDB1 isoform 1 (LL5β)	IPI00413100	823	0,32	15,1	16

Figure S3. Identification of MICAL3 as a binding partner of ELKS (Related to Figure 3)

(A) Streptavidin pull down assay from HeLa cells expressing BioGFP or BioGFP-ELKS together with BirA. Proteins were analyzed by a Coomassie-stained SDS-PAGE. BioGFP-ELKS is indicated by an arrowhead.

(B) Mass spectrometry-based identification of MICAL3 in BioGFP-ELKS pull down. The values for the known partner of ELKS, LL5β, are shown for comparison.

(C) Sequence of MICAL3 with the peptides identified by mass spectrometry indicated in red. The polypeptide sequence present in the sequence NP_056056 but absent from the sequence BAG10388 (the full length MICAL3 isoform used in this study) is underlined. Note that no peptides corresponding to this sequence were recovered.

(D) Extracts of HeLa cells transfected with the indicated siRNAs were analyzed by Western blotting with the indicated antibodies three days after transfection. CLIP-170 was used as a loading control.

(E) Streptavidin pull down assays from extracts of HEK293T co-expressing BirA, BioGFP or bioGFP-MICAL1 or MICAL3. Western blotting was performed with antibodies against GFP or ELKS C-terminus. Calculated molecular mass is indicated in parentheses in cases where it is not possible to show the marker position.

(F and H) IPs from HEK293T cells coexpressing the indicated constructs using anti-GFP (F) or anti-FLAG (H) antibodies. Western blotting was performed with antibodies against GFP or FLAG tag. In panel F, 6% of the input and 40% of the precipitate were loaded on gel. In panel H, 6% of the input was loaded on gel; 40% of the precipitate was analysed with anti-GFP antibodies and 20% with anti-FLAG antibodies.

(G) Streptavidin pull down assays from extracts of HEK293T co-expressing BirA, BioGFP or bioGFP-Rab6A. Western blotting was performed with antibodies against GFP or ELKS N-terminus. 2% of the input and 20% of the precipitate was loaded on gel.

Grigoriev, et al. – Suppl. Figure S4

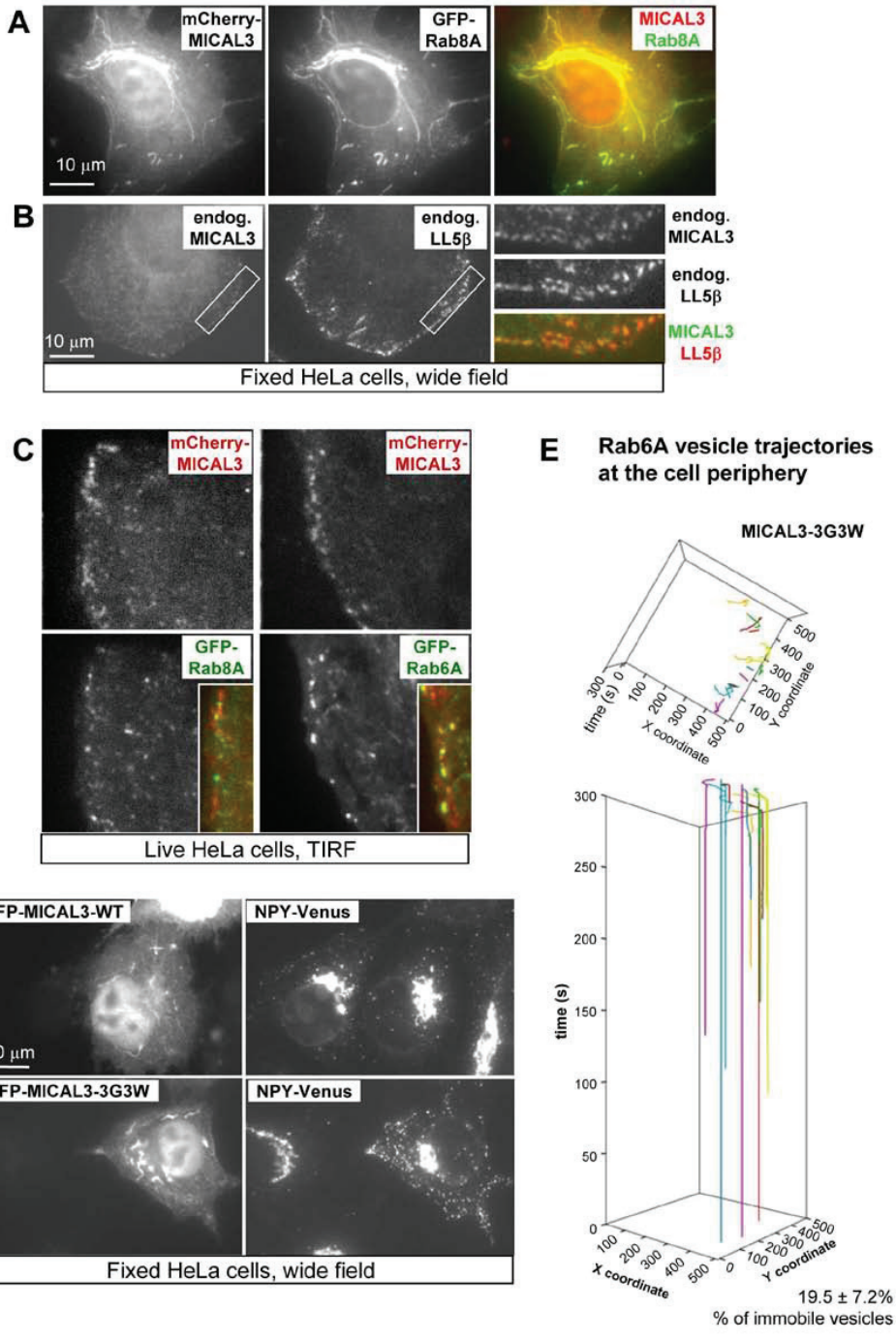

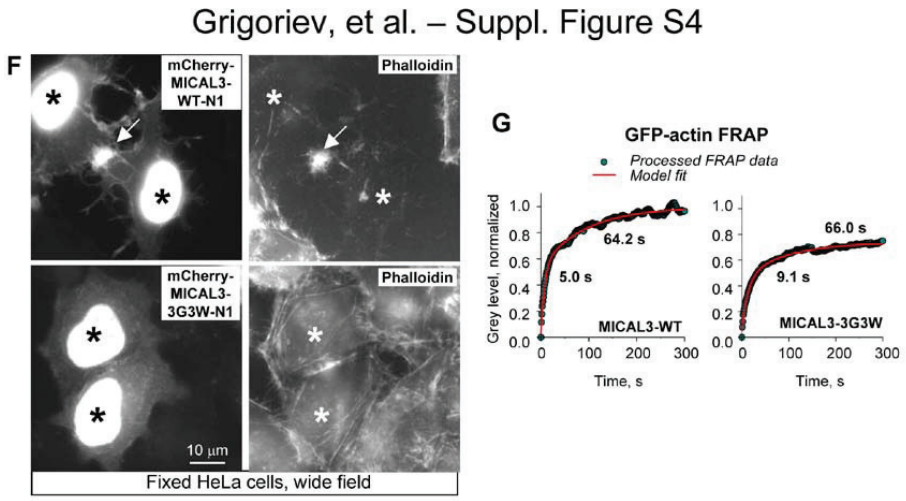

Figure S4. Localization of MICAL3 in HeLa cells, and the effect of MICAL3 mutants on secretory vesicles and the actin cytoskeleton (Related to Figure 4)

(A) HeLa cells were transiently transfected with the indicated fluorescent fusions, fixed one day later with paraformaldehyde and imaged using wide-field fluorescence microscopy.

(B) HeLa cells were fixed with methanol and stained with the indicated antibodies. Panels on the right show enlargements of the boxed areas.

(C) Analysis of colocalization of mCherry-MICAL3 with the indicated GFP fusions at low expression levels in live HeLa cells using TIRFM. Insets show overlays of the two channels, with GFP signal in green and mCherry in red.

(D) HeLa cells, stably expressing NPY-Venus were transiently transfected with the indicated GFP-MICAL3 fusions, fixed one day later with paraformaldehyde and imaged directly.

(E) Two-dimensional kymographs (X and Y displacements of vesicles over time shown on the Z-axis), illustrating the behavior of individual GFP-Rab6A vesicles (shown by different colors) at the cell periphery in a cell transfected with mCherry-MICAL3-3G3W. Straight vertical lines represent the terminal pauses between vesicle docking and fusion. Percentage of vesicles that were immobile throughout the movie (300 s) is indicated.

(F) HeLa cells were transiently transfected with the indicated mCherry-MICAL3 fusions, fixed one day with paraformaldehyde and stained with fluorescently labeled

phalloidin. Transfected cells are indicated with asterisks. The arrow indicates the residual actin staining at the midbody region. mCherry-MICAL3-N1 caused strong loss of filamentous actin, while the same MICAL3 fragment bearing an inactive monooxygenase domain does not have such an effect.

(G) HeLa cells were transiently transfected with GFP-actin and mCherry-MICAL3-WT or mCherry-MICAL3-3G3W, and GFP-actin turnover was analyzed by FRAP. The plots show processed FRAP data (green dots) and their fitting to a two-exponential model (red lines); see Experimental Procedures and Table S1 for details. The recovery halftimes for the two components are indicated.

Table S1. Analysis of the FRAP data

Percentage and recovery halftime for each protein population were determined by fitting of a two-component model to FRAP curves. Halftime of fluorescence recovery $t_{1/2}$, 95% confidence interval (95% conf. int.) for each $t_{1/2}$ and percentage of each protein population are indicated.

FRAP analysis of GFP-MICAL3 turnover						
	1st component			**2nd component**		
	$t_{1/2}$ [s]	95% conf. int. [s]	Amount [%]	$t_{1/2}$ [s]	95% conf. int. [s]	Amount [%]
MICAL3	5.9 s	(5.1, 6.9)	63	53.3 s	(46.2, 63.0)	37
MICAL3-3G3W	49.5 s	(40.8, 63.0)	41	346.6 s	(231.0, 693.1)	59
FRAP analysis of GFP-actin turnover in cells expressing mCherry-MICAL3-WT or 3G3W						
	1st component			**2nd component**		
	$t_{1/2}$ [s]	95% conf. int. [s]	Amount [%]	$t_{1/2}$ [s]	95% conf. int. [s]	Amount [%]
GFP-actin + MICAL3-WT	5.0 s	(4.5, 5.6)	53	64.2 s	(59.8, 70.0)	47
GFP-actin + MICAL3-3G3W	9.1 s	(8.4, 10.1)	59	66.0 s	(58.7, 75.3)	41

Movie 1. Exit of Rab8A-positive vesicles from the Golgi (Related to Figure 1)
Cells were transfected with PAGFP-Rab8A and mCherry-GT (a Golgi marker). Red and green images were collected simultaneously using a Spinning Disk microscope equipped with a beam splitter, with 500 ms exposure and no delay between frames. A transfected cell was identified by mCherry fluorescence, and the Golgi area (indicated by a stippled line if Fig. 1F) was photoactivated using a 408 nm laser. The image series comprises 120 frames (20 frames before photo-activation and 100 frames after), covering a period of 60s. Images were processed in MetaMorph, Blur filter was applied. Frame rate: 15 frames/s.

Movie 2. Fusion of Rab8A/Rab6A double positive vesicles with the plasma membrane (Related to Figure 1)
Cells were transfected with PAGFP-Rab8A and mStrawberry-Rab6A. Red and green images were collected simultaneously using a TIRF microscope equipped with a beam splitter, with 100 ms exposure and no delay between frames. A transfected cell was identified by mStrawberry fluorescence. An area in the peripheral cytoplasm was photoactivated using 407 nm laser. The image series comprises 520 frames (20 frames before photo-activation and 500 frames after), covering a period of 52s. Images were processed in MetaMorph. Frame rate: 15 frames/s. One exocytosis event is indicated by an arrow.

EXPERIMENTAL PROCEDURES

Cell culture, transfection of plasmids and siRNAs, and flow cytometry-based secretion assays

HeLa, HEK293T, MRC5-SV and hTert-RPE1 cells (Clontech) were maintained as described previously [1]. PolyFect (Qiagen), Lipofectamine 2000 (Invitrogen) or FuGENE 6 (Roche) were used for plasmid transfection. The stable GFP-Rab6A and NPY-Venus HeLa lines [2] were cultured in the presence of 0.4 mg/ml G418 (Roche).

siRNAs were synthesized by Ambion; the target sequences of control, Rab6A and ELKS siRNAs were described previously [2]. Rab8A siRNA corresponded to the target sequence GGAAAGCACAAATGAAGGA. MICAL3 was knocked down using ON-TARGETplus SMARTpool L-024432 (Dharmacon). Cells were transfected with 5 nM siRNAs using HiPerFect (Qiagen) and analyzed 3 days after transfection.

The stable C1 HeLa cell line expressing SS-GFP-FM4-FCS-hGH [3] construct was a gift of A. Peden (University of Cambridge, UK). It was cultured in the presence of 1.66 μg/ml puromycin. Flow cytometry-based secretion assay was performed essentially as described previously [3] using a FACS Scan equipped with a 488nm laser (BD). Secretion was induced by adding to the culture medium 1 μM AP21998 (Ariad Pharmaceuticals, http://www.ariad.com). At least 9.000 live cells were analyzed in 4 independent samples for each condition.

Expression constructs

We used the following previously described expression vectors: GFP-Rab6A [4], mStrawberry-Rab6A, the rescue constructs GFP-ELKSε (designated GFP-ELKS in this paper) and GFP-ELKS-N2 (designated previously GFP-ELKSε-ΔC) [2], NPY-Venus [5] (a gift of Dr. A. Miyawaki, RIKEN, Wako City, Japan), BirA [1], GFP-Rab8-WT, Q67L and T22N [6] (a gift of Dr. I. Mellman, Yale University, New Haven, USA), mCherry-GT) [7] (a gift of Dr. I. Kaverina, Vanderbilt University, Nashville, USA) and pEF-BOS-FLAG-Rab7 [8]. pEF-BOS-FLAGRab8A was generated by PCR from pGEX-Rab6A [9] and pEGFP-Rab8A [10]. Biotinylation and GFP-tagged ELKS (isoform ELKSε) was generated from GFP- ELKSε by cloning in front of the GFP a linker encoding the amino acid sequence MASGLNDIFEAQKIEWHEGGG. GFP-ELKS-N1 rescue plasmid was generated from the full-length rescue construct GFP-ELKSε by digesting the plasmid with EcoRV and NotI, blunting the ends and religating it. PAGFP, mCherry and

mStrawberry fusions of Rab8A and ELKS were generated by substituting the GFP open reading frame in the fusion proteins for PAGFP [11] (a gift of J. Lippincott-Schwartz, NIH. Bethesda, USA), mCherry or mStrawberry [12] (a gift of R. Tsien, University of California, San Diego, USA). GFP- or mCherry-MICAL3 were generated from human cDNA clone, pF1KA0819 [13] using a modified pEGFP-C1 vector. The MICAL3-3G3W mutant constructs were generated from GFP- or mCherry-MICAL3 by a PCR-based strategy. GFP-MICAL3-C1 was a gift of A. Barnekow (University of Muenster, Germany). Other MICAL3 deletion mutants were derived from GFP-MICAL3-C1 using a PCR-based strategy and subcloned into pEGFP-C1. GST-tagged MICAL1-CC (amino acids 902-1048 of NP_612188, derived by RT-PCR from mouse cDNA) and MICAL3-CC (Fig. 3B, derived by PCR from GFP-MICAL3-C1) were inserted into pGEX4T-1 vector.

GST and streptavidin pull down assays

Constructs encoding GST fusions were transformed in BL21 and Rosetta *E. coli*, induced with 0.5 mM IPTG and purified using Glutathione Sepharose 4B beads (GE Healthcare) according to the protocol of the manufacturer. HEK293T cells were co-transfected with GFP-fusion constructs using 1 mg/ml Polyethylenimine (PEI; Polysciences) for 36 hrs. Cells were pelleted and lysed in ice-cold lysis buffer (50 mM HEPES, pH 7.5, 150 mM KCl, 1% Triton X-100) supplemented with protease inhibitors (Complete, Roche). Soluble fraction of the whole cell lysate was obtained by centrifuging the whole cell lysate at 16,000 × *g* for 10 min; it was then incubated with GST fusion proteins on Glutathione Sepharose 4B beads, washed five times in the ice-cold wash buffer, containing 50 mM HEPES, pH 7.5, 150 mM KCl, 0.5% Triton X-100, and analyzed by Western blotting.

For streptavidin pull down assays, BioGFP-fusion constructs together with a plasmid encoding BirA were co-transfected into HEK293T cells using PEI. Transfected cells were harvested in phosphate-buffered saline (PBS), lysed in 50 mM HEPES, pH 7.5, 150 mM KCl, 1% Triton X-100 with protease inhibitors (Complete, Roche). The soluble fraction was collected by centrifugation at 16,000 × *g* for 10 min and incubated with Dynabeads M-280 Streptavidin (Invitrogen) for 2 hrs at 4 ºC. Dynabeads were washed five times with ice-cold lysis buffer and analyzed by Coomassie staining or Western blotting.

Immunoprecipitation (IP)

For the IP of endogenous proteins, purified polyclonal antibodies against MICAL1 and MICAL3 and control IgG were coupled to Affi-Prep protein A beads (Biorad) for 1 hour at room temperature, washed three times in 0.2 M sodium borate, pH 9.0 and crosslinked with Dimethylpimelimidate [14]. HeLa cells were pelleted and lysed in 50 mM Tris, pH 8.0, 250 mM NaCl, 1% Triton X-100 with protease inhibitors (Complete, Roche). Soluble fraction of the lysate was incubated with the antibody-coupled protein A beads for 4 hrs at 4 ºC. The beads were washed for 5 times with ice-cold wash buffer (50 mM Tris pH 8.0, 125 mM NaCl, 0.25% Triton X-100) and analyzed by Western blotting.

For detection of the complex of Rab8A, MICAL3, ELKS, we cotransfected HEK293T cells with combinations of pEF-BOS-FLAG-Rab8A or pEF-BOS-FLAG-Rab7, GFP-ELKS and GFP-MICAL3 constructs. After 20 hr, the cells were solubilized in 20 mM HEPES pH 7.5, 100 mM NaCl, 1% Triton X-100 and 20 μM GMP-PNP (lysis buffer). Lysates were centrifuged for 10 min at 16,000 × *g* in a cooled microfuge and supernatants were incubated with washed FLAG M2 agarose beads for 1 hr at 4 °C under continuous agitation. Beads were subsequently washed four times with the lysis buffer. Anti-GFP IPs were performed using the same protocol. Protein complexes were analyzed by Western blotting.

Antibodies, immunofluorescent staining, immunoprecipitation, and Western blotting

Rabbit polyclonal antibodies against MICAL1 and MICAL3 were raised against GST-MICAL1/3-CC by Absea (Bejing, China). BioGFP-MICAL1/3 fusions immobilized on Dynabeads and washed with the high-salt buffer containing 50 mM HEPES pH 7.5, 500 mM KCl, 1% Triton X-100. Antibodies against MICAL1 and MICAL3 were then incubated with the BioGFP-mMICAL1/3-coupled Dynabeads for 2 hrs at 4 ºC, washed 5 times with PBS, and antibodies were eluted with 0.1 M glycine, pH 2.4.

Further, we used rabbit polyclonal antibodies against ELKS (a gift of Dr. F. Melchior, Heidelberg University, Germany) and Rab8A [15], mouse monoclonal antibodies against Rab8A (BD Biosciences), Rab6 (which recognizes Rab6A and Rab6A', a gift of A. Barnekow, University of Muenster, Germany), FLAG and β-tubulin (Sigma), actin (Chemicon) and LL5β [16] (a gift of Dr. J. Sanes, Harvard University, Cambridge, USA). Secondary goat antibodies against rabbit, rat and mouse IgG, conjugated to Alexa 350, Alexa 488 and Alexa 594, and the Alexa 488-

conjugated phalloidin were purchased from Invitrogen. Fresh medium was added to cells ~1-2 h before fixation. For vesicle visualization, cells were fixed with 4% paraformaldehyde in PBS for 15 min at room temperature. For staining endogenous MICAL3 and LL5β, cells were fixed with methanol at -20ºC for 10 min. Staining procedures were described previously [4].

Western blotting was performed as described previously using alkaline phosphatase-conjugated goat anti-mouse or anti-rabbit antibodies (Sigma) [1] or IRDye 800CW goat anti-rabbit and anti-mouse antibodies, which were detected using Odyssey Infrared Imaging system (Li-Cor Biosciences).

Fluorescence microscopy

Images of fixed cells were collected with a Leica DMRBE microscope equipped with a PL Fluotar 100x 1.3 N.A. oil objective, FITC/EGFP filter 41012 (Chroma) and Texas Red filter 41004 (Chroma) and an ORCA-ER-1394 CCD camera (Hamamatsu). 12-bit images were projected onto the CCD chip at a magnification of 0.1 μm/pixel.

For live cell imaging we used Nikon Eclipse Ti-E inverted microscope with perfect focus system (PFS), equipped with CFI Apo TIRF 100x 1.49 N.A. oil objective (Nikon), a TI-TIRF-E motorized TIRF illuminator (Nikon), QuantEM 512SC EMCCD camera (Photometrics, Roper Scientific). The system was controlled with MetaMorph 7.5 software (Molecular Devices). For excitation we used either mercury lamp HBO-100W/2 (Osram) or 491nm 50mW Calypso (Cobolt) and 561nm 50mW Jive (Cobolt) lasers (for regular wide-field epi-fluorescence and for TIRF, respectively). For simultaneous imaging of green and red fluorescent signals we used the ET-mCherry/GFP filter set (59022, Chroma) together with DV2 beam splitter (MAG Biosystems, Roper) equipped with dichroic filter 565dcxr (Chroma) and HQ530/30m emission filter (Chroma). To keep cells at 37 °C we used a stage top incubator (model INUG2E-ZILCS, Tokai Hit). 16-bit images were projected onto the CCD chip at a magnification of 0.065 μm/pixel with intermediate magnification 2.5X (Nikon C mount adapter 2.5X). FRAP assay was carried out using FRAP scanning system I-Las/I-Launch (Roper Scientific France/ PICT-IBiSA, Institut Curie) using the same lasers as described above**.**

For spinning disc confocal microscopy we used an almost identical microscope setup based on Nikon Ti-E, which was equipped with CFI Apo TIRF

100x 1.49 N.A. oil objective (Nikon), Yokogawa motorized CSU-X1-A1 confocal head and a custom ordered TI-FL epi-fluorescent double illuminator (Nikon, MEY10021) for the attachment of the FRAP scanning system I-Las/I-Launch (Roper Scientific France/ PICT-IBiSA, Institut Curie), which was used for photo-activation of PAGFP. Photoactivation was performed using a 44 mW 408 nm laser (model 56 RCS 001/HV, Melles Griot). For simultaneous excitation of PAGFP and mStrawberry we used 491nm 50mW Calypso (Cobolt) and 561nm 50mW Jive (Cobolt) lasers together with DV2 beam splitter (MAG Biosystems, Roper) equipped with dichroic filter 565dcxr (Chroma) and HQ630/50m emission filter (Chroma). To keep cells at 37 °C we used a stage top incubator (model INUG2E-ZILCS, Tokai Hit). The 16-bit images were projected onto the CCD chip with intermediate lens 2.0X (Edmund Optics) at a magnification of 0.068 μm/pixel.

Imaging of exocytotic events with PAGFP-Rab8A was performed on the upgraded inverted research microscope Nikon Eclipse TE2000E (Nikon) with a CFI Apo TIRF 100x 1.49 N.A. oil objective (Nikon), described earlier [2]. It was equipped with Evolve 512 EMCCD camera (Photometrics, Roper) and controlled by MetaMorph 7.7 software (Molecular Devices). For photoactivation of PAGFP we used the FRAP scanning system FRAP L5 D – CURIE (Roper Scientific France/ PICT-IBiSA, Institut Curie) and 47 mW 407 nm laser (model 561CS/2695, Melles Griot). For simultaneous excitation of PAGFP and mStrawberry we used 113 mW 488nm laser line of argon laser (Spectra-Physics Lasers) and 11 mW 561nm diode-pumped solid-state laser (Melles Griot) and ET-mCherry/GFP filter set (59022, Chroma) together with DV2 beam splitter (MAG Biosystems, Roper) equipped with dichroic filter 565dcxr (Chroma) and HQ530/30m emission filter (Chroma). The 16-bit images were projected onto the CCD chip with intermediate lens 2.5X (Nikon C mount adapter 2.5X) at a magnification of 0.067 μm/pixel.

Image analysis

Images of fixed samples were prepared using Adobe Photoshop by converting them to 8 bit and linear adjustment of “Levels”; Unsharp Mask and Gaussian Blur filtering sometimes was used. Images of live cells were prepared in MetaMorph software (Molecular Devices) and Adobe Photoshop. Frame averaging (each 5 frames; self-written algorithm) and color overlay (build-in option) was done in MetaMorph; linear

adjustment of "Levels" and using Unsharp Mask and Gaussian Blur filtering sometimes was used in Adobe Photoshop.

To quantify co-localization of Rab proteins on the vesicles, we counted all vesicles in lamella labeled with the green marker, all vesicles in the same area labeled with the red marker and all vesicles in the same area labeled with both markers. The percentage of green and red double-positive vesicles compared to the total number of green and red vesicles was calculated.

Statistical analysis was performed using non-parametric Mann-Whitney U-test in Statistica for Windows and SigmaPlot.

Acquisition and processing of FRAP data

To measure the turnover of mStrawberry-Rab8A on the moving exocytotic vesicles labelled with GFP-Rab6A, we performed single vesicle FRAP assay. We used the 561 nm laser line in order to specifically bleach the red fluorescent marker without affecting the green marker. Stream acquisition (10 fps, 100 ms exposure time with no delay between frames) was performed using the DV2 beam splitter for simultaneous imaging of green and red markers. Photobleaching was performed during acquisition by a mouse click at the position of the mouse cursor ("FRAP-on-Fly" option of I-Las/I-Launch FRAP scanning system (Roper Scientific France/ PICT-IBiSA, Institut Curie). The diameter of the laser beam on the image plane was approximately 1.0 μm. To quantify the fluorescence recovery we plotted a kymograph along the vesicle path before and after photobleaching using MetaMorph software. First, we traced the GFP-Rab6A trajectory on the kymograph using "Trace Line" tool (MetaMorph) and then transferred this traced line into mStrawberry-Rab8A kymograph and measured the intensities along the track of the vesicle in the kymograph using the Linescan option of the MetaMorph. The intensities along both lines (GFP-Rab6A and mStrawberry-Rab8A) were transferred to SigmaPlot software. To be able to average the data from the different cells we corrected the intensities along each vesicle path for the surrounding background intensities. All data points corresponding to laser pulses during photobleaching were deleted. Finally, we normalized the intensity of each vesicle to the average of 20 data points before laser pulse and averaged the data (GFP-Rab6A and mStrawberry-Rab8A channels) for all vesicles.

To study the turnover of GFP-MICAL3, we used a fixed position region of interest (ROI) of the size of ~100 μm^2. We used the same I-Las/I-Launch FRAP

scanning system (Roper Scientific France/ PICT-IBiSA, Institut Curie) as described above. We acquired 6 frames before photobleaching (500 ms exposure, 10 s between frames), photobleached the ROI (300 ms duration, 491nm laser line), and then performed time-lapse imaging of 60-90 frames after photobleaching (500 ms exposure, 10 s between frames). Fluorescence intensities in the ROI outlining the cortical patches in the bleached area and non-bleached area were transferred to SigmaPlot software. To study the actin turnover in presence of MICAL3-WT or MICAL3-3G3W we used the same approach as for the turnover of MICAL3-WT but with different time sampling: we performed time-lapse imaging of 6 frames before photobleaching (500 ms exposure, 1 s between frames), then photobleached the ROI (300 ms duration, 491nm laser line), and then carried out time-lapse imaging of 300 frames after photobleaching (500 ms exposure, 1 s between frames).

FRAP data for GFP-MICAL3 and GFP-actin were first preprocessed using the double normalization [17], which involves normalization of the recovery signal to the average prebleach signal and, at the same time, takes into account the loss of total signal due to the bleaching during subsequent imaging. A two-exponential model was fitted to the preprocessed data using a custom made routines written within the MatLab programming environment (The MathWorks, Natick, MA). The nonlinear regression was performed using nlinfit function. The confidence intervals were estimated using the MatLab's nlparci function. Fitting a simpler, one-exponential model and performing *F*-test for comparing two statistical models resulted in rejecting the null hypothesis (p-values $<< 0.05$) in favor of the alternative one, meaning that the FRAP data are better explained using the two-exponential model. Fitting more complicated three-exponential models did not produce a better fit, justifying the assumed two-exponential model.

Mass spectrometry

1D SDS-PAGE gel lanes were cut into 2-mm slices using an automatic gel slicer and subjected to in-gel reduction with dithiothreitol, alkylation with iodoacetamide and digestion with trypsin (Promega, sequencing grade), essentially as described by [18]. Nanoflow LC-MS/MS was performed on an 1100 series capillary LC system (Agilent Technologies) coupled to either an LTQ-Orbitrap mass spectrometer (Thermo) both operating in positive mode and equipped with a nanospray source. Peptide mixtures were trapped on a ReproSil C18 reversed phase column (Dr Maisch GmbH; column

dimensions 1.5 cm × 100 µm, packed in-house) at a flow rate of 8 µl/min. Peptide separation was performed on another ReproSil C18 reversed phase column (column dimensions 15 cm × 50 µm, packed in-house) using a linear gradient from 0 to 80% B (A = 0.1 % formic acid; B = 80% (v/v) acetonitrile, 0.1 % formic acid) in 70 min and at a constant flow rate of 200 nl/min using a splitter. The column eluent was directly sprayed into the ESI source of the mass spectrometer. Mass spectra were acquired in continuum mode; fragmentation of the peptides was performed in data-dependent mode. Peak lists were automatically created from raw data files using the Mascot Distiller software (version 2.1; MatrixScience). The Mascot search algorithm (version 2.2, MatrixScience) was used for searching against the IPI database (release IPI_human_20090729.fasta). The peptide tolerance was set to 10 ppm and the fragment ion tolerance was set to 0.8 Da. A maximum number of 2 missed cleavages by trypsin were allowed and carbamidomethylated cysteine and oxidized methionine were set as fixed and variable modifications, respectively. The Mascot score cut-off value for a positive protein hit was set to 60. Individual peptide MS/MS spectra with Mascot scores below 40 were checked manually and either interpreted as valid identifications or discarded. Proteins present in the negative controls (pull down assays with bioGFP alone) were regarded as background.

SUPPLEMENTAL REFERENCES

1. Lansbergen, G., Grigoriev, I., Mimori-Kiyosue, Y., Ohtsuka, T., Higa, S., Kitajima, I., Demmers, J., Galjart, N., Houtsmuller, A.B., Grosveld, F., and Akhmanova, A. (2006). CLASPs attach microtubule plus ends to the cell cortex through a complex with LL5beta. Dev Cell *11*, 21-32.

2. Grigoriev, I., Splinter, D., Keijzer, N., Wulf, P.S., Demmers, J., Ohtsuka, T., Modesti, M., Maly, I.V., Grosveld, F., Hoogenraad, C.C., and Akhmanova, A. (2007). Rab6 regulates transport and targeting of exocytotic carriers. Dev Cell *13*, 305-314.

3. Gordon, D.E., Bond, L.M., Sahlender, D.A., and Peden, A.A. (2010). A targeted siRNA screen to identify SNAREs required for constitutive secretion in mammalian cells. Traffic *11*, 1191-1204.

4. Matanis, T., Akhmanova, A., Wulf, P., Del Nery, E., Weide, T., Stepanova, T., Galjart, N., Grosveld, F., Goud, B., De Zeeuw, C.I., Barnekow, A., and Hoogenraad, C.C. (2002). Bicaudal-D regulates COPI-independent Golgi-ER transport by recruiting the dynein-dynactin motor complex. Nat Cell Biol *4*, 986-992.

5. Nagai, T., Ibata, K., Park, E.S., Kubota, M., Mikoshiba, K., and Miyawaki, A. (2002). A variant of yellow fluorescent protein with fast and efficient maturation for cell-biological applications. Nat Biotechnol *20*, 87-90.

6. Ang, A.L., Folsch, H., Koivisto, U.M., Pypaert, M., and Mellman, I. (2003). The Rab8 GTPase selectively regulates AP-1B-dependent basolateral transport in polarized Madin-Darby canine kidney cells. J Cell Biol *163*, 339-350.

7. Efimov, A., Kharitonov, A., Efimova, N., Loncarek, J., Miller, P.M., Andreyeva, N., Gleeson, P., Galjart, N., Maia, A.R., McLeod, I.X., Yates, J.R., 3rd, Maiato, H., Khodjakov, A., Akhmanova, A., and Kaverina, I. (2007). Asymmetric CLASP-dependent nucleation of noncentrosomal microtubules at the trans-Golgi network. Dev Cell *12*, 917-930.

8. Rojas, R., van Vlijmen, T., Mardones, G.A., Prabhu, Y., Rojas, A.L., Mohammed, S., Heck, A.J., Raposo, G., van der Sluijs, P., and Bonifacino, J.S. (2008). Regulation of retromer recruitment to endosomes by sequential action of Rab5 and Rab7. J Cell Biol *183*, 513-526.

9. Echard, A., Opdam, F.J., de Leeuw, H.J., Jollivet, F., Savelkoul, P., Hendriks, W., Voorberg, J., Goud, B., and Fransen, J.A. (2000). Alternative splicing of the human Rab6A gene generates two close but functionally different isoforms. Mol Biol Cell *11*, 3819-3833.

10. Linder, M.D., Uronen, R.L., Holtta-Vuori, M., van der Sluijs, P., Peranen, J., and Ikonen, E. (2007). Rab8-dependent recycling promotes endosomal cholesterol removal in normal and sphingolipidosis cells. Mol Biol Cell *18*, 47-56.

11. Patterson, G.H., and Lippincott-Schwartz, J. (2002). A photoactivatable GFP for selective photolabeling of proteins and cells. Science *297*, 1873-1877.

12. Shaner, N.C., Campbell, R.E., Steinbach, P.A., Giepmans, B.N., Palmer, A.E., and Tsien, R.Y. (2004). Improved monomeric red, orange and yellow fluorescent proteins derived from Discosoma sp. red fluorescent protein. Nat Biotechnol *22*, 1567-1572.

13. Nagase, T., Yamakawa, H., Tadokoro, S., Nakajima, D., Inoue, S., Yamaguchi, K., Itokawa, Y., Kikuno, R.F., Koga, H., and Ohara, O. (2008). Exploration of human ORFeome: high-throughput preparation of ORF clones and efficient characterization of their protein products. DNA Res *15*, 137-149.

14. Cheeseman, I.M., and Desai, A. (2005). A combined approach for the localization and tandem affinity purification of protein complexes from metazoans. Sci STKE *2005*, pl1.

15. Peranen, J., Auvinen, P., Virta, H., Wepf, R., and Simons, K. (1996). Rab8 promotes polarized membrane transport through reorganization of actin and microtubules in fibroblasts. J Cell Biol *135*, 153-167.

16. Kishi, M., Kummer, T.T., Eglen, S.J., and Sanes, J.R. (2005). LL5beta: a regulator of postsynaptic differentiation identified in a screen for synaptically enriched transcripts at the neuromuscular junction. J Cell Biol *169*, 355-366.

17. Phair, R.D., and Misteli, T. (2000). High mobility of proteins in the mammalian cell nucleus. Nature *404*, 604-609.

18. Wilm, M., Shevchenko, A., Houthaeve, T., Breit, S., Schweigerer, L., Fotsis, T., and Mann, M. (1996). Femtomole sequencing of proteins from polyacrylamide gels by nano-electrospray mass spectrometry. Nature *379*, 466-469.

Chapter 5

Characterization of MICAL proteins and their interacting partners

Ka Lou Yu[1], Qingyang Liu [1], Shasha Hua [1], Kai Jiang [1],
Jeroen Demmers[2], Eljo Y. van Battum[3],
Jeroen Pasterkamp [3], Anna Akhmanova[1]

A part of this chapter was published in:

Van Battum, E.Y., R.A. Gunput, S. Lemstra, E.J. Groen, K.L. Yu, Y. Adolfs, Y. Zhou, C.C. Hoogenraad, Y. Yoshida, M. Schachner, A. Akhmanova, and R.J. Pasterkamp. 2014. The intracellular redox protein MICAL-1 regulates the development of hippocampal mossy fibre connections. Nat Commun. 5:4317.

[1] Cell Biology, Faculty of Science, Utrecht University, Padualaan 8, 3584 CH Utrecht, The Netherlands
[2] Proteomics Center, Erasmus Medical Center, PO Box 2040, 3000 CA Rotterdam, The Netherlands
[3] Department of Neuroscience and Pharmacology, Rudolf Magnus Institute of Neuroscience, University Medical Center Utrecht, Utrecht, The Netherlands.

Abstract

MICALs are large multidomain monooxygenase enzymes that can catalyze oxidation of specific actin residues and lead to actin disassembly. In *Drosophila*, Mical is encoded by a single gene and is important for motor axon guidance and other actin-dependent morphogenetic processes. In mammals, there are three Mical homologues, MICAL-1, MICAL-2 and MICAL-3, which can also regulate the behavior and organization of the actin cytoskeleton, but their biological functions are not yet clear. Here, we used a knockout cell model to show that MICAL-1 contributes to the organization of filamentous actin and affects the distribution of exocytotic vesicles. These results help to explain the neurodevelopmental phenotypes of the *MICAL-1* knockout mouse. We also addressed the function of MICAL-3 by searching for its binding partners, and identified the components of the centralspindlin complex. We demonstrate that MICAL-3 localizes to the central spindle and the midbody, indicating that it has a potential role in the regulation of cytokinesis.

Introduction

MICALs represent an evolutionary conserved family of signaling proteins, which regulate cytoskeletal organization and trafficking. The mammalian MICAL-1 (molecule interacting with CasL) derives its name from its association with CasL (a homologue of the signaling adaptor protein p130Cas), to the SH3 domain of which MICAL-1 binds through its proline-rich region (Suzuki et al., 2002). The distinguishing property of the MICAL proteins is the presence of an N-terminal flavoprotein monooxynase domain, which is related to bacterial flavin adenine dinucleotide (FAD)-containing aromatic monooxynases, such as the *p*-hydroxybenzoate hydroxylase (PHBH), which oxidates small molecules (Giridharan and Caplan, 2014; Hung and Terman, 2011; Vanoni et al., 2013; Zhou et al., 2011b). In addition, MICALs possess a calponin homology (CH) domain, a Lin11, Isl-1 and Mec-3 (LIM) domain and a C-terminal coiled-coil region.

Important insights into the function of MICAL family proteins were initially obtained using fruit flies as a model system. The single *Drosophila* homologue, Mical, was identified as an important player mediating the remodeling of the actin cytoskeleton downstream of plexin, a receptor activated by axon repulsion signaling factors semaphorins (Terman et al., 2002). Other indications that Mical is an actin regulator in flies were provided by finding a role of this protein in the control of myofilament organization and synaptic structure (Beuchle et al., 2007), dendritic pruning (Kirilly et al., 2009) and by the observation that Mical mutants have abnormally shaped bristles, hair-like protrusions, the morphology of which critically depends on actin dynamics (Hung and Terman, 2011; Hung et al., 2010). Biochemical analysis demonstrated that Mical can induce the disassembly of the actin filaments through specific oxidation of two methionine residues (Met44 and Met47) located at the pointed end of the actin monomer(Hung et al., 2011). One of them, Met44, was shown to be critical for the Mical-dependent actin regulation in vivo (Hung et al., 2011). Mical catalyzes methionine sulfoxidation using its FAD-binding monooxygenase domain and requires nicotinamide adenine dinucleotide phosphate (NADPH) as a cofactor. In this reaction, one atom of molecular oxygen is used to generate methionine sulfoxide, while the second one is reduced to water.

Exciting recent data showed that actin oxidation by the fly and mammalian Micals is reversible. The methionine sulfoxide reductase MsrB, which stereose-

lectively reduces one of the two diastereomers of methionine sulfoxide, Met-R-SO, can reverse the oxidative modification introduced by Mical, while the MsrA enzyme, specific for the other diastereomer, Met-S-SO, is unable to perform this reaction (Hung et al., 2013; Lee et al., 2013). This indicates that methionine sulfoxidation induced by Mical is also stereospecfic and thus a direct effect of the Mical activity on actin rather than a product of oxidation caused by reactive oxygen species (ROS) generated by Mical. These data further demonstrate that Mical is a part a redox system which acts similarly to other reversible post-translational modifications, such as phosphorylation.

Mammalian genomes contain three homologues of the fly Mical, MICAL-1, MICAL-2 and MICAL-3 (Pasterkamp et al., 2006; Suzuki et al., 2002; Terman et al., 2002). The function of these proteins is beginning to be understood. Similar to the fly Mical, the mammalian MICALs can also regulate the actin cytoskeleton in different settings (Giridharan et al., 2012; Lee et al., 2013; Lundquist et al., 2014). Also similar to fly Mical, the mammalian MICAL-1 can bind to plexin and cause cytoskeletal reorganization (Schmidt et al., 2008), while the chicken MICAL-3 was implicated in semaphorin-plexin-dependent positioning of motor neurons during embryonic development (Bron et al., 2007). Micals bind to plexin through the C-terminal coiled-coil domains (Schmidt et al., 2008; Terman et al., 2002). There are strong indications that in the context of the full length molecules, these C-terminal regions have an autoinhibitory function (Giridharan et al., 2012; Grigoriev et al., 2011; Schmidt et al., 2008). Partner binding to the C-termini of MICAL can be an important way to relieve the autoinhibition (Schmidt et al., 2008). This suggests that the localization of the binding partners of the C-terminal coiled-coil domain of MICALs can determine the site where the actin-depolymerizing activity of these enzymes is deployed.

Importantly, in addition to the interaction with plexins, the C-termini of MICAL-1 and MICAL-3 can interact with multiple members of the Rab GTPase family, including Rab8, Rab10, Rab13 and Rab35 (Fukuda et al., 2008; Grigoriev et al., 2011; Yamamura et al., 2008), suggesting that MICALs can play a role in membrane trafficking. This view is supported by our data on the involvement of MICAL-3, together with its binding partners ELKS and Rab8, and the ELKS-interacting small GTPase Rab6 in the fusion of constitutive secretion carriers with the plasma membrane (Grigoriev et al., 2011). By binding to Rab8 and ELKS through two non-overlapping sites, MICAL-3 can form a triple complex with these proteins. The available data support a model in which

MICAL-3 is recruited to the cortex by ELKS; at the cortex the interaction of MICAL-3 and ELKS with the two Rab GTPases, Rab8 and Rab6, present on the vesicles, promotes vesicle docking and fusion with the plasma membrane. The enzymatic activity of MICAL-3 is required for this process, because vesicles very efficiently dock but fail to fuse when an enzymatically dead version of MICAL-3 is expressed (Grigoriev et al., 2011).

The function and regulation of the mammalian MICAL-2 is likely to be distinct from the other two family members, because MICAL-2 misses the autoinhibitory C-terminal coiled -coil domain (Giridharan and Caplan, 2014; Giridharan et al., 2012). The loss of the C-terminal domain by MICAL-2 in mammals seems to be an evolutionarily recent event because zebrafish genome contains a gene encoding a "complete" MICAL-2 isoform (Bron et al., 2007; Giridharan and Caplan, 2014). The C-terminal MICAL-2 exons are still present in the mammalian genome but seem to be expressed as a part of a separate gene (named MICAL-cl in (Fukuda et al., 2008)), the function of which is unknown. MICAL-2 enzyme affects the organization of cytoplasmic actin fibers (Giridharan et al., 2012), and in addition, it also localizes to the nucleus and plays a role in Serum Response Factor (SRF) signaling pathway by controlling nuclear actin (Lundquist et al., 2014).

In spite of this very significant progress, many questions concerning the biological functions of MICALs and the underlying molecular mechanisms remain unanswered. For example, we do not know whether actin is the only protein that can be specifically oxidized by MICALs or whether additional substrates exist. Analysis of MICAL-1 activity induced by semaphorin-plexin signaling provided indications that collapsin response mediator protein (CRMP) inhibits MICAL-1 and might also act as its substrate (Schmidt et al., 2008). Another function that does not seem to be connected to actin depolymerization involves the ability of MICAL-1 to interfere with apoptotic signaling by binding to NDR (nuclear Dbf2-related) kinases and competing with their activator (Zhou et al., 2011a).

Our work showed that the enzymatic activity of MICAL-3 promotes its own turnover at the cell cortex, and that the block in exocytosis induced by the enzymatically dead MICAL-3 version could not be relieved by actin depolymerization, suggesting that additional substrates might be involved (Grigoriev et al., 2011). The mechanistic analysis of MICAL-3 function in exocytosis was complicated by the potential redundancy with other MICALs, particular-

ly MICAL-1, which can bind to Rab8 similar to MICAL-3 (Grigoriev et al., 2011). Here, we used a *MICAL-1* knockout cell model to address the role of this MICAL family member in secretion mediated by Rab6-positive vesicles. This approach provides clear advantages to the siRNA-mediated knockdown because it results in a complete rather than a partial loss of the protein of interest, an important feature in a case of an enzyme, which might exert physiologically relevant effects even when present at low levels. We found that the loss of MICAL-1 causes accumulation of Rab6 vesicles at the cell periphery, suggesting a secretion delay. This most likely occurred due to alterations in the actin cytoskeleton, and not through the direct participation of MICAL-1 in the ELKS-dependent vesicle docking and fusion.

We also attempted to get further insight into the molecular mechanisms of MICAL-3 function by performing a mass spectrometry-based screen for its binding partners. While this approach did not reveal any obvious leads on the MICAL-3 activity in the secretory pathway, it provided an unexpected link to the machinery responsible for cytokinesis through identification of the two components of the centralspindlin complex (White and Glotzer, 2012) among the highest hits in the screen. Since cytokinesis and abscission involve dramatic actin and membrane remodeling, this finding identifies MICAL-3 is an exiting potential regulator of these processes.

Results and discussion

Monooxygenase domains of MICAL-1 and MICAL-3 show similar actin depolymerization activity

The *Drosophila* Mical and mammalian MICAL-1 and MICAL-2 were shown to disassemble actin filaments in vitro (Hung et al., 2010; Lee et al., 2013). To assess if MICAL-3 displays a similar activity we have purified from *E. coli* recombinant enzymatic domains of MICAL-1 and MICAL-3, either alone or in combination with the CH domains, which might contribute to the actin binding (Fig. 1A). Actin filaments were generated by polymerizing purified muscle actin (a preparation consisting predominantly of α-actin) or non-muscle actin (consisting of β- and γ-actin). Subsequently, the F-actin preparations were incubated with equal concentrations of purified MICAL fragments, and the polymerized and non-polymerized actin fractions were separated by centrifugation. We found that all four MICAL protein fragments were able to increase the amount of soluble actin in this assay, suggesting that they induced depolymerization of actin filaments (Fig. 1B, C). This effect was specific, as it was not observed if NADPH, an essential co-factor of MICALs, was not added (Fig. 1B, C). The presence of CH-domains had no detectable effect on the efficiency of actin depolymerization in these conditions (Fig. 1C). Although not quantitative, this assay showed that the enzymatic domains of MICAL-1 and MICAL-3 were able to disassemble polymerized actin, and the activity of MICAL-3 was comparable or slightly higher than that of MICAL-1. This is in line with our observations in cells, which showed that the N-terminal parts of MICAL-1 and MICAL-3 reduce the abundance of actin filaments in cells (compare Fig. 2A, B to Supplementary Figure S4F in (Grigoriev et al., 2011)). It should be noted that higher expression levels of MICAL-3 N-terminus compared to MICAL-1 N-terminus were needed to disassemble cytoplasmic actin, because all N-terminal fragments of MICAL-3 tended to strongly accumulate in the cytoplasm. Taken together, these data suggest that MICAL-1 and MICAL-3 could have both specific and redundant cellular functions.

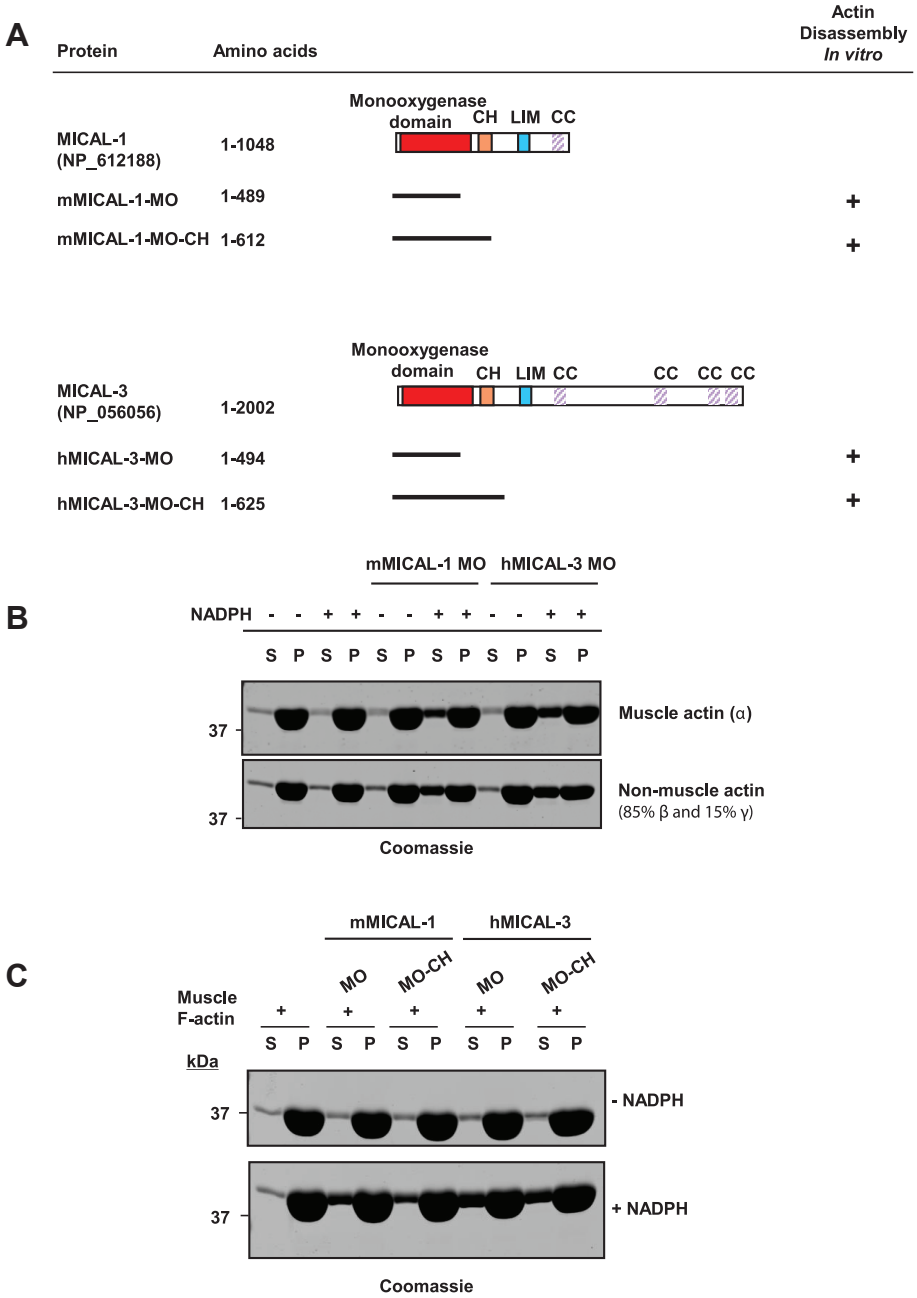

Figure 1. The enzymatic domains of MICAL-1 and MICAL-3 disassemble actin filaments in vitro.
A. Schemes of MICAL-1 and MICAL-3 proteins and fragments used in the in vitro assays.
B, C. Actin pelleting assays. Equal amounts of polymerized actin were incubated with the same concentration of the indicated MICAL fragments in the presence or absence of NADPH. The pellets (P) and the supernatants (S) were analyzed on Coomassie stained gels.

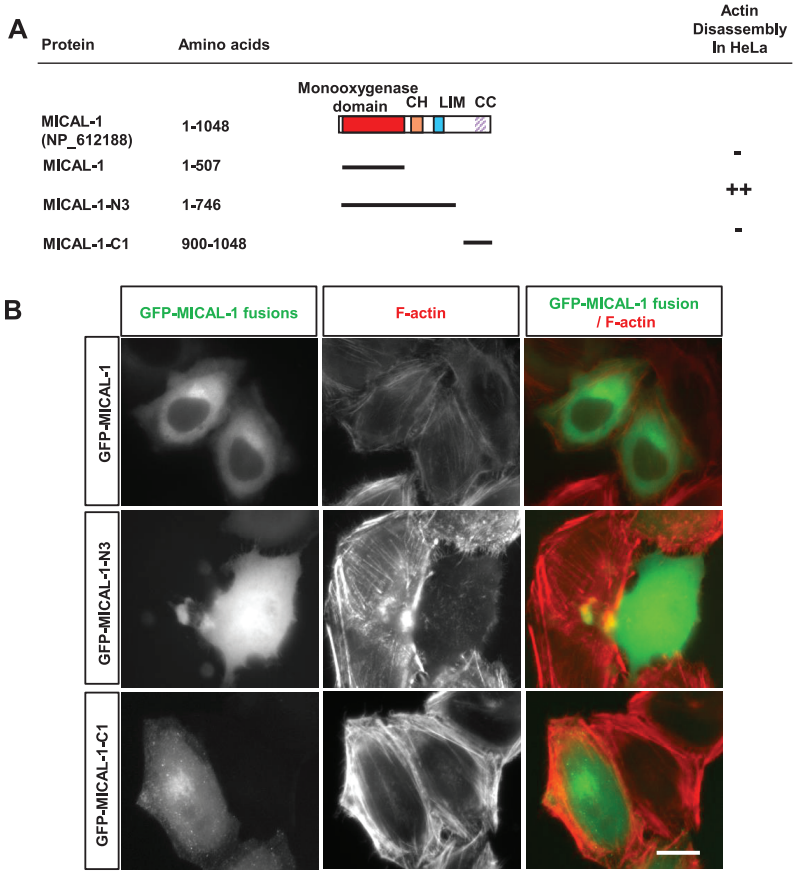

Figure 2. MICAL-1 N-terminus efficiently disassembles actin filaments in cells.
A. A scheme of MICAL-1 and the protein fragments used in the assay.
B. HeLa cells, transiently transfected with the indicated MICAL-1 fragments were stained for F-actin using fluorescent phalloidin. Scale bar, 10 μm.

MICAL-1 controls actin organization and exocytotic vesicle fusion in mouse embryonic fibroblasts

We next set out to investigate whether MICAL-1 might participate in the fusion of secretory vesicles, similar to MICAL-3 (Grigoriev et al., 2011). For these experiments, we used mouse embryonic fibroblasts (MEFs) isolated from the embryos of *MICAL1*$^{-/-}$ mice, which were generated by deleting the first three exons of the *MICAL-1* gene, including the translation start site and the part encoding ~500 N-terminal amino acids of the protein (Van Battum et al., 2014). MEFs from *MICAL-1*$^{+/+}$ embryos were used as a control. MEFs were stained for endogenous Rab6 and actin (Fig.3A). We have quantified the density of Rab6 vesicles in the whole cytoplasm, excluding the Golgi area, as well as the density of Rab6 vesicles

in four randomly selected areas at the cell periphery. Although the overall density of Rab6 vesicles was unchanged in *MICAL-1*$^{-/-}$ MEFs, as compared with control MEFs, the number of Rab6 vesicles at the cell periphery was significantly increased (Fig. 3B, P<0.0001; unpaired t-test). Furthermore, many *MICAL-1*$^{-/-}$ MEFs displayed a compact, round morphology, contrasting with their normal fibroblast-like irregular shape. Total cell area values obtained from analyses of whole-cell Rab6 density, showed that *MICAL-1*$^{-/-}$ MEFs were significantly smaller as compared to control cells (Fig.3C, P<0.001; unpaired t-test). Since the abnormal morphology of *MICAL-1*$^{-/-}$ MEFs hinted at cytoskeletal changes, we next assessed the F-actin distribution. In *MICAL-1*$^{-/-}$ MEFs, F-actin appeared strongly bundled at the cell margin, the amount of peripheral F-actin was increased (Fig. 3A, D, P<0.0001; unpaired t-test) and the vast majority of Rab6 vesicles at the periphery of *MICAL-1*$^{-/-}$ MEFs accumulated in dense F-actin bundles (Fig.3A).

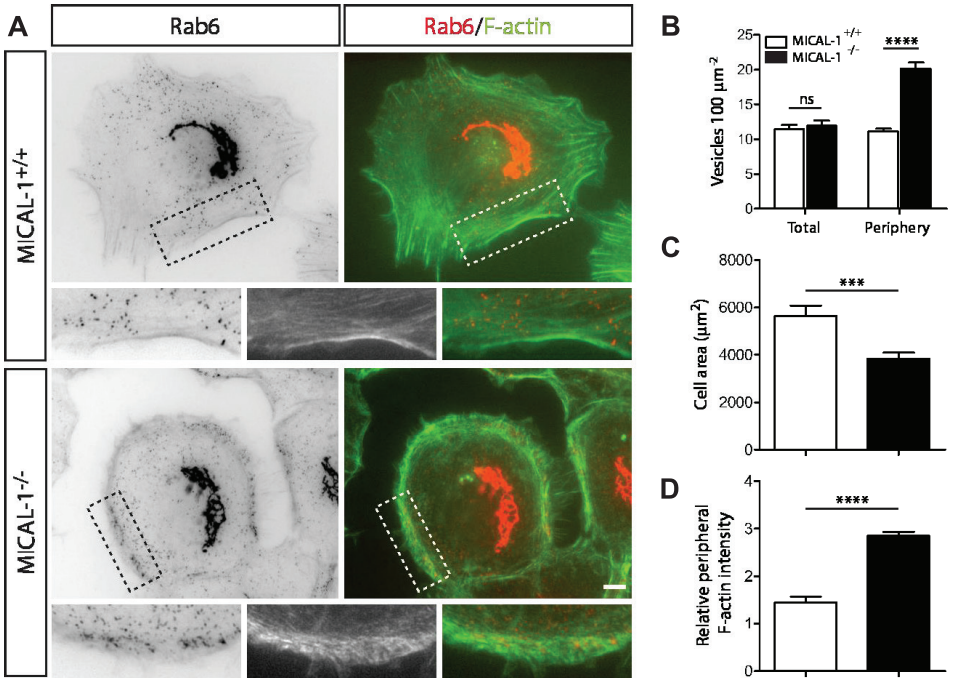

Figure 3. The distribution of F-actin and Rab6 vesicles is perturbed in *MICAL-1*$^{-/-}$ MEFs.
A. Immunofluorescent staining for Rab6 (red) together with phalloidin staining (green) in MEFs. Panels on the left show inverted contrast images of the Rab6 staining. Higher magnifications are derived from the boxed areas. Scale bar, 10 µm.
B-D. Quantification of the number of Rab6 vesicles per 100 µm^{-2} (**B**), MEF cell area (**C**), and the intensity ratio between staining for F-actin at the cell periphery and in the central domain of the cell (**D**), MEFs were used at passage number 6. Rab6 data was obtained from 15 WT and 15 knockout MEFs, peripheral F-actin was quantified from seven wild type and nine knockout MEFs. Area was measured from 19 WT and 22 KO MEFs. Unpaired t-test, ***P<0.001, ****P<0.0001. Data are presented as mean±S.E.M.

The accumulation of vesicles at the periphery of *MICAL-1*$^{-/-}$ MEFS could be explained by defects in vesicle fusion. However, in contrast to MICAL-3, MICAL-1 binds to Rab8A but not to ELKS (Fukuda et al., 2008; Grigoriev et al., 2011; Yamamura et al., 2008). Consistent with this observation, MICAL-1-GFP was not recruited to the peripheral cortical regions enriched in mCherry-MICAL-3 or mCherry-ELKS, as observed in HeLa cells using total internal reflection fluorescence microscopy (Fig. 4). These results, coupled with our observation that MICAL-1 is not visibly enriched at the plasma membrane, argue against a prominent role for MICAL-1 as a molecular linker during vesicle docking or fusion. The accumulation of Rab6 vesicles at the cell margin in *MICAL-1*$^{-/-}$ MEFs is thus most likely due to the more dense actin cytoskeleton in these cells. Interestingly, similar abnormalities of actin and Rab6 vesicle distribution were also observed in the growth cones of neurons derived from the *MICAL-1*$^{-/-}$ knockout mice (Van Battum et al., 2014). These cytological changes correlated with defects in secretion and surface expression of the immunoglobulin superfamily adhesion molecules (IgCAMs) in vivo, and were the likely underlying cause of the abnormalities in axonal targeting and inappropriate neuronal connections observed in mouse hippocampus (Van Battum et al., 2014).

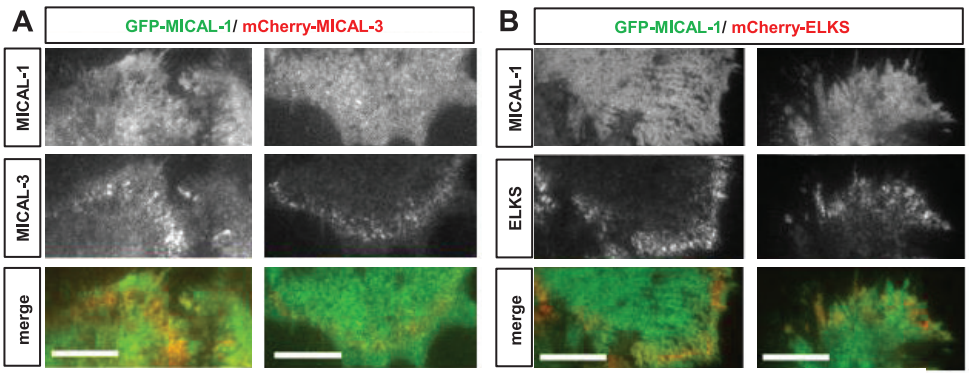

Figure 4. MICAL-1 does not colocalize with ELKS and MICAL-3 in peripheral patches.
A,B. GFP-MICAL-1 was transiently transfected into HeLa cells together with mCherry-MICAL-3 (**A**), or mCherry-ELKS (**B**), and the cells were imaged one day later by TIRF microscopy. Still images from TIRF movies of two independent cells are shown. Scale bar, 10 μm.

Identification of the binding partners of MICAL3 by mass spectrometry

To get a better insight into the function of MICALs, we performed a mass spectrometry-based screen for the binding partners of MICAL-3. MICAL-3 with a biotinylation and GFP (bioGFP) tag was transiently expressed in HEK293 cells together with the protein-biotin ligase BirA, and the lysates of these cells

were used for streptavidin pull down assays as described previously (van der Vaart et al., 2013). Cells expressing BioGFP together with BirA were used as a control. The isolated proteins were analyzed on a Coomassie-stained gel (Fig.5) or by mass spectrometry (Table 1). BioGFP-MICAL-3 was visibly enriched in the pull down (Fig.5). The additional bands visible in the gel represent either the partners of MICAL-3 or background proteins, such as naturally biotinylated proteins or proteins non-specifically binding to streptavidin beads. In the mass spectrometry analysis, specific hits were distinguished from the background by their presence in the pull downs with BioGFP alone.

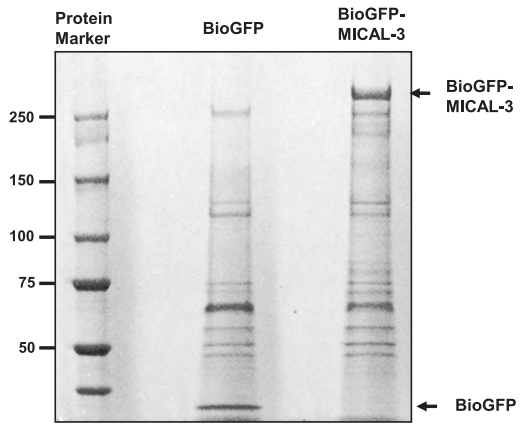

Figure 5. Steptavidin pull down of BioGFP-MICAL-3 from HEK293 cells.
Streptavidin pull down assays were performed with lysates of HEK293 cells transiently expressing the biotin ligase BirA together with BioGFP or BioGFP-MICAL-3, and the resulting proteins were analyzed on a 3-8% gradient polyacrylamide gel (NuPAGE® Novex® Tris-Acetate gel) stained with Coomassie.

MICAL-3 was the highest specific hit in this experiment, as expected, and the already known partners of MICAL-3, ELKS and Rab8A, were also identified with high confidence, confirming the validity of our approach. The homologue of ELKS, ERC2 (CAST1) and Rab10, a Rab family member related to Rab8, were also found, albeit with a lower number of peptides (Table 1). MICAL-1 and MICAL-2 were not detected, supporting the published data, which indicated that different MICAL family members do not form heterooligomers (Van Battum et al., 2014).

The other specific hits in this screen included a broad range of proteins from different cellular compartments. Potentially interesting MICAL-3 partners are a- and b-spectrins, large cortical proteins involved in the control of mechanical stability of cellular membranes and assembly of specialized membrane domains, including signaling and adhesion complexes (Baines, 2009; Bennett and Baines, 2001; Bennett and Healy, 2009). A functionally related protein, ankyrin-G, was

also found in the screen. The interaction of MICAL-3 with these proteins is plausible because of the possible role in the regulation of the organization of the cortical actin, a function to which spectrins and ankyrins are intimately connected.

To confirm that MICAL-3 indeed interacts with ankyrin-G, we performed streptavidin pull down assays from HEK293 cells. We observed that both the enzymatically active and inactive version of MICAL-3 pulled down endogenous ankyrin-G as well as ELKS, which was included as a positive control in this experiment (Fig.6). Identification of ankyrin-G as MICAL-3 partner is exciting, because ankyrin-G acts as a scaffold in organizing of the axon initial segment, a proximal axonal domain which has been shown to function as the action potential initiator, as a diffusion barrier for both cytoplasmic and membrane proteins and as a gatekeeper for axonal cargo transport (Jenkins and Bennett, 2001; Petersen et al., 2014; Song et al., 2009; Watanabe et al., 2012). Spectrin and actin filaments have very specific organization in the axons, as they form regularly spaced rings (Xu et al., 2013), and it would be interesting to know whether MICAL-3 activity contributes to this cytoskeletal patterning.

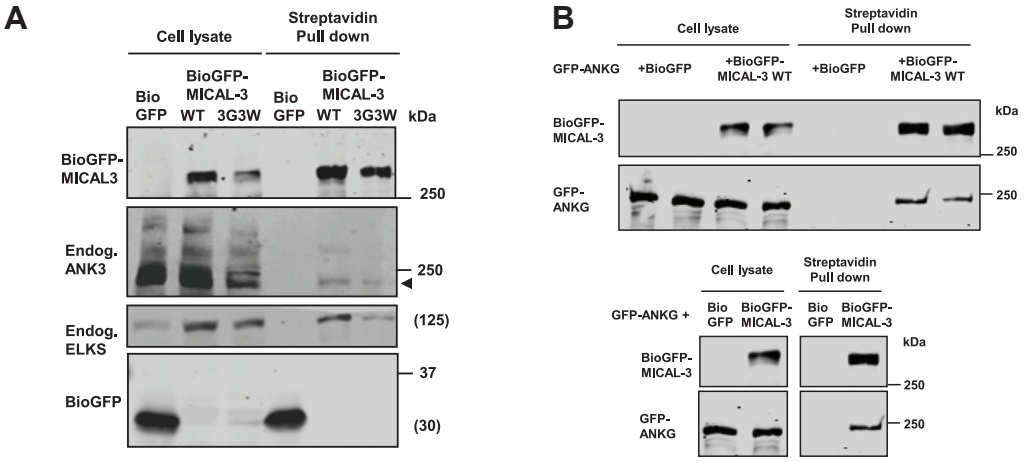

Figure 6. MICAL-3 interacts with Ankyrin-G.
Streptavidin pull down assays were performed with lysates of HEK293 cells transiently expressing the biotin ligase BirA, BioGFP or the indicated BioGFP-MICAL-3 fusions, and the resulting proteins were analyzed by Western blotting with antibodies against GFP, ELKS or ankyrin-G.

The other major hits in the screen were two components of the centralspindlin complex, the kinesin-6 KIF23, also known as MKLP1 (mitotic kinesin-like protein 1; Pavarotti in Drosophila, and ZEN-4 in C. elegans) and the Rac GTPase activating protein 1, (also known as CYK-4 or MgcRacGAP) (Table 1). The centralspindlin complex plays a crucial role in the assembly of the central spindle

and the midbody, activation of RhoA GTPase, positioning of the cleavage furrow and abscission (White and Glotzer, 2012). The validity of the identified interactions is supported by the fact that MICAL-3 was previously reported as one of the potential partners of MKLP1 by mass spectrometry using HeLa cells expressing a carboxy-terminally tagged version of MKLP1 from a bacterial artificial chromosome transgene (Maliga et al., 2013). Several other proteins that were previously identified as MKLP1 binding partners were also present in MICAL-3 pull down. Among these was SHCBP (SHC SH2 domain-binding protein 1; the homologue of the *Drosophila* Nessun Dorma), which also plays a role in cytokinesis (Asano et al., 2013; Montembault et al., 2010), as well as CD2AP (CD2-associated protein), an multifunctional adaptor involved in the regulation of the actin cytoskeleton by binding to the actin capping protein (Edwards et al., 2014). Interestingly, the fly homologue of CD2AP was also implicated in cytokinesis (Haglund et al., 2010). MKLP1, CYK-4 and CD2AP were also found in our previously performed mass spectrometry-based search for the binding partners of ELKS (Table 1) (van der Vaart et al., 2013, see also Chapter 6), suggesting that MICAL-3 might act in cytokinesis in conjunction with ELKS. It should be noted that apart from these proteins, the overlap between the MICAL-3 and ELKS interactomes was limited, and was mostly found for low hits in both screens, the significance of which is unclear.

Among actin regulators, the capping protein, which is the binding partner of CD2AP, was also present (Table 1). No other prominent actin regulators were detected in MICAL-3 pull down. Another potentially interesting partner of MICAL-3 is ninein-like protein (Nlp), a molecule implicated in centrosome maturation, formation of the mitotic spindle and tumorigenesis (Casenghi et al., 2003; Shao et al., 2010; Zhao et al., 2010). One report demonstrated the localization of Nlp at the midbody and implicated it in cytokinesis (Yan et al., 2010), suggesting that Nlp and MICAL-3 might act together at the late stages of the cell division. Interestingly, Nlp was shown to interact with and be regulated by the APC/C (anaphase-promoting complex or the cyclosome, en E3 ubiquitin ligase that marks target cell cycle proteins for degradation by the 26S proteasome) (Wang and Zhan, 2007). We found several components of APC/C (APC1, APC4, APC5, APC8) in the MICAL-3 pull down, suggesting that there might be a functional connection between MICAL-3 and the regulation of protein degradation during cell division.

MICAL-3 pull down contained several enzymes involved in signal transduction, such as casein kinase II and cyclin-dependent kinase 1 (Table 1). Whether these regulatory proteins control the activity of MICAL-3, or whether, converse-

ly, MICAL-3-dependent oxidation is somehow involved in controlling signalling molecules, remains to be determined. Furthermore, different nuclear proteins such as transcription factors have been identified. At least some of them might be relevant MICAL-3 partners, because MICAL-3 can be readily detected in the nucleus (our observations and Lundquist et al., 2014), and the homologue of MICAL-3, MICAL-2 was shown to regulate transcription by redox modification of nuclear actin (Lundquist et al., 2014). Other hits represented mostly metabolic enzymes, mitochondrial proteins, ribosomal proteins, splicing and translation factors. Whether any of these proteins specifically interact with MICAL-3 is uncertain as they often show up in pull down assays with very different baits, likely due to the abundance and possible "stickiness" (Mellacheruvu et al., 2013; Yu et al., 2011).

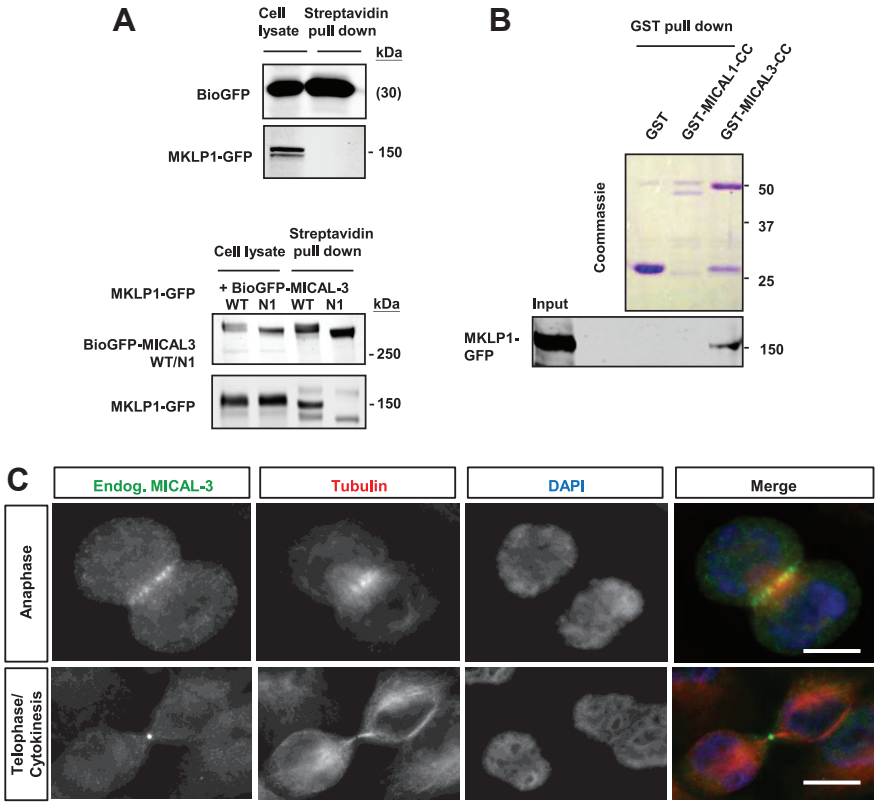

Figure 7. MICAL-3 interacts with MKLP1 and localizes to the central spindle and the midbody.
A. Streptavidin pull down assays were performed with lysates of HEK293 cells transiently expressing the biotin ligase BirA, BioGFP or the indicated BioGFP-MICAL-3 fusions, and MKLP1-GFP, and the resulting proteins were analyzed by Western blotting with antibodies against GFP.
B. GST pull down assays with the indicated GST fusions and extracts of HEK293 cells transiently expressing MKLP1-GFP. Western blot was incubated with antibodies against MKLP1.
C. HeLa cells were fixed with –20°C methanol and stained with antibodies against the endogenous MICAL-3, α-tubulin and DAPI. Scale bar, 10 μm.

MICAL-3 is a potential player in the regulation of cytokinesis or abscission

To confirm the interaction between MICAL-3 and MKLP1, we performed streptavidin pull down assays from HEK293 cells co-expressing GFP-MKLP1 and BirA together with bioGFP, bioGFP-MICAL-3 or bioGFP-MICAL-3-N1, a deletion mutant missing 206 C-terminal amino acids (Fig. 7A, Fig.8A). We found that GFP-MKLP1 was effectively precipitated by the full length bioGFP-MICAL-3 but not by bioGFP-MICAL-3-N1 or by bioGFP alone. By using a GST pull down assay, we showed that MKLP1 binds to the C-terminal portion of MICAL-3 (Fig. 7B, Fig.8A). The C-terminus of MICAL-1 showed no interaction with MKLP1 in this assay (Fig. 7B), but the data were not entirely conclusive because the quality of the C-terminal fragment of MICAL-1 was less good than that of MICAL-3. These data confirm the results obtained by mass spectrometry and suggest that MKLP1 binds to the same part of MICAL-3 that is responsible for the interaction with Rab8 (Grigoriev et al., 2011).

We next examined the localization of endogenous MICAL-3 in mitotic cells using our previously described antibody (Grigoriev et al., 2011). While no conspicuous localization of MICAL-3 could be detected at the early stages of cell division, MICAL-3 was clearly enriched at the central spindle starting from anaphase and strongly accumulated at the midbody in telophase and cytokinesis (Fig. 7C). This localization nicely matches the distribution pattern of the centralspidlin complex. Indeed, fluorescently tagged MICAL-3 colocalized with endogenous MKLP1 at the midbodies and midbody remnants (Fig. 8B). This localization did not depend on the enzymatic activity of MICAL-3 as it was observed with the enzymatically dead version of the protein (Fig. 8A, B). In contrast, MICAL-3-N1, which did not co-precipitate with MKLP1, did not associate with the midbodies or midbody remnants (Fig. 8B), while two different C-terminal fragments of MICAL-3 prominently accumulated with these structures (Fig. 8C). Our data thus indicate that MICAL-3 associates with the centralspindlin complex through the C-terminal domain, and this binding is likely responsible for targeting the protein to the central spindle and the midbody. The C-terminal part of MICALs thus emerges as a general targeting module of MICAL proteins, which might determine, through different binding partners, where these enzymes are activated.

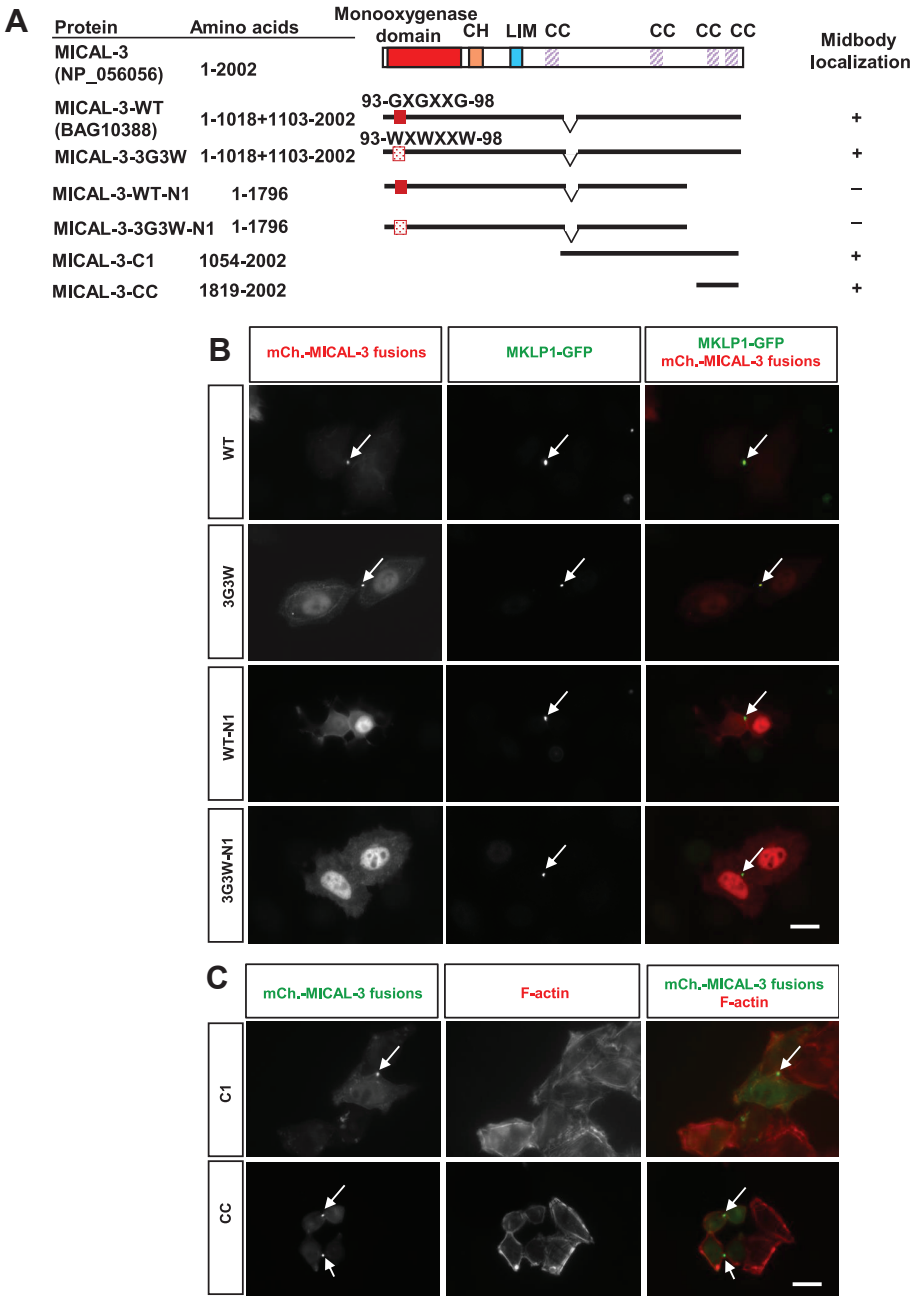

Figure 8. MICAL-3 localizes to the midbody through its C-terminal domain.
A. A scheme of MICAL-3 and the protein fragments used in the assay.
B. HeLa cells stably expressing MKLP-GFP and transiently expressing the indicated mCherry-MICAL-3 fusion constructs were fixed with 4% paraformaldehyde and stained for MKLP1.
C. HeLa cells transiently expressing the indicated mCherry-MICAL-3 fusion constructs were fixed with 4% paraformaldehyde one day after transfection and stained for F-actin with phalloidin. Midbodies and midbody remnants are indicated by arrows. Scale bar, 10 μm.

We next performed some preliminary experiments in order to investigate whether MICAL-3 or the other two MICAL proteins play a role in cytokinesis. We observed no enrichment in mitotic cells that would suggest a mitotic delay, and there were no clear mitotic defects when MICAL-3 was depleted (Fig. 9 and data not shown). It should be noted that we were not able to fully deplete MICAL-3 (data not shown), and therefore the absence of phenotype might be due to the residual activity of the protein. We also depleted MICAL-1 and MICAL-2, either singly or together with MICAL-3 (Fig. 9 and data not shown). A strong phenotype was observed only when all three MICALs were depleted simultaneously (Fig.9). In these conditions, we found that cells exiting mitosis displayed reduced spreading and had a denser peripheral actin cytoskeleton (Fig. 9). The separation of the daughter cells exiting mitosis appeared inhibited to some extent (Fig.9 and data not shown). MKLP1 localization was not affected by the depletion of any of the MICAL proteins (as MKLP1 was still present at the central spindle, midbodies and was also present at midbody remnants), indicating that centralspindlin complex is unlikely to require MICALs for its normal subcellular distribution (Fig. 9). Taken together, our data suggest that-MICALs could play a role in regulating the organization of the actin cortex and/or abscission, but more studies are needed to characterize these potential functions.

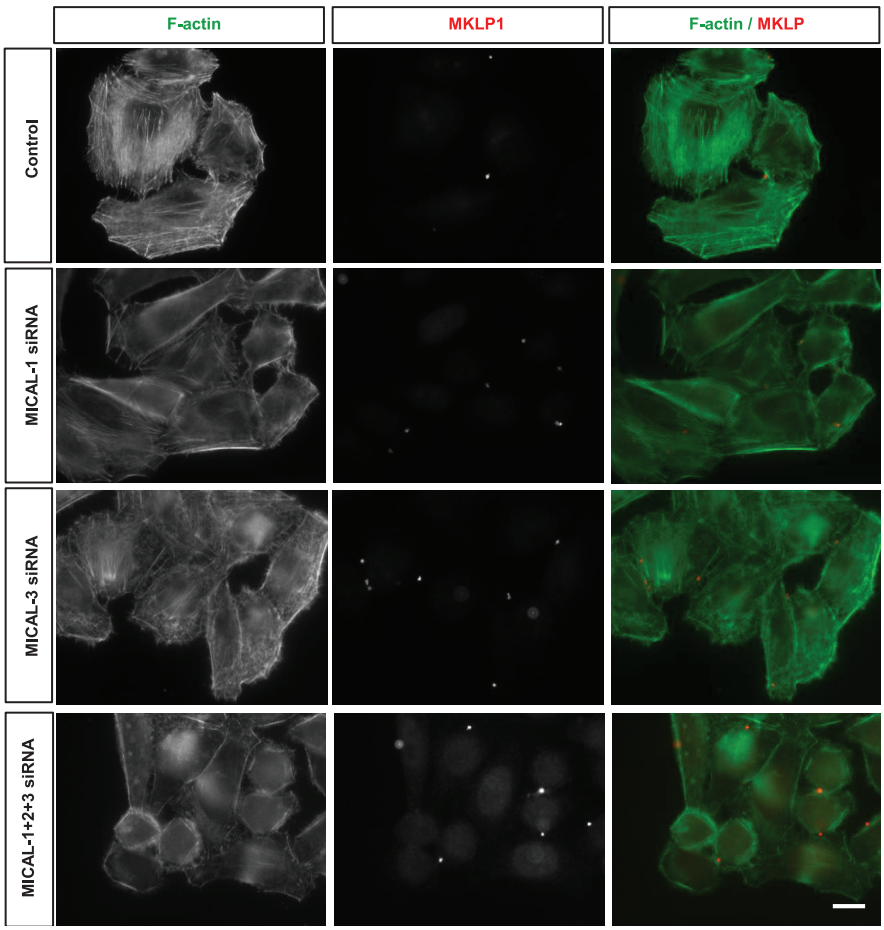

Figure 9. Simultaneous depletion of the three mammalian MICALs perturbs cell spreading during mitotic exit.
HeLa cells transfected with the indicated siRNAs were fixed with 4% paraformaldehyde three days after transfection and stained for MKLP1, which visualizes the midbodies and midbody remnants, and for F-actin. Scale bar, 10 μm.

Conclusions

In this chapter, we have shown that both MICAL-1 and MICAL-3 can affect actin organization by inducing actin disassembly. Analysis of *MICAL-1*$^{-/-}$ MEFs indicated that actin regulation is an important function of this protein, which has consequences for other cellular processes such as vesicle trafficking. The ability of MICALs to destabilize actin might also be important during mitotic exit, because we observed that simultaneous depletion of three MICALs affected post-mitotic cell spreading, which might be due to the inability to reduce the tension at the cell cortex.

Whether actin is the only target oxidized by MICALs remains to be determined. Our biochemical work showed that MICAL-3 can bind to numerous partners, and preliminary experiments confirmed the interactions with two of these partners, ankyrin-G and centralspindlin. It remains to be investigated in detail wither these partners are shared by MICAL-1. It should also be mentioned that even if MICAL-1 does not interact with MKLP1, it might still be targeted to the midbody through the previously characterized interactions with Rab GTPases, such as Rab8 and Rab35, which are known to be present at this cellular site (Dambournet et al., 2011; Fukuda et al., 2008; Grigoriev et al., 2011; Kaplan and Reiner, 2011; Yamamura et al., 2008). Supporting this possibility, a protein related to MICALs, MICAL-L1, which lacks the enzymatic domain but contains the Rab-interacting C-terminus is localizes to the midbody and plays a role in cytokinesis (Reinecke et al., 2015). The function of MICALs during cell division and their potential redundancy thus require additional studies.

Materials and Methods

Expression constructs, cell culture and transfection of plasmids and siRNAs

We used the following previously described expression vectors: BirA (Lansbergen et al., 2006), GFP- or mCherry-MICAL-3 fusions (Grigoriev et al., 2011); MKLP1-GFP was a gift from Dr. Stephen Doxsey (University of Massachussetts, U.S.A).

HeLa and HEK293T were maintained as described previously (Grigoriev et al., 2011). PolyFect (Qiagen) or FuGENE 6 (Roche) were used for plasmid transfection. The stable MKLP1-GFP HeLa cell line was obtained from the Mitocheck consortium (Maliga et al., 2013). We used the following siRNAs: human MICAL-1 – s34928 & s230028 (Ambion), human MICAL-2 – s18546 & s18547 (Ambion), human MICAL-3 – s230763 & s230764 (Ambion) and human MICAL-3 ON-TARGETplus SMARTpool L-024432 (Dharmacon) (see Table II for sequences). Cells were transfected with 5 nM siRNAs using HiPerFect (Qiagen) and analyzed 3 days after transfection.

To obtain mouse embryonic fibroblasts (MEFs), E14.5 embryos were dissected from the uterus and their head, hart and liver were removed. Carcasses were held in MEF tissue culture media containing DMEM with 4.5 g/L glucose (Gibco) supplemented with 10% FCS, P/S, L-Glutamine, non-essential amino acids and β-mercaptoethanol. Carcasses were rinsed to remove blood clots and minced thoroughly. Cell clumps were trypsinized for 10 minutes at 37ºC and the tissue was dissociated into a single cell suspension using 1 ml pipette tips. Cells were seeded in MEF medium and cultured in culture flasks in a humidified incubator at 37˚C and 5% CO_2 and passaged every week. Several independent MEF lines were generated from *MICAL-1*$^{-/-}$ and *MICAL-1*$^{+/+}$ embryos. For immunofluorescent cell staining, MEFs between passage 4 and 10 were seeded on PDL-coated glass coverslips. To visualize Rab6 vesicles and F-actin, fresh medium was added to the MEFs 2 h prior fixation.

Immunofluorescent cell staining

Cells were fixed with 4% paraformaldehyde at room temperature for 15 min or with -20˚C methanol for 10 min, permeablized with 0.2% Triton X-100 in PBS and blocked with 1% bovine serum albumin in PBS. Labeling with primary and secondary antibodies was performed in PBS supplemented with 1% BSA followed by subsequent washes in PBS containing 0.15% Tween-20.

Slides were air-dried and mounted in Vectashield mounting medium (Vector laboratories).

We used the following primary antibodies: mouse monoclonal antibodies against Rab6 (which recognizes Rab6A and Rab6A' (a gift of A. Barnekow, University of Muenster, Germany) ; rat monoclonal antibody against α-tubulin (clone YL1/2; Pierce); rabbit polyclonal antibodies against ELKS (a gift of Dr. F. Melchior, Heidelberg University, Germany), MICAL-3 (Grigoriev et al., 2011), MKLP1 (Santa Cruz, sc-) and mouse monoclonal ankyrin-G (Zymed). F-actin was stained with Alexa 488 or Alexa 594-conjugated phalloidin (Invitrogen). Secondary goat antibodies against rabbit, rat and mouse IgG, conjugated to Alexa 350, Alexa 488 and Alexa 594 were purchased from Invitrogen.

Western blotting was performed as described previously using IRDye 800CW goat anti-rabbit and anti-mouse antibodies, which were detected using Odyssey Infrared Imaging system (Li-Cor Biosciences).

Image acquisition, processing and analysis for fixed cells

Images of fixed cells were taken with a Nikon Eclipse 80i upright fluorescence microscope equipped with UPLFLN 40xO /1,3 Universal Plan Fluorite oil objective and Photometrics CoolSNAP HQ2 CCD (Roper Scientific) camera. Images were acquired using NIS-Elements BR3.2 software (Nikon) and processed using Adobe Photoshop by converting them to 8 bit and adapting linear adjustment of "Levels".

Image analysis was carried out using ImageJ (Rasband). Whole-cell Rab6 vesicle density, excluding the Rab6-positive Golgi area, was quantified using a custom ImageJ plugin, Comdet, and the average number of Rab6 vesicles per 100 μm^2 was plotted. For peripheral Rab6 vesicle density measurements, four circular regions of 50 μm^2 at the cell periphery were selected randomly per cell and the number of Rab6 vesicles were quantified. The average number of peripheral Rab6 vesicles was calculated for wild type and knockout and plotted. Data were analyzed with an unpaired t-test using GraphPad Prism software. For F-actin intensity quantification, five circular regions of 50 μm^2 at the cell periphery and cell center were selected randomly per cell. Average fluorescence intensities of the F-actin staining in the peripheral and central cell regions were calculated. The ratio of the average peripheral F-actin intensity against the central F-actin intensity for wild type and knockout MEFs was plotted.

Total Internal Reflection Fluorescence (TIRF) microscopy

Live cell imaging of HeLa cells was performed on an inverted research microscope Nikon Eclipse Ti-E (Nikon) with the perfect focus system (PFS) (Nikon), equipped with Nikon CFI Apo TIRF 100x 1.49 N.A. oil objective (Nikon), Photometrics Evolve 512 EMCCD (Roper Scientific) and controlled with MetaMorph 7.7 software (Molecular Devices). The microscope was equipped with TIRF-E motorized TIRF illuminator modified by Roper Scientific France/PICT-IBiSA, Institut Curie. 491nm 100mW Calypso (Cobolt) and 561nm 100mW Jive (Cobolt) lasers were used for excitation. We used ET-GFP filter set (Chroma) for imaging of proteins tagged with GFP; ET-mCherry filter set (Chroma) for imaging of proteins tagged with mCherry. For simultaneous imaging of green and red fluorescence we used triple-band TIRF polychroic ZT405/488/561rpc (Chroma) and triple-band laser emission filter ZET405/488/561m (Chroma), mounted in the metal cube (Chroma, 91032) together with Optosplit III beamsplitter (Cairn Research Ltd, UK) equipped with double emission filter cube configured with ET525/50m, ET630/75m and T585LPXR (Chroma). To keep cells at 37˚C we used stage top incubator (model INUBG2E-ZILCS Tokai Hit).

Protein expression and purification

Four truncation constructs containing the mono-oxygenase (MO) domain or/and calponin homology (CH) domain were tested in the F-Actin and MICAL High-speed Co-sedimentation assays. Mouse MICAL1-MO (amino acids 1-489) and MICAL1-MO-CH (amino acids 1-612 of NP_612188, derived by RT-PCR from mouse cDNA) and human MICAL3-MO (amino acids 1-494) and MICAL3-MO-CH (amino acids 1-625 of human cDNA clone, pF1KA0819) were generated using a PCR-based strategy and inserted into *Bam*HI/*Sal*I-digested pET28A vector.

The His-tagged MICAL fragments were expressed in BL21/DE3 (Agilent Technologies), and induced by the addition of 0.1 mM IPTG, cells were grown at 16˚C before harvesting by centrifugation. The MICAL proteins were purified using Ni-NTA agarose (QIAGEN). The purified proteins were dialyzed in storage buffer (50 mM Tris-HCl, 150 mM NaCl, pH 8.0).

GST fusions and their purification, as well as the GST-pull down assays were described previously (Grigoriev et al., 2011).

F-Actin and MICAL High-speed Co-sedimentation Assays

Purified non-muscle actin (85% β-actin, 15% γ-actin; Cytoskeleton, Inc.) or muscle actin (Cytoskeleton, Inc.) was resuspended to 1 mg/mL in actin resuspension buffer (5 mM Tris-HCl, pH 8.0; 0.2 mM $CaCl_2$). The resuspended actin was then added to a standard actin polymerization buffer (50 mM KCl, 2 mM $MgCl_2$, and 1 mM ATP) and allowed to polymerize for 1 hour at room temperature. This generated an F-actin stock at 23 μM actin. MICAL proteins at final concentration of 0.2-1 μM were subjected to initial (clarification) high-speed centrifugation at 150,000 x g for 1 hour at 4˚C. Proteins were added to individual eppendorfs and incubated with F-actin at a final concentration of 20 μM in the absence or presence of NADPH at a final concentration of 200 μM for 30 minutes at room temperature. An F-actin only sample was also incubated for 30 minutes at room temperature. All samples were then subjected to high-speed centrifugation at 150,000 x g for 30 min at 25˚C. Supernatants and pellets were carefully separated and mixed with sample buffer before loading on a SDS-PAGE. Pellets were resuspended vigorously in the sample buffer, incubated on ice for 10 minutes, resuspended with repeated pipeting right before loading on a SDS-PAGE. The gel was then stained with Coomassie blue using standard approaches.

Mass spectrometry and data analysis

Mass spectrometry was performed as described previously (Grigoriev et al., 2011). 1D SDS-PAGE gel lanes were cut into 2-mm slices using an automatic gel slicer and subjected to in-gel reduction with dithiothreitol, alkylation with iodoacetamide and digestion with trypsin (Promega, sequencing grade), essentially as described by [18]. Nanoflow LC-MS/MS was performed on an 1100 series capillary LC system (Agilent Technologies) coupled to either an LTQ-Orbitrap mass spectrometer (Thermo) both operating in positive mode and equipped with a nanospray source. Peptide mixtures were trapped on a ReproSil C18 reversed phase column (Dr Maisch GmbH; column dimensions 1.5 cm × 100 μm, packed in-house) at a flow rate of 8 μl/min. Peptide separation was performed on another ReproSil C18 reversed phase column (column dimensions 15 cm × 50 μm, packed in-house) using a linear gradient from 0 to 80% B (A = 0.1% formic acid; B = 80% (v/v) acetonitrile, 0.1% formic acid) in 70 min and at a constant flow rate of 200 nl/min using a splitter. The column eluent was directly sprayed into the ESI source of the mass spectrometer. Mass

spectra were acquired in continuum mode; fragmentation of the peptides was performed in data-dependent mode. Peak lists were automatically created from raw data files using the Mascot Distiller software (version 2.1; MatrixScience). The Mascot search algorithm (version 2.2, MatrixScience) was used for searching against the IPI database (release IPI_human_20090729.fasta). The peptide tolerance was set to 10 ppm and the fragment ion tolerance was set to 0.8 Da. A maximum number of 2 missed cleavages by trypsin were allowed and carbamidomethylated cysteine and oxidized methionine were set as fixed and variable modifications, respectively. The Mascot score cut-off value for a positive protein hit was set to 60. Individual peptide MS/MS spectra with Mascot scores below 40 were checked manually and either interpreted as valid identifications or discarded. Proteins present in the negative controls (pull down assays with bioGFP alone) were regarded as background.

Table I. Identification of interacting partners of MICAL3 and ELKS by mass spectrometry.

Protein	Uniprot _ID	Gene names	MICAL3 Unique peptides	ELKS Unique peptides
MICAL3	Q7RTP6	Protein-methionine sulfoxide oxidase MICAL3	149	0
SPTB2	Q01082	Spectrin beta chain, non-erythrocytic 1	58	0
SPTA2	Q13813	Spectrin alpha chain, non-erythrocytic 1	54	0
KIF23	Q02241	Kinesin-like protein KIF23 (MKLP1)	48	8
RGAP	Q9H0H5	Rac GTPase-activating protein 1 (CYK4)	36	5
NINL	Q9Y2I6	Ninein-like protein	25	0
CSK22	P19784	Casein kinase II subunit alpha' (CK II alpha')	21	0
TBA1B	P68363	Tubulin alpha-1B chain	20	0
ELKS	Q8IUD2	ELKS/Rab6-interacting/CAST family member 1	17	125
SHCBP	Q8NEM2	SHC SH2 domain-binding protein 1	17	0
PGAM5	Q96HS1	Serine/threonine-protein phosphatase PGAM5, mitochondrial	15	0
RAB8A	P61006	Ras-related protein Rab-8A (Oncogene c-mel)	10	0
CSK2B	P67870	Casein kinase II subunit beta (CK II beta)	10	0
ADT1	P12235	ADP/ATP translocase 1 (Solute carrier family 25 member 4)	10	0
CD2AP	Q9Y5K6	CD2-associated protein	9	30
APC1	Q9H1A4	Anaphase-promoting complex subunit 1	9	0
ANK3	Q12955	Ankyrin-3 (ANK-3) (Ankyrin-G)	9	0
CCHCR	Q8TD31	Coiled-coil alpha-helical rod protein 1 (Pg8)	9	0
TAF6L	Q9Y6J9	TAF6-like RNA polymerase II p300/ CBP -associated factor-associated factor 65 kDa	8	0

HAX1	O00165	HCLS1-associated protein X-1 (HAX-1)	8	0
MIA40	Q8N4Q1	Mitochondrial intermembrane space import and assembly protein 40	8	0
APC5	Q9UJX4	Anaphase-promoting complex subunit 5	7	0
SNUT1	O43290	U4/U6.U5 tri-snRNP-associated protein 1	7	0
WDR82	Q6UXN9	WD repeat-containing protein 82 (TMEM113)	7	0
G3BP1	Q13283	Ras GTPase-activating protein-binding protein 1 (ATP-dependent DNA helicase VIII)	6	0
LDHB	P07195	L-lactate dehydrogenase B chain	6	0
KAD2	P54819	Adenylate kinase 2, mitochondrial (AK 2)	6	0
HACD3	Q9P035	Very-long-chain (3R)-3-hydroxyacyl-CoA dehydratase 3	6	0
LDHA	P00338	L-lactate dehydrogenase A chain	6	0
RM15	Q9P015	39S ribosomal protein L15, mitochondrial	6	0
PP1A	P62136	Serine/threonine-protein phosphatase PP1-alpha catalytic subunit (PP-1A)	5	0
CAPR1	Q14444	Caprin-1 (GPI-anchored membrane protein 1)	5	0
LRC59	Q96AG4	Leucine-rich repeat-containing protein 59 (p34)	5	0
U2AF1	Q01081	Splicing factor U2AF 35 kDa subunit	5	0
NASP	P49321	Nuclear autoantigenic sperm protein (NASP)	5	0
MIPO1	Q8TD10	Mirror-image polydactyly gene 1 protein	5	0
LS14A	Q8ND56	Protein LSM14 homolog A (Protein FAM61A)	5	0
G3BP2	Q9UN86	Ras GTPase-activating protein-binding protein 2	5	0
IMA2	P52292	Importin subunit alpha-1 (SRP1-alpha)	5	0
TTC19	Q6DKK2	Tetratricopeptide repeat protein 19, mitochondrial (TPR repeat protein 19)	5	0
RBP2	P49792	E3 SUMO-protein ligase RanBP2	5	0
CUX1	P39880	Homeobox protein cut-like 1 (CCAAT displacement protein)	4	4

SIX1	Q15475	Homeobox protein SIX1 (Sine oculis homeobox homolog 1)	4	0
HXB6	P17509	Homeobox protein Hox-B6	4	0
S30BP	Q9UHR5	SAP30-binding protein (Transcriptional regulator protein HCNGP)	4	0
YTHD1	Q9BYJ9	YTH domain-containing family protein 1 (DACA-1)	4	0
IF4A1	P60842	Eukaryotic initiation factor 4A-I (eIF-4A-I)	4	0
FUT4	P22083	Alpha-(1,3)-fucosyltransferase 4	4	0
CAZA1	P52907	F-actin-capping protein subunit alpha-1 (CapZ alpha-1)	4	0
VIGLN	Q00341	Vigilin (High density lipoprotein-binding protein)	4	0
EF1D	P29692	Elongation factor 1-delta (EF-1-delta) (Antigen NY-CO-4)	4	0
THIO	P10599	Thioredoxin (Trx) (ATL-derived factor) (ADF)	4	0
DIM1	Q9UNQ2	Probable dimethyladenosine transferase	4	0
MDHM	P40926	Malate dehydrogenase, mitochondrial	4	0
CDK1	P06493	Cyclin-dependent kinase 1 (CDK1)	3	0
B3GT6	Q96L58	Beta-1,3-galactosyltransferase 6	3	0
ATX2L	Q8WWM7	Ataxin-2-like protein (Ataxin-2 domain protein)	3	0
CPSF7	Q8N684	Cleavage and polyadenylation specificity factor subunit 7	3	0
TOX4	O94842	TOX high mobility group box family member 4	3	0
JPH1	Q9HDC5	Junctophilin-1 (JP-1) (Junctophilin type 1)	3	0
APC4	Q9UJX5	Anaphase-promoting complex subunit 4	3	0
RAB10	P61026	Ras-related protein Rab-10	3	0
CN166	Q9Y224	UPF0568 protein C14orf166 (CLE7 homolog)	3	0
ERC2	O15083	ERC protein 2	3	0
GHC2	Q9H1K4	Mitochondrial glutamate carrier 2 (GC-2)	3	0
SMN	Q16637	Survival motor neuron protein (Gemin-1)	3	0
PDIP3	Q9BY77	Polymerase delta-interacting protein 3 (SKAR)	3	0

PUF60	Q9UHX1	Poly(U)-binding-splicing factor PUF60	2	2
PRKRA	O75569	Interferon-inducible double-stranded RNA-dependent protein kinase activator A	2	0
HS105	Q92598	Heat shock protein 105 kDa	2	0
RS10	P46783	40S ribosomal protein S10	2	0
SFXN4	Q6P4A7	Sideroflexin-4	2	0
FA98A	Q8NCA5	Protein FAM98A	2	0
SUMO1	P63165	Small ubiquitin-related modifier 1 (SUMO-1)	2	0
RM44	Q9H9J2	39S ribosomal protein L44, mitochondrial	2	0
RM03	P09001	39S ribosomal protein L3, mitochondrial	2	0
AT2A2	P16615	Sarcoplasmic/endoplasmic reticulum calcium ATPase 2 (SERCA2)	2	0
NEK9	Q8TD19	Serine/threonine-protein kinase Nek9	2	0
NDUA9	Q16795	NADH dehydrogenase [ubiquinone] 1 alpha subcomplex subunit 9, mitochondrial	2	0
1433G	P61981	14-3-3 protein gamma	2	0
CRKL	P46109	Crk-like protein	2	0
H3C	Q6NXT2	Histone H3.3C (Histone H3.5)	2	0
AATM	P00505	Aspartate aminotransferase, mitochondrial	2	0
SMRC1	Q92922	SWI/SNF complex subunit SMARCC1	2	0
P66B	Q8WXI9	Transcriptional repressor p66-beta (p66/p68)	2	0
PSMD3	O43242	26S proteasome regulatory subunit S3	2	0
VDAC1	P21796	Voltage-dependent anion-selective channel protein 1 (VDAC-1) ((Porin 31HM)	2	0
ZF106	Q9H2Y7	Zinc finger protein 106 (Zfp-106)	2	0
PRPS2	P11908	Ribose-phosphate pyrophosphokinase 2	2	0
RM01	Q9BYD6	39S ribosomal protein L1, mitochondrial	2	0
PRPS1	P60891	Ribose-phosphate pyrophosphokinase 1	2	0
ZBTB9	Q96C00	Zinc finger , BTB domain-containing protein 9	2	0

ADDA	P35611	Alpha-adducin	2	0
DHB12	Q53GQ0	Estradiol 17-beta-dehydrogenase 12	2	0
OST48	P39656	Dolichyl-diphosphooligosaccharide--protein glycosyltransferase 48 kDa subunit	2	0
1433T	P27348	14-3-3 protein theta	2	0
MKL2	Q9ULH7	MKL/myocardin-like protein 2	2	0
ZFHX4	Q86UP3	Zinc finger homeobox protein 4	2	0
CDC23	Q9UJX2	Anaphase-promoting complex subunit 8	2	0
TADA1	Q96BN2	Transcriptional adapter 1 (STAF42)	2	0
TF3C5	Q9Y5Q8	General transcription factor 3C polypeptide 5	2	0
CRTC2	Q53ET0	CREB-regulated transcription coactivator 2	1	7
TITIN	Q8WZ42	Titin (Connectin)	1	10
KIF14	Q15058	Kinesin-like protein KIF14	1	1
EPB41	P11171	Protein 4.1 (P4.1) (4.1R) (Band 4.1) (EPB4.1)	1	1
OBSCN	Q5VST9	Obscurin (Obscurin-RhoGEF)	1	2
TRIM4	Q9C037	Tripartite motif-containing protein 4	1	3
UTRO	P46939	Utrophin (Dystrophin-related protein 1)	1	2
POLH	Q9Y253	DNA polymerase eta	1	2
NCLN	Q969V3	Nicalin (Nicastrin-like protein)	1	2
LUC7L	Q9NQ29	Putative RNA-binding protein Luc7-like 1	1	2
SNTB2	Q13425	Beta-2-syntrophin (Syntrophin-3) (SNTL)	1	1
PDIA3	P30101	Protein disulfide-isomerase A3 (ERp60)	1	1
DJC11	Q9NVH1	DnaJ homolog subfamily C member 11	1	1

Table II. Sequences of siRNAs used in this study.

siRNAs	Target Sequences	Catalogue number/ Supplier
Human MICAL1	GAACCGGAAGAAAACCUAtt	s34928/Ambion
Human MICAL1	CAGGCACCAUGAAUAACUAtt	s230028/Ambion
Human MICAL2	GGCCUUUCACCAUCCAUGAtt	s18546/Ambion
Human MICAL2	GUGAAGCAUUUGUAUAUCAtt	s18547/Ambion
Human MICAL3	CCAAGAGAAUGAACGGAUAtt	s230763/Ambion
Human MICAL3	CAACCGAAAUACAACAGCAtt	s230764/Ambion
Human MICAL3 ON-Targetplus SMARTpool	CCAAGAGAAUGAACGGAUA	J-024432-09/Thermo Scientific
Human MICAL3 ON-Targetplus SMARTpool	GGGAAAGUAUUUACAGGUU	J-024432-10/Thermo Scientific
Human MICAL3 ON-Targetplus SMARTpool	CCGUACAGCCAUCGACUUA	J-024432-11/Thermo Scientific
Human MICAL3 ON-Targetplus SMARTpool	CGGCCUACGCCUACGACAU	J-024432-12/Thermo Scientific

References

Asano, E., H. Hasegawa, T. Hyodo, S. Ito, M. Maeda, M. Takahashi, M. Hamaguchi, and T. Senga. 2013. The Aurora-B-mediated phosphorylation of SHCBP1 regulates cytokinetic furrow ingression. *J Cell Sci*. 126:3263-70.

Baines, A.J. 2009. Evolution of spectrin function in cytoskeletal and membrane networks. *Biochem Soc Trans*. 37:796-803.

Bennett, V., and A.J. Baines. 2001. Spectrin and ankyrin-based pathways: metazoan inventions for integrating cells into tissues. *Physiol Rev*. 81:1353-92.

Bennett, V., and J. Healy. 2009. Membrane domains based on ankyrin and spectrin associated with cell-cell interactions. *Cold Spring Harb Perspect Biol*. 1:a003012.

Beuchle, D., H. Schwarz, M. Langegger, I. Koch, and H. Aberle. 2007. Drosophila MICAL regulates myofilament organization and synaptic structure. *Mech Dev*. 124:390-406.

Bron, R., M. Vermeren, N. Kokot, W. Andrews, G.E. Little, K.J. Mitchell, and J. Cohen. 2007. Boundary cap cells constrain spinal motor neuron somal migration at motor exit points by a semaphorin-plexin mechanism. *Neural Dev*. 2:21.

Casenghi, M., P. Meraldi, U. Weinhart, P.I. Duncan, R. Korner, and E.A. Nigg. 2003. Polo-like kinase 1 regulates Nlp, a centrosome protein involved in microtubule nucleation. *Dev Cell*. 5:113-25.

Dambournet, D., M. Machicoane, L. Chesneau, M. Sachse, M. Rocancourt, A. El Marjou, E. Formstecher, R. Salomon, B. Goud, and A. Echard. 2011. Rab35 GTPase and OCRL phosphatase remodel lipids and F-actin for successful cytokinesis. *Nat Cell Biol*. 13:981-8.

Edwards, M., A. Zwolak, D.A. Schafer, D. Sept, R. Dominguez, and J.A. Cooper. 2014. Capping protein regulators fine-tune actin assembly dynamics. *Nat Rev Mol Cell Biol*. 15:677-89.

Fukuda, M., E. Kanno, K. Ishibashi, and T. Itoh. 2008. Large scale screening for novel rab effectors reveals unexpected broad Rab binding specificity. *Mol Cell Proteomics*. 7:1031-42.

Giridharan, S.S., and S. Caplan. 2014. MICAL-family proteins: Complex regu-

lators of the actin cytoskeleton. *Antioxid Redox Signal*. 20:2059-73.

Giridharan, S.S., J.L. Rohn, N. Naslavsky, and S. Caplan. 2012. Differential regulation of actin microfilaments by human MICAL proteins. *J Cell Sci*. 125:614-24.

Grigoriev, I., K.L. Yu, E. Martinez-Sanchez, A. Serra-Marques, I. Smal, E. Meijering, J. Demmers, J. Peranen, R.J. Pasterkamp, P. van der Sluijs, C.C. Hoogenraad, and A. Akhmanova. 2011. Rab6, Rab8, and MICAL3 Cooperate in Controlling Docking and Fusion of Exocytotic Carriers. *Curr Biol*. 21:967-74.

Haglund, K., I.P. Nezis, D. Lemus, C. Grabbe, J. Wesche, K. Liestol, I. Dikic, R. Palmer, and H. Stenmark. 2010. Cindr interacts with anillin to control cytokinesis in Drosophila melanogaster. *Curr Biol*. 20:944-50.

Hung, R.J., C.W. Pak, and J.R. Terman. 2011. Direct redox regulation of F-actin assembly and disassembly by Mical. *Science*. 334:1710-3.

Hung, R.J., C.S. Spaeth, H.G. Yesilyurt, and J.R. Terman. 2013. SelR reverses Mical-mediated oxidation of actin to regulate F-actin dynamics. *Nat Cell Biol*. 15:1445-54.

Hung, R.J., and J.R. Terman. 2011. Extracellular inhibitors, repellents, and semaphorin/plexin/MICAL-mediated actin filament disassembly. *Cytoskeleton (Hoboken)*. 68:415-33.

Hung, R.J., U. Yazdani, J. Yoon, H. Wu, T. Yang, N. Gupta, Z. Huang, W.J. van Berkel, and J.R. Terman. 2010. Mical links semaphorins to F-actin disassembly. *Nature*. 463:823-7.

Jenkins, S.M., and V. Bennett. 2001. Ankyrin-G coordinates assembly of the spectrin-based membrane skeleton, voltage-gated sodium channels, and L1 CAMs at Purkinje neuron initial segments. *J Cell Biol*. 155:739-46.

Kaplan, A., and O. Reiner. 2011. Linking cytoplasmic dynein and transport of Rab8 vesicles to the midbody during cytokinesis by the doublecortin domain-containing 5 protein. *J Cell Sci*. 124:3989-4000.

Kirilly, D., Y. Gu, Y. Huang, Z. Wu, A. Bashirullah, B.C. Low, A.L. Kolodkin, H. Wang, and F. Yu. 2009. A genetic pathway composed of Sox14 and Mical governs severing of dendrites during pruning. *Nat Neurosci*. 12:1497-505.

Lansbergen, G., I. Grigoriev, Y. Mimori-Kiyosue, T. Ohtsuka, S. Higa, I. Kitajima, J. Demmers, N. Galjart, A.B. Houtsmuller, F. Grosveld, and A.

Akhmanova. 2006. CLASPs attach microtubule plus ends to the cell cortex through a complex with LL5beta. *Dev Cell*. 11:21-32.

Lee, B.C., Z. Peterfi, F.W. Hoffmann, R.E. Moore, A. Kaya, A. Avanesov, L. Tarrago, Y. Zhou, E. Weerapana, D.E. Fomenko, P.R. Hoffmann, and V.N. Gladyshev. 2013. MsrB1 and MICALs regulate actin assembly and macrophage function via reversible stereoselective methionine oxidation. *Mol Cell*. 51:397-404.

Lundquist, M.R., A.J. Storaska, T.C. Liu, S.D. Larsen, T. Evans, R.R. Neubig, and S.R. Jaffrey. 2014. Redox modification of nuclear actin by MICAL-2 regulates SRF signaling. *Cell*. 156:563-76.

Maliga, Z., M. Junqueira, Y. Toyoda, A. Ettinger, F. Mora-Bermudez, R.W. Klemm, A. Vasilj, E. Guhr, I. Ibarlucea-Benitez, I. Poser, E. Bonifacio, W.B. Huttner, A. Shevchenko, and A.A. Hyman. 2013. A genomic toolkit to investigate kinesin and myosin motor function in cells. *Nat Cell Biol*. 15:325-34.

Mellacheruvu, D., Z. Wright, A.L. Couzens, J.P. Lambert, N.A. St-Denis, T. Li, Y.V. Miteva, S. Hauri, M.E. Sardiu, T.Y. Low, V.A. Halim, R.D. Bagshaw, N.C. Hubner, A. Al-Hakim, A. Bouchard, D. Faubert, D. Fermin, W.H. Dunham, M. Goudreault, Z.Y. Lin, B.G. Badillo, T. Pawson, D. Durocher, B. Coulombe, R. Aebersold, G. Superti-Furga, J. Colinge, A.J. Heck, H. Choi, M. Gstaiger, S. Mohammed, I.M. Cristea, K.L. Bennett, M.P. Washburn, B. Raught, R.M. Ewing, A.C. Gingras, and A.I. Nesvizhskii. 2013. The CRAPome: a contaminant repository for affinity purification-mass spectrometry data. *Nat Methods*. 10:730-6.

Montembault, E., W. Zhang, M.R. Przewloka, V. Archambault, E.W. Sevin, E.D. Laue, D.M. Glover, and P.P. D'Avino. 2010. Nessun Dorma, a novel centralspindlin partner, is required for cytokinesis in Drosophila spermatocytes. *J Cell Biol*. 191:1351-65.

Pasterkamp, R.J., H.N. Dai, J.R. Terman, K.J. Wahlin, B. Kim, B.S. Bregman, P.G. Popovich, and A.L. Kolodkin. 2006. MICAL flavoprotein monooxygenases: expression during neural development and following spinal cord injuries in the rat. *Mol Cell Neurosci*. 31:52-69.

Petersen, J.D., S. Kaech, and G. Banker. 2014. Selective microtubule-based transport of dendritic membrane proteins arises in concert with axon specification. *J Neurosci*. 34:4135-47.

Reinecke, J.B., D. Katafiasz, N. Naslavsky, and S. Caplan. 2015. Novel Functions

for the Endocytic Regulatory Proteins MICAL-L1 and EHD1 in Mitosis. *Traffic*. 16:48-67.

Schmidt, E.F., S.O. Shim, and S.M. Strittmatter. 2008. Release of MICAL autoinhibition by semaphorin-plexin signaling promotes interaction with collapsin response mediator protein. *J Neurosci*. 28:2287-97.

Shao, S., R. Liu, Y. Wang, Y. Song, L. Zuo, L. Xue, N. Lu, N. Hou, M. Wang, X. Yang, and Q. Zhan. 2010. Centrosomal Nlp is an oncogenic protein that is gene-amplified in human tumors and causes spontaneous tumorigenesis in transgenic mice. *J Clin Invest*. 120:498-507.

Song, A.H., D. Wang, G. Chen, Y. Li, J. Luo, S. Duan, and M.M. Poo. 2009. A selective filter for cytoplasmic transport at the axon initial segment. *Cell*. 136:1148-60.

Suzuki, T., T. Nakamoto, S. Ogawa, S. Seo, T. Matsumura, K. Tachibana, C. Morimoto, and H. Hirai. 2002. MICAL, a novel CasL interacting molecule, associates with vimentin. *J Biol Chem*. 277:14933-41.

Terman, J.R., T. Mao, R.J. Pasterkamp, H.H. Yu, and A.L. Kolodkin. 2002. MICALs, a family of conserved flavoprotein oxidoreductases, function in plexin-mediated axonal repulsion. *Cell*. 109:887-900.

Van Battum, E.Y., R.A. Gunput, S. Lemstra, E.J. Groen, K.L. Yu, Y. Adolfs, Y. Zhou, C.C. Hoogenraad, Y. Yoshida, M. Schachner, A. Akhmanova, and R.J. Pasterkamp. 2014. The intracellular redox protein MICAL-1 regulates the development of hippocampal mossy fibre connections. *Nat Commun*. 5:4317.

van der Vaart, B., W.E. van Riel, H. Doodhi, J.T. Kevenaar, E.A. Katrukha, L. Gumy, B.P. Bouchet, I. Grigoriev, S.A. Spangler, K.L. Yu, P.S. Wulf, J. Wu, G. Lansbergen, E.Y. van Battum, R.J. Pasterkamp, Y. Mimori-Kiyosue, J. Demmers, N. Olieric, I.V. Maly, C.C. Hoogenraad, and A. Akhmanova. 2013. CFEOM1-associated kinesin KIF21A is a cortical microtubule growth inhibitor. *Dev Cell*. 27:145-60.

Vanoni, M.A., T. Vitali, and D. Zucchini. 2013. MICAL, the Flavoenzyme Participating in Cytoskeleton Dynamics. *Int J Mol Sci*. 14:6920-59.

Wang, Y., and Q. Zhan. 2007. Cell cycle-dependent expression of centrosomal ninein-like protein in human cells is regulated by the anaphase-promoting complex. *J Biol Chem*. 282:17712-9.

Watanabe, K., S. Al-Bassam, Y. Miyazaki, T.J. Wandless, P. Webster, and D.B. Arnold. 2012. Networks of polarized actin filaments in the axon initial

segment provide a mechanism for sorting axonal and dendritic proteins. *Cell Rep*. 2:1546-53.

White, E.A., and M. Glotzer. 2012. Centralspindlin: at the heart of cytokinesis. *Cytoskeleton (Hoboken)*. 69:882-92.

Xu, K., G. Zhong, and X. Zhuang. 2013. Actin, spectrin, and associated proteins form a periodic cytoskeletal structure in axons. *Science*. 339:452-6.

Yamamura, R., N. Nishimura, H. Nakatsuji, S. Arase, and T. Sasaki. 2008. The interaction of JRAB/MICAL-L2 with Rab8 and Rab13 coordinates the assembly of tight junctions and adherens junctions. *Mol Biol Cell*. 19:971-83.

Yan, J., S. Jin, J. Li, and Q. Zhan. 2010. Aurora B interaction of centrosomal Nlp regulates cytokinesis. *J Biol Chem*. 285:40230-9.

Yu, K.L., N. Keijzer, C.C. Hoogenraad, and A. Akhmanova. 2011. Isolation of novel +TIPs and their binding partners using affinity purification techniques. *Methods Mol Biol*. 777:293-316.

Zhao, X., S. Jin, Y. Song, and Q. Zhan. 2010. Cdc2/cyclin B1 regulates centrosomal Nlp proteolysis and subcellular localization. *Cancer Biol Ther*. 10:945-52.

Zhou, Y., Y. Adolfs, W.W. Pijnappel, S.J. Fuller, R.C. Van der Schors, K.W. Li, P.H. Sugden, A.B. Smit, A. Hergovich, and R.J. Pasterkamp. 2011a. MICAL-1 is a negative regulator of MST-NDR kinase signaling and apoptosis. *Mol Cell Biol*. 31:3603-15.

Zhou, Y., R.A. Gunput, Y. Adolfs, and R.J. Pasterkamp. 2011b. MICALs in control of the cytoskeleton, exocytosis, and cell death. *Cell Mol Life Sci*. 68:4033-44.

Chapter 6

Generation of ELKS knockout and GFP knock-in mice

Ka Lou Yu[1], Eugene A. Katrukha[1], Qingyang Liu [1,2], Ivar Noordstra[1], Jeroen Demmers[3], Dick Jaarsma[4], Harm Post[2], A. F. Maarten Altelaar [2], Albert J. R. Heck [2] and Anna Akhmanova[1]

[1] Cell Biology, Faculty of Science, Utrecht University, Padualaan 8, 3584 CH Utrecht, The Netherlands
[2] Biomolecular Mass Spectrometry and Proteomics, Bijvoet Center for Biomolecular Research, Utrecht Institute for Pharmaceutical Sciences and The Netherlands Proteomics Centre, Utrecht University, Padualaan 8, 3584 CH Utrecht, The Netherlands
[3] Proteomics Center, Erasmus Medical Center, PO Box 2040, 3000 CA Rotterdam, The Netherlands
[4] Department of Neuroscience, Erasmus Medical Center, PO Box 2040, 3000 CA Rotterdam, The Netherlands.

Manuscript in preparation

Abstract

ELKS is a multifunctional coiled coil adaptor protein implicated in the regulation of secretion, microtubule organization and NF-κB signalling. To address the function of ELKS in vivo, we have generated a knockout allele of the mouse ELKS-encoding gene, *ELKS1*. The targeting of the *ELKS1* gene was designed in such a way that Cre-mediated recombination could be used to convert a knockout allele into a knock-in allele, in which the N-terminus of the ELKS protein would be fused to the biotinylation and a GFP tag (BioGFP). We found that while heterozygous *ELKS1* knockout mice were viable and fertile and displayed no obvious defects, the homozygous knockout mice were embryonically lethal. In contrast, both the hetero- and homozygous BioGFP-ELKS knock-in mice were viable and fertile, and displayed no abnormalities, indicating that the BioGFP-ELKS fusion can substitute for the function of the endogenous ELKS protein. Using *ELKS1* knockout and knock-in mouse embryonic cultured cells, we could confirm that ELKS is required for the fusion of Rab6A-positive exocytotic vesicles with the plasma membrane. We also found that ELKS knockout cells migrate faster than the matching BioGFP-ELKS knock-in cells. Finally, we have used the BioGFP tag to isolate ELKS from cells expressing the endogenous levels of the protein and analyzed the associated proteome. The generated mice with the targeted *ELKS1* allele represent an excellent tool to investigate ELKS function, localization and intracellular dynamics.

Results and Discussion

ELKS knockout mice are embryonically lethal while the BioGFP-ELKS knock-in mice are viable and fertile

ELKS is a ubiquitously expressed scaffolding protein which has been implicated in a plethora of cellular functions, including constitutive secretion (Grigoriev et al., 2007), regulated secretion in neurons, pancreatic β cells and mast cells (Hida and Ohtsuka, 2010; Nomura et al., 2009; Ohara-Imaizumi et al., 2005), cytoskeletal organization and cell migration (Astro et al., 2014; Lansbergen et al., 2006) and NF-κB signalling (Ducut Sigala et al., 2004; Wu et al., 2006). However, a significant part of our current knowledge on the ELKS function is derived from the work in cultured cell lines. In order to address the function of ELKS in vivo we have set out to generate an ELKS knockout mouse.

The mouse ELKS-encoding gene, *ELKS1* (*ERC1*) consists of 22 exons, with the major translation start in exon 3 (Fig. 1A). To generate an *ELKS1* knockout allele, we used homologous recombination in embryonic stem (ES) cells to introduce directly in front of the ATG translation initiation codon in exon 3 an insertion, which included a biotinylation tag (a short peptide with a lysine that can be biotinylated by the bacterial biotin ligase BirA (de Boer et al., 2003)) fused in frame with the N-terminus of EGFP (termed BioGFP), followed by loxP-pMC1neo-loxP cassette (Fig.1A). The cassette was constructed in such a way that the transcription of the neomycin-resistance gene (Neo) was antisense with respect to the *ELKS1* gene. The removal of the pMC1neo cassette by Cre-mediated recombination at the loxP sites would result in an in frame fusion of the BioGFP-loxP with the ELKS coding sequence (Fig. 1B). We have previously used a very similar strategy to generate knockout and GFP-knock-in mouse alleles of the gene encoding the microtubule plus end tracking protein CLIP-170 (Akhmanova et al., 2005).

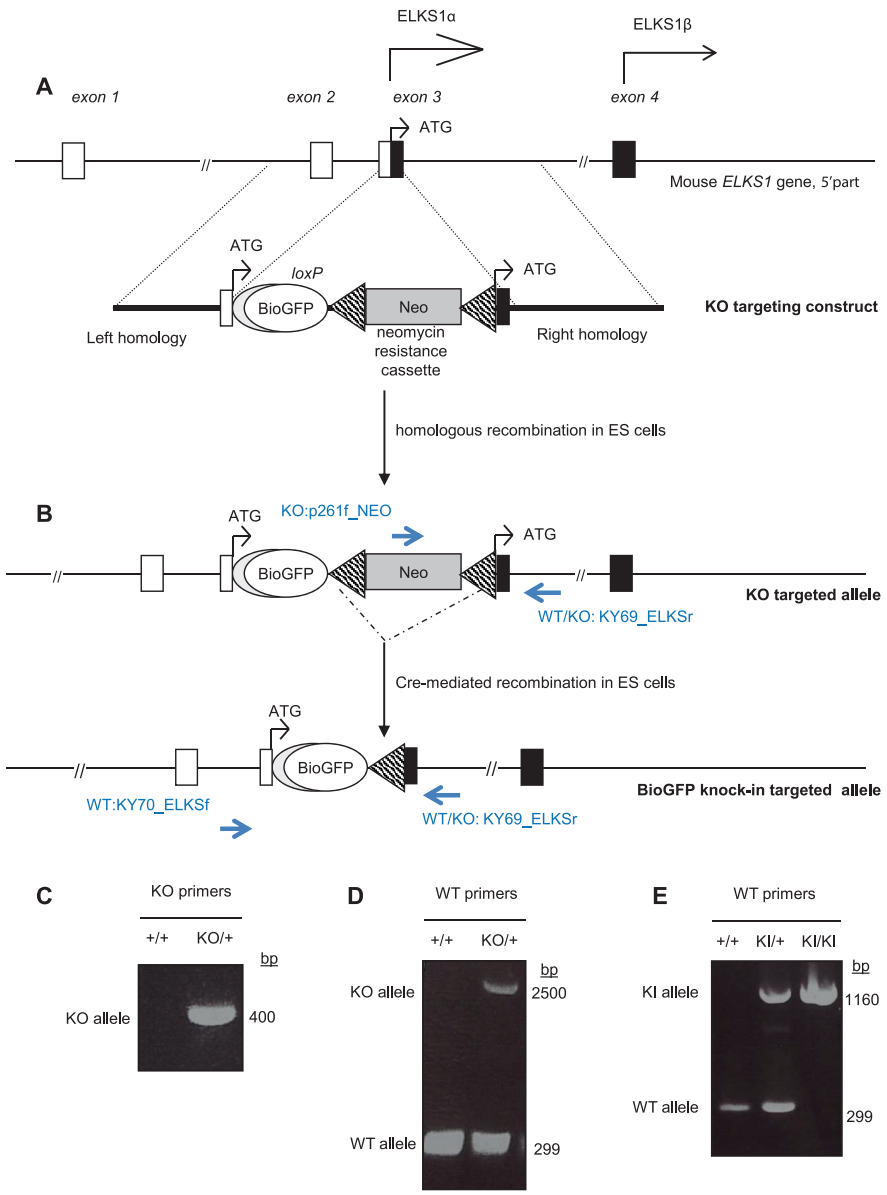

Figure 1. Targeting strategy for the generation of ELKS knockout and BioGFP-ELKS knock-in allele.
A. The top line represents the first four exons of *ELKS1* gene on mouse chromosome 6. A scheme of the ELKS knockout (KO) targeting construct where BioGFP and neomycin resistance cassette (NEO) have been inserted into exon 3. The LoxP sites are indicated with arrows flanking next the NEO.
B. A scheme of the ELKS targeted allele before and after Cre-mediated recombination in ES cells. The positions of the primers used for genotyping are indicated in blue.
C. Tail genomic DNA of wild type (WT, +/+) and heterozygous ELKS knockout (KO/+) mice was subjected to genotyping PCR using the knockout primers.
D. Tail genomic DNA of wild type and heterozygous ELKS knockout mice was subjected to genotyping PCR using the WT primers.
E. Tail genomic DNA of wild type (WT), heterozygous (KI/+) and homozygous (KI/KI) BioGFP-ELKS mice was subjected to genotyping PCR using WT primers.

The targeting construct contained 3.6 kb upstream and 3.8 kb downstream homologous sequences. The positive ES cell clones were identified using PCR (Fig. 1C). The targeting efficiency in ES cells was 10.3% (24 positives out of 232 analyzed clones). To delete pMC1neo, targeted ES cells were transfected with a plasmid expressing Cre recombinase. We have selected several ES cell clones, which upon transient transfection with Cre exhibited an appearance of an additional band on Western blots with ELKS antibodies, corresponding in expected size of the BioGFP-ELKS fusion protein (Fig. 2A). Subsequent subcloning of these cells demonstrated that they were heterozygous of bioGFP-ELKS knock-in, as determined by PCR and Western blotting (Fig. 2B). The relative intensity of the endogenous, unmodified ELKS protein and the BioGFP-ELKS fusion on Western blot was very similar, indicating that the two proteins exhibited similar levels of expression and stability (Fig. 2B). Fluorescence microscopy showed that after Cre-mediated recombination, the targeted ES cells exhibited GFP fluorescence, which co-localized with the staining for the endogenous ELKS in patches at the ventral cell cortex, a pattern similar to that described for ELKS and LL5β in mouse 3T3 fibroblasts (Lansbergen et al., 2006). Taken together, these data suggest that we have correctly targeted the *ELKS1* gene, and that the targeted allele could be converted to the GFP-ELKS knock-in allele by Cre-mediated recombination.

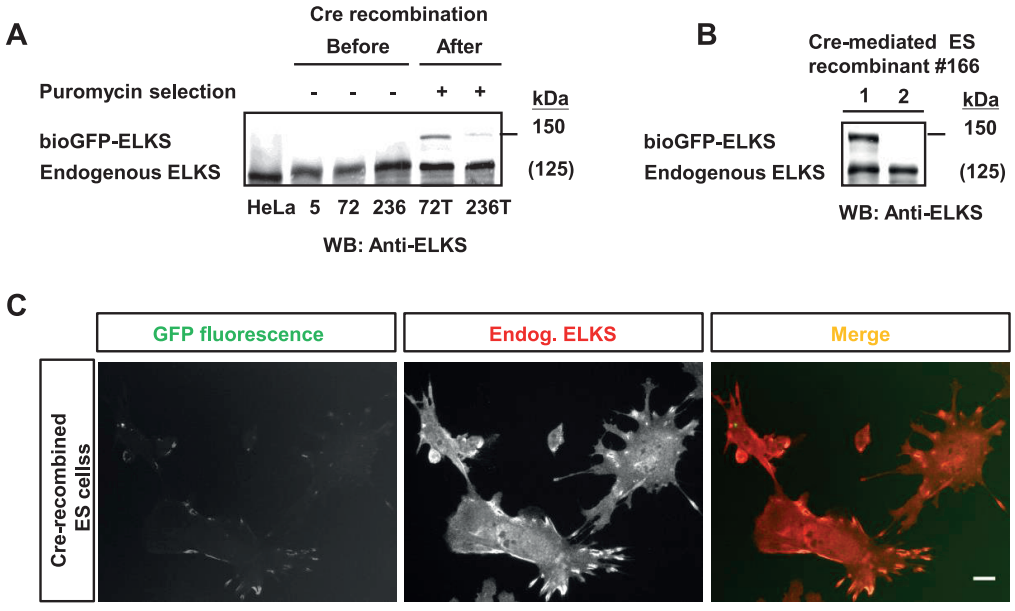

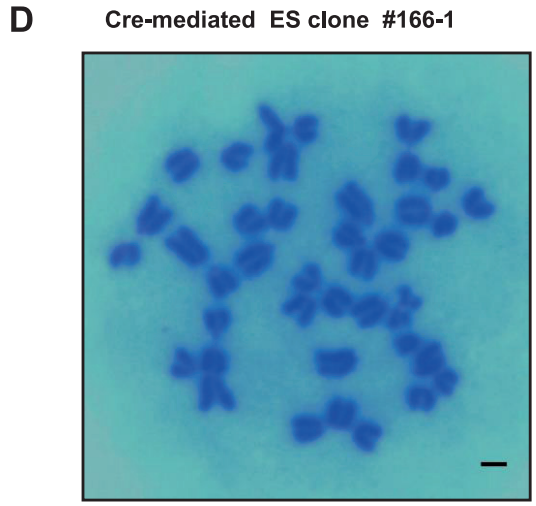

Figure 2. Recombination of the targeted *ELKS1* allele in ES cells.
A. Western blots of extracts of targeted ELKS-knockout ES cell clones before and after transfection with a Cre-expressing plasmid. Expression of the endogenous ELKS and BioGFP-ELKS was detected using rabbit anti-ELKS antibodies.
B. Western blot with rabbit anti-ELKS antibodies of lysates of a targeted ELKS-knockout ES cell clone before and after Cre recombination. Cre-recombinase expressing cells were selected for puromycin resistance.
C. Detection of BioGFP-ELKS at the cortex of BioGFP-ELKS knock-in ES cells after Cre recombination by direct GFP fluorescence and staining with anti-ELKS antibodies. Scale bar: 10 μm.
D. Karyotyping of the BioGFP-ELKS knock-in ES clone before blastocyst injection. Scale bar: 10 μm

We chose one targeted ES cell clone, as well as one clone with the correctly excised PMC1neo, which had normal karyotypes (Fig. 2D and data not shown), to inject into blastocysts to allow germline transmission of the mutated alleles. We bred the modified *ELKS1* alleles back to the C57BL/6 background and generated heterozygous ELKS knockout and BioGFP-knock-in mice. We then bred these heterozygous mice to obtain homozygous animals. The heterozygous knockout and knock-in mice had no overt phenotypes and were fertile. However, we failed to obtain any homozygous knockout mice in 10 mouse litters, while heterozygous animals were born as could be expected according to the Mendelian ratio (Table I). Subsequent analysis showed that the homozygous ELKS knockout mice died as embryos; strong abnormalities in development became visible already before embryonic day 9 (data not shown). While this work was in progress, two other groups have published data on ELKS knockout mice. One of the groups removed exons 2 and 3, including the major translation start site (Liu et al., 2014), while the other group

used a gene trap insertion between exons 5 and 6 (Wu et al., 2010). Both mutations resulted in embryonic lethality, similar to our results. We conclude that *ELKS1* is an essential mouse gene. Further, these data support the view that the existing minor ELKS transcript, the translation of which initiates in exon 4 and which is not expected to be perturbed by our targeting strategy (Fig.1A), cannot rescue ELKS function, in line with its very low abundance (Liu et al., 2014).

In contrast to the ELKS knockout, the homozygous BioGFP-ELKS knock-in mice were born in Mendelian ratios (Table II), were viable, fertile and displayed no obvious deviations. Since ELKS is an essential gene, this suggests that the N-terminal fusion to BioGFP does not strongly perturb the ELKS function. We next used Western blotting to investigate the relative expression of the untagged, endogenous ELKS and the BioGFP-ELKS. In thymus, lung and testis, we observed a single specific ELKS band in the wild type animals (Fig.3,4). This band was shifted up in the mice bearing the BioGFP-ELKS allele; the relative abundance of BioGFP-ELKS was comparable or slightly lower than that of untagged ELKS, suggesting that the addition of the BioGFP tag had only a mild effect, if any, on the ELKS expression in these tissues. In the spleen and skin, two bands were observed but only one of them shifted up, suggesting that the bottom band might be unspecific or represent an isoform of the ELKS homologue CAST (Fig.3). Western blotting of the heart and kidney showed a more complex pattern, with at least two distinct bands that were shifted up in the BioGFP-ELKS mice, suggesting the existence of multiple ELKS isoforms with the same N-termini (Fig.3). These data are in line with previous work which demonstrated the existence of two major splice forms with different C-termini and 3' untranslated regions (ELKS1A and ELKS1B), as well several alternative splicing of small exons in the middle of the protein (Liu et al., 2014; Nakata et al., 2002).

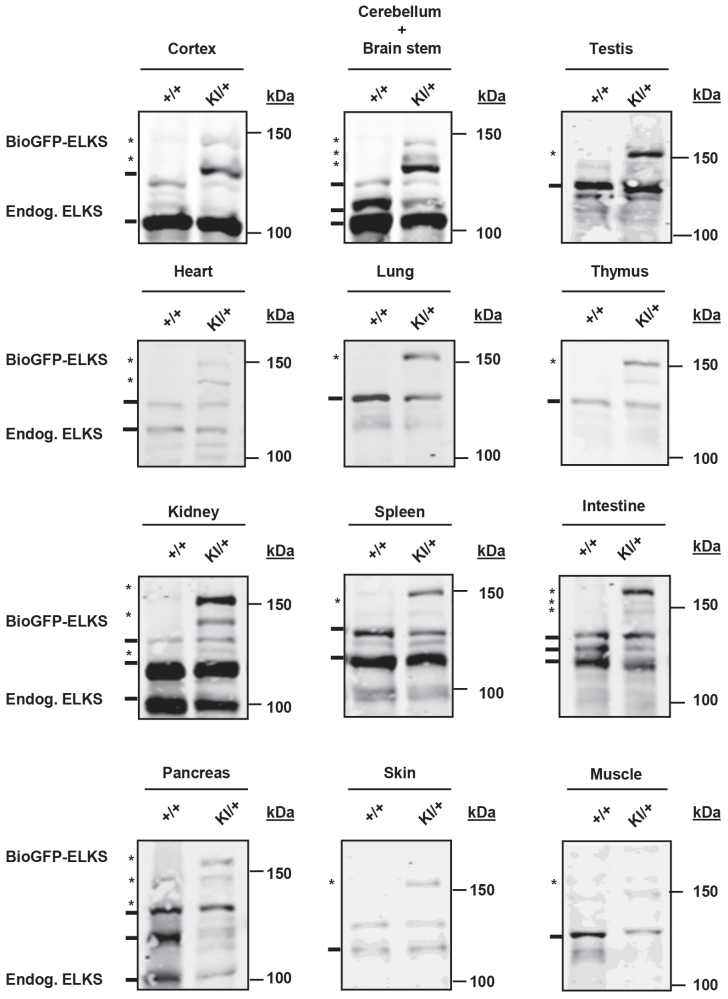

Figure 3. ELKS expression in tissues of wild type and heterozygous BioGFP-ELKS mice.
Western blots of the indicated mouse tissues with rabbit anti-ELKS antibodies. The bands corresponding to unmodified ELKS and BioGFP-ELKS are indicated.

In cerebral cortex, ELKS antibodies strongly cross reacted with the ELKS homologue CAST, which is known to constitute approximately 50% of the total pool of the ELKS/CAST protein this brain area (Liu et al., 2014), a conclusion supported by Western blot analysis of the homozygous ELKS knock-in mice (Fig. 3,4). In the cerebellum, ELKS is highly abundant and constitutes the major part of the total ELKS/CAST pool, as could be seen from the Western blots of homozygous knock-in animals (Fig.4), in agreement with the fact that CAST cannot be observed in this part of the brain (Kaeser et al., 2009). In the cerebellum, as well as in the olfactory bulb, the addition of BioGFP appears to reduce

the expression level of the ELKS protein (Fig. 4). Taken together, our data show that BioGFP-ELKS can be detected in a broad variety of tissues. The addition of the tag had little effect on the expression of the protein in some tissues and led to some reduction in the protein expression levels in other tissues; however, given the absence of obvious phenotype in BioGFP-ELKS mice, the remaining ELKS levels were sufficient to sustain ELKS function.

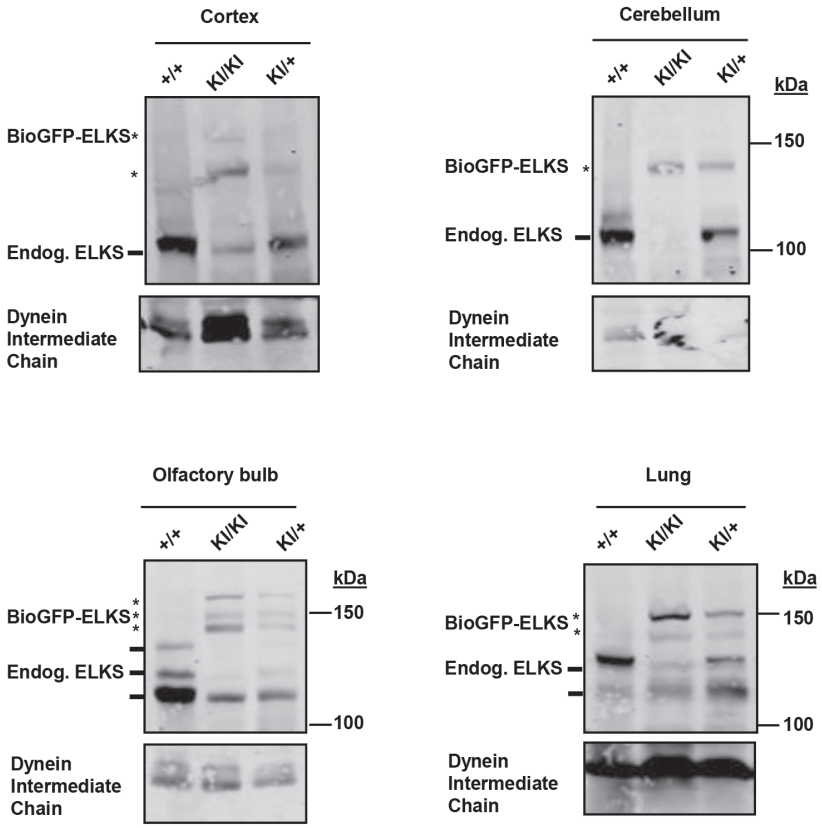

Figure 4. ELKS expression in tissues of wild type, heterozygous and homozygous knock-in mice.
Western blots of the indicated mouse tissues with rabbit anti-ELKS antibodies. The bands corresponding to unmodified ELKS and BioGFP-ELKS are indicated. Antibodies against dynein intermediate chain were used as a loading control.

We next used fluorescence microscopy to examine the BioGFP-ELKS expression in tissues. GFP fluorescence could be detected directly on the gelatine-embedded sections of the cerebellum and lung (Fig.5A). In the lung, the signal was excluded from the nuclei, as could be expected because ELKS is a cytosolic protein; some enrichment of the signal along membranes could be observed, consistent with the cortical localization of the protein observed in cell

culture. In the cerebellum, the GFP signal was present in the molecular layer, where it showed a clear punctate localization consistent with the distribution of the synapses between granule and Purkinje cells, as described previously (Billings et al., 2012) (Fig. 5B). Taken together, these data suggest that the GFP signal in the BioGFP-ELKS mouse can be used to study ELKS localization.

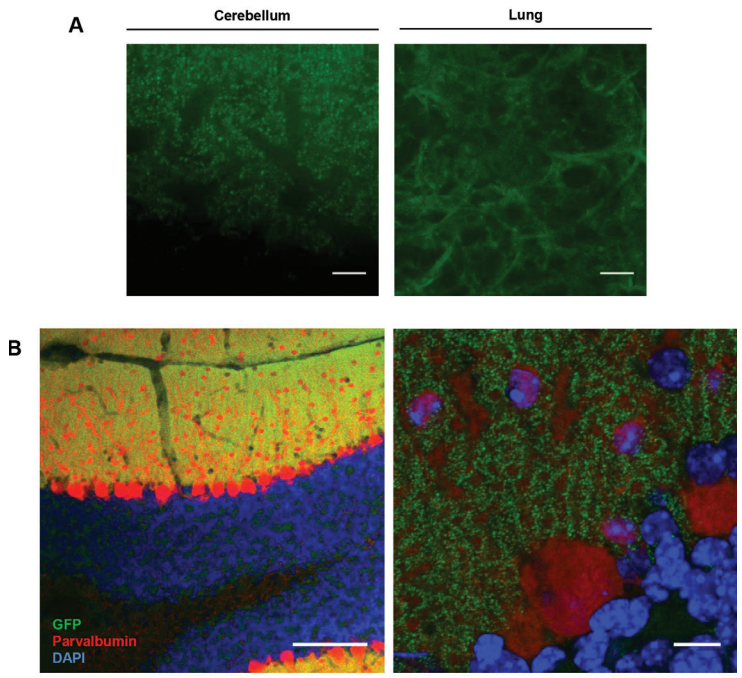

Figure 5. Detection of BioGFP-ELKS expression in cerebellum and lung of BioGFP-ELKS knock-in mouse.
A. Confocal imaging of the direct GFP fluorescence of BioGFP-ELKS was detected in the gelatin-embedded sections of the cerebellum and the lung. Scale bar: 10 μm.
B. Confocal imaging of immunofluorescence staining for GFP and parvalbumin in cerebellum section of BioGFP-ELKS mouse. DNA was stained with DAPI. Scale bar: left, 100 μm, right, 10 μm.

To test whether the BioGFP tag fused to ELKS in the knock-in mouse can be biotinylated, we have crossed the BioGFP-ELKS mouse to the transgenic ROSA26^{HABirA} mice, which has a hemagglutinin (HA)-tagged bacterial biotin ligase BirA-encoding gene was inserted into the *Gt(ROSA)26Sor* locus (Driegen et al., 2005). The embryos derived from these mice were used to isolate mouse embryonic fibroblasts (MEFs). We successfully isolated MEFs heterozygous for the BioGFP-ELKS knock-in allele and the ROSA26^{HABirA} allele (the low frequency of homozygous BioGFP-ELKS knock-in mice expressing BirA was due to the fact that both alleles are located on chromosome 6). In fibroblasts,

the expression of BioGFP-ELKS and unmodified EKLS protein was comparable (Fig. 6A). Using pull downs with streptavidin beads, we could specifically isolate the bioGFP-ELKS from fibroblasts (Fig.6B). The endogenous ELKS lacking the tag was not co-purified, suggesting that ELKS either forms no dimers or oligomers, or forms them co-translationally, so that no di- or oligomers between the tagged and untagged version of the protein are present (Fig.6B). We conclude that the BioGFP-ELKS fusion protein can be biotinylated with BirA and used for the isolation of ELKS expressed at endogenous levels.

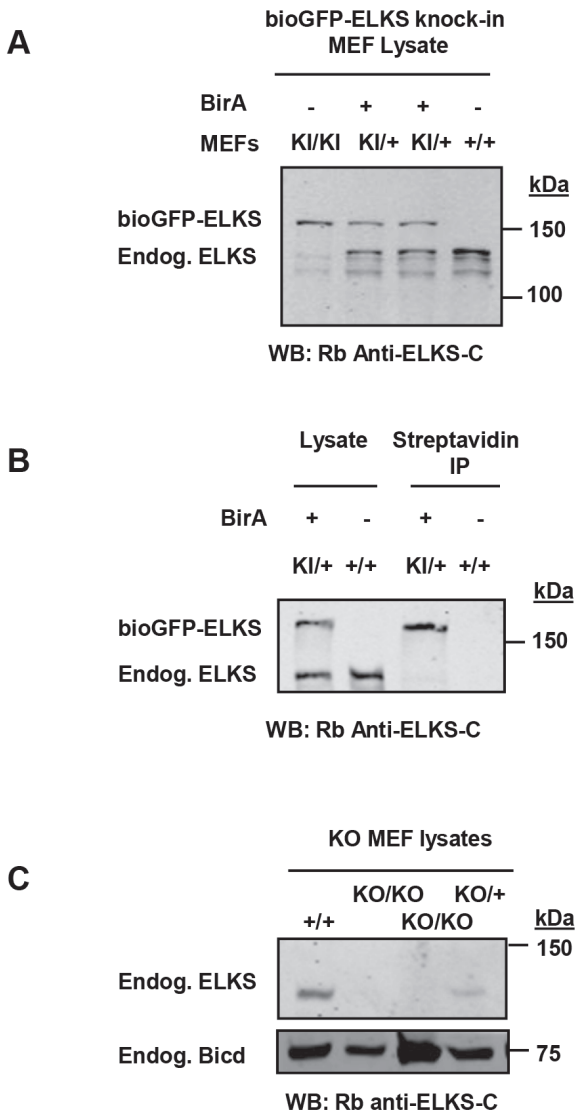

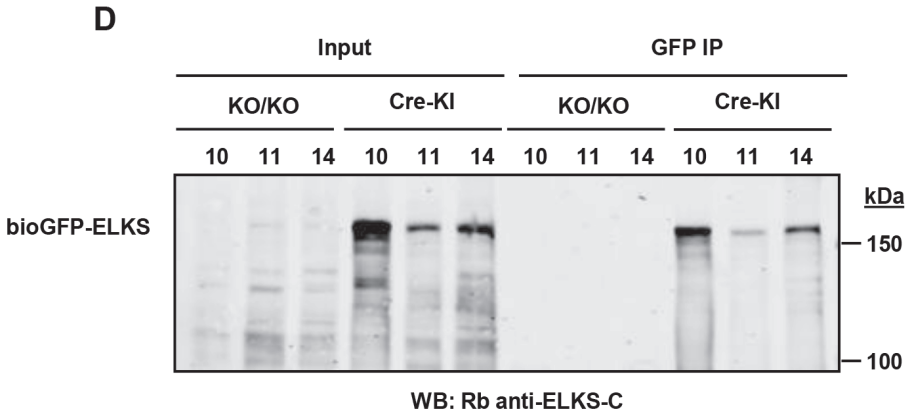

Figure 6. Characterization of ELKS expression in cultured cells isolated from bioGFP-ELKS knock-in and ELKS knockout mice.
A. Analysis of wild type, heterozygous and homozygous BioGFP-ELKS knock-in MEF lysates using Western blotting with antibodies against ELKS.
B. Streptavidin pull-down assays with lysates of wild type and BioGFP-ELKS knock-in /BirA MEFs. 1% of the input and 20% of the precipitates were loaded.
C. Analysis of wild type, heterozygous and homozygous ELKS knockout embryonic cells.
D. Pull-down assay with anti-GFP antibodies with lysates of ELKS knockout cells before and after Cre recombination. 1% of inputs and 20% of the precipitates were loaded.

Analysis of ELKS function in cultured cells

Although the embryonic development of the homozygous ELKS mice was clearly abnormal already before the embryonic day 9, we were able to isolate knockout cells from ELKS knockout embryos at day 9.5 of gestation (Fig. 6C). While this work was in progress, another group has shown that ELKS knockout fibroblasts could be maintained in culture, although they displayed some defects in NF-κB signaling activated by genotoxic stress (Wu et al., 2010). Therefore, ELKS function is not essential for cell viability in culture. We did notice that ELKS knockout cells were much smaller and less well spread than the MEFs isolated from wild type and bioGFP-ELKS knock-in embryos (data not shown). Since the knockout embryos used to isolate these cells were abnormal, it is possible that these cells were derived from tissues other than those normally giving rise to cultured MEFs. We therefore could not directly compare the knockout and wild type fibroblasts in any assays such as secretion and motility, due to their very different morphology and size. To overcome this problem, we have expressed in three ELKS knock-out clones Cre recombinase and obtained mixed cell populations, in which approximately 50% of the cells were converted to BioGFP-ELKS knock-in cells, from which the BioGFP-ELKS fusion protein could be immunoprecip-

itated using GFP antibodies (Fig.6D). Fluorescent microscopy showed that BioGFP-ELKS was strongly concentrated at the cortex of the protruding lamella (Fig.7A), as described previously (Astro et al., 2014; Lansbergen et al., 2006).

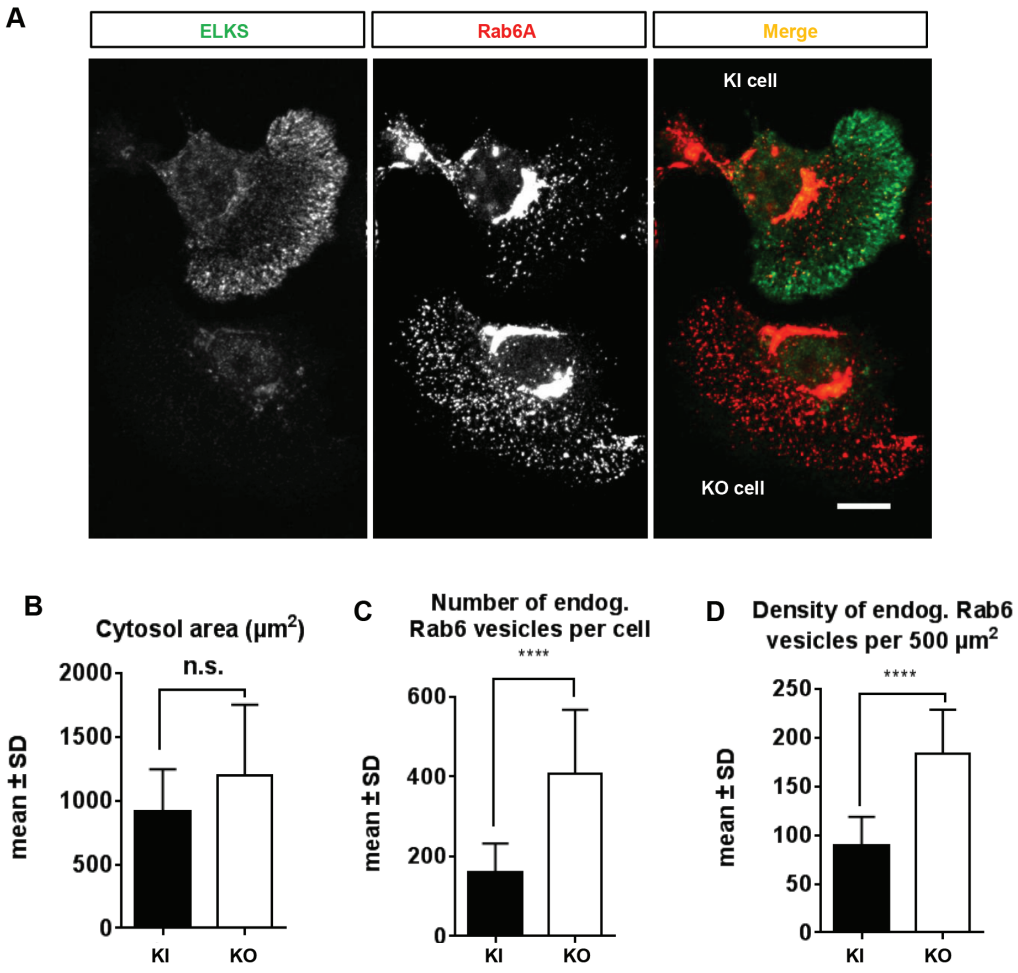

Figure 7. Rab6 vesicles accumulate in ELKS knockout but not in BioGFP-ELKS knock-in cells.
A. Representative confocal images showing the staining of endogenous Rab6 vesicles in ELKS knockout and knock-in cells using immunofluorescence staining with antibodies against Rab6. The cell at the top is a recombined knock-in cell showing BioGFP-ELKS signal enriched at the cell cortex, while the cell at the bottom is a knockout cell that lacks ELKS expression. Scale bar, 10 μm.
B. Quantification of the cytosol area excluding the Golgi and the nuclei in ELKS knockout and knock-in cells.
C. Quantification of Rab6-positive vesicles in ELKS knockout and knock-in cells.
D. Quantification of Rab6vesicle density per 500 μm^2 for the same dataset as in B and C.
24 knock-in and 20 knockout cells were analysed. Error bars indicate SD. Values significantly different from control are indicated by asterisks ($p<0.0001$, Mann-Whitney U test).

The restoration of ELKS expression in ELKS knockout cells had no dramatic effect on cell spreading or morphology (Fig. 7A,B). However, in line with the previous observations based on siRNA-mediated ELKS knockdown in HeLa cells (Grigoriev et al., 2007), we found that ELKS knockout cells displayed a dramatic increase in the number of Rab6A-positive vesicles, which represent secretory carriers (Fig.7C,D). The restoration of ELKS expression by Cre-mediated conversion of the knockout to BioGFP-ELKS knock-in rescued this phenotype, as the number of Rab6 vesicles was strongly reduced (Fig. 7C,D). To confirm these observations made in fixed cells, we used Total Internal Reflection Fluorescence (TIRF) microscopy-based live cell imaging of fluorescently labeled Rab6A. We found that TagRFP-T-Rab6A-positive vesicles strongly accumulated in knockout but not in knock-in cells, which could be distinguished by the presence of GFP fluorescence (Fig. 8A, B). In spite of the much higher number of Rab6-vesicles in ELKS knockout cells, events of fusion with the plasma membrane were less frequent, demonstrating that Rab6 vesicle accumulation in the absence of ELKS is indeed due to a fusion defect, as proposed previously (Grigoriev et al., 2007).

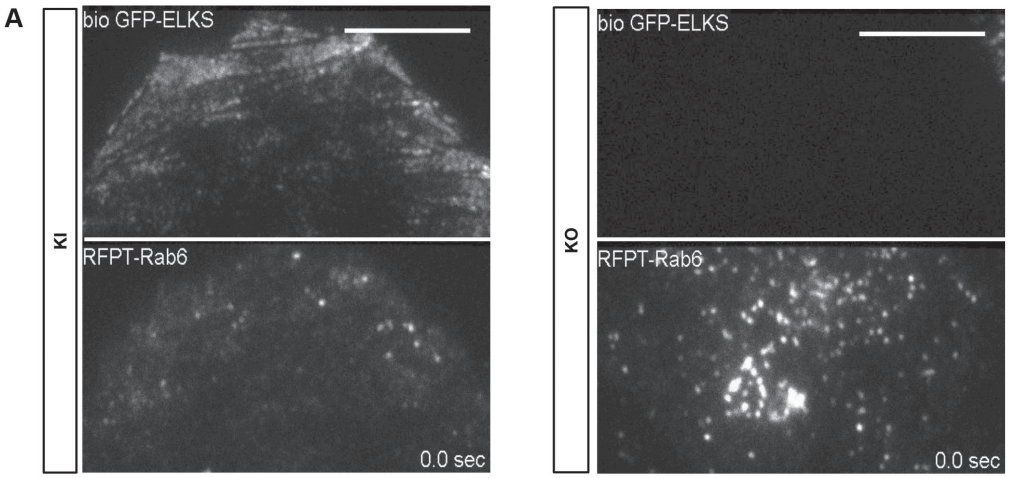

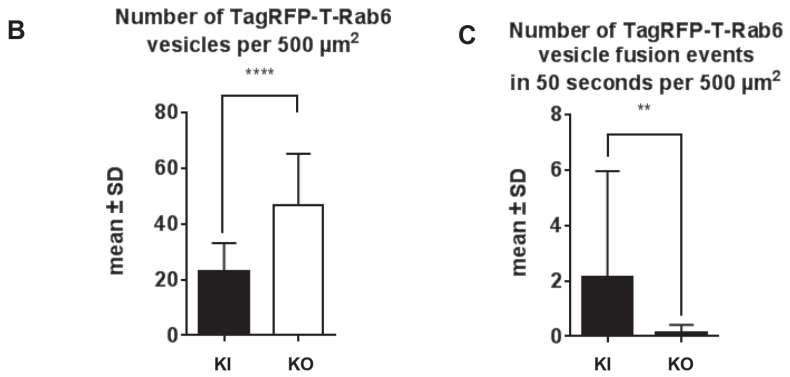

Figure 8. Live imaging of ELKS knockout and knock-in embryonic cells shows that knockout cells are impaired in Rab6 vesicle fusion.
A. ELKS knockout and knock-in cells were transfected with Tag-RFP-T-Rab6A and imaged using TIRF microscopy. Representative frames of a simultaneous two-color movie of knock-in and knockout cells expressing Tag-RFP-T-Rab6A. BioGFP-ELKS knock-in cells are distinguished by the GFP signal. Tag-RFP-R-Rab6A-labeled vesicles accumulate at the cortex of knockout cells. Scale bar, 10 µm.
B. Quantification of Tag-RFP-T-Rab6A vesicles per 500 µm² in knock-in and knockout cells.
C. Quantification of the number of fusion events of Tag-RFP-T-Rab6A vesicles per 500 µm² in ELKS knock-in and knockout cells, plotted over a period of 50 seconds. 26 knock-in cells and 19 knockout cells were analyzed. Error bars indicate SD. Values significantly different from control are indicated by asterisks ($p<0.0001$ in B and $p<0.01$ in C, Mann-Whitney U test).

Comparison between the ELKS knock-in and knockout cells revealed no strong differences in the distribution and size of focal adhesions and actin stress fibers (Fig.9A,B), or the appearance of the microtubule cytoskeleton, which was quite sparse in these cells and displayed no clear organization at the cell margin (Fig. 9C). In agreement with this observation, we detected no accumulation of the microtubule-stabilizing factors CLASP1 and CLASP2 at the plus ends of microtubules at the leading cell edges, which is different from, for example, mouse 3T3 fibroblasts or HeLa cells, which show dense and stable microtubule arrays polarized towards the leading edges (Akhmanova et al., 2001; Lansbergen et al., 2006). The binding partner of ELKS, LL5β, was still present at the cortex and localized in a dot-like pattern in the protruding lamellae (Fig.9D). Due to the strong variability of the distribution of this protein it was not possible to say whether its clustering was affected by the absence of ELKS. Taken together, our data show that ELKS strongly affects the abundance of Rab6-positive vesicles but has no clear impact on the distribution of cytoskeletal markers.

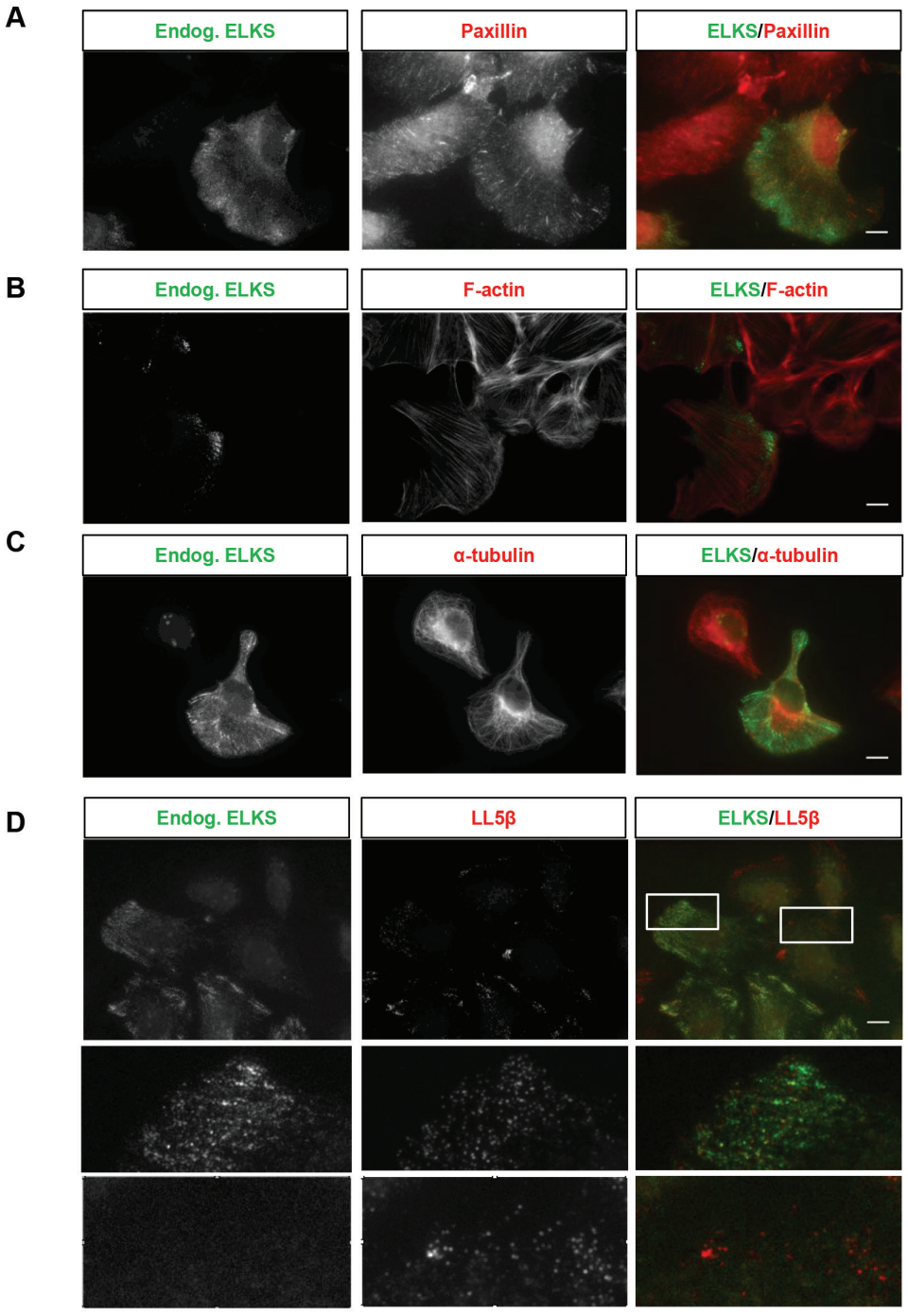

Figure 9. Staining of BioGFP-ELKS knock-in and ELKS knockout cells for cytoskeletal markers.
A-D. The mixed population of BioGFP-ELKS knock-in and ELKS knockout cells was stained with the indicated antibodies. Scale bar, 10 μm.

The existence of a mixed ELKS knockout and BioGFP-ELKS knock-in population derived from the same cell isolate allowed us to investigate how ELKS affects fibroblast migration using monolayer wound healing assays. The knock-in cells could be distinguished from the knockout cells by the presence of GFP fluorescence, which was strongly enriched at the leading cell edges (Fig.10A). Surprisingly, the knockout cells migrated faster and somewhat more persistently than the knock-in ones (Fig.10A-C). This effect is different from that observed in breast cancer cells, where reduced migration and invasion was found after ELKS depletion (Astro et al., 2014). This difference in results is likely due to the very different origin of these cells. In our experiments, we have subjected the cells to selection for the ability to grow in culture in without ELKS, a procedure which might have induced compensatory changes in gene expression. The mechanistic basis of the alterations in migration caused by ELKS loss or re-expression are currently unclear, but might involve changes in focal adhesion turnover, for example by affecting integrin endocytosis (Astro et al., 2014). CLASP and LL5β were proposed to increase focal adhesion turnover by promoting localized delivery of Rab6A-positive exocytotic vesicles bearing matrix metalloproteinases to the vicinity of focal adhesions, where the LL5β-ELKS-CLASP patches are often located (Stehbens et al., 2014). Our data provide no support for this model, as ELKS knockout cells display a very strong defect in the fusion of Rab6A-positive vesicles with the plasma membrane, and yet cell migration is enhanced rather that inhibited. Further studies of the biochemical function of the ELKS protein will be necessary to reveal mechanistic basis of its involvement in cell adhesion and motility.

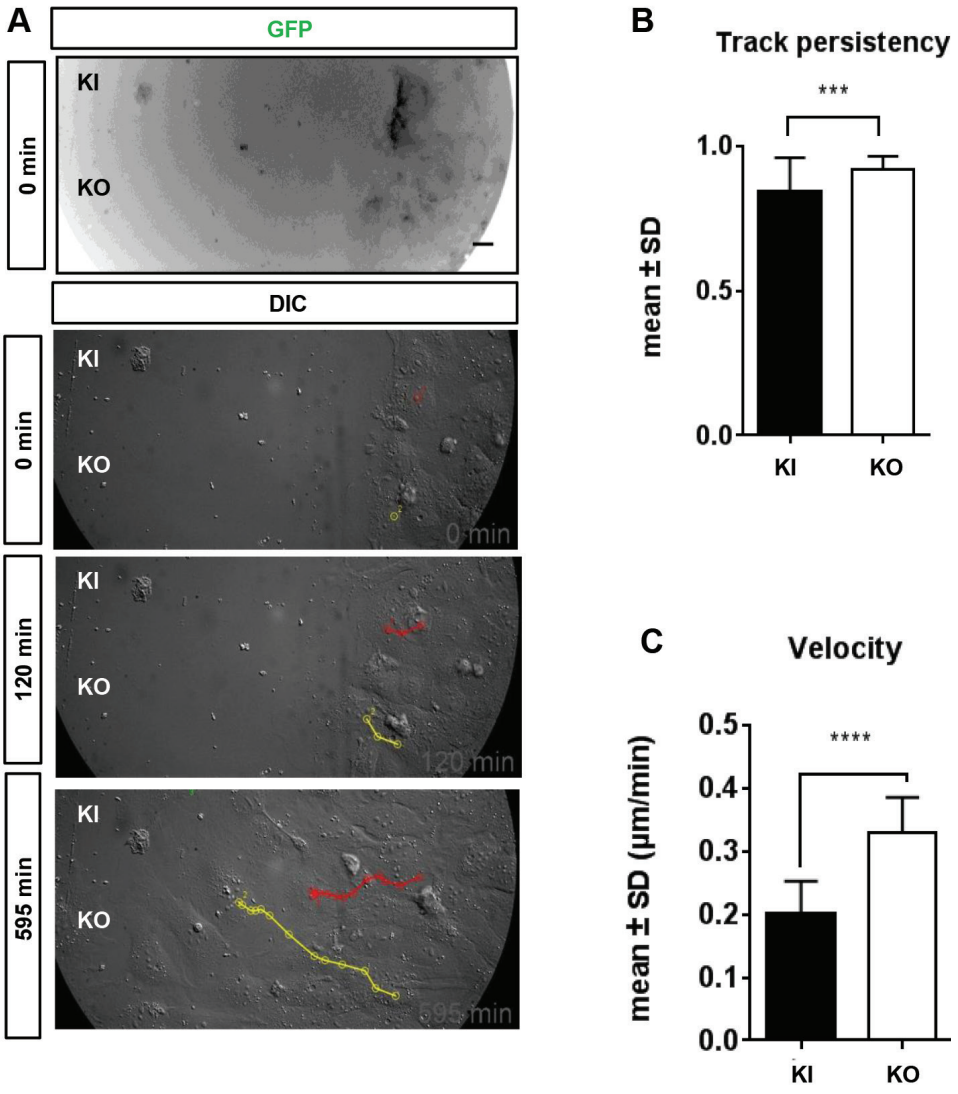

Figure 10. ELKS knockout cells migrate faster than knock-in cells in monolayer wound healing assays.
A. Representative frames showing the DIC imaging of knockout (lower) and knock-in (upper) cells in heterogeneous mixed population during monolayer wound healing assay. One frame of GFP signal was imaged to distinguish the knock-in cells from knockout cells. DIC imaging was performed for the entire experiment. Cells were imaged at a frame rate of 1 minute for a period of 10 hours. Scale bar, 10 µm.
B. Analysis of track persistency of cell movement. Stacks of the DIC images were processed, and the migration of knockout and knock-in cells were tracked manually using ImageJ plugin MTrackJ. Track persistency is the ratio of the net distance (from point 1 to point 2) a cell moves over the total distance a cell moves along the track. When a cell moves along a straight line directionally, the track persistency is 1. When a cell changes direction over the time of tracking, the total distance of the track becomes larger than the net distance, and the track persistency is less than 1.
C. Velocity of the ELKS knockout and knock-in cells was quantified using ImageJ plugin MTrackJ and plotted.
41 knock-in cells and 45 knockout cells were analyzed. Error bars indicate SD. Values significantly different are indicated by asterisks ($p<0.001$ in B and $p<0.0001$ in C, Mann-Whitney U test).

Analysis of ELKS binding partners in MEFs

To get further insight into the ELKS function, we have searched for its binding partners using pull down assays combined with mass spectrometry. First, we have overexpressed BioGFP-ELKS together with BirA in HEK293T cells and performed streptavidin pull downs. BioGFP-LL5β, the binding partner of ELKS (Lansbergen et al., 2006), was included in this experiment for comparison (Fig.11) (some results of this experiment were published in (Grigoriev et al., 2011; van der Vaart et al., 2013)). Second, we performed streptavidin pull downs from heterozygous MEFs expressing BioGFP-ELKS and BirA (Fig. 6B). Third, we performed immunoprecipitations with anti-GFP antibodies from BioGFP-ELKS-expressing cells, which were generated from the ELKS knockout cells by Cre-mediated recombination (Cre/BioGFP-ELKS clone 10, Fig. 6D). The resulting proteins were analyzed by mass spectrometry (Tables III, IV, V).

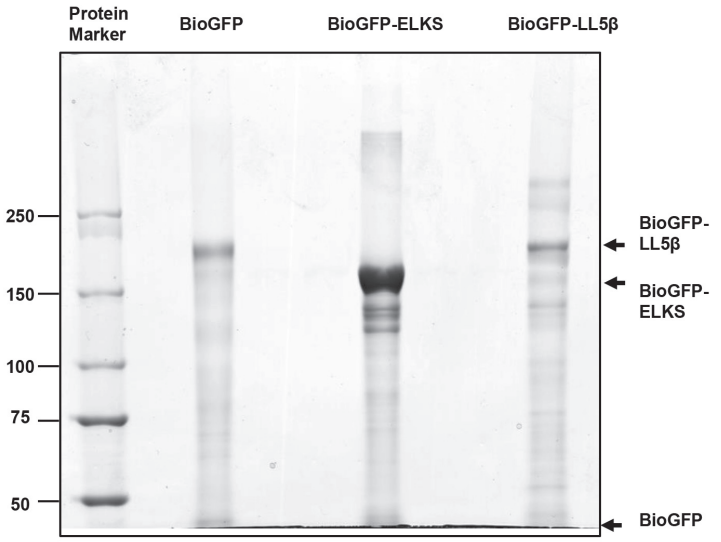

Figure 11. Steptavidin pull down of BioGFP-ELKS and BioGFP-LL5β from HEK293T cells.
Streptavidin pull down assays were performed with lysates of HEK293T cells transiently expressing the biotin ligase BirA together with BioGFP or BioGFP-ELKS or BioGFP-LL5β, and the resulting proteins were analyzed on a 3-8% gradient polyacrylamide gel (NuPAGE Novex Tris-Acetate gel) stained with Coomassie.

Pull downs from HEK293T cells resulted in a very strong enrichment of the ELKS protein (Table III). ELKS homologue CAST (ERC2), and the previously known binding partners of ELKS, LL5β (PHLDB2) and liprin-α1 (PPFIA1) (Ko et al., 2003; Lansbergen et al., 2006; van der Vaart et al., 2013) were also present in the pull down. The homologue of LL5β, LL5α (PHLDB1) and liprin-β1, which tightly associates with liprin-α1, were also present. As al-

ready discussed in Chapters 4 and 5, we have identified MICAL-3 as one of the major hits (Grigoriev et al., 2011). MICAL-3 binding partner kinesin-6 MKLP1 (KIF23) was also present in the ELKS pull down (Table III), and the other component of the centralspindlin complex, the Rac GTPase activating protein 1 (also known as CYK-4 or MgcRacGAP) was also identified, albeit with a lower abundance (5 peptides). MLKP1 was also present in the LL5β pull down, although the number of peptides was lower than in the ELKS pull down. Interestingly, two other proteins strongly implicated in cytokinesis, Citron kinase and the kinesin-3 KIF14 (Bassi et al., 2013; Gruneberg et al., 2006), were also abundantly present in both the ELKS and LL5β pull downs, suggesting that ELKS, MICAL-3 and LL5β might participate in cytokinesis together by forming a complex with centralspindlin, Citron kinase and KIF14.

Other common partners of ELKS and LL5β included CYLD, a deubiquitinating enzyme with tumor suppressor properties, which, similar to ELKS, has been implicated in the regulation of NF-κB signalling (Courtois, 2008; Harhaj and Dixit, 2012). Interestingly, CYLD removes K63- or linear-linked ubiquitin chains, and ELKS has been shown to be modified by K63-linked polyubiquitin chains as a part of the NF-κB signalling cascade (Niu et al., 2011). It is thus possible that CYLD is the enzyme which deubiquitinates ELKS. Another potential link to ubiquitination pathways is provided by TRIM26, a member of tripartite family of RING finger E3 ubiquitin ligases (Ikeda and Inoue, 2012), although the function of this particular TRIM protein is unknown. A potential link to signalling for both ELKS and LL5β is also provided by Daple (Dishevelled-associating protein with a high frequency of leucine residues), a protein connected to Wnt and Rac pathways and cell motility (Ishida-Takagishi et al., 2012). Most of the other numerous proteins found in the ELKS pull down did not seem to associate with LL5β. Many of them were nuclear proteins, and the significance of their potential interaction with ELKS was unclear since ELKS does not seem to be present in the nucleus.

The pull downs with bioGFP-ELKS expressed at endogenous levels (Tables IV and V) contained much fewer ELKS peptides, as would be expected because of the much lower abundance of the bait protein in the cell extracts. The overlap between the two pull downs was low, likely because only a few peptides of each potential partner protein were found in each experiment. However, most of the proteins identified in either of these two "endogenous" pull down experiments were found in the HEK293T cell pull down as well (Table IV and V).

Among the already known partners, LL5β was present in the streptavidin pull down (Table IV), and one MICAL-3 peptide was present in the immunoprecipitates with anti-GFP antibodies. CYLD was also found in the same bioGFP-ELKS purification, supporting its abundant co-purification with ELKS from HEK293T cells. Tumor necrosis factor (TNF) receptor-associate factor 2 (TRAF2), an important player in the NF-κB activation (Au and Yeh, 2007; Courtois, 2008), was also identified in the anti-GFP immunoprecipitation, supporting the connection between NF-κB signalling and the ELKS function (Ducut Sigala et al., 2004). Other potentially interesting hits deserving a follow up study included the phosphatidylinositol 3-kinase regulatory subunit, which might participate in the recruitment of the ELKS-LL5β complexes to the cell cortex, a process regulated by the binding of the pleckstrin homology domain of LL5β to the phosphatidylinositol 3, 4, 5-trisphosphate (PIP3) (Astro et al., 2014; Lansbergen et al., 2006; Paranavitane et al., 2003). Another interesting potential partner was kinesin-3 KIF1B, because this kinesin was implicated in the transport of Rab6-positive secretory vesicles, which fuse with the plasma membrane in an ELKS-dependent manner (Schlager et al., 2014). Additional work will be needed to determine the functional significance of all these newly identified ELKS interactions.

To conclude, we have successfully generated a genetically modified mouse with BioGFP- tagged ELKS version, which can be used to study the localization, behavior and binding partners of the ELKS protein. Our experiments support the functionality of the BioGFP-ELKS fusion protein, opening the way to use it as a tool to study the role and the dynamics of ELKS in the context of different mouse tissues.

Materials and Methods

Expression constructs, cell culture and transfection of plasmids, siRNAs and antibodies

We used the following previously described expression vectors: BirA, BioGFP (Lansbergen et al., 2006), BioGFP-ELKS and BioGFP-LL5β (Lansbergen et al., 2006), CrePac (Akhmanova et al., 2005), TagRFP-T-Rab6A (a gift of Dr. Y. Mimori-Kiyosue, RIKEN CDB Kobe, Japan).

HEK293T were maintained as described previously (Grigoriev et al., 2011). BioGFP-ELKS MEFs and ELKS knockout embryonic cells are transfected using Fugene HD (Promega).

We used the following primary antibodies: mouse monoclonal antibodies against Rab6 (which recognizes both Rab6A and Rab6A', a gift of A. Barnekow, University of Muenster, Germany), dynein intermediate chain y (Dynein IC1/2 (74-1); Santa Cruz), paxillin (BD Biosciences), α-tubulin (Sigma), parvalbumin (Sigma) and LL5β (a gift of Dr. J. Sanes, Harvard University, Cambridge, USA), rabbit polyclonal antibodies against ELKS C-terminus (a gift of F. Melchior, ZMBH, Heidelberg, Germany) and GFP (ab290, Abcam). Secondary goat antibodies against rabbit, rat and mouse IgG, conjugated to Alexa 350, Alexa 488 and Alexa 594 were purchased from Invitrogen.

Animals

All animal experiments were performed in compliance with the institutional and approved by the Animal Ethical Review Committee (DEC) of the Erasmus Medical Center and Utrecht University.

Generation of ELKS knockout and bioGFP-ELKS knock-in mice

The knockout targeting construct was generated by inserting bioGFP and neomycin resistance cassette in front of the start codon of the mouse *ELKS1* gene in the exon 3 using a PCR-based strategy. The construct was linearized and electroporated into IB10 (embryonic stem) ES cells, which were cultured in BRL-cell conditioned medium as described previously (Hoogenraad et al., 2002). Targeted ES cells were further selected with G418 (200 μg ml^{-1}) for neomycin resistance, and individual clones were picked and expanded. Genotyping by PCR was performed to check for the positive clones. 24 positive clones were obtained out of 234 analyzed ES clones.

The bio-GFP-ELKS knock-in allele was generated by Cre recombination of the ELKS knockout ES cells by electroporating a linearized Cre recombinase construct with a puromycin resistance gene. Targeted ES cell clones were selected for puromycin resistance; genotyping was performed by PCR.

The positive ES cell clones containing the ELKS knockout targeted allele or the bio-GFP-ELKS allele and correct karyotype were injected into blastocysts. Male chimera mice were mated with C57Bl/6 mice to transmit the ELKS knockout allele to the germline. We determined the genotypes of the ELKS knockout mice by PCR analysis using the primer sets indicated in Fig. 1B,C.

The ELKS targeted knockout and bioGFP-ELKS knock-in chimeras were crossed into the C57BL/6 inbred background. The bioGFP-ELKS mice were also crossed to homozygous ROSA26^{HABirA} mice to induce biotinylation of the BioGFP-ELKS protein for pull-down experiments of bio-GFP-ELKS MEFs.

Adult mice were sacrificed by cervical dislocation for the isolation of tissues and primary cultures or an overdose of pentobarbital followed by transcardial perfusion for immunocytochemistry.

Preparation of tissues for immunocytochemistry

Mice were anaesthetized with an overdose of pentobarbital and perfused transcardially with 4% paraformaldehyde (PFA). Tissues were dissected and transferred into 10% glucose/2% PFA solution for overnight incubation. Tissues were then placed into warm 10% gelatin/10% sucrose solution and allowed to solidify into gelatin-embedded blocks. They were further immersed in 10% formalin/10% sucrose solution for 2 hrs and transferred into 30% sucrose solution for overnight incubation. Gelatin-embedded tissues were sectioned using a vibratome GFP signals were detected directly or indirectly, using anti-GFP antibody. Sections were mounted on coverslips, placed on glass slides and examined with Zeiss LSM 510 confocal laser scanning microscope using 20x or 63x/1.4 oil-immersion objectives (0.7 digital zoom).

Preparation of tissue extracts

To detect ubiquitous expression of ELKS, cortex, cerebellum, heart, lung, spleen, kidney, testis, muscle and skin wild-type, bio-GFP-ELKS$^{+/-}$ and bioGFP-ELKS$^{+/+}$ adult mice from the same litter were dissected and placed in ice-cold PBS, pH 7.4. Samples were weighted and individually homogenized in ice-cold homogenization buffer (50 mM Tris, 150mM NaCl, 0.1% v/v SDS, 0.5%

v/v NP-40 pH8, 1x Complete protease inhibitor, Roche) with stainless metal beads (Qiagen) using the TissueLyser II (Qiagen) for 30 minutes. Tissue lysates were then centrifuged at 16, 000 × *g* at 4 ˚C for 60 minutes. Supernatants of the tissue lysates were collected, resuspended in 1x SDS sample buffer and boiled for 10 minutes. Detection of ELKS and bio-GFP-ELKS proteins on Western blots was performed using rabbit polyclonal anti-ELKS antibodies.

Isolation and culture of primary mouse embryonic fibroblasts (MEFs)

For embryo dissection, the morning on which a vaginal plug was detected was considered embryonic day 0.5 (E0.5). To isolate bio-GFP-ELKS MEFs, timed-pregnant bio-GFP-ELKS$^{+/-}$ female mothers crossed to heterozygous males were sacrificed by cervical dislocation, embryos at E13.5 were dissected and placed in ice-cold PBS, pH 7.4. To isolate knockout cells, embryos at E9.5 were dissected from heterozygous ELKS knockout pregnant female mothers that have been crossed to a heterozygous knockout male. The embryos were individually trypsinized for 30 minutes in PBS, thoroughly resuspended in medium containing DMEM with 4.5 g/L glucose (Gibco), Ham's 10 (Gibco) supplemented with 10% FCS, penicillin/streptomycin, L-Glutamine, non-essential amino acids and β-mercaptoethanol and seeded for expansion. To detect the ELKS expression, cells were harvested in ice-cold lysis buffer containing 40 mM HEPES, 150 mM KCl, 1% Triton X-100, 1x Complete protease inhibitor (Roche), pH 8.5 and analyzed by Western blotting using rabbit polyclonal antibodies against ELKS.

Coversion of ELKS knockout cells to BioGFP-ELKS knock-in cells

To remove the LoxP-Neo cassette from the targeted ELKS knockout allele in cultured cells, we transfected a Cre-expressing construct using Fugene HD in 3 homozygous ELKS knockout cell lines. Cells were transiently selected for puromycin resistance (1μg/μl). This transient selection resulted in a mixed population of knockout and knock-in cells that was analyzed with immunofluorescence cell staining, TIRFM, Western blotting and wound healing assay in combination of DIC live imaging.

Streptavidin pull down and GFP pull down assays

Streptavidin pull down assays with BioGFP-ELKS and BioGFP-LL5β were performed as described previously (Grigoriev et al., 2011). For streptavidin pull down assays or GFP pull down assays, bioGFP-ELKS MEFs or the Cre-re-

combined bioGFP-ELKS knock-in cells were harvested in phosphate-buffered saline (PBS), lysed in 40 mM HEPES, pH 7.5, 150 mM KCl, 1% Triton X-100 with 1x Complete protease inhibitors (Roche). The soluble fraction was collected by centrifugation at 16,000 × *g* for 10 min and incubated with Streptavidin Dynabeads M-280 (Invitrogen) or GFP-Trap® (Chromotek) beads for 2 hrs at 4 ºC. Dynabeads or GFP-Trap® beads were washed five times with ice-cold lysis buffer and analyzed by Coomassie staining or Western blotting and further processed for mass spectrometry analysis.

Western blotting was performed as described previously using alkaline phosphatase-conjugated goat anti-mouse or anti-rabbit antibodies (Sigma) or IRDye 800CW goat anti-rabbit and anti-mouse antibodies, which were detected using Odyssey Infrared Imaging system (Li-Cor Biosciences).

Mass spectrometry and data analysis

30 µl of each sample was run on a 12% Bis-Tris 1D SDS-PAGE gel (Biorad) either for 2-3 cm or ran completely and stained with colloidal Coomassie dye G-250 (Gel Code Blue Stain Reagent, Thermo Scientific). Each lane was cut into bands, which were treated with 6.5 mM dithiothreitol (DTT) for 1 hour at 60 ˚C for reduction and 54 mM iodoacetamide for 30 min for alkylation. The proteins were digested overnight with trypsin (Promega) at 37°C. The peptides were extracted with acetonitrile (ACN) and dried in a vacuum concentrator.

The data for the anti-GFP immunoprecipitation from mouse cells were acquired using an LTQ-Orbitrap coupled to an Agilent 1200 system. Peptides were first trapped (Dr Maisch Reprosil C18, 3 µm, 2 cm x 100 µm) before being separated on an analytical column (50 µm x 400 mm, 3 µm, 120 Å Reprosil C18-AQ). Trapping was performed at 5 µl/min for 10 min in solvent A (0.1 M acetic acid in water), and the gradient was as follows; 10 - 37% solvent B in 30 min, 37-100% B in 2 min, 100% B for 3 min, and finally solvent A for 15 min. Flow was passively split to 100 nl min^{-1}. Data was acquired in a data-dependent manner, to automatically switch between MS and MS/MS. Full scan MS spectra from m/z 350 to 1500 were acquired in the Orbitrap at a target value of 5e5 with a resolution of 60,000 at m/z 400. The five most intense ions were selected for fragmentation in the linear ion trap at a normalized collision energy of 35% after the accumulation of a target value of 10,000.

The data for streptavidin pull downs from MEFs were acquired using Orbitrap Q Exactive mass spectrometer. The samples were first trapped (Dr Maisch

Reprosil C18, 3 µm, 2 cm x 100 µm) before being separated on an analytical column (Zorbax SB-C18, 1.8 µm, 40 cm x 50 µm), using a gradient of 60 min at a column flow of 150 nl min^{-1}. Trapping was performed at 8 µl/min for 10 min in solvent A (0.1 M acetic acid in water) and the gradient was as follows 7-30% solvent B (0.1 M acetic acid in acetonitrile) in 31 min, 30-100% in 3 min, 100% solvent B for 5 min, and 7% solvent B for 13 min. Full scan MS spectra from *m/z* 350 – 1500 were acquired at a resolution of 35.000 at *m/z* 400 after accumulation to a target value of 3e6. Up to ten most intense precursor ions were selected for fragmentation. HCD fragmentation was performed at normalised collision energy of 25% after the accumulation to a target value of 5e4. MS/MS was acquired at a resolution of 17.500. In all cases nano-electrospray was performed at 1.7 kV using an in-house made gold-coated fused silica capillary (o.d. 360 µm; i.d. 20 µm; tip i.d. 10 µm).

Raw files were processed using Proteome Discoverer 1.4 (version 1.3.0.339, Thermo Scientific, Bremen, Germany). The database search was performed against the Swissprot house mouse database, taxonomy (version August 2014) using Mascot (version 2.4.1, Matrix Science, UK) as search engine. Carbamidomethylation of cysteines was set as a fixed modification and oxidation of methionine was set as a variable modification. Trypsin was specified as enzyme and up to two miss cleavages were allowed. Data filtering was performed using percolator, resulting in 1% false discovery rate (FDR). Additional filter was Mascot ion score >20. Raw files corresponding to one sample were merged into one result file. Data was further analysed with Saint (REF) using the Crapome web interface (www.crapome.org) in order to identify interacting proteins. Default settings were used for calculating the FC-A and FC-B score. The probability score was calculated using Saint Express performing 20.000 iterations.

The acquisition and analysis of the data for bioGFP-ELKS pull down from HEK293T cells was described earlier (Grigoriev et al., 2011; van der Vaart et al., 2013).

Immunofluorescence cell staining

Cells were fixed with 4% paraformaldehyde at room temperature for 15 min, permeabilized with 0.2% Triton X-100 in PBS and blocked with 1% bovine serum albumin in PBS. Labeling with primary and secondary antibodies was performed in PBS supplemented with 1% BSA followed by subsequent washes in PBS containing 0.15% Tween-20. Slides were air-dried and mounted in Vectashield

mounting medium (Vector laboratories). Images of fixed cells were collected with a Leica DMRBE microscope equipped with a PL Fluotar 100x 1.3 N.A. oil objective, FITC/EGFP filter 41012 (Chroma) and Texas Red filter 41004 (Chroma) and an ORCA-ER-1394 CCD camera (Hamamatsu) or a Nikon Eclipse 80i equipped with a Plan Apo VC 100x 1.4 N.A., 60x 1.4 N.A. or Plan Fluor 40x 1.3 N.A. oil objectives and a CoolSNAP HQ2 camera (Roper Scientific).

Quantification of endogenous Rab6 vesicles in fixed cells

Confocal images were obtained using a LSM700 confocal microscope (Zeiss) equipped with a Plan-Apochromat 20x 0.8 N.A., EC Plan-Neofluar 40x 1.30 N.A. and Plan-Apochromat 63x 1.40 N.A. oil objectives. Each image was a z-series of images; the obtained stacks were combined into a single image using maximum projection. Cytosol area excluding the Golgi and nuclei were measured manually. Number of endogenous Rab6 vesicles was quantified using ImageJ plugin, Comdet. Results were plotted using GraphPad Prism software.

Fluorescence microscopy of live cells

For live cell imaging, we used Nikon Eclipse Ti-E inverted microscope with perfect focus system (PFS), equipped with CFI Apo TIRF 100x 1.49 N.A. oil objective (Nikon), a TI-TIRF-E motorized TIRF illuminator (Nikon), QuantEM 512SC EMCCD camera (Photometrics, Roper Scientific). The system was controlled with MetaMorph 7.5 software (Molecular Devices). For excitation we used either mercury lamp HBO-100W/2 (Osram) or 491nm 50mW Calypso (Cobolt) and 561nm 50mW Jive (Cobolt) lasers (for regular wide-field epi-fluorescence and for TIRF, respectively). For simultaneous imaging of green and red fluorescent signals we used the ET-mCherry/GFP filter set (59022, Chroma) together with DV2 beam splitter (MAG Biosystems, Roper) equipped with dichroic filter 565dcxr (Chroma) and HQ530/30m emission filter (Chroma). To keep cells at 37 °C we used a stage top incubator (model INUG2E-ZILCS, Tokai Hit). 16-bit images were projected onto the CCD chip at a magnification of 0.065 μm/pixel with intermediate magnification 2.5X (Nikon C mount adapter 2.5X). FRAP assay was carried out using FRAP scanning system I-Las/I-Launch (Roper Scientific France/ PICT-IBiSA, Institut Curie) using the same lasers as described above.

Live imaging of Rab6 vesicles in knockout and knock-in embryonic cells

To visualize Rab6 vesicles in knockout and knock-in cells, we transiently expressed Tag-RFP-T-Rab6A using Fugene HD for 2 days and analyzed the

number of Rab6 vesicles per 500 μm^2 by imageJ plugin. We also manually counted the number of the fusion events that took place in 50 seconds per 500 μm^2 during live imaging at a frame rate of 100 ms with no delay between frames. These data were analyzed and plotted using GraphPad Prism software; Mann-Whitney U test was used for statistical analysis.

Wound healing assay and Differential Interference Contrast (DIC) imaging

We used wound healing assay to analyze the migration properties of the embryonic knockout and knock-in cells. A scratch was made in a confluent cell monolayer and cell debris were cleared by washing 3-5 times with full medium. Cells were further incubated for 1 hr so that cells at the edge of the scratch were allowed reorient the leading edge towards the monolayer wound before DIC imaging. To distinguish knock-in cells that express bio-GFP-ELKS from ELKS knockout cells, one image of GFP fluorescence was taken with a focus on the cell cortex at the beginning of each experiment. Live DIC images were acquired for 10 hours at a rate of 1 min per frame. Images of the migrating cells were processed using ImageJ. The tracking was performed using MTrackJ (Meijering et al., 2012). The track persistency and velocity of the knockout and knock-in cells were plotted and analyzed with Mann-Whitney U test using GraphPad Prism software.

Acknowledgements

We are grateful to Dr. Martine Jaegle, Dr. Vera van Dis, Ingrid M. Bergen, Dr. Rudi Hendriks, John Kongasandati, Dr. Alex Maas, Dr. Ger J. A. Arkesteijn for their help with the experiments. We tahnk Dr. Esther de Graaf, Dr. Jacqueline Deschamps, Dr. Catherine Robin and Dr. Robbert Rottier for their scientific input. We thank all animal care takers at the animal facilities of Erasmus Medical Center and Utrecht University. We also thank Dr. Dies Meijer for providing the ROSA26^{HABirA} mice, Dr. A Barnekow and Dr. F.Melchior for the gift of antibodies and Dr. Y.Mimori-Kiyosue for the TagRFP-T-Rab6 plasmid. The work is supported by the Netherlands Organization for Health Research (ZonMw) TOP grant, the Netherlands Organization for Scientific Research NWO-ALW-VICI grant and European Foundation for the Study of Diabetes (EFSD) grant to A. A.

Table I. Numbers of mice with different genotypes obtained by crossing heterozygous ELKS knockout mice. The expected numbers were calculated assuming that the heterozygous and homozygous animals are born in a 2:1 ratio.

	KO/+ (Male)	KO/+ (Female)	+/+ (Male)	+/+ (Female)	Total	Number of litters
Number	13	19	9	10	51	10
Observed Number	32		19		51	
Expected Number	34		17		51	

Table II. Numbers of mice with different genotypes obtained by crossing heterozygous BioGFP-ELKS knock-in mice. The expected numbers were calculated assuming that the heterozygous and homozygous animals are born in 1:2:1 ratio.

	KI/KI Male	KI/KI Female	KI/+ Male	KI/+ Female	+/+ Male	+/+ Female	Total	Number of litters
Number	14	11	21	27	13	14	100	13
Observed number	25		48		27		100	
Expected number	25		50		25		100	

Table III. Identification of interacting partners of ELKS and LL5β by mass spectrometry in streptavidin pull downs of BioGFP-ELKS from lysates of HEK293T cells. Proteins identified with 9 or more peptides in the ELKS pull down are included.

Protein names	ELKS Total peptides	LL5β Total peptides
ERC1 Isoform 1 of ELKS/RAB6-interacting/CAST family member 1	2643	627
ERC2 Isoform 2 of ERC protein 2	550	159
PRKDC Isoform 1 of DNA-dependent protein kinase catalytic subunit	186	9
MICAL3 microtubule associated monoxygenase, calponin and LIM domain containing 3 isoform 1	80	0
CD2AP CD2-associated protein	78	22
RPA1 Replication protein A 70 kDa DNA-binding subunit	72	0
PTPN13 Isoform 1 of Tyrosine-protein phosphatase non-receptor type 13	58	0
TTF2 Isoform 1 of Transcription termination factor 2	50	0
PARP1 Poly [ADP-ribose] polymerase 1	47	0
HOMER2 Isoform 1 of Homer protein homolog 2	46	0
ANKRD27 Ankyrin repeat domain-containing protein 27	45	0
XRCC5 ATP-dependent DNA helicase 2 subunit 2	44	0
LIG3 Isoform Beta of DNA ligase 3	42	0
TFCP2 Transcription factor CP2, isoform CRA_d	41	0
LEMD2 LEM domain-containing protein 2	39	0
PHLDB1 Isoform 1 of Pleckstrin homology-like domain family B member 1	37	53
HLTF Isoform 1 of Helicase-like transcription factor	37	4
EEF1A1;EEF1AL3 Putative elongation factor 1-alpha-like 3	36	37
XRCC6 ATP-dependent DNA helicase 2 subunit 1	36	0
ILVBL Isoform 1 of Acetolactate synthase-like protein	35	0
CIT Citron	33	67
TMPO Isoform Beta of Lamina-associated polypeptide 2, isoforms beta/gamma	32	0
LMNB1 Lamin-B1	30	0
PPFIBP1 Isoform 4 of Liprin-beta-1	30	0
LMNA Isoform A of Lamin-A/C	29	1
TOP2B Isoform Beta-1 of DNA topoisomerase 2-beta	26	0

CIT Isoform 3 of Citron Rho-interacting kinase	26	0
TOP2B 134 kDa protein	26	0
DHX29 ATP-dependent RNA helicase DHX29	26	0
TFE3 Putative uncharacterized protein TFE3	25	0
TOP2A Isoform 4 of DNA topoisomerase 2-alpha	24	0
PHLDB2 Isoform 1 of Pleckstrin homology-like domain family B member 2	24	2966
CEP350 Centrosome-associated protein 350	23	0
CYLD Isoform 2 of Probable ubiquitin carboxyl-terminal hydrolase CYLD	21	14
XRCC1 DNA repair protein XRCC1	20	0
GOLGA3 Isoform 1 of Golgin subfamily A member 3	19	0
PPFIA1 Isoform 1 of Liprin-alpha-1	19	5
HSPA1B;HSPA1A 25 kDa protein	19	0
UBP1 Isoform 1 of Upstream-binding protein 1	18	0
PPP2R1A cDNA FLJ56053, highly similar to Serine/threonine-protein phosphatase 2A 65 kDa regulatory subunit A alpha isoform	18	2
LMNB2 Lamin-B2	17	0
CHD1L Isoform 2 of Chromodomain-helicase-DNA-binding protein 1-like	16	0
FMR1 Isoform 4 of Fragile X mental retardation 1 protein	16	10
CTTN Cortactin, isoform CRA_a	16	0
EVPL Envoplakin	15	0
DNAJC13 DnaJ homolog subfamily C member 13	15	0
DDX3Y ATP-dependent RNA helicase DDX3Y	14	0
SHPRH Isoform 1 of E3 ubiquitin-protein ligase SHPRH	14	0
SHPRH SNF2 histone linker PHD RING helicase isoform a	14	0
FBXO28 F-box only protein 28	13	0
BTAF1 TATA-binding protein-associated factor 172	13	0
SPATA2 Spermatogenesis-associated protein 2	13	4
LOC100289922;TIMP2 cDNA FLJ32655 fis, clone TESTI1000025, weakly similar to DDC8	12	0
KIF23 Isoform 1 of Kinesin-like protein KIF23	12	3
SMC4 7 kDa protein	12	0
FGFR1OP Isoform 1 of FGFR1 oncogene partner	12	0
CPVL Probable serine carboxypeptidase CPVL	11	0
ZC3HAV1 Isoform 1 of Zinc finger CCCH-type antiviral protein 1	11	9
CCDC88C Isoform 1 of Protein Daple	11	12

- cDNA FLJ16186 fis, clone BRTHA2007060, moderately similar to EUKARYOTIC TRANSLATION INITIATION FACTOR 3 SUBUNIT 10	11	0
RBM4;RBM14 Isoform 1 of RNA-binding protein 14	11	5
DNAH14 Isoform 1 of Dynein heavy chain 14, axonemal	10	3
TRIM26 Tripartite motif-containing protein 26	10	44
DYNC2H1 Isoform 2 of Cytoplasmic dynein 2 heavy chain 1	10	6
PARP2 Isoform 2 of Poly [ADP-ribose] polymerase 2	10	0
PARP2 Isoform 1 of Poly [ADP-ribose] polymerase 2	10	0
VCAN Isoform Vint of Versican core protein	10	12
CRTC2 CREB-regulated transcription coactivator 2	10	0
ZFP161 Zinc finger protein 161 homolog	10	0
DNAH14 dynein, axonemal, heavy polypeptide 14 isoform 1	10	3
DYNC2H1 Isoform 1 of Cytoplasmic dynein 2 heavy chain 1	10	6
KIF14 Kinesin-like protein KIF14	9	33
HIC2 Isoform 1 of Hypermethylated in cancer 2 protein	9	0
GRAMD1A Isoform 2 of GRAM domain-containing protein 1A	9	0
HIC2 Isoform 2 of Hypermethylated in cancer 2 protein	9	0
GRAMD1A cDNA FLJ39896 fis, clone SPLEN2016972	9	0
HOXA10 Isoform 1 of Homeobox protein Hox-A10	9	0
FOXC1 Forkhead box protein C1	9	0
GRAMD1A Isoform 3 of GRAM domain-containing protein 1A	9	0

Table IV. Identification of interacting partners of ELKS by mass spectrometry in streptavidin pull downs of BioGFP-ELKS from lysates of BioGFP-ELKS knock-in MEFs expressing biotin ligase BirA. The numbers of total peptides for the same proteins identified by streptavidin pull downs in HEK293T cells over-expressing BioGFP-ELKS (Table III) or by immunoprecipitation with anti-GFP antibodies from lysates of BioGFP-ELKS knock-in cells (Table V) are included for comparison. Proteins identified with 2 or more peptides are included.

Protein names	Streptavidin pull down, MEFs Total peptides	Anti-GFP IP MEFs Total peptides	Streptavidin pull down, HEK293T Total peptides
ELKS/Rab6-interacting/CAST family member 1 ERC1	54	43	2643
ERC protein 2 ERC2	10	12	550
Poly [ADP-ribose] polymerase 1 PARP1	8	0	47
DNA ligase 3 DNLI3	5	9	42
Fragile X mental retardation protein 1 FMR1	4	0	16
DNA repair protein XRCC1	3	2	20
Pleckstrin homology-like domain family B member 2 PHLB2	3	0	24
Double-stranded RNA-binding protein Staufen homolog 1 STAU1	3	0	6
Sorbin and SH3 domain-containing protein 1 SRBS1	3	0	2
Protein disulfide-isomerase A3 PDIA3	3	0	1
Inactive serine/threonine-protein kinase VRK3	2	2	3
Transcription factor E3 TFE3	2	0	25
Serine/threonine-protein phosphatase 2A 65 kDa regulatory subunit A alpha isoform Ppp2r1a	2	0	18
Insulin-like growth factor 2 mRNA-binding protein 3 Igf2bp3	2	0	4

Table V. Identification of interacting partners of ELKS by mass spectrometry using immunoprecipitation with anti-GFP antibodies from lysates of BioGFP-ELKS knock-in cells. The number of total peptides for the same proteins identified by streptavidin pull downs in HEK293T cells overexpressing BioGFP-ELKS (Table III) or BioGFP-ELKS knock-in MEFs (Table IV) are included for comparison. Proteins identified with 2 or more peptides are included.

Protein names	Anti-GFP IP MEFs Total peptides	Streptavidin pull down, MEFs Total peptides	Streptavidin pull down, HEK293T Total peptides
ELKS/Rab6-interacting/CAST family member 1 ERC1	43	54	2643
ATP-dependent RNA helicase Dhx29	16	0	26
ERC protein 2 ERC2	12	10	550
DNA ligase 3 DNLI3	9	5	42
Nesprin-1 SYNE1	4	0	2
E3 SUMO-protein ligase CBX4	3	0	8
Probable ATP-dependent RNA helicase DDX41	3	0	7
Polyhomeotic-like protein 2 PHC2	3	0	3
Phosphatidylinositol 3-kinase regulatory subunit beta P85B	3	0	2
Kinesin-like protein KIF1B	3	0	2
Ubiquitin carboxyl-terminal hydrolase CYLD	2	0	21
DNA repair protein XRCC1	2	3	20
Upstream-binding protein 1 UBIP1	2	0	18
Cytoplasmic dynein 2 heavy chain 1 DYHC2	2	0	10
Inactive serine/threonine-protein kinase VRK3	2	2	3
TNF receptor-associated factor 2 TRAF2	2	0	2
F-box/WD repeat-containing protein 11 FBW1B	2	0	2
Smoothelin SMTN	2	0	2
Ran GTPase-activating protein 1 RANGAP1	2	0	2
E3 ubiquitin-protein ligase HUWE1	2	0	2
Dynactin subunit 1 DCTN1	2	0	2
WD repeat-containing protein 48 WDR48	2	0	2
Transcriptional activator GLI3	2	0	1
Chromobox protein homolog 6 CBX6]	2	0	1

References

Akhmanova, A., C.C. Hoogenraad, K. Drabek, T. Stepanova, B. Dortland, T. Verkerk, W. Vermeulen, B.M. Burgering, C.I. De Zeeuw, F. Grosveld, and N. Galjart. 2001. Clasps are CLIP-115 and -170 associating proteins involved in the regional regulation of microtubule dynamics in motile fibroblasts. *Cell*. 104:923-35.

Akhmanova, A., A.L. Mausset-Bonnefont, W. van Cappellen, N. Keijzer, C.C. Hoogenraad, T. Stepanova, K. Drabek, J. van der Wees, M. Mommaas, J. Onderwater, H. van der Meulen, M.E. Tanenbaum, R.H. Medema, J. Hoogerbrugge, J. Vreeburg, E.J. Uringa, J.A. Grootegoed, F. Grosveld, and N. Galjart. 2005. The microtubule plus-end-tracking protein CLIP-170 associates with the spermatid manchette and is essential for spermatogenesis. *Genes Dev*. 19:2501-15.

Astro, V., S. Chiaretti, E. Magistrati, M. Fivaz, and I. de Curtis. 2014. Liprin-alpha1, ERC1 and LL5 define polarized and dynamic structures that are implicated in cell migration. *J Cell Sci*. 127:3862-76.

Au, P.Y., and W.C. Yeh. 2007. Physiological roles and mechanisms of signaling by TRAF2 and TRAF5. *Adv Exp Med Biol*. 597:32-47.

Bassi, Z.I., M. Audusseau, M.G. Riparbelli, G. Callaini, and P.P. D'Avino. 2013. Citron kinase controls a molecular network required for midbody formation in cytokinesis. *Proc Natl Acad Sci U S A*. 110:9782-7.

Billings, S.E., G.L. Clarke, and H. Nishimune. 2012. ELKS1 and Ca(2+) channel subunit beta4 interact and colocalize at cerebellar synapses. *Neuroreport*. 23:49-54.

Courtois, G. 2008. Tumor suppressor CYLD: negative regulation of NF-kappaB signaling and more. *Cell Mol Life Sci*. 65:1123-32.

de Boer, E., P. Rodriguez, E. Bonte, J. Krijgsveld, E. Katsantoni, A. Heck, F. Grosveld, and J. Strouboulis. 2003. Efficient biotinylation and single-step purification of tagged transcription factors in mammalian cells and transgenic mice. *Proc Natl Acad Sci U S A*. 100:7480-5.

Driegen, S., R. Ferreira, A. van Zon, J. Strouboulis, M. Jaegle, F. Grosveld, S. Philipsen, and D. Meijer. 2005. A generic tool for biotinylation of tagged proteins in transgenic mice. *Transgenic Res*. 14:477-482.

Ducut Sigala, J.L., V. Bottero, D.B. Young, A. Shevchenko, F. Mercurio, and

I.M. Verma. 2004. Activation of transcription factor NF-kappaB requires ELKS, an IkappaB kinase regulatory subunit. *Science*. 304:1963-7.

Grigoriev, I., D. Splinter, N. Keijzer, P.S. Wulf, J. Demmers, T. Ohtsuka, M. Modesti, I.V. Maly, F. Grosveld, C.C. Hoogenraad, and A. Akhmanova. 2007. Rab6 regulates transport and targeting of exocytotic carriers. *Dev Cell*. 13:305-14.

Grigoriev, I., K.L. Yu, E. Martinez-Sanchez, A. Serra-Marques, I. Smal, E. Meijering, J. Demmers, J. Peranen, R.J. Pasterkamp, P. van der Sluijs, C.C. Hoogenraad, and A. Akhmanova. 2011. Rab6, Rab8, and MICAL3 Cooperate in Controlling Docking and Fusion of Exocytotic Carriers. *Curr Biol*. 21:967-74.

Gruneberg, U., R. Neef, X. Li, E.H. Chan, R.B. Chalamalasetty, E.A. Nigg, and F.A. Barr. 2006. KIF14 and citron kinase act together to promote efficient cytokinesis. *J Cell Biol*. 172:363-72.

Harhaj, E.W., and V.M. Dixit. 2012. Regulation of NF-kappaB by deubiquitinases. *Immunol Rev*. 246:107-24.

Hida, Y., and T. Ohtsuka. 2010. CAST and ELKS proteins: structural and functional determinants of the presynaptic active zone. *J Biochem*. 148:131-7.

Hoogenraad, C.C., B. Koekkoek, A. Akhmanova, H. Krugers, B. Dortland, M. Miedema, A. van Alphen, W.M. Kistler, M. Jaegle, M. Koutsourakis, N. Van Camp, M. Verhoye, A. van der Linden, I. Kaverina, F. Grosveld, C.I. De Zeeuw, and N. Galjart. 2002. Targeted mutation of Cyln2 in the Williams syndrome critical region links CLIP-115 haploinsufficiency to neurodevelopmental abnormalities in mice. *Nat Genet*. 32:116-27.

Ikeda, K., and S. Inoue. 2012. TRIM proteins as RING finger E3 ubiquitin ligases. *Adv Exp Med Biol*. 770:27-37.

Ishida-Takagishi, M., A. Enomoto, N. Asai, K. Ushida, T. Watanabe, T. Hashimoto, T. Kato, L. Weng, S. Matsumoto, M. Asai, Y. Murakumo, K. Kaibuchi, A. Kikuchi, and M. Takahashi. 2012. The Dishevelled-associating protein Daple controls the non-canonical Wnt/Rac pathway and cell motility. *Nat Commun*. 3:859.

Kaeser, P.S., L. Deng, A.E. Chavez, X. Liu, P.E. Castillo, and T.C. Sudhof. 2009. ELKS2alpha/CAST deletion selectively increases neurotransmitter release at inhibitory synapses. *Neuron*. 64:227-39.

Ko, J., M. Na, S. Kim, J.R. Lee, and E. Kim. 2003. Interaction of the ERC family of RIM-binding proteins with the liprin-alpha family of multidomain

proteins. *J Biol Chem*. 278:42377-85.

Lansbergen, G., I. Grigoriev, Y. Mimori-Kiyosue, T. Ohtsuka, S. Higa, I. Kitajima, J. Demmers, N. Galjart, A.B. Houtsmuller, F. Grosveld, and A. Akhmanova. 2006. CLASPs attach microtubule plus ends to the cell cortex through a complex with LL5beta. *Dev Cell*. 11:21-32.

Liu, C., L.S. Bickford, R.G. Held, H. Nyitrai, T.C. Sudhof, and P.S. Kaeser. 2014. The active zone protein family ELKS supports Ca2+ influx at nerve terminals of inhibitory hippocampal neurons. *J Neurosci*. 34:12289-303.

Meijering, E., O. Dzyubachyk, and I. Smal. 2012. Methods for cell and particle tracking. *Methods Enzymol*. 504:183-200.

Nakata, T., T. Yokota, M. Emi, and S. Minami. 2002. Differential expression of multiple isoforms of the ELKS mRNAs involved in a papillary thyroid carcinoma. *Genes Chromosomes Cancer*. 35:30-7.

Niu, J., Y. Shi, K. Iwai, and Z.H. Wu. 2011. LUBAC regulates NF-kappaB activation upon genotoxic stress by promoting linear ubiquitination of NEMO. *EMBO J*. 30:3741-53.

Nomura, H., T. Ohtsuka, S. Tadokoro, M. Tanaka, and N. Hirashima. 2009. Involvement of ELKS, an active zone protein, in exocytotic release from RBL-2H3 cells. *Cell Immunol*. 258:204-11.

Ohara-Imaizumi, M., T. Ohtsuka, S. Matsushima, Y. Akimoto, C. Nishiwaki, Y. Nakamichi, T. Kikuta, S. Nagai, H. Kawakami, T. Watanabe, and S. Nagamatsu. 2005. ELKS, a protein structurally related to the active zone-associated protein CAST, is expressed in pancreatic beta cells and functions in insulin exocytosis: interaction of ELKS with exocytotic machinery analyzed by total internal reflection fluorescence microscopy. *Mol Biol Cell*. 16:3289-300.

Paranavitane, V., W.J. Coadwell, A. Eguinoa, P.T. Hawkins, and L. Stephens. 2003. LL5beta is a phosphatidylinositol (3,4,5)-trisphosphate sensor that can bind the cytoskeletal adaptor, gamma-filamin. *J Biol Chem*. 278:1328-35.

Schlager, M.A., A. Serra-Marques, I. Grigoriev, L.F. Gumy, M. Esteves da Silva, P.S. Wulf, A. Akhmanova, and C.C. Hoogenraad. 2014. Bicaudal d family adaptor proteins control the velocity of Dynein-based movements. *Cell Rep*. 8:1248-56.

Stehbens, S.J., M. Paszek, H. Pemble, A. Ettinger, S. Gierke, and T. Wittmann. 2014. CLASPs link focal-adhesion-associated microtubule capture to

localized exocytosis and adhesion site turnover. *Nat Cell Biol*. 16:561-73.

van der Vaart, B., W.E. van Riel, H. Doodhi, J.T. Kevenaar, E.A. Katrukha, L. Gumy, B.P. Bouchet, I. Grigoriev, S.A. Spangler, K.L. Yu, P.S. Wulf, J. Wu, G. Lansbergen, E.Y. van Battum, R.J. Pasterkamp, Y. Mimori-Kiyosue, J. Demmers, N. Olieric, I.V. Maly, C.C. Hoogenraad, and A. Akhmanova. 2013. CFEOM1-associated kinesin KIF21A is a cortical microtubule growth inhibitor. *Dev Cell*. 27:145-60.

Wu, Z.H., Y. Shi, R.S. Tibbetts, and S. Miyamoto. 2006. Molecular linkage between the kinase ATM and NF-kappaB signaling in response to genotoxic stimuli. *Science*. 311:1141-6.

Wu, Z.H., E.T. Wong, Y. Shi, J. Niu, Z. Chen, S. Miyamoto, and V. Tergaonkar. 2010. ATM- and NEMO-dependent ELKS ubiquitination coordinates TAK1-mediated IKK activation in response to genotoxic stress. *Mol Cell*. 40:75-86.

Chapter 7

ELKS at the cortex: functions and dynamics

Ka Lou Yu*, Eugene A. Katrukha*, Anael Chazeau, Ilya Grigoriev, Ivar Noordstra, Casper C. Hoogenraad, Lukas C. Kapitein and Anna Akhmanova

Cell Biology, Faculty of Science, Utrecht University, Padualaan 8, 3584 CH Utrecht, The Netherlands

* These authors have contributed equally to this chapter.

Manuscript in preparation

Abstract

ELKS is a coiled coil adaptor protein implicated in constitutive and regulated secretion, cytoskeletal organization and NF-κB signalling. A significant part of the cellular pool of the ELKS protein is localised at the cell cortex to distinct sites at the leading edges of migrating cells and in the vicinity of focal adhesions. Here we show that the cortical localization of ELKS strongly depends on liprin-α1 and liprin-β1. ELKS also affects the localization of several cortical proteins, such as the spectraplakin ACF7/MACF1, and, to a lesser extent LL5β and the two liprins, which contribute to microtubule stabilization at the cell periphery. Analysis of cells in which the endogenous ELKS protein was tagged with GFP showed that ELKS forms clusters that are excluded from focal adhesions and ventral stress fibers. ELKS clusters undergo complex dynamics, and although ELKS targeting to the plasma membrane does not require actin, ELKS distribution and motility at the cortex is controlled by the actin cytoskeleton and actomyosin-dependent flows. Fluorescence recovery after photobleaching (FRAP) experiments showed that cortical ELKS exchanges with the cytoplasmic pool in the form of dimers. Analysis of GFP-ELKS at the cortex of pancreatic β cells, where ELKS clusters serve as docking sites for the insulin granules, demonstrated that the pattern of ELKS distribution is similar to that found in HeLa cells and fibroblasts. ELKS turnover in β cells is regulated by glucose, indicating that the docking machinery for insulin granules is controlled by signals which activate insulin secretion. Taken together, our data show that ELKS is a part of a multiprotein cortical assembly, which is targeted to the plasma membrane independently of actin but is linked to the actin cortex and can be affected by signalling controlling regulated exocytosis.

Results and Discussion

Mutual dependence of ELKS, liprins, LL5β and ACF7 for their cortical localization

ELKS is a coiled coil adaptor protein, which has been implicated in a number of different cellular processes including secretion, synaptic function, microtubule organization and NF-κB signaling (Ducut Sigala et al., 2004; Hida and Ohtsuka, 2010; Lansbergen et al., 2006). The cortical function of ELKS in non-neuronal cells was originally identified in a search for the partners of the microtubule plus end tracking proteins CLASP1/2, which can stabilize microtubules at the leading edge of migrating fibroblasts (Akhmanova et al., 2001; Lansbergen et al., 2006). Biochemical analysis showed that CLASPs do not associate with ELKS directly, but bind to the ELKS-interacting protein LL5β (Lansbergen et al., 2006). LL5β is a phosphatidylinositol-3,4,5-triphosphate (PIP3) binding protein, which localizes to the cell cortex in a manner that is in part dependent on the activity of phosphatidylinositol-4,5-bisphosphate 3-kinase (Lansbergen et al., 2006; Paranavitane et al., 2003). ELKS requires LL5β for its cortical recruitment; in turn, ELKS affects to some extent the clustering of LL5β at the cortex, the recruitment of CLASPs and microtubule stabilization (Lansbergen et al., 2006). CLASP- and LL5α/β-dependent microtubule stabilization at the basal cell cortex plays a role in the regulation of epithelial polarity as well as epiblast integrity during embryogenesis (Hotta et al., 2010; Nakaya et al., 2013). In muscle cells, CLASP and LL5β are present at the post-synaptic side of the neuromuscular junction, where they control important aspects of the postsynaptic architecture such as the delivery of acetylcholine receptors (Basu et al., 2015; Basu et al., 2014; Kishi et al., 2005; Proszynski et al., 2009; Proszynski and Sanes, 2013; Schmidt et al., 2012). ELKS is also present at the neuromuscular junctions (Tokoro et al., 2007) and likely participates in these processes.

Proteomics-based searches for the partners of LL5β and ELKS and subsequent analyses identified additional partners of the complex, including scaffolding proteins liprin-α1, liprin-β1, KANK1/2 and the kinesin-4 KIF21A (van der Vaart et al., 2013). The finding of the liprins was not surprising, because liprin-α1 is a known binding partner of ELKS (Ko et al., 2003), and α- and β-liprins are known to bind to each other (Spangler and Hoogenraad, 2007).

Here, we set out to test the mutual dependence of liprins and ELKS for their cortical localization. Depletion of both liprin-α1 and liprin-β1 very strongly reduced ELKS enrichment at the peripheral cortex of HeLa cells (Fig. 1A-D,G). The depletion of each of the two liprins also reduced the cortical clustering of the other one as well as that of LL5β (Fig.2A-C, G). Conversely, the knockdown of LL5β reduced the cortical clustering of liprins (Fig.2D,G). Combined with our previous results (Lansbergen et al., 2006), we conclude that in HeLa cells ELKS is targeted to the cortex by the combined action of liprin-α1, liprin-β1 and LL5β. Liprin-α1 and LL5β can contribute to the localization of ELKS through the previously identified direct interactions (Ko et al., 2003; Lansbergen et al., 2006). It should be noted that the ELKS interacts with liprin-α1 and LL5β through overlapping coiled coil domains in the N-terminal part of the protein (Ko et al., 2003; Lansbergen et al., 2006), and it is currently unknown whether ELKS can interact with the two proteins simultaneously. Liprin-β1 might also interact with ELKS directly, since it was a highly significant hit in the ELKS pull down from HEK293T cells (Chapter 6). In contrast to ELKS, LL5β and liprins do not strictly require each other for the cortical recruitment, but their concentration at the cell periphery is mutually dependent (Fig. 2A-D,G). In particular, liprin-β1 appears to be important for the peripheral clustering of the other proteins (Fig.1D, 2C). Liprin-β1 interacts with KANK1 and KANK2, two other cortical scaffolding factors, and co-clustering with these proteins likely contributes to the organization of LL5β-liprin "patches" at the cortex (van der Vaart et al., 2013). We conclude that ELKS is targeted to the cell cortex by LL5β and liprins, but due to the mutual dependencies of these proteins it is not possible to establish a hierarchy of their recruitment to the plasma membrane.

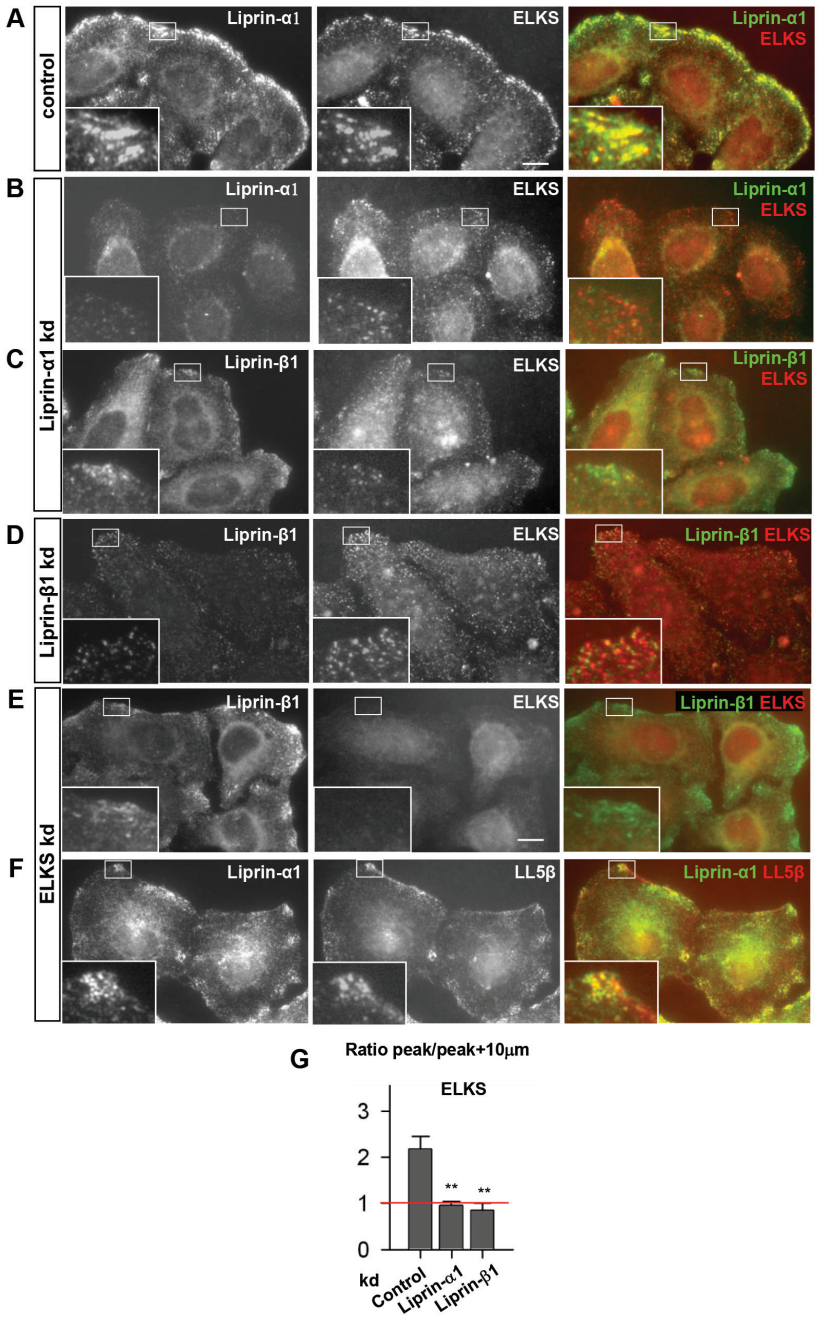

Figure 1. Analysis of the interdependence of liprins and ELKS for the cortical recruitment and clustering. A-F. HeLa cells were transiently transfected with different siRNAs. 3 days later, the cells were fixed and stained with the indicated antibodies. The insets show enlargements of the boxed areas.
G. Ratio of the peak value of average intensity of ELKS staining to the average intensity in the internal cytoplasm at a 10 μm distance from the peak along the same radius. Measurements were performed in 10 cells per condition; error bars indicate standard error of mean (SEM). The ratio equal to 1, indicating absence of enrichment at the peripheral cortex, is indicated by a red line. Scale bar, 10 μm.

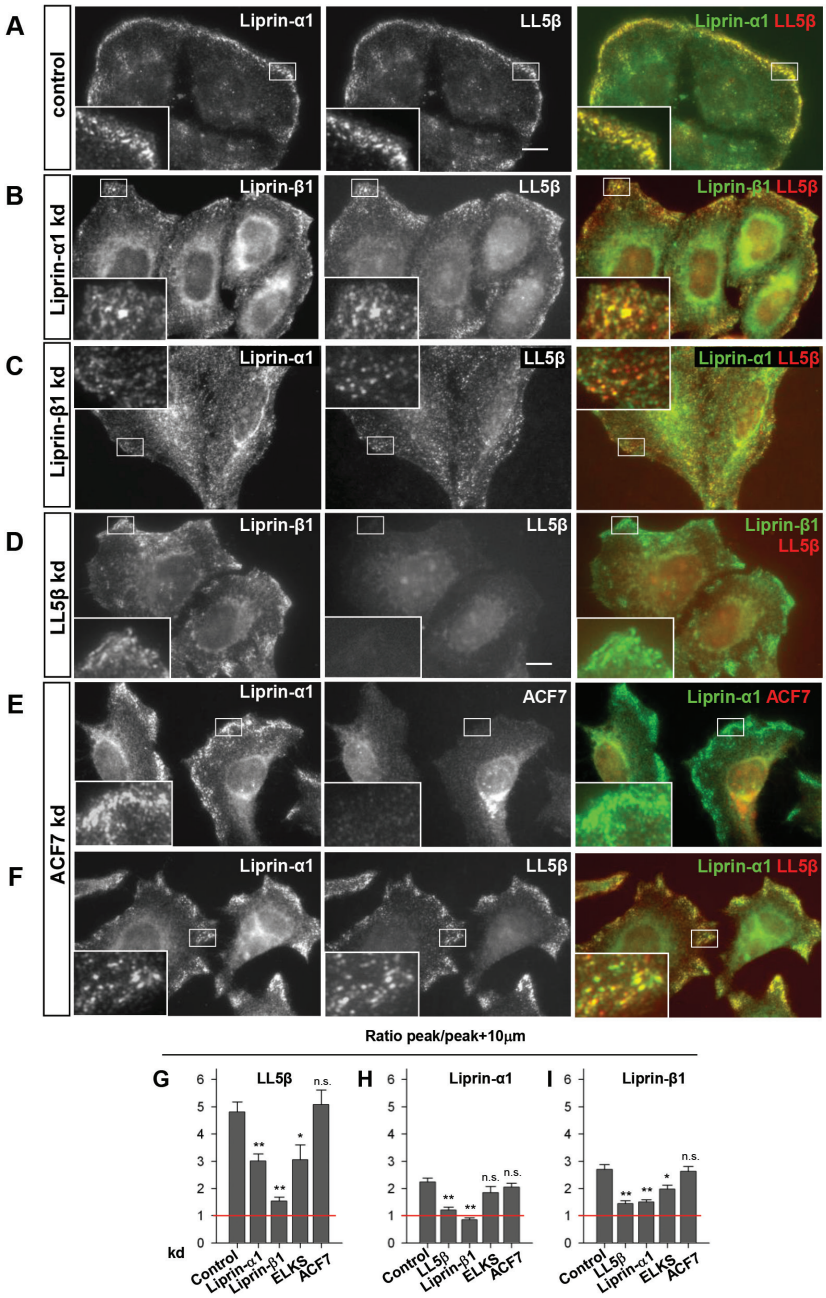

Figure 2. Analysis of the interdependence of liprins, LL5β and ACF7 for the cortical recruitment and clustering.

A-F. HeLa cells were transiently transfected with different siRNAs. 3 days later, the cells were fixed and stained with the indicated antibodies. The insets show enlargements of the boxed areas.

G. Ratio of the peak value of average intensity of LL5β, liprin-α1 or liprin-β1 staining to the average intensity in the internal cytoplasm at a 10 μm distance from the peak along the same radius. The plots were prepared in the same way as described for Fig. 1G. Measurements were performed in 10 cells per condition. Scale bar, 10 μm.

We next investigated the importance of ELKS for the cortical localization of liprins. Previous work has shown that ELKS is not essential for the cortical localization of LL5β, but contributes to its clustering (Lansbergen et al., 2006). Similarly, ELKS was not required for the cortical localization of the two liprins (Fig. 1E,F). Interestingly, although there is no evidence for the direct binding between the two liprins and LL5β, they still display a significant degree of colocalization in ELKS-depleted cells (Fig.1F), indicating that ELKS is not the only link that can connect them. While this work was in progress, a study performed in breast cancer cells MDA-231 showed that, similar to HeLa cells, liprin-α1 and LL5α/β depend on each other for efficient accumulation in cell protrusions, recruit ELKS to the protruding lamella but are not strictly dependent on ELKS for their localization (Astro et al., 2014). Taken together, these data suggest that LL5s and liprins are the mutually dependent core components of the cortical "patches", while ELKS depends on both of them and contributes to their clustering but is not essential for their membrane recruitment.

Another protein, which was reported to colocalize with CLASPs at the peripheral cortex of HeLa cells and contribute to CLASP recruitment is the spectraplakin ACF7 (actin cross-linking factor 7, also known as microtubule-actin cross-linking factor 1 (MACF1), macrophin, trabeculin α, and ABP620) (Drabek et al., 2006). Spectraplakins are huge cytoskeletal proteins, which contain domains that can bind to actin, microtubules and the microtubule plus end tracking protein EB1 (Huelsmann and Brown, 2014; Roper et al., 2002). We investigated which of the cortical proteins discussed here are required for the cortical targeting of ACF7. We found that the localization of ACF7 showed low sensitivity to the depletion of LL5β but was strongly affected by the depletion of both liprins and ELKS (Fig.3A-F). Since ACF7 contributes to the localization of CLASPs to the cortex and can also bind and organize microtubules (Drabek et al., 2006; Kodama et al., 2003), these data explain the relatively strong effect of the knockdown of liprins and ELKS on the microtubule density at the periphery of HeLa cells (Lansbergen et al., 2006; van der Vaart et al., 2013). The depletion of ACF7 had no significant effect on the localization of liprins or LL5β (Fig.2E-G), suggesting that, similar to CLASPs, the spectraplakin has only a peripheral role in the organization of cortical complexes, and its main function is related to the regulation of microtubules and/or actin.

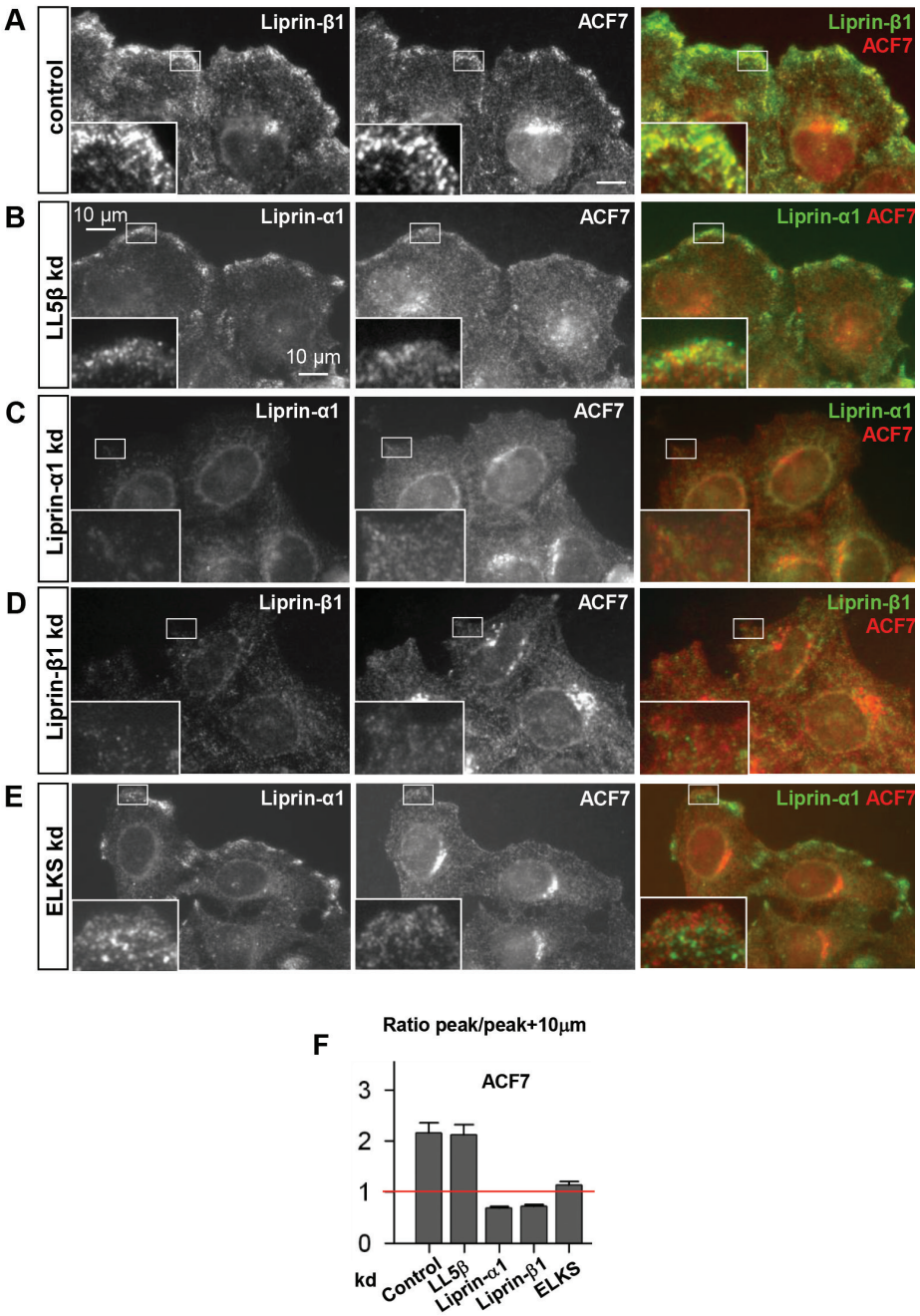

Figure 3. Analysis of the cortical recruitment and clustering of ACF7.
A-E. HeLa cells were transiently transfected with different siRNAs. 3 days later, the cells were fixed and stained with the indicated antibodies. The insets show enlargements of the boxed areas.
F. Ratio of the peak value of average intensity of ACF7 staining to the average intensity in the internal cytoplasm at a 10 μm distance from the peak along the same radius. The plots were prepared in the same way as described for Fig. 1G. Measurements were performed in 10 cells per condition. Scale bar, 10 μm.

Cortical patches containing ELKS, LL5β and liprin-α1 are a common property of insulin-producing cells and fibroblasts

Our work in HeLa cells and fibroblasts showed that ELKS is required in for constitutive secretion (Chapter 6, (Grigoriev et al., 2007; Grigoriev et al., 2011)). However, ELKS is also abundantly present in cells involved in regulated secretion, such as neurons and pancreatic β cells. In neurons, ELKS is part of the cytomatrix at the active zone (CAZ), which includes liprin-α and multiple specialize components such as Bassoon, Piccolo and RIM1 that interact with ELKS (Takao-Rikitsu et al., 2004; Wang et al., 2002), but seems to lack LL5s that are poorly expressed in neurons (our unpublished data). In pancreatic β cells, ELKS localizes to the docking sites of the insulin granules at the plasma membrane, and the reduction of ELKS expression by RNA interference reduced the glucose-induced insulin release (Ohara-Imaizumi et al., 2005). Bassoon was found to co-localize with ELKS in insulinoma cells (Ohara-Imaizumi et al., 2005), and RIM1 was implicated in insulin secretion (Iezzi et al., 2000), suggesting that the sites of docking and fusion of insulin granules share similarity with the CAZ. Using cultured rat insulinoma INS1 cells, we could confirm that ELKS was distributed in cortical clusters, and that insulin granules colocalized with these clusters (Fig.4A). Interestingly, we found that LL5β and liprin-α1 were abundantly present at the cortex of INS1 cells, where they colocalized with each other and with ELKS clusters (Fig.4B,C). A similar colocalization pattern was observed in different types of fibroblasts, including mouse embryonic fibroblasts (MEFs, data not shown) and the bioGFP-ELKS expressing mouse cells (termed BioGFP-ELKS/Cre cells, Fig.5), which we have generated by Cre-mediated recombination from ELKS knockout cells (Chapter 6). We conclude that cortical colocalization of ELKS, LL5s and liprins is a very general property of many non-neuronal cell types and that insulin docking and fusion sites in pancreatic β cells appear to share features both with the neuronal CAZ and with the sites of constitutive exocytosis in fibroblasts and epithelia.

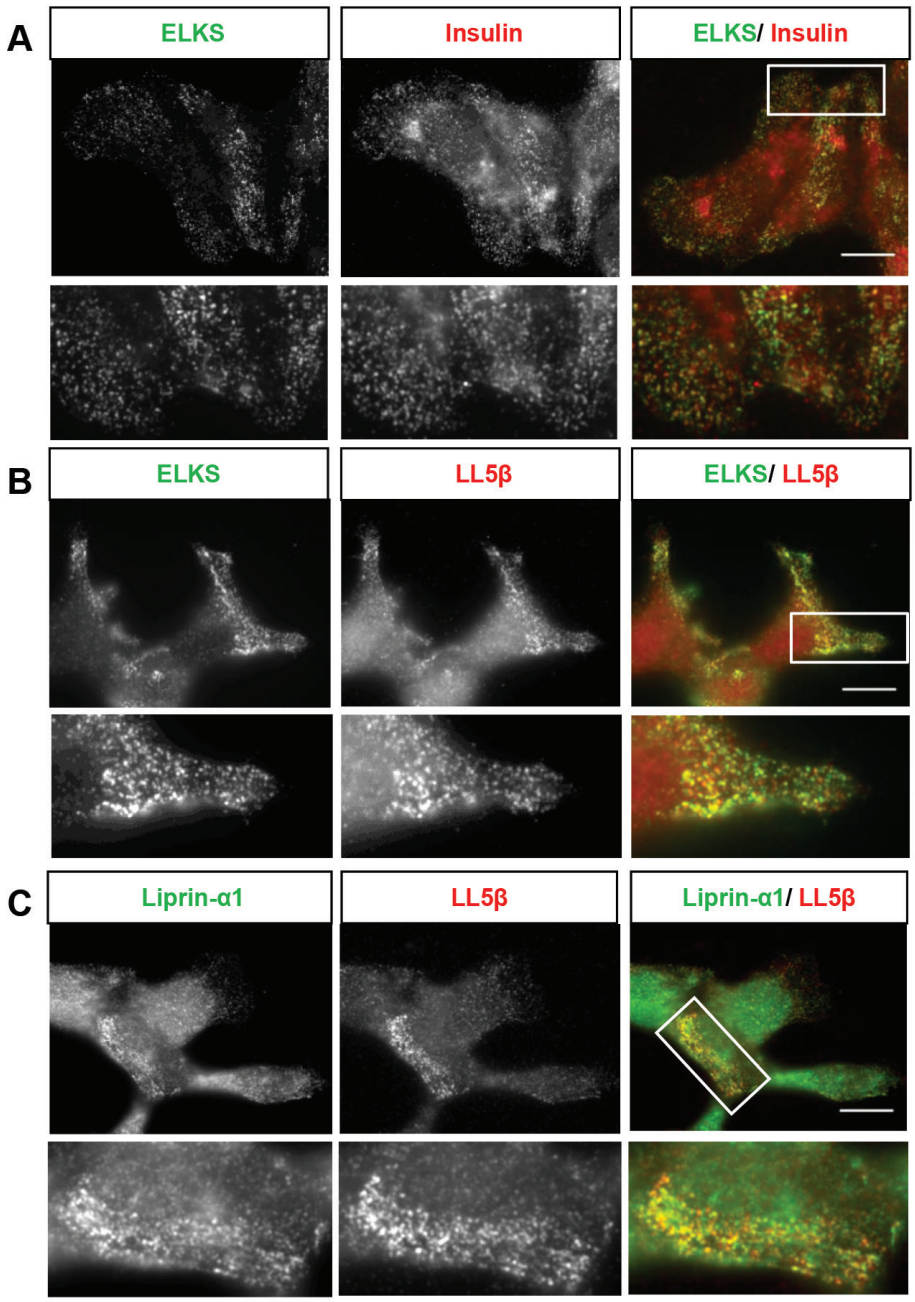

Figure 4. ELKS, LL5β and liprin-α1 colocalize in INS1 rat insulinoma cells.
A.INS1 cells were fixed in 4% PFA and stained with antibodies against ELKS and insulin.
B, C. INS1 cells were fixed in -20°C methanol and stained with antibodies against ELKS and LL5β (B) or liprin-α1 and LL5β (C). Scale bar, 10 μm.

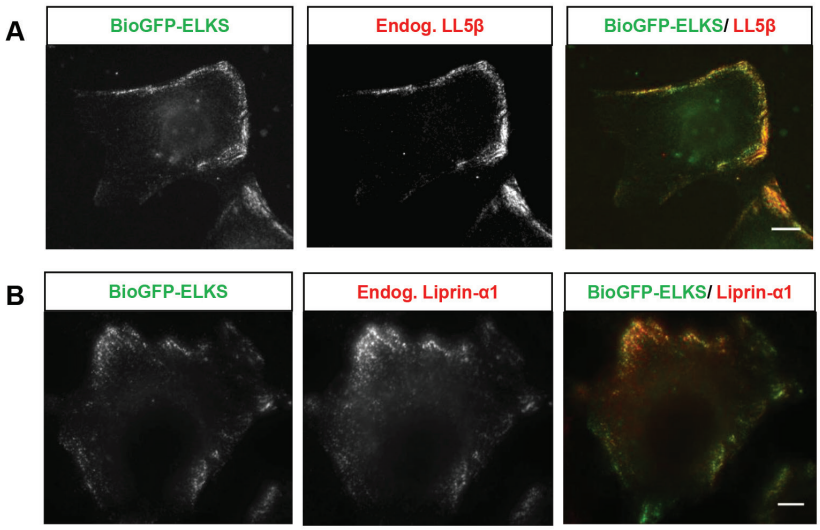

Figure 5. ELKS, LL5β and liprin-α1 colocalize in BioGFP-ELKS/Cre cells.
A,B. BioGFP-ELKS/Cre cells were fixed in -20°C methanol and stained with antibodies against LL5β (A) or liprin-α1 (B). BioGFP-ELKS was detected by direct GFP fluorescence. Scale bar, 10 μm.

Cortical dynamics of ELKS clusters

In Chapter 6, we have described the generation of BioGFP-ELKS knock-in mouse and provided strong data indicating that the BioGFP-ELKS protein is functional and expressed at levels close to endogenous, suggesting that tissues and cells derived from this mouse can be used to investigate ELKS distribution and dynamics. To investigate ELKS dynamics at the cortex, we focused on two model systems. The first one was the BioGFP-ELKS/Cre cell line generated by Cre-mediated recombination from ELKS knockout cells (Chapter 6). This cell culture model was more convenient compared to bioGFP-ELKS MEFs isolated directly from bioGFP-ELKS knock-in embryos, because the BioGFP-ELKS/Cre cells had uniform morphology, were highly motile in culture and, in contrast to most MEF isolates could be easily transfected using lipofection reagents. In these motile cells, BioGFP-ELKS strongly accumulated in protruding lamellae at the leading cell edge (Fig. 6A), as described previously (Astro et al., 2014; Lansbergen et al., 2006). ELKS clusters were excluded from focal adhesions (Fig.6A), and their recruitment to the cortex over time lagged slightly behind the formation of focal adhesions at the leading edge (Fig.6B). These data suggest that ELKS accumulation at the cortex is likely to be triggered by integrin-based adhesion and might be controlled by polarized signaling molecules such as the active Rac.

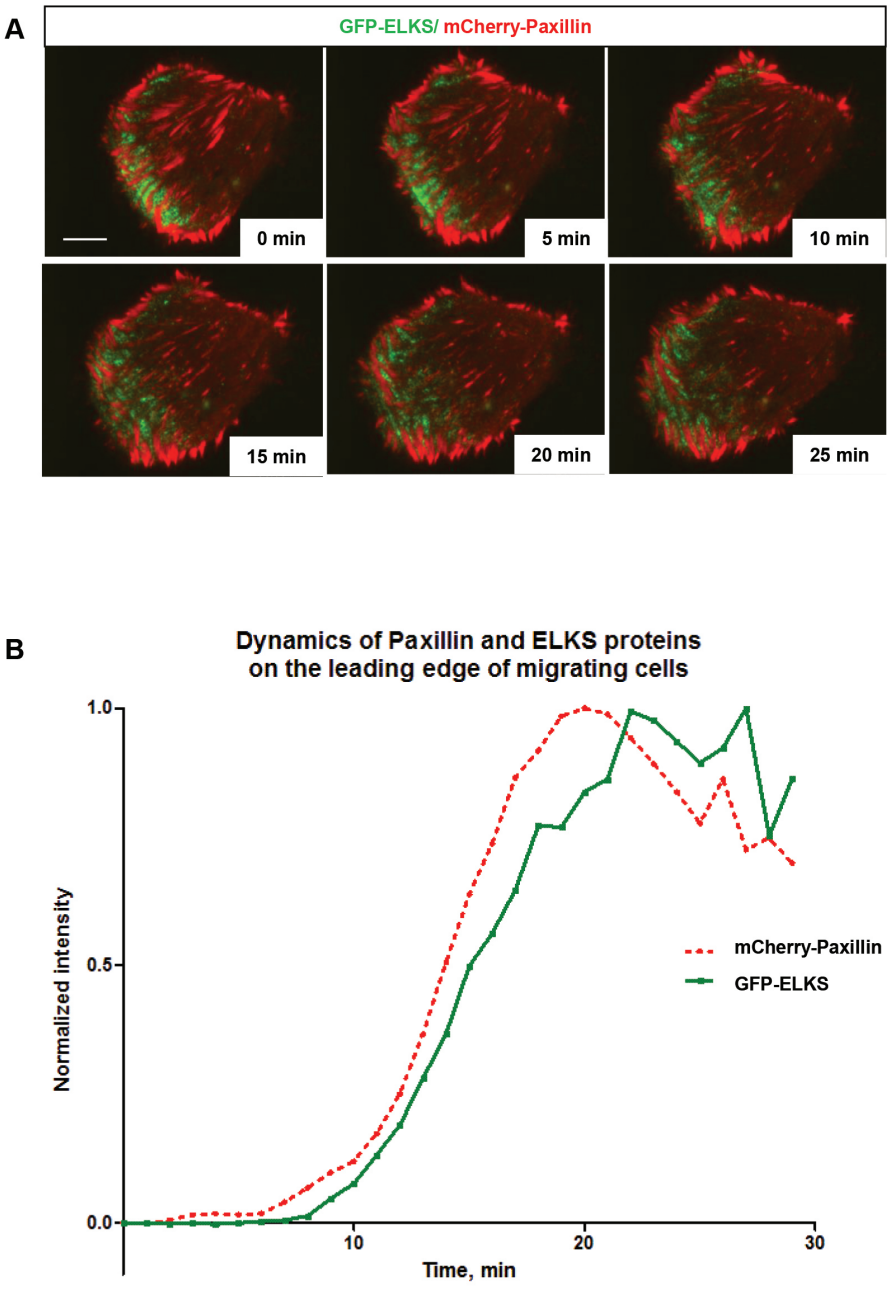

Figure 6. Dynamics of BioGFP-ELKS and paxillin in a migrating BioGFP-ELKS/Cre cell.
A. Frames from a two color movie showing BIoGFP-ELKS and mCherry-paxillin at the leading edge of a migrating BioGFP-ELKS/Cre cell over 30 min using TIRFM at a frame rate of 1 min per frame. Scale bar, 10 μm
B. Analysis of the fluorescence intensity of mCherry-paxillin and GFP-ELKS at the leading edge of a migrating cell over 30 minutes using TIRFM. Intensities of both proteins, with GFP signal in green and mCherry in red, are depicted over time.

Secondly, we have imaged isolated pancreatic islets from BioGFP-ELKS knock-in mice. The islets were isolated by excising the pancreas and collagenase digestion of the surrounding tissue. Islets were cultured on coverslips coated with extracellular matrix (ECM); this resulted in adherence of the islets and allowed their imaging by Total internal Reflection Fluorescence Microscopy (TIRFM) and confocal microscopy. Staining of the islets with antibodies against insulin (specific for β cells) and glucagon (specific for α cells) showed that GFP-ELKS predominantly colocalized with β cells (Fig.7), as described previously (Ohara-Imaizumi et al., 2005).

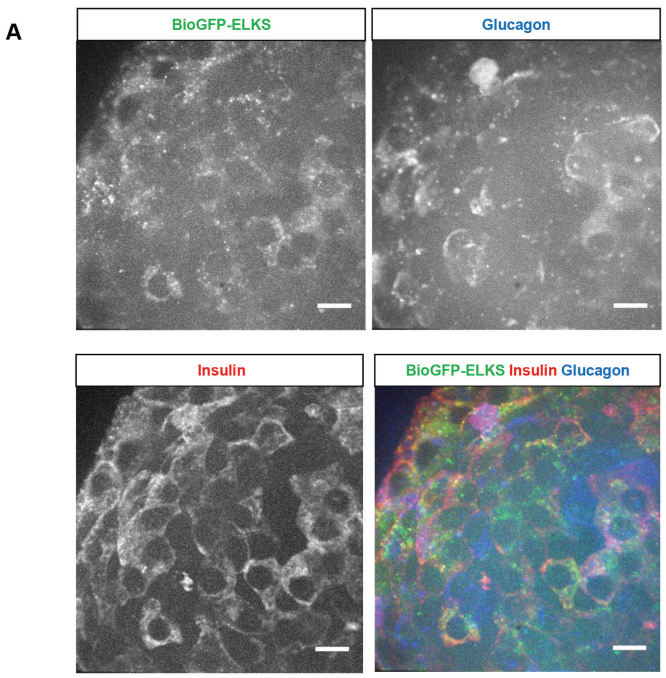

Figure 7. BioGFP-ELKS is present in *β*-cells in pancreatic islets.
Confocal images showing a BioGFP-ELKS islet that was fixed with 4% PFA and stained with antibodies against GFP (in green), insulin (in red) and glucagon (in blue). Scale bar,10 μm.

In islets adhered to the coverslips, ELKS was distributed as clusters, which could be easily detected at the cell surface by staining with anti-ELKS antibodies (in islets from wild type mice) or by direct GFP fluorescence in islets derived from BioGFP-ELKS mice (Fig.8). ELKS clusters partially colocalized with insulin granules in basal culture conditions (11 mM glucose, Fig.8). The isolated islets could respond to glucose stimulation, because insulin granules were not abundant at the cell surface in glucose-starved islets (Fig.9A), but were strongly recruited to the cortex 5 min after stimulation with 22 mM glucose (Fig.9B); strong colocalization

of ELKS clusters and insulin granules was observed in such glucose-stimulated islets (Fig. 9B). After 1 hour of glucose stimulation, the accumulation of insulin granules at the plasma membrane was reduced, as could be expected due to insulin secretion (Fig. 9C), but the colocalization between the insulin and ELKS signals was still observed, suggesting that both the first, rapid phase and the second, slow (sustained) phase of insulin secretion occur by granule fusion at ELKS clusters. In line with the view that ELKS-insulin colocalization correlates with insulin secretion, treatment of islets with the drug diazoxide, a potassium channel activator, which prevents calcium influx and thus inhibits insulin secretion (Hansen et al., 2004), led to a reduction of colocalization between insulin granules and ELKS (Fig. 10A). In contrast, short treatment of the islets with tolbutamide, a potassium channel blocker that activates insulin secretion by inducing membrane depolarization and promoting calcium influx, caused rapid accumulation of insulin granules on the ELKS-positive site (Fig.10B). We conclude that we can isolate and maintain in culture insulin-responsive pancreatic islets, and that BioGFP-ELKS can be detected by GFP fluorescence in a characteristic punctate pattern at the cortex of these islets.

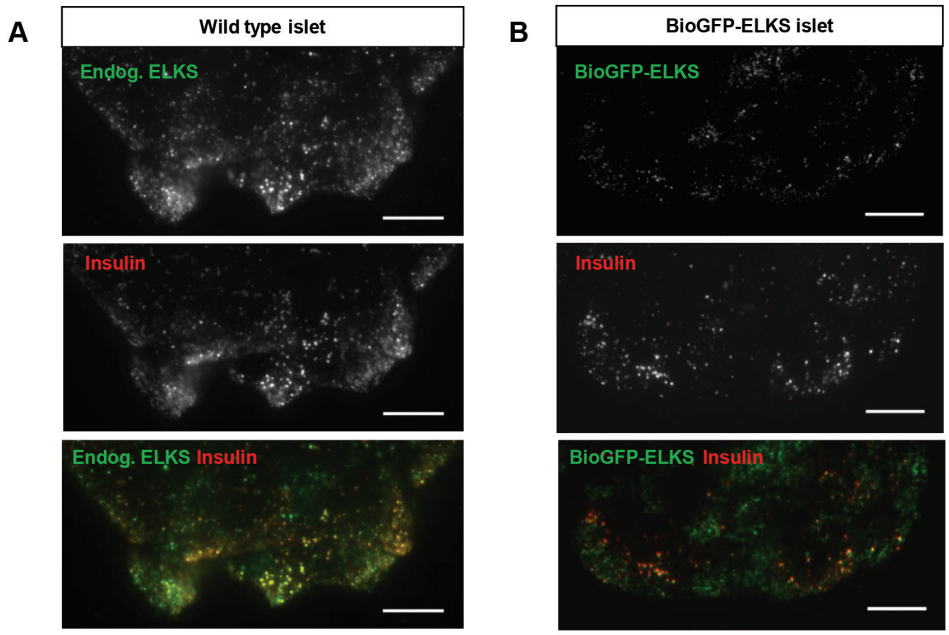

Figure 8. ELKS clusters colocalize with insulin granules in pancreatic islets.
A. Staining of endogenous ELKS and insulin in a fixed wild type pancreatic islet cultured in 11 mM glucose.
B. Insulin staining in a fixed BioGFP-ELKS pancreatic islet cultured in 11 mM glucose; BioGFP-ELKS was detected by direct GFP fluorescence. Imaging was performed using TIRFM. Scale bar, 10 μm.

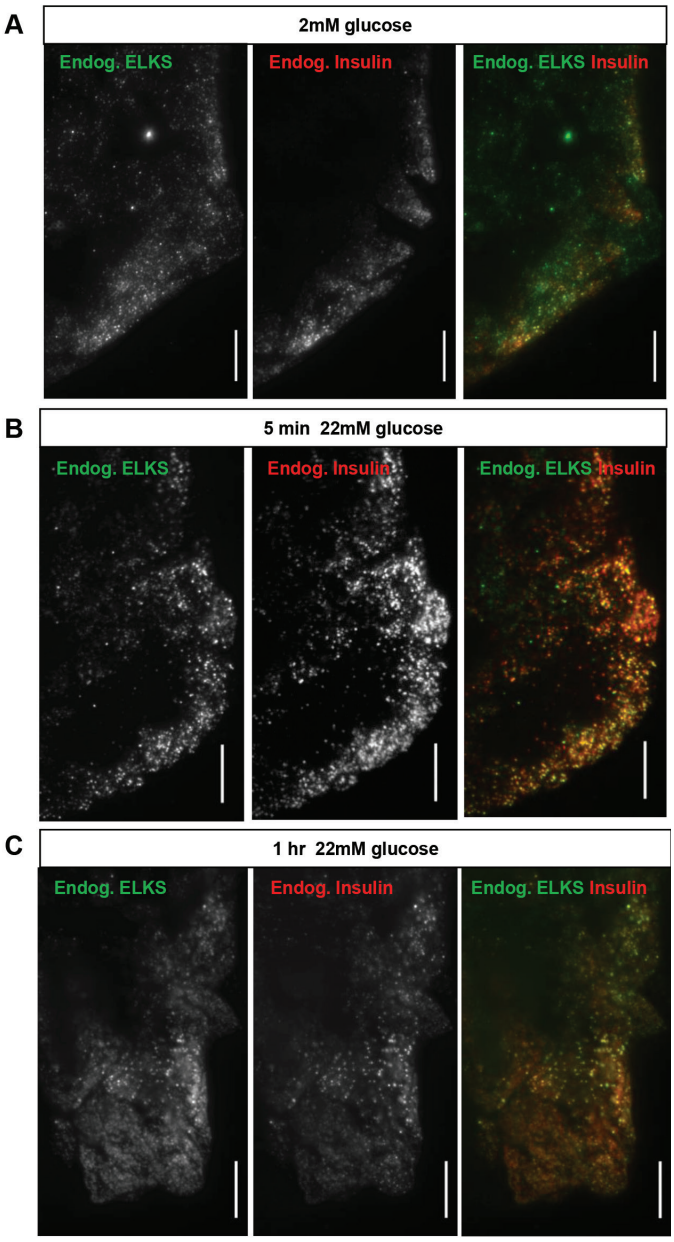

Figure 9. ELKS clusters colocalize with insulin granules in pancreatic islets during glucose-stimulated insulin secretion.
A-C. Staining of endogenous ELKS and insulin in a fixed wild type pancreatic islet cultured in 2 mM glucose overnight (A), or first cultured in 2 mM glucose overnight and then stimulated with 22 mM glucose for 5 min (B) or 1 hr (C). Imaging was performed using TIRFM. Scale bar, 10 μm.

We next set out to investigate whether the ELKS turnover at the cortex can be regulated by the secretion status of the islets. We compared the behaviour of

ELKS in islets cultured in 2 mM glucose (glucose-starved, when no insulin secretion is expected, termed "low glucose") and 11 mM glucose (conditions where insulin granules are present at the cortex and basal levels of insulin secretion take place, termed "high glucose"). Two types of FRAP experiments were performed. In one set of experiments ("whole cell" FRAP, Fig. 11A) we bleached all BioGFP-ELKS clusters visible at the cell surface. In this setup it was possible to observe and analyze simultaneous fluorescence recovery dynamics of many clusters of the same cell from a statistical point of view. The drawback of this approach is that a substantial fraction of the overall BioGFP-ELKS pool is expected to be bleached. This approach preserves the kinetics of recovery (characteristic time), but it can affect the final recovery plateau, because of the depletion of total cell's GFP-ELKS pool (Lippincott-Schwartz et al., 2003). To complement it, we performed a second set of experiments ("region" FRAP) where we bleached only a round region of constant area (~3 μm in diameter) containing approximately 10-20 clusters (Fig. 11B). In this case, the photobleaching does not significantly reduce the overall BioGFP-ELKS pool, which can be considered constant. Both experimental designs were applied to the islets under the high and low glucose concentration conditions.

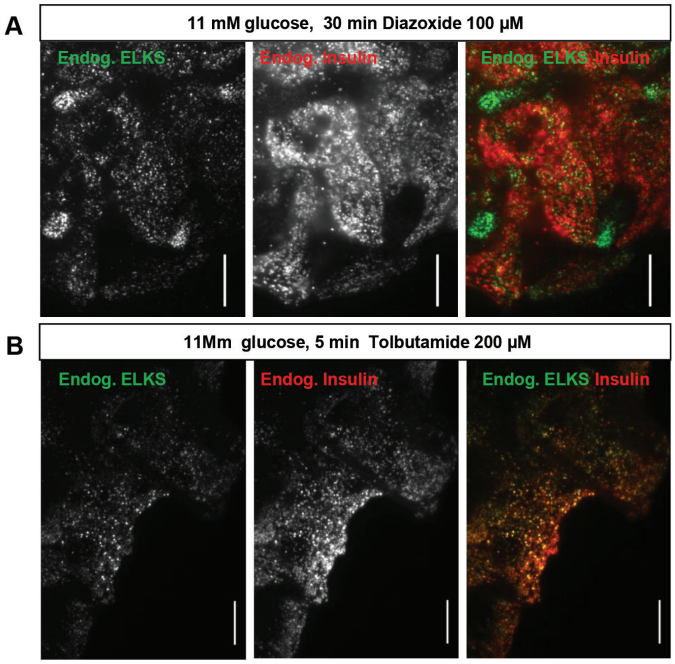

Figure 10. Effects of drugs on colocalizaion of ELKS clusters and insulin granules.
A,B. Staining of endogenous ELKS and insulin in a fixed wild type pancreatic islet cultured in 11 mM glucose and treated with 100 μM diazoxide for 30 min (A) or with 200 μM Tolbutamide for 5 min (B). Imaging was performed using TIRFM. Scale bar, 10 μm.

In all cases, the fastest phase of recovery occurred during the first five minutes of observation (Fig. 11C,D). Independently of design of the FRAP experiment, under the low glucose concentration, the recovery was substantially slower. To characterize FRAP dynamics in detail, we performed fitting with one and two-exponential FRAP models. Final fit was chosen on the basis of statistical extra sum-of-squares F test (a simpler one-exponential model was selected unless P value was less then 0.05). Analysis showed that in almost conditions a one exponential model worked better (Table 1). As an exception, high glucose, "whole cell" FRAP condition showed two-exponential recovery with a very slow second component.

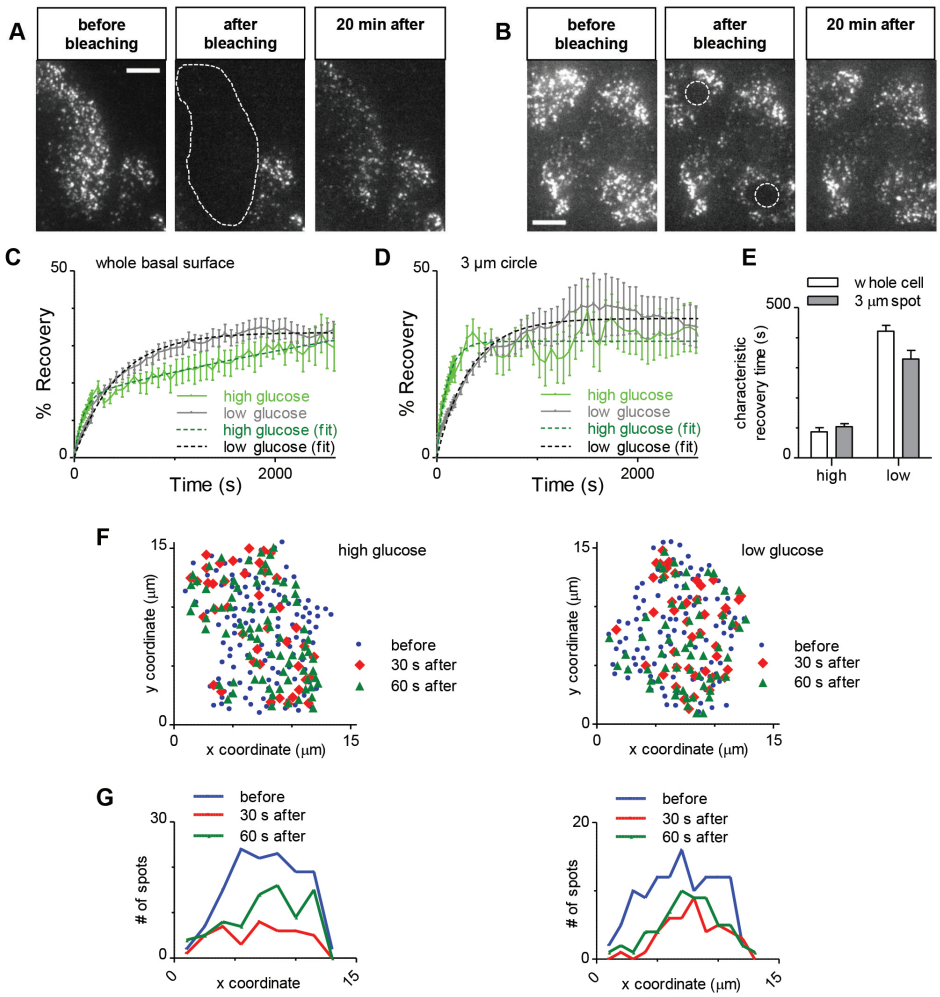

Figure 11. Analysis of ELKS dynamics in pancreatic islets from BioGFP-ELKS knock-in mice by FRAP. A, B. Single frames from a time lapse TIFRM recording of FRAP experiments of BioGFP-ELKS in islets under the condition of whole basal membrane (A) and 3 µm diameter round region of interest (ROI) (B) bleaching. Scale bar, 5 µm. The dashed white line indicates the bleached region.

C-E. Quantification of BioGFP-ELKS recovery after photobleaching. Normalized intensity time traces of BIoGFP-ELKS after photobleaching in islets in the case of whole basal membrane (C) and 3 μm diameter round ROI (D) bleaching. Concentration of glucose in the medium was 2 mM ("low", grey) or 11 mM ("high", green). Error bars indicate SEM. Fits of the data to exponential decay dependence are shown with dashed lines. (N=26 for high and N=40 cells for low glucose, whole membrane condition, and n=31 for high and n=39 for low glucose small ROI bleaching). The corresponding characteristic recovery times are plotted in (E). Error bars in (E) represent the SE of the fit.
F,G. The distribution of BioGFP-ELKS clusters before and during recovery after photobleaching under "high" (left) and "low" (right) glucose concentrations (F). The same data binned by x-coordinate is shown in G.

The values of the plateaus were slightly lower in the case of the "whole cell FRAP", which can be explained by the GFP-ELKS pool depletion as described above (Table 2). On the long time scale in the region of plateau (more than 5 minutes) the variance in the recovery values of "region" FRAP was much higher (compare error bars in Fig.11C and 11D). This can be explained by the inhomogeneous distribution of ELKS clusters across cell membrane (Fig.11A, B). On the long timescale, FRAP dynamics appears to be dominated by the slow motion of the cell or cortical flows (see below), rather than by molecules exchanging inside ELKS clusters. This view is corroborated by the fact that curves for "whole cell" FRAP do not seem to reach their plateau even at the end of observation (45 min). Since we were interested in the kinetics of ELKS turnover inside the clusters we focused our further research on the short timescale (3-5 minutes).

In all experiments, the kinetics of fast recovery (on the short timescale) of GFP-ELKS clusters at the high glucose concentration were four times faster, as seen by comparison of recovery half times (Fig. 11E, Table 1). This result indicates that the state of the docking machinery for insulin granules is regulated by glucose levels, and that ELKS association with some of its cortical partners is subject to regulation. Whether the faster ELKS turnover is the consequence of more frequent insulin fusion (for example, because the docking sites are modified after each fusion), or whether this faster exchange is regulated by some signalling pathways activated by glucose, remains to be determined.

Next, we examined whether the BioGFP-ELKS recovery occurs through exchange with the cytoplasmic pool or by lateral movement on the membrane. In the first scenario, the fluorescence recovery should be independent of the size and shape of the bleached region. In contrast, if recovery occurs because unbleached clusters can migrate from the adjacent unbleached membrane regions, the half time of recovery will depend on the area and perimeter of the bleached spot. The larger area will require more time to recover and the first phase of re-

covery will be more prominent at the boundary of the bleached region. The conclusion in favour of the first scenario could be drawn from the fact that recovery half times in cases of the "whole cell" and "region" FRAP were the same and depended only on the glucose concentration (Fig. 11C-E, Table 1) indicating that the recovery time is independent of the area of bleaching. To further confirm this conclusion we examined the positions of visible ELKS clusters during different time points of recovery (Fig. 11F,G). Both in cases of high and low glucose concentration the recovery occurred homogeneously without preference for boundaries. This means that on the short timescale ELKS clusters undergo exchange with the cytosolic pool.

A punctate ELKS distribution was also observed in BioGFP-ELKS MEFs (data not shown) and in BioGFP-ELKS/Cre cells (Fig.12A). FRAP experiments showed that that ELKS recovery was more complete on short time scale (~3 min) and the characteristic time of recovery was somewhat faster than in pancreatic islets (~ 40 s compared to ~90 s in islets cultured with 11 mM glucose) (Fig.12B). The pattern of ELKS recovery was also similar, supporting the idea that BioGFP-ELKS turns over at the cortex by exchanging with the cytosolic pool (data not shown). Using the quantitative fluorescence approach, we have quantified the number of BioGFP-ELKS molecules per cluster (Fig.12C). We found that dimers were the most frequent species, followed by tetramers and hexamers, and then larger oligomers (Fig.12C). During fluorescence recovery after photobleaching, dimers were again by far the most abundant BioGFP-ELKS species, which appeared first, followed by tetramers, and then the much less abundant larger oligomers (Fig.12D). We conclude that ELKS exists in cells as dimers, and that on a short time scale (within 3 min) the cortical ELKS pool of ELKS recovers through the exchange with ELKS dimers in the cytoplasm. Interestingly, our streptavidin pull down from heterozygous BioGFP-ELKS MEFs showed that BioGFP-ELKS does not coprecipitate the untagged ELKS present in the same cell (Chapter 6). This result can most easily be explained if ELKS dimers form co-translationally and are highly stable.

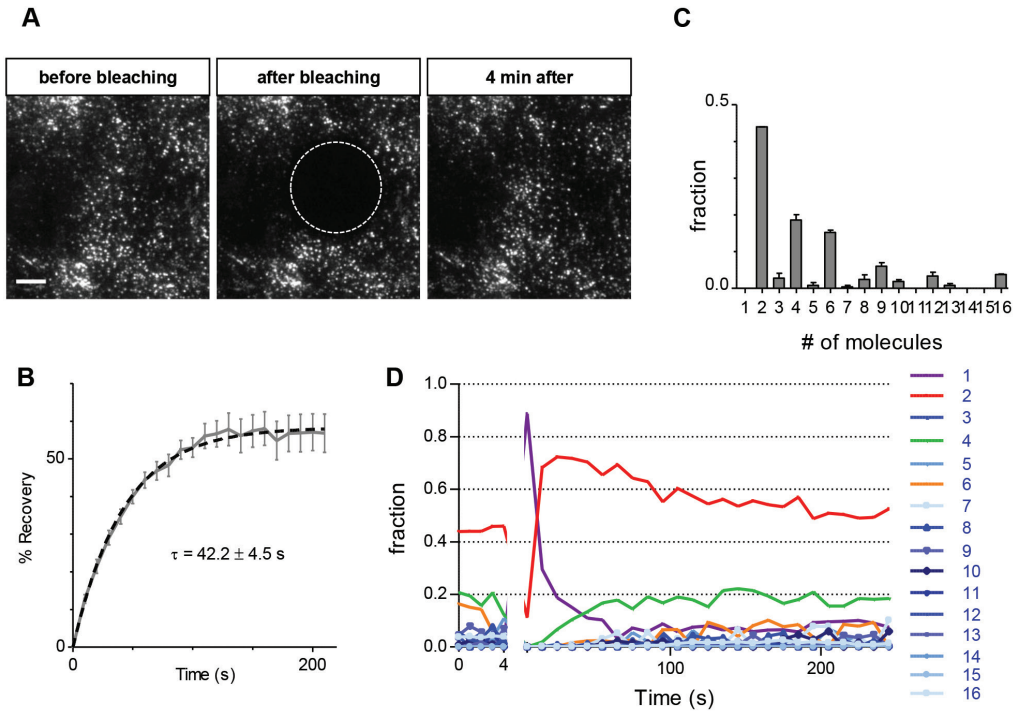

Figure 12. Analysis of ELKS dynamics in BioGFP-ELKS/Cre cells by FRAP.
A. Single frames from a time lapse TIFRM recording of FRAP experiments in BioGFP-ELKS/Cre cells. Scale bar, 5 μm. The dashed white line indicates the bleached region.
B. Quantification of BioGFP-ELKS recovery after photobleaching. Normalized intensity time traces of BioGFP-ELKS in BioGFP-ELKS/Cre cells after photobleaching and the corresponding exponential fit (N=10).
C. The distribution of the number of BioGFP-ELKS molecules per cluster in the bleached area before bleaching (N=10 ROIs, average over the first 3 frames). Error bars indicate SEM.
D. Change in the fractional distribution of the number of molecules in a BioGFP-ELKS cluster during FRAP.

Cortical ELKS distribution and dynamics are regulated by actomyosin contractility

As indicated above, in fibroblasts and epithelial cells, ELKS clusters are enriched in protruding lamella and around focal adhesions but do not overlap with focal adhesions (Fig.6A), suggesting that ELKS is excluded from the regions where dense actin fibers originate. To extend these observations we have used direct stochastical optical reconstruction microscopy (dSTORM) to examine the relative localization of bioGFP-ELKS and actin fibers in BioGFP-ELKS/Cre cells with a high spatial resolution (Fig.13). BioGFP-ELKS was detected using a nanobody against GFP, and actin was detected with fluorescent phalloidin (see Materials and Methods for details). We found that ELKS clusters were mostly excluded from the regions occupied by thick actin fibers (Fig.13). This localization explains the "striped" pattern of ELKS often observed at the cortex of different cell types.

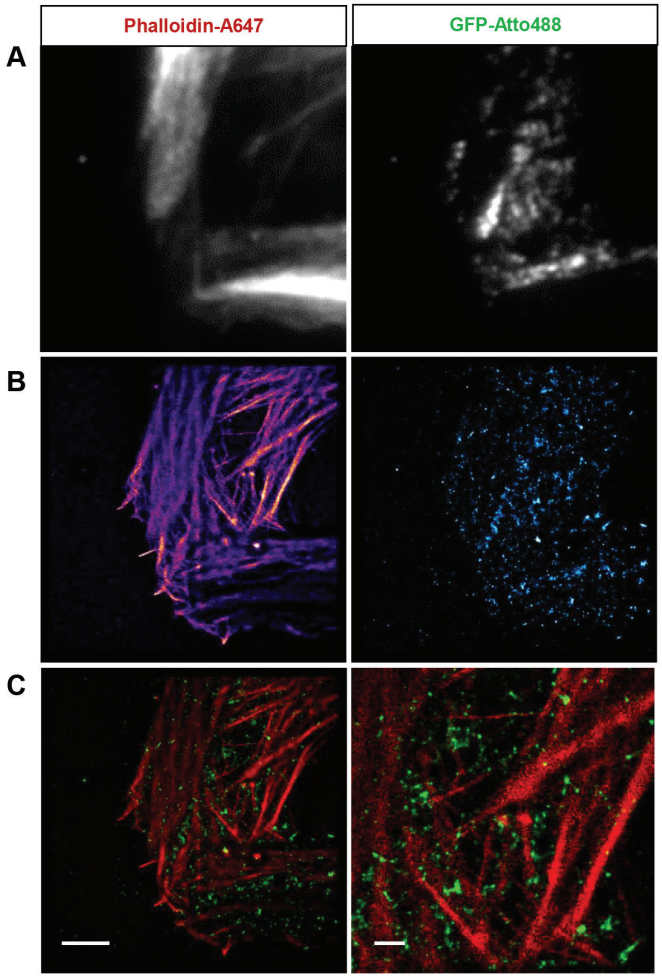

Figure 13. Distribution of actin filaments and BioGFP-ELKS in recombined BioGFP-ELKS embryonic cells by super-resolution microscopy.
A. Fluorescence microscopy of the actin filaments and BioGFP-ELKS at the cell cortex of a BioGFP-ELKS/Cre cell using Phalloidin-A647 and Atto-A488 secondary antibodies.
B. Dual-color dSTORM super-resolution microscopy of the actin filaments and BioGFP-ELKS using Phalloidin-A647 and nanobodies coupled to Atto-A488 antibodies.
C. Overlay of the images of dual-color dSTORM super-resolution microscopy. The overlay shows actin in red and GFP-ELKS in green. Scale bar, 2 µm. An enlarged image of the overlay is shown on the right (scale bar, 500 nm).

Next, we examined how the BioGFP-ELKS distribution is affected by perturbing the cytoskeleton in BioGFP-ELKS/Cre cells. A 1 hr treatment with 10 µM nocodazole, a concentration sufficient to disassemble most microtubules, did not reduce and even slightly enhanced ELKS accumulation in patches at the peripheral cell cortex, in line with previous observations (Lansbergen et al., 2006) (Fig.14A,B). This effect correlates with

the strong activation of Rho GTPase activity and actomyosin contractility induced by microtubule disassembly due to the activation of the microtubule-bound Rho GEF, GEFH1 (Krendel et al., 2002). To inhibit myosin contractility, we used myosin II inhibitor blebbistatin and the inhibitors of its two upstream activators, myosin light chain kinase (MLCK), ML-7, and the ROCK1 kinase (Y-27632). ML-7 had little effect on bioGFP-ELKS distribution or actin organization (Fig.14C), suggesting that MLCK might play a minor role in regulating contractility in this cell type. In contrast, the ROCK1 inhibitor strongly reduced the thickness and abundance of stress fibers, and BioGFP-ELKS patches became much more diffuse (Fig. 14D). Blebbistatin-treated cells showed strongly reduced spreading and a loss of stress fibers; however, BioGFP-ELKS was still present at the cortex and could even display polarized distribution in some cells (Fig. 14E). Also actin disassembly with latrunculin B did not lead to the removal of ELKS from the cortex, although its pattern was altered (Fig 14F). The inhibitors of actin nucleation- and polymerisation-promoting factors, CK666, which inhibits Arp2/3, and SMIFH2, a formin inhibitor, also affected actin fiber formation and the pattern of cortical ELKS clustering (Fig.15). Taken together, our results show that ELKS does not require either microtubules or actin to localize to the cell cortex, but the distribution of the ELKS clusters at the plasma membrane is affected by actomyosin contractility and the localization of actin stress fibers.

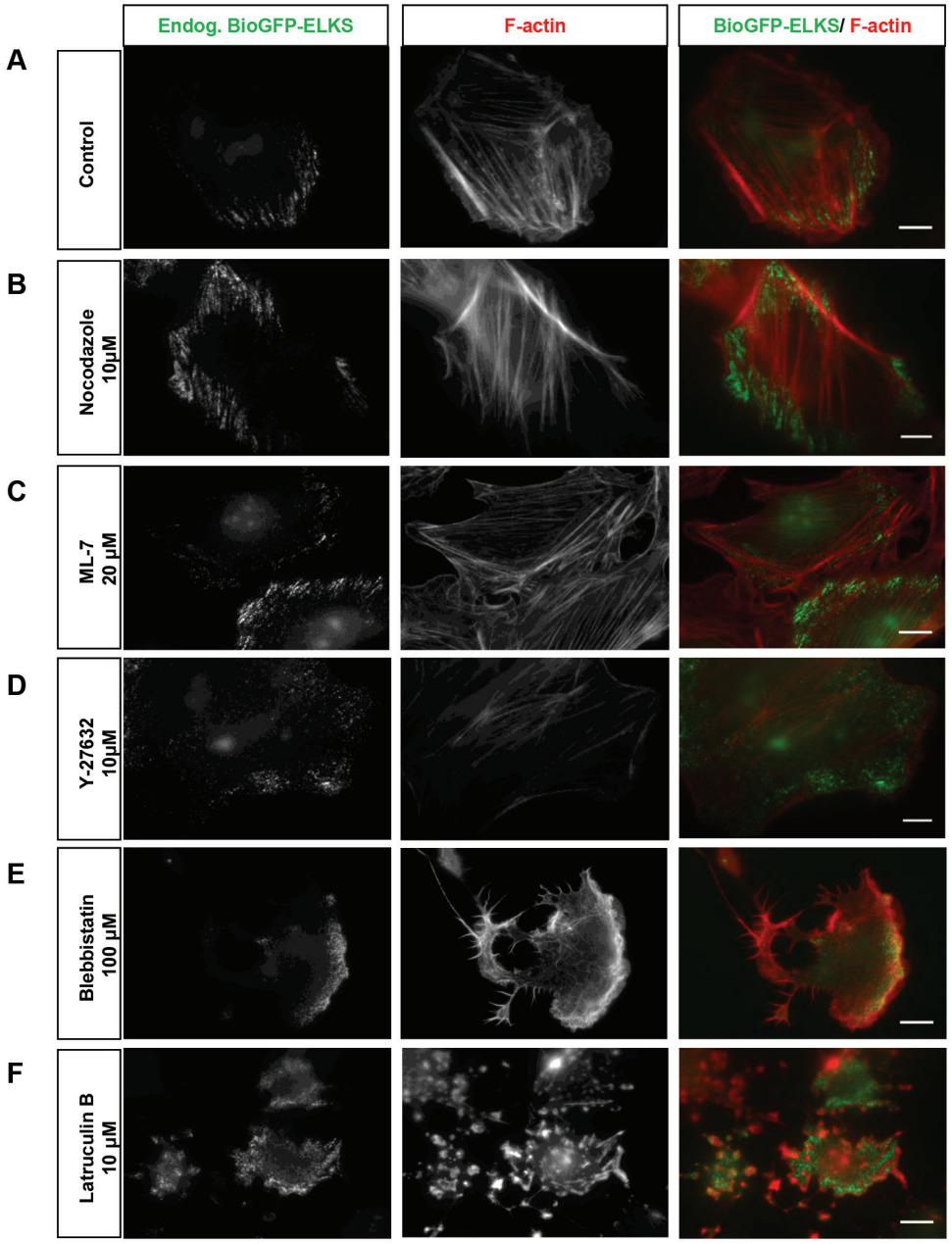

Figure 14. Distribution of BioGFP-ELKS clusters and actin filaments after treatment with different cytoskeletal drugs.
BioGFP-ELKS/Cre cells were incubated with the indicated concentrations of different drugs for 1 hr, fixed in 4% PFA and stained with Phalloidin conjugated to Alexa 594. BioGFP-ELKS was detected by direct GFP fluorescence. Scale bar,10 µm.

Based on these results, we hypothesized that the status of the actin cytoskeleton might affect the slow phase of ELKS dynamics at the cortex. The observation of BioGFP-ELKS islets or fibroblasts on the time scale of 20-40 min revealed the existence of clearly detectable linear flows of ELKS clusters with the velocity on the order of 0.6÷1 μm/min (Fig.16A, C). Interestingly, the organization of ELKS puncta into linear "stripes" and directional flows were much more frequently observed in islets grown in 11 mM glucose as compared to glucose-starved cells, where the clusters frequently showed a random pattern and stochastic "boiling" movement (Fig.16B). Since the "striped" patterns of ELKS clusters are induced by actin fibers, this observation is most easily explained by the rearrangement of cortical actin induced by glucose, an idea that is line with previous work from other labs which showed that glucose induces actin remodelling in β cells (Wang and Thurmond, 2009).

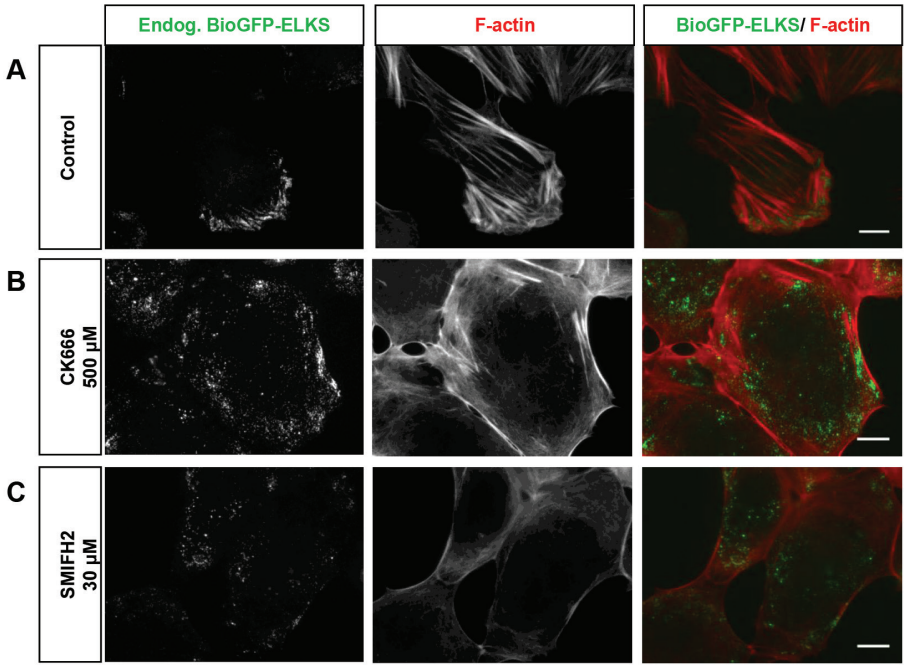

Figure 15. Distribution of BioGFP-ELKS clusters and actin filaments after treatment with CK666 and SMIFH2
BioGFP-ELKS/Cre cells were incubated with the indicated concentrations of different drugs for 1hr, fixed in 4% PFA and stained with Phalloidin conjugated to Alexa 594. BioGFP-ELKS was detected by direct GFP fluorescence. Scale bar,10 μm.

To gain further support for the idea that actomyosin contractility affects cortical dynamics, we have compared in detail the behavior of ELKS clusters in control cells and in cells treated with the ROCK1 inhibitor Y-27632, because

this inhibitor strongly disrupted the ELKS distribution pattern at the cortex without causing cell contraction. We found that the treatment with Y-27632 completely abolished the flows of BioGFP-ELKS (Fig. 16E), showing that these flows are indeed actomyosin- mediated. To characterize the change in the behaviour of the clusters, we performed Fourier analysis of individual pixel intensity changes over the course of a 20 min movie in control and Y-27632 treated cells. The average spectrum (Fig. 16D) showed increased amplitudes of higher frequencies in the presence of Y-27632. This means that the observed spatial intensity distribution is less stable and more dynamic in drug-treated cells. This difference can be characterized by the spectral decay rate parameter, which is equal to the exponential rate of the amplitude decay in the spectrum (Fig.16D, F). This parameter has a dimension of time and represents the characteristic time of change of the corresponding intensity pattern. If its value is high, the change is mostly slow, and when its value is low (like in the presence of Y-27632) the intensity change over time is occurring fast. The color map distribution of this parameter (Fig. 16G, H) highlights long-lived "striped" patterns in control cells and a dimmer, quickly changing interior in Y-27632 treated cells. In the latter case, the majority of ELKS clusters can unrestrictedly move in the plane of the membrane. This confirms that actomyosin cortex regulates the spatial dynamics of BioGFP-ELKS clusters on the scale of a cell.

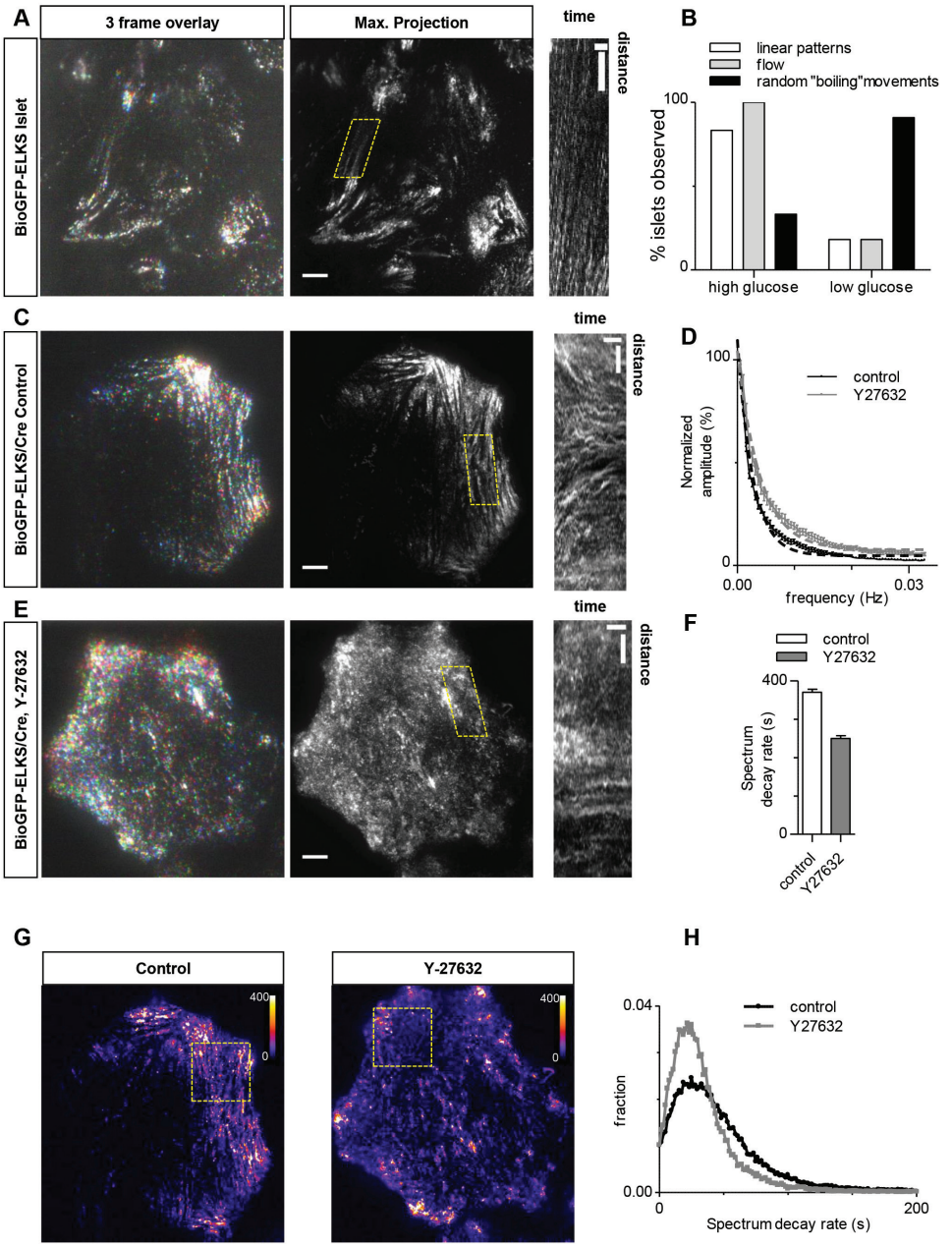

Figure 16. Cortical flows and actomyosin contractility control slow ELKS dynamics at the cortex.
A. Three consecutive frames with one minute difference from a BioGFP-ELKS time lapse recording of a pancreatic islet, color-coded in blue, green and red (left). Maximum intensity projection of the corresponding 45 min time lapse movie with 1 min interval between frames (middle). The dashed line indicates the region used for the kymograph shown on the right. Scale bars are 2 μm and 10 min.
B. Frequency of the observations of different BioGFP-ELKS cluster patterns and their behavior in islets under the conditions of "low" (2 mM) and "high" (11 mM) glucose.

C,E. Three consecutive frames with one minute difference from a BIoGFP-ELKS time lapse recording of a BioGFP-ELKS/Cre cell, color-coded in blue, green and red (left). Maximum intensity projection of the corresponding 20 min time lapse movie with 15 s interval between frames (middle). The dashed line indicates the region used for the kymograph shown on the right. Scale bars are 2 μm and 5 min. A control cell is shown in (C) and a cell treated for 1 hr with 10 μM Y-27632 in (E).
D. Average spectrum of pixel fluorescent intensity change over time in the control condition (black) and after the addition of Y-27632 (grey) (N=8 and 7). Error bars depict SE.
F. Spectrum decay rate for the control and Y-27632-treated cells determined from the fits shown in (D). Error bars depict SE of fit.
G. Color map of the spectrum decay rate for the individual pixels from time lapse recordings shown in (C) and (E).
H. Histograms of spectrum decay rates built for the cell regions shown in the boxed areas in (G).

Conclusions

We have demonstrated that in non-neuronal cells ELKS is recruited to the cortex by the combined activity of LL5β and liprins; in turn, ELKS has only a minor effect on the distribution of these proteins but contributes to the cortical targeting of the spectraplakin ACF7, which helps to explain why ELKS has an impact on cortical microtubule organization. Further, we found that the BioGFP-ELKS mouse is a very useful tool to study the distribution and dynamics of the ELKS protein. ELKS exists as a stable dimer, and cortical ELKS clusters form by the exchange of these dimers with the cytoplasmic pool. The distribution of ELKS clusters at the cortex is affected by actin, because ELKS clusters are excluded from the cortical regions occupied by the actin fibers. Furthermore, the pattern of ELKS cluster movement is controlled by actomysin contractility. In pancreatic islets both the ELKS turnover and its cortical flow are regulated by glucose. Since ELKS marks the sites of insulin granule attachment to the cortex, our data show that the insulin granule docking machinery is subject to remodelling when insulin secretion is stimulated.

Materials and methods

Cell culture

HeLa, COS-7 and HEK293T were cultured as described previously (Akhmanova et al., 2001). INS1 rat insulinoma cells were a gift of Dr. Eelco de Koning (Hubrecht Institute, the Netherlands). INS1 cells and islets were cultured at 37 ˚C and 5% CO_2 and maintained in RPMI medium (Sigma), which was supplemented with 11 mM glucose, 10% fetal bovine serum, penicillin/streptomycin and 100 μM β-mercaptoethanol.

siRNAs

siRNAs were synthesized by Ambion or Dharmacon; they were directed against the following target sequences: control: GCACUCAUUAUGACUCCAU (Mimori-Kiyosue et al., 2005), liprin-α1: GGCUGAAAAAAAAUCGUAAA, liprin-β1: GAUUCGAGAUUUGGAGUUU, LL5β: GGAGATTTTGGATCATCTA (Lansbergen et al., 2006), ELKS: GTAGGGAAAACCCTTTCAAT (Lansbergen et al., 2006), ACF7: UUGCAGCAGGUGAAUGGAC (Drabek et al., 2006). Synthetic siRNAs were transfected using HiPerFect (Qiagen) at a concentration of 5 nM and cells were analyzed 72 hr after transfection.

Expression constructs and cell transfection

We used the following expression constructs: TagRFP-actin (Evrogen) and mCherry-paxillin, provided by Dr. Benjamin P. Bouchet (Utecht Uiversity). Transfections were performed using Fugene HD (Promega).

Antibodies

We used rabbit polyclonal antibodies against ELKS (a gift of Dr. F. Melchior, ZMBH, University of Heidelberg, Germany), liprin-α1 (Spangler et al., 2011), liprin-β1 (van der Vaart et al., 2013); guinea pig antibody against insulin (DAKO), mouse antibodies against paxillin (BD Biosciences), glucagon (Abcam), α-tubulin (Sigma), ACF7/MACF (Abnova) and LL5β (a gift of Dr. J. Sanes, Harvard University, Cambridge, USA). F-actin was stained with Alexa 594-conjugated phalloidin (Invitrogen). Secondary goat antibodies against rabbit, guinea pig and mouse IgG, conjugated to Alexa 647, Alexa 488 and Alexa

594 were purchased from Invitrogen. Antibodies used for dSTORM imaging were anti-GFP primary antibody (598, MBL) and VHH (single-domain antibodies engineered from heavy-chain antibodies) against GFP coupled to Atto 488 NHS (Sigma) (Yau et al., 2014).

Immunofluorescence staining of HeLa, INS1 and BioGFP-ELKS/Cre cells

HeLa cells were fixed with –20 ˚C methanol for 10 min. INS1 cells were fixed either in 4% paraformaldehyde (PFA) dissolved in Dulbecco's Phosphate-Buffered Saline (PBS) at room temperature (insulin staining), or in -20˚ C methanol (liprin and LL5β staining) for 10 minutes. Cells were permeabilized with 0.25% Triton/PBS, blocked with 1% BSA/PBS, incubated with primary antibodies diluted in 1% BSA/PBS for 1hr, washed 3 times with 0.025% Tween-100 in PBS, incubated with secondary antibodies for 1 hr followed by 3 washes in 0.025% Tween-100 in PBS. At the end, slides were rinsed in 100% ethanol (with the exception of phalloidin-stained samples), air-dried and mounted in Vectashield mounting medium (Vector laboratories).

Animals

All animal experiments were performed in compliance with the institutional guidelines for the welfare of experimental animals approved by the Animal Ethical Review Committee (DEC) of the Erasmus Medical Center and Utrecht University, the Netherlands.

Isolation of islets from the murine pancreas

Murine pancreatic islets were isolated from adult heterozygous and homozygous BioGFP-ELKS 3-6 months old mice that were sacrificed by cervical dislocation. Pancreas was excised from the abdomen, washed and chopped with scissors in Hank's Balanced Salt Solution (HBSS with $CaCl_2$ and $MgCl_2$ (Life Technologies)) and digested in 10 ml HBSS containing 0.5 mg/ml collagenase P from Clostridium histolyticum (Sigma) for 20 minutes at 37 ˚C with shaking. To separate the exocrine tissue, the islets were washed with 10 ml HBSS and centrifuged 3 times at 300 x g at 4˚C. Islets were then resuspended in RPMI medium (Sigma) supplemented with 11 mM glucose, 10% fetal bovine serum and penicillin/streptomycin and hand-picked using a stereomicroscope. The isolated islets (5-10 islets/dish) were attached to ECM-pre-coated glass bottom culture dishes (MatTek; P35G-1.5-10-C; 10 mm glass, No. 1.5 thickness). Coating

(200 µl per glass) was performed overnight at room temperature with ECM Gel from Engelbreth-Holm-Swarm murine sarcoma (Sigma; E1270; diluted in cold PBS at 1:20; final concentration 0.4-0.6 mg/ml). Islets were maintained at 37 ˚C and 5% CO_2 for 3 days before TIRFM live imaging, FRAP analysis or immunofluorescence staining.

Immunofluorescence staining of fixed murine islets

For immunofluorescence of the islets, prior to fixation they were refreshed with RPMI medium (Sigma) supplemented with 2 mM, 11 mM or 22 mM glucose, 10% fetal bovine serum and penicillin/streptomycin for 1-2 hours. Cultured islets were fixed in 4% PFA at room temperature for 30 minutes, permeabilized with 0.5% Triton/PBS at room temperature for 1 hr and incubated at 4˚C overnight, blocked in 1% BSA in PBS for two hours and incubated with primary antibodies in 1% BSA in PBS at 4 ˚C overnight, followed by washing in 0.025% Tween-100 in PBS and incubation with secondary antibodies in 1% BSA at room temperature for 2 hours, washed with 0.025% Tween-100 in PBS, and mounted in Vectashield mounting medium (Vector Laboratories).

Drug treatments

We used the following drugs to treat BioGFP-ELKS/Cre cells: nocodazole (Sigma), Y-27632 (Sigma), blebbistatin (Enzo Life Sciences), myosin light chain kinase inhibitor ML-7 (Enzo Life Sciences), latruculin B, CK666 and SMIFH2 (Sigma). Cells were seeded on glass coverslips for 24-36 hr. Prior to drug treatment, media were refreshed for 2 hr, and then cells were treated with medium only or medium containing one of the following drugs: 10 µM nocodazole, 10 µM Y-27632, 100 µM blebbistatin, 20 µM ML-7, 500 µM CK666 or 30 µM SMIFH2 for approximately one hour before fixation or live imaging.

Pancreatic islets were treated with tolbutamide and diazoxide (Sigma). To induce insulin release in pancreatic islets, after refreshing the islets with RPMI medium supplemented with 11 mM glucose, 10% fetal bovine serum and penicillin/streptomycin, they were treated with medium containing 11 mM glucose and 200 µM tolbutamide and fixed at 5 min after treatment. To inhibit insulin release, refreshed islets were treated with medium with 11 mM glucose and 100 µM diazoxide and fixed at 30 min after treatment.

Image acquisition, processing and analysis for fixed cells

Images of fixed cells were collected with a Leica DMRBE microscope equipped with a PL Fluotar 100x 1.3 N.A. oil objective, FITC/EGFP filter 41012 (Chroma) and Texas Red filter 41004 (Chroma) and an ORCA-ER-1394 CCD camera (Hamamatsu) or a Nikon Eclipse 80i equipped with a Plan Apo VC 100x 1.4 N.A., 60x 1.4 N.A. or Plan Fluor 40x 1.3 N.A. oil objectives and a CoolSNAP HQ2 camera (Roper Scientific). Confocal images were obtained using a LSM700 confocal microscope (Zeiss) equipped with a EC Plan-Neofluar 40x 1.30 N.A. oil objective. Images were processed using ImageJ.

dSTORM imaging of fixed BioGFP-ELKS/Cre mouse cells

For BioGFP-ELKS and actin co-staining, BioGFP-ELKS/Cre mouse cells were first extracted for 1.5 minutes with 0.3% glutaraldehyde (GA) and 0.25% Triton X-100 in Cytoskeleton Buffer (CB; 5 mM $MgCl_2$; 150 mM NaCl; 5 mM glucose; 5 mM EGTA in 10 mM MES; pH 6.1). Extraction was followed by a 10 min fixation using 2% GA in CB. After fixation, auto-fluorescence was quenched using 10 mM of $NaBH_4$ for 7 minutes followed by extensive washing with PBS. Cells were further permeabilized for 7 minutes using 0.25% Triton X-100 in PBS, washed and incubated for 30 min in blocking solution (2% BSA; 0.2% gelatin; 10 mM glycine; 50 mM NH_4Cl in PBS, pH 7.4). Cells were first incubated with rabbit anti-GFP primary antibody for 1 hr in blocking solution (1:400), washed and incubated with anti-rabbit coupled to Atto 488 (1:100) in blocking solution. Stained cells were then incubated overnight with freshly prepared Alexa-647 conjugated phalloidin in PBS (1:14). Samples were quickly washed twice in PBS just before imaging.

Imaging was performed using 5 mM MEA (β-Mercaptoethylamine), 5% w/v glucose, 700 μg/ml glucose oxidase, 40 μg/ml catalase in PBS. dSTORM microscopy was performed on an inverted microscope with Perfect Focus System (Nikon Eclipse Ti, Nikon) equipped with a Apo TIRF 100x NA 1.49 oil objective, a 2.5x Optovar (to achieve an effective pixel size of 64 nm), and a DU-897D EMCCD camera (Andor) which were all controlled using Micro-Manager software (Edelstein et al., 2010). Sequential imaging of Alexa-Fluor-647 and Atto488 was performed by continuous oblique laser illumination with 640 nm diode laser and 491 nm DPSS laser, respectively. For Atto488 the sample was also illuminated with 405 nm diode laser. Between 7000 and 15000 frames were recorded per acquisition with exposure times of 30 ms. Single molecule

localization was performed as previously described (Yau et al., 2014). A particle table with molecule coordinates and errors was used to reconstruct a super resolution image. A 10 nm pixel size is used for image display (Fig.13). For two color imaging, chromatic corrections obtained from images with multichromatic 100 nm-beads (Tetraspeck, Invitrogen) were applied to the Atto488 particle table. For sample drift during acquisition, a correction algorithm was applied (Mlodzianoski et al., 2011).

Live imaging and FRAP experiments in pancreatic islets

Islets were refreshed in RPMI medium (Sigma) supplemented with 2 mM or 11mM glucose, 10% fetal bovine serum and penicillin/streptomycin, 2 hr prior to live imaging. The islets were imaged on an inverted microscope (Nikon Eclipse Ti-E; Nikon) with perfect focus system (Nikon), equipped with Nikon CFI Apo TIRF 100×, 1.49 N.A. oil objective (Nikon), Evolve 512 EMCCD and CoolSNAP HQ2 (Photometrics), and controlled with MetaMorph 7.7.5 software (Molecular Devices). The microscope was equipped with TIRF-E motorized TIRF illuminator. For excitation of GFP we used a 491 nm 100 mW Calypso (Cobolt) laser and ET-GFP filter set (Chroma) for emission. The images were projected onto the chip of 16-bit Evolve 512 camera with the intermediate lens 2.5× (Nikon C mount adapter 2.5×) or onto the chip of the CoolSNAP HQ2 without an additional lens. In both cases, the final magnification was equal to 0.064 μm per pixel. Photobleaching was performed using the scanning head FRAP L5 D–CURIE (Curie Institute) and the same laser at maximum intensity. FRAP time lapse movies were acquired with the exposure of 100 ms in the following order: 5 frames with 1 s interval, then bleaching and then immediately consecutive two time lapse acquisitions: 20 frames with 10 s interval and 45 frames with 1 min interval. The calculation of integrated FRAP curves was performed according to (Axelrod et al., 1976; Lippincott-Schwartz et al., 2003).

FRAP and stoichiometric intensity quantifications in BioGFP-ELKS/Cre mouse cells

FRAP experiments with BioGFP-ELKS/Cre mouse cells were performed on the same TIRFM setup described above. FRAP time lapse movies were acquired with the exposure of 100 ms in the following order: initial 5 frames with 1 s interval, then bleaching and then immediately 25 frames with 10 s interval. Following each time lapse a stream acquisition with 100 ms for 500 frames

was performed until the total bleaching of GFP signal was achieved. Image processing routines were automated using ImageJ macros or custom build plugins. Curve fittings and all other statistical and numerical data analysis were performed in Matlab (MATLAB R2011b; MathWorks) and GraphPad Prism (ver.5.02, GraphPad Software). Intensity peaks corresponding to positions of single GFP-ELKS clusters were detected and fitted using the same procedure described above for dSTORM imaging. The intensity distribution of single GFP molecules $\rho_1(I)$ was estimated from the stream bleaching movies as a distribution of BioGFP-ELKS cluster intensities at the last frame before the disappearance of the cluster. The corresponding "basis" intensity distribution of N colocalized independent GFP molecules $\rho_N(I)$ was calculated recursively as a series of convolution integrals according to (Moertelmaier et al., 2005). Observed distributions of BioGFP-ELKS clusters intensities $\rho_{ELKS}(I,t)$ in each frame were fitted with linear combination of "basis" distributions using maximum likelihood minimization routine custom-written in Matlab. Corresponding weights of each distribution in the final linear combination are presented on Fig.12 C,D.

Fourier analysis

Timelapse imaging of BioGFP-ELKS/Cre mouse cells were performed on the same TIRFM setup described above with exposure time of 100ms and 15 seconds time interval between frames for 20 minutes. Movies were corrected for the microscope stage drift using "Template Matching and Slice Alignment" ImageJ plugin from Qingzong Tseng loaded into Matlab. The average value was subtracted for each pixel intensity time series and analyzed using Matlab's built-in *fft* function to get the spectrum. Spectra of all pixels in the 9 μm^2 square ROI within a cell were averaged, normalized with respect to the highest and lowest amplitude and averaged again among different cells to get Fig.16D. The resulting curve was fitted with the exponential decay equation. Spectrum of each pixel of the recorded movie was fitted with decay exponential to build the colormap distribution presented of Fig.16G.

Acknowledgements

We are grateful to F. Ringnalda and E. de Koning for sharing reagents, INS1 cells and their scientific input, B. P. Bouchet for the gift of construct. We thank all animal care takers at the animal facilities of Erasmus Medical Center and Utrecht University. We also thank J. Sanes and Dr. F. Melchior for the gift of antibodies. The work is supported by the Netherlands Organization for Health Research (ZonMw) TOP grant, by the Netherlands Organization for Scientific Research (NWO) ALW-VICI grant and European Foundation for the Study of Diabetes (EFSD) grant to A. A.

Table 1. Characteristic times of BioGFP-ELKS FRAP curves in pancreatic islets derived from fitting.

Dataset \ Condition	High glucose	Low glucose
"Whole cell" FRAP	τ^{fast} = 87 s τ^{slow} = 6127 s	τ = 421 s
Fixed area ROI FRAP	τ = 104 s	τ = 329 s

Table 2. Characteristic saturation plateaus of BioGFP-ELKS FRAP curves derived from fitting.

Dataset \ Condition	High glucose	Low glucose
"Whole cell" FRAP	25 %	33 %
Fixed area ROI FRAP	31 %	37 %

References

Akhmanova, A., C.C. Hoogenraad, K. Drabek, T. Stepanova, B. Dortland, T. Verkerk, W. Vermeulen, B.M. Burgering, C.I. De Zeeuw, F. Grosveld, and N. Galjart. 2001. Clasps are CLIP-115 and -170 associating proteins involved in the regional regulation of microtubule dynamics in motile fibroblasts. *Cell*. 104:923-35.

Astro, V., S. Chiaretti, E. Magistrati, M. Fivaz, and I. de Curtis. 2014. Liprin-alpha1, ERC1 and LL5 define polarized and dynamic structures that are implicated in cell migration. *J Cell Sci*. 127:3862-76.

Axelrod, D., D.E. Koppel, J. Schlessinger, E. Elson, and W.W. Webb. 1976. Mobility measurement by analysis of fluorescence photobleaching recovery kinetics. *Biophys J*. 16:1055-69.

Basu, S., S. Sladecek, Y.V.I. Martinez de la Pena, M. Akaaboune, I. Smal, K. Martin, N. Galjart, and H.R. Brenner. 2015. CLASP2-dependent microtubule capture at the neuromuscular junction membrane requires LL5beta and actin for focal delivery of acetylcholine receptor vesicles. *Mol Biol Cell*.

Basu, S., S. Sladecek, H. Pemble, T. Wittmann, J.A. Slotman, W. van Cappellen, H.R. Brenner, and N. Galjart. 2014. Acetylcholine receptor (AChR) clustering is regulated both by glycogen synthase kinase 3beta (GSK-3beta)-dependent phosphorylation and the level of CLIP-associated protein 2 (CLASP2) mediating the capture of microtubule plus-ends. *J Biol Chem*. 289:30857-67.

Drabek, K., M. van Ham, T. Stepanova, K. Draegestein, R. van Horssen, C.L. Sayas, A. Akhmanova, T. Ten Hagen, R. Smits, R. Fodde, F. Grosveld, and N. Galjart. 2006. Role of CLASP2 in microtubule stabilization and the regulation of persistent motility. *Curr Biol*. 16:2259-64.

Ducut Sigala, J.L., V. Bottero, D.B. Young, A. Shevchenko, F. Mercurio, and I.M. Verma. 2004. Activation of transcription factor NF-kappaB requires ELKS, an IkappaB kinase regulatory subunit. *Science*. 304:1963-7.

Edelstein, A., N. Amodaj, K. Hoover, R. Vale, and N. Stuurman. 2010. Computer control of microscopes using microManager. *Curr Protoc Mol Biol*. Chapter 14:Unit14 20.

Grigoriev, I., D. Splinter, N. Keijzer, P.S. Wulf, J. Demmers, T. Ohtsuka, M. Modesti, I.V. Maly, F. Grosveld, C.C. Hoogenraad, and A. Akhmanova. 2007. Rab6 regulates transport and targeting of exocytotic carriers. *Dev Cell*. 13:305-14.

Grigoriev, I., K.L. Yu, E. Martinez-Sanchez, A. Serra-Marques, I. Smal, E. Meijering, J. Demmers, J. Peranen, R.J. Pasterkamp, P. van der Sluijs, C.C. Hoogenraad, and A. Akhmanova. 2011. Rab6, Rab8, and MICAL3 Cooperate in Controlling Docking and Fusion of Exocytotic Carriers. *Curr Biol*. 21:967-74.

Hansen, J.B., P.O. Arkhammar, T.B. Bodvarsdottir, and P. Wahl. 2004. Inhibition of insulin secretion as a new drug target in the treatment of metabolic disorders. *Curr Med Chem*. 11:1595-615.

Hida, Y., and T. Ohtsuka. 2010. CAST and ELKS proteins: structural and functional determinants of the presynaptic active zone. *J Biochem*. 148:131-7.

Hotta, A., T. Kawakatsu, T. Nakatani, T. Sato, C. Matsui, T. Sukezane, T. Akagi, T. Hamaji, I. Grigoriev, A. Akhmanova, Y. Takai, and Y. Mimori-Kiyosue. 2010. Laminin-based cell adhesion anchors microtubule plus ends to the epithelial cell basal cortex through LL5alpha/beta. *J Cell Biol*. 189:901-17.

Huelsmann, S., and N.H. Brown. 2014. Spectraplakins. *Curr Biol*. 24:R307-8.

Iezzi, M., R. Regazzi, and C.B. Wollheim. 2000. The Rab3-interacting molecule RIM is expressed in pancreatic beta-cells and is implicated in insulin exocytosis. *FEBS Lett*. 474:66-70.

Kishi, M., T.T. Kummer, S.J. Eglen, and J.R. Sanes. 2005. LL5beta: a regulator of postsynaptic differentiation identified in a screen for synaptically enriched transcripts at the neuromuscular junction. *J Cell Biol*. 169:355-66.

Ko, J., M. Na, S. Kim, J.R. Lee, and E. Kim. 2003. Interaction of the ERC family of RIM-binding proteins with the liprin-alpha family of multidomain proteins. *J Biol Chem*. 278:42377-85.

Kodama, A., I. Karakesisoglou, E. Wong, A. Vaezi, and E. Fuchs. 2003. ACF7: an essential integrator of microtubule dynamics. *Cell*. 115:343-54.

Krendel, M., F.T. Zenke, and G.M. Bokoch. 2002. Nucleotide exchange factor GEF-H1 mediates cross-talk between microtubules and the actin cytoskeleton. *Nat Cell Biol*. 4:294-301.

Lansbergen, G., I. Grigoriev, Y. Mimori-Kiyosue, T. Ohtsuka, S. Higa, I.

Kitajima, J. Demmers, N. Galjart, A.B. Houtsmuller, F. Grosveld, and A. Akhmanova. 2006. CLASPs attach microtubule plus ends to the cell cortex through a complex with LL5beta. *Dev Cell*. 11:21-32.

Lippincott-Schwartz, J., N. Altan-Bonnet, and G.H. Patterson. 2003. Photobleaching and photoactivation: following protein dynamics in living cells. *Nat Cell Biol*. Suppl:S7-14.

Mimori-Kiyosue, Y., I. Grigoriev, G. Lansbergen, H. Sasaki, C. Matsui, F. Severin, N. Galjart, F. Grosveld, I. Vorobjev, S. Tsukita, and A. Akhmanova. 2005. CLASP1 and CLASP2 bind to EB1 and regulate microtubule plus-end dynamics at the cell cortex. *J Cell Biol*. 168:141-53.

Mlodzianoski, M.J., J.M. Schreiner, S.P. Callahan, K. Smolkova, A. Dlaskova, J. Santorova, P. Jezek, and J. Bewersdorf. 2011. Sample drift correction in 3D fluorescence photoactivation localization microscopy. *Opt Express*. 19:15009-19.

Moertelmaier, M., M. Brameshuber, M. Linimeier, G.J. Schutz, and H. Stockinger. 2005. Thinning out clusters while conserving stoichiometry of labelling. *Applied Physics Letters*. 87:263903.

Nakaya, Y., E.W. Sukowati, and G. Sheng. 2013. Epiblast integrity requires CLASP and Dystroglycan-mediated microtubule anchoring to the basal cortex. *J Cell Biol*. 202:637-51.

Ohara-Imaizumi, M., T. Ohtsuka, S. Matsushima, Y. Akimoto, C. Nishiwaki, Y. Nakamichi, T. Kikuta, S. Nagai, H. Kawakami, T. Watanabe, and S. Nagamatsu. 2005. ELKS, a protein structurally related to the active zone-associated protein CAST, is expressed in pancreatic beta cells and functions in insulin exocytosis: interaction of ELKS with exocytotic machinery analyzed by total internal reflection fluorescence microscopy. *Mol Biol Cell*. 16:3289-300.

Paranavitane, V., W.J. Coadwell, A. Eguinoa, P.T. Hawkins, and L. Stephens. 2003. LL5beta is a phosphatidylinositol (3,4,5)-trisphosphate sensor that can bind the cytoskeletal adaptor, gamma-filamin. *J Biol Chem*. 278:1328-35.

Proszynski, T.J., J. Gingras, G. Valdez, K. Krzewski, and J.R. Sanes. 2009. Podosomes are present in a postsynaptic apparatus and participate in its maturation. *Proc Natl Acad Sci U S A*. 106:18373-8.

Proszynski, T.J., and J.R. Sanes. 2013. Amotl2 interacts with LL5beta, local-

izes to podosomes and regulates postsynaptic differentiation in muscle. *J Cell Sci*. 126:2225-35.

Roper, K., S.L. Gregory, and N.H. Brown. 2002. The 'spectraplakins': cytoskeletal giants with characteristics of both spectrin and plakin families. *J Cell Sci*. 115:4215-25.

Schmidt, N., S. Basu, S. Sladecek, S. Gatti, J. van Haren, S. Treves, J. Pielage, N. Galjart, and H.R. Brenner. 2012. Agrin regulates CLASP2-mediated capture of microtubules at the neuromuscular junction synaptic membrane. *J Cell Biol*. 198:421-37.

Spangler, S.A., and C.C. Hoogenraad. 2007. Liprin-alpha proteins: scaffold molecules for synapse maturation. *Biochem Soc Trans*. 35:1278-82.

Spangler, S.A., D. Jaarsma, E. De Graaff, P.S. Wulf, A. Akhmanova, and C.C. Hoogenraad. 2011. Differential expression of liprin-alpha family proteins in the brain suggests functional diversification. *J Comp Neurol*. 519:3040-60.

Takao-Rikitsu, E., S. Mochida, E. Inoue, M. Deguchi-Tawarada, M. Inoue, T. Ohtsuka, and Y. Takai. 2004. Physical and functional interaction of the active zone proteins, CAST, RIM1, and Bassoon, in neurotransmitter release. *J Cell Biol*. 164:301-11.

Tokoro, T., S. Higa, M. Deguchi-Tawarada, E. Inoue, I. Kitajima, and T. Ohtsuka. 2007. Localization of the active zone proteins CAST, ELKS, and Piccolo at neuromuscular junctions. *Neuroreport*. 18:313-6.

van der Vaart, B., W.E. van Riel, H. Doodhi, J.T. Kevenaar, E.A. Katrukha, L. Gumy, B.P. Bouchet, I. Grigoriev, S.A. Spangler, K.L. Yu, P.S. Wulf, J. Wu, G. Lansbergen, E.Y. van Battum, R.J. Pasterkamp, Y. Mimori-Kiyosue, J. Demmers, N. Olieric, I.V. Maly, C.C. Hoogenraad, and A. Akhmanova. 2013. CFEOM1-associated kinesin KIF21A is a cortical microtubule growth inhibitor. *Dev Cell*. 27:145-60.

Wang, Y., X. Liu, T. Biederer, and T.C. Sudhof. 2002. A family of RIM-binding proteins regulated by alternative splicing: Implications for the genesis of synaptic active zones. *Proc Natl Acad Sci U S A*. 99:14464-9.

Wang, Z., and D.C. Thurmond. 2009. Mechanisms of biphasic insulin-granule exocytosis - roles of the cytoskeleton, small GTPases and SNARE proteins. *J Cell Sci*. 122:893-903.

Yau, K.W., S.F. van Beuningen, I. Cunha-Ferreira, B.M. Cloin, E.Y. van Battum, L. Will, P. Schatzle, R.P. Tas, J. van Krugten, E.A. Katrukha, K. Jiang, P.S. Wulf, M. Mikhaylova, M. Harterink, R.J. Pasterkamp, A. Akhmanova, L.C. Kapitein, and C.C. Hoogenraad. 2014. Microtubule minus-end binding protein CAMSAP2 controls axon specification and dendrite development. *Neuron*. 82:1058-73.

Chapter 8

General Discussion

Ka Lou Yu

In this thesis, we have investigated several aspects of intracellular membrane trafficking. The major goal of our work was to understand the function of adaptor proteins controlling different trafficking steps in the secretory pathway. Much of our work was focused on the conserved scaffolding protein ELKS, which is strongly involved in the last step of secretion – docking and fusion of exocytotic vesicles with the plasma membrane. By combining proteomics, gene knockout and knockdown approaches with advanced imaging techniques we have obtained interesting insights into the architecture and dynamics of cortical structures which capture secretory carriers and promote their fusion with the target membrane. In the course of this work we have explored different methodologies for mass spectrometry-based protein partner identification and uncovered a number of novel molecular connections important for different trafficking steps in the secretory pathway. In this Chapter, we discuss the implications of our results and provide an outlook on how the knowledge and tools that we have generated can be used for future research.

Early steps of the secretory pathway: the role of VAPB and YIF1A

Newly synthesized proteins enter the secretory pathway by being imported into the Endoplasmic Reticulum (ER). After the initial processing, modification and quality control, these proteins are transported to the Golgi apparatus, where they are further processed and sorted into different carriers in order to be delivered to target compartments. In Chapter 3, we have focused on the ER-to-Golgi transport and the role of two transmembrane molecules, VAPB and YIF1A in this process. Our interest in VAPB was initially triggered by the identification of mutations in the VAPB-encoding gene in patients suffering from the motor neuron disease amyotrophic lateral sclerosis type 8 (ALS8) (Chen et al., 2010; Nishimura et al., 2004; van Blitterswijk et al., 2012). VAPB (vesicle-associated membrane protein (VAMP) associated protein B) is a member of a conserved protein family, which has a transmembrane domain responsible for the localization to the ER membrane and a cytosolic part composed of a coiled coil and an MSP domain (a homologue of the worm major sperm protein). VAPB has been implicated in numerous functions associated with membrane compartment morphology, lipid transfer, membrane transport and ER quality control (Kuijpers et al., 2013a; Lev et al., 2008; Moustaqim-Barrette et al., 2014). Furthermore it was shown that the MSP-domain-containing part of VAPB can be

secreted through some sort of unconventional pathway and can participate in signaling important for neuronal function (Tsuda et al., 2008).

We have searched for the partners of VAPB using pull downs from lysates of HeLa cells overexpressing the biotinylation (Bio)-tagged VAPB and identified the transmembrane protein YIF1A (Yip1-interacting factor homologue A), a protein implicated in early secretory transport (Matern et al., 2000; Yoshida et al., 2008), as a potential partner. We confirmed this interaction by both biochemical and functional assays and showed that the two proteins are required for ER-to-Golgi transport in neurons, where they regulate membrane delivery into dendrites (Kuijpers et al., 2013b). The molecular mechanism underlying the activity of the VAPB-YIF1A complex during secretion is not yet clear. YIF1A recycles between the ER and the Golgi, and is mainly located in the ER-Golgi intermediate compartment. The VAPB pool is mostly located in the ER, and it is possible that the two proteins coordinate protein sorting steps at the ER exit sites. In this respect, it is interesting to note that through its MSP domain, the VAPs can mediate trans-interactions with other membrane compartments by binding to proteins having a FFAT (two phenylalanines in an acidic tract) motif (Mikitova and Levine, 2012). An example of such interaction is the binding of the cholesterol sensor oxysterol-binding protein ORP1L located in the late endosomes to VAP in the ER, a process which controls dynein-mediated endosome motility (Rocha et al., 2009). Recently, VAPB was also shown to participate in the formation of contacts between the ER and mitochondria (Stoica et al., 2014). It would be interesting to know if some trans-interactions between membrane compartments are part of the function of the VAPB-YIF1A complex at the Golgi-ER interface. Importantly, while VAPB and YIF1A are expressed ubiquitously, the pathology associated with VAPB mutations mainly occurs in motor neurons, suggesting that these neurons might be either particularly sensitive to the quality of the trafficking steps associated with VAPB, or might utilize this protein for some specific functions. Altogether, the evidence that perturbation of early secretory steps can have a strong impact in the context of neurodegenerative disease is steadily increasing (Gershoni-Emek et al., 2015; Hetz et al., 2013; Mercado et al., 2013), indicating that more studies are required to reveal the underlying mechanisms.

Tethering, docking and fusion of secretory vesicles: the role of ELKS

The last step of protein secretion is the fusion of the exocytotic membrane carriers with the plasma membrane. The actual process of fusion is mediated by

SNAREs (soluble N-ethylmaleimide-sensitive factor (NSF) adaptor proteins receptors), coiled coil proteins, which bring the vesicle and target membranes into close proximity by forming four-helix bundles (Sudhof and Rothman, 2009). However, numerous factors regulate SNARE-mediated membrane fusion to ensure the specificity and control the timing of the cargo delivery steps. These factors include small GTPases and various tethering proteins, scaffolds and adaptors which can capture the vesicles, bring them in proximity of the target membrane and couple membrane fusion to signaling events such as calcium influx in neurons or hormone-secreting cells.

The mammalian ELKS was identified as a protein needed for both constitutive and regulated secretion. A very large body of data shows that ELKS is part of the presynaptic protein network known as the cytomatrix at the active zone (CAZ) (see Chapter 1 for review). At the CAZ, ELKS binds many of the major CAZ components, including RIM1, Piccolo and Bassoon, Munc13, liprin-α and voltage-gated calcium channels, but the exact function of ELKS and its close homologue CAST is not yet clear. The two proteins contribute to the recruitment of some of their CAZ partners but are not essential for the CAZ formation, at least at the synapses of cultured hippocampal neurons (Kaeser et al., 2009; Liu et al., 2014). When both proteins are deleted, the readily releasable pool of synaptic vesicles is not changed, but neurotransmitter release at the inhibitory synapses is reduced due to altered calcium influx, indicating that ELKS can affect the function of calcium channels (Liu et al., 2014). The existing data provide no evidence to suggest that ELKS is directly involved in capturing synaptic vesicles in the mammalian system.

The situation might be different during constitutive secretion. In HeLa cells and fibroblasts, the carriers of constitutive exocytosis are abundantly decorated by the small GTPase Rab6, which serves as a convenient marker of these carriers (Grigoriev et al., 2007). Previous work has shown that ELKS depletion in HeLa cells leads to accumulation of Rab6 vesicles at the cell periphery (Grigoriev et al., 2007). Our high-resolution live imaging demonstrated that both the docking step (the step after the vesicle arrives to the plasma membrane and before it immobilizes) and the actual fusion step (the time between vesicle immobilization and cargo release) occur slower when ELKS is depleted (Chapter 4, (Grigoriev et al., 2011)). Since these data were obtained using one siRNA in HeLa cells, it was important to confirm these results in an independent system. We used knockout cells derived from ELKS knockout mouse embryos to investi-

gate Rab6 vesicle behavior and found that Rab6 vesicles indeed accumulated in the absence of ELKS due to a fusion defect, fully supporting the previous work (Chapter 6). Prolonged culture of ELKS knockout cells did not alleviate this defect, providing no evidence for potential compensatory mechanisms. Excessive Rab6 vesicle accumulation was completely rescued by re-expression of the endogenous ELKS protein N-terminally linked to the BioGFP tag, indicating that this fusion protein is fully functional in the exocytotic vesicle fusion.

ELKS can bind to Rab6 directly through a C-terminal domain which does not seem to be involved in the interaction with its cortical partners, LL5β and liprin-α1 (Ko et al., 2003; Lansbergen et al., 2006; Monier et al., 2002), and this Rab6-binding domain of ELKS is essential for promoting fusion of Rab6 vesicles with the plasma membrane (Grigoriev et al., 2007). It thus seems likely that during constitutive exocytosis, ELKS directly participates in the capture of Rab6 vesicles arriving at the plasma membrane by binding to Rab6 GTPase. During constitutive exocytosis, ELKS would thus work somewhat similarly to its fly homologue Bruchpilot (BRP), which is the physical constituent of the presynaptic active zone projections (T-bars) that tether synaptic vesicles (Kittel et al., 2006; Wagh et al., 2006). In flies, the synaptic vesicle tethering process depends on the outmost BRP C-terminus, while the N-terminal part is located more closely to the plasma membrane and interacts with the calcium channels (Hallermann et al., 2010). The synaptic vesicle-interacting C-terminal part is absent in mammalian ELKS; at the mammalian synapse the interactions with synaptic vesicles depend on other CAZ components including Bassoon, Piccolo and RIMs. This distinction likely explains the existence of two ELKS isoforms, the shorter neuronal one, which has a C-terminal PDZ-binding domain that interacts with RIMs, and the longer ubiquitously expressed version, which cannot interact with RIMs (Wang et al., 2002). Part of the Rab6 binding domain is located in the C-terminal extension specific for the long ubiquitous ELKS version (Monier et al., 2002), and the last 121 C-terminal amino acids of this ELKS isoform are required for Rab6 vesicle fusion (Grigoriev et al., 2007). We thus favor the idea that Rab6-ELKS interaction forms a part of the physical connection between the exocytotic vesicle and the cell cortex when the vesicles dock before fusion.

To identify additional proteins involved in ELKS function, we have performed several screens for binding partners of ELKS, using both the overexpressed protein and the endogenous tagged fusion protein, the functionality of

which was carefully tested (Chapters 4 and 6). We have identified MICAL-3 as prominent binding partner of ELKS (Chapter 4, (Grigoriev et al., 2011)). We found that MICAL-3 colocalizes with ELKS at the cortex and binds to another small GTPase present on the vesicles, Rab8. We also found that Rab8 is needed for Rab6 vesicle docking and fusion, and the phenotype associated with Rab8 depletion was similar to that of ELKS depletion or knockout. Mapping of the interactions between ELKS, MICAL-3, Rab6 and Rab8 indicated that a cortical complex containing MICAL-3 and ELKS might be able to interact with the two Rabs through the C-termini of MICAL-3 and ELKS (Chapter 4).

While the interactions with Rab6, Rab8, ELKS and MICAL-3 help to explain the vesicle-tethering function of ELKS, they do not provide the connection to the fusion machinery. In neurons, ELKS binds to RIM1 and Munc13, with the latter directly interacting with SNAREs (Chapter 1). However, our mass spectrometry-based searches for the partners of ELKS, MICAL-3 and LL5β, another binding partner of ELKS, revealed no major hits that would directly lead us to SNAREs (Chapters 4-6). It is possible that the relevant link is provided by Rab8. In budding yeast, the homologue of Rab8, Sec4, is required for the last secretion step because it binds to the tethering complex exocyst (Guo et al., 1999). Also the mammalian Rab8 can bind to exocyst (Das and Guo, 2011), however, no strong indications have been found in our lab supporting a strong involvement of exocyst subunits in Rab6 vesicle exocytosis in HeLa cells (A. Marques, personal communication). Rab8 also binds to the synaptotagmin-like protein 4 (Slp4), which interacts with the SNARE Syntaxin 3 during apically-directed secretion in epithelial cells (Galvez-Santisteban et al., 2012). It is reasonable to assume that the Rab8-Slp4 complex has a general function in constitutive exocytosis, a possibility that would need to be tested. In this scenario, the function of ELKS in fusion would be to ensure vesicle tethering through the interaction with Rab6 and MICAL-3, while Rab8 present on the vesicle would contribute to tethering through MICAL-3 but also promote the fusion step by providing a binding site for Slp4, which would in turn connect the whole complex to SNAREs.

ELKS is also abundantly present in pancreatic β cells, and in insulinoma cells, insulin granules were shown to dock and undergo fusion while colocalizing with ELKS clusters (Ohara-Imaizumi et al., 2005). We have confirmed strong colocalization between individual ELKS clusters and insulin granules in isolated pancreatic islets and showed that this colocalization is regulated by

glucose, being most prominent within a short time period after glucose addition (Chapter 7). However, some colocalization between insulin and ELKS persisted also after longer glucose treatment, suggesting that both the first (rapid) phase and the second (slow) phase of insulin secretion are likely to occur at the ELKS clusters. Since insulin secretion is strongly regulated by calcium influx, it utilizes some of the proteins active in neurotransmitter release; for example, the small GTPase Rab3 is present on the insulin granules, similar to synaptic vesicles, and Munc13 acts as priming factor (Wang and Thurmond, 2009). However, there are also differences: for example, in addition to Rab3, insulin granules also contain Rab27, which is required glucose-evoked insulin secretion (Kasai et al., 2008). The abovementioned Slp4 (also known as granuphilin) is a Rab27 effector, which participates in docking of insulin granules (Gomi et al., 2005). Interestingly, the knockout of Slp4/granulophilin, while abolishing stable granule docking, accelerated rather than inhibited both the spontaneous and evoked fusion of insulin granules (Kasai et al., 2008). The underlying mechanism likely involves an increase in fusion-competent pool of the SNARE syntaxin 1A (Gomi et al., 2005; Wang and Thurmond, 2009). A more tight control of the spontaneous secretion thus appears to occur at the expense of the speed of induced insulin granule fusion. Interestingly, in the case of constitutive secretion, a similar phenomenon was observed: the depletion of Rab6 resulted in faster rather than slower exocytotic vesicle fusion after the initial docking (Grigoriev et al., 2007). However, the spatial control of vesicle fusion was lost: instead of fusing predominantly in the peripheral cellular regions where ELKS-LL5β patches are located, exocytotic vesicle fusion now occurred randomly throughout the cell (Grigoriev et al., 2007). The elaborate machinery of vesicle docking, including ELKS, thus seems to have evolved in order to enable tight control of the time and the place where vesicle fusion occurs.

The importance of temporal control of fusion at the neuronal synapses or in endocrine cells is obvious, because it ensures the proper response to external stimuli. The need to regulate secretion spatially is related to the architecture of cells and tissues. In migrating cells, the complex of LL5β, ELKS and CLASPs is strongly concentrated at the leading cell edges in the vicinity of focal adhesions (Chapter 6, (Akhmanova et al., 2001; Astro et al., 2014; Lansbergen et al., 2006)). The delivery of secretory cargo, such as matrix metalloproteinases, to these sites can promote focal adhesion turnover and migration in keratinocytes (Stehbens et al., 2014). We note, however, that our own experiments with ELKS

knockout cells do not support this model: while ELKS knockout did cause a strong defect in the fusion of the exocytic vesicles with the plasma membrane, these cells migrated faster than matching controls where ELKS expression was restored (Chapter 6), suggesting that focal adhesion turnover is not delayed by ELKS depletion. It should be noted that Stehbens et al. (2014) did not deplete ELKS, so some additional effects of the loss of this protein might affect migration. Furthermore, the difference between our study and that by Stehbens et al. might be due to the different cell types used.

Rapid migration on solid support might not necessarily be a beneficial characteristic of every cell type. For example, for epithelia, the ability to form stable layers might be a more evolutionarily relevant property, and LL5β and ELKS, which are expected to localize to the basolateral side due to the their dependence on integrin-based adhesions, might contribute to stable attachment of epithelial cells to the basal lamina. While there is little information on ELKS function in this context, LL5β and CLASPs are indeed present at the basal side in polarized epithelial cells and appear to contribute to epithelial polarity and integrity (Hotta et al., 2010; Nakaya et al., 2013). ELKS, together with its binding partners, also concentrates at podosomes. ELKS might be relevant for organizing secretion at these structures, a possibility that would be important to test, especially as podosomes-like assemblies containing LL5β and ELKS play an important role in the maturation of neuromuscular junctions (NMJ) (Proszynski and Sanes, 2013), and LL5β and CLASPs were shown to participate in the delivery of acetylcholine receptors to the NMJ (Basu et al., 2015). The BioGFP-ELKS knock-in mouse, which we have generated, will be a very useful tool to investigate the participation of ELKS in the process of formation of NMJs and in the development and maintenance of epithelial layers.

The role of ELKS in the organization of cortical structures

Is participation in secretion the only function of the cortical ELKS pool? LL5-liprin-CLASP complexes, in which ELKS participates, have a major function in microtubule plus end attachment to the cortex (Lansbergen et al., 2006; van der Vaart et al., 2013). In this way, the routes responsible for fast vesicle delivery by microtubule plus end-directed kinesins are directly coupled to the vesicle docking and fusion machinery. While ELKS does not play a direct role in microtubule binding or stabilization, it does contribute to some extent to the clustering of its binding partners and thus indirectly affects cortical microtubule

organization. In addition, we found that ELKS is required for the efficient recruitment of the microtubule-actin-cross linking factor MACF1/ACF7 to the peripheral cell cortex (Chapter 7). ACF7 in turn contributes, through as yet unknown mechanism, to CLASP recruitment (Drabek et al., 2006). This likely explains why ELKS can have a significant impact on the cortical microtubule organization without having a direct biochemical interaction with these cytoskeletal filaments. It should be noted that the cortical microtubule stabilization machinery dependent on LL5s, CLASPs, ACF7, liprins and ELKS is highly cell type specific – for example, it did not seem to be particularly active in the mouse BioGFP-ELKS knock-in and knockout cells that we have isolated, and therefore we were not able to study the function of this system in the ELKS knockout cell migration model, which we have developed.

How is ELKS recruited to the cortex? ELKS is a coiled coil protein, which lacks membrane-binding domains or motifs. In non-neuronal cells, ELKS association with specific sites at the plasma membrane appears to depend on two proteins, LL5β (and its homologue LL5α, if it is expressed in the cell type in question) and on liprin-α1 and liprin-β1 (Chapter 7, (Astro et al., 2014; Lansbergen et al., 2006)). ELKS binds to LL5β and liprin-α1 through overlapping domains (Ko et al., 2003; Lansbergen et al., 2006), and it is not known whether it can bind to both proteins simultaneously. The analysis of the hierarchy of cortical protein recruitment is complicated by the fact that LL5s and liprins strongly depend on each other for their cortical localization (Chapter 7, (Astro et al., 2014; van der Vaart et al., 2013)). In neuronal cells, LL5s do not seem to be expressed at significant levels, but the dependence of ELKS/CAST on liprin-α holds true, also in flies and worms (Dai et al., 2006; Fouquet et al., 2009; Kittelmann et al., 2013; Spangler et al., 2013), indicating that it is a conserved feature of the organization of ELKS-containing cortical structures. How liprins are recruited to the plasma membrane is not completely clear. The interaction with the transmembrane receptor protein tyrosine phosphatase LAR, which in turn is connected to extracellular ligands and cadherins, is likely to play a role in this process, at least in neurons (Kypta et al., 1996; Stryker and Johnson, 2007), but additional interactions are likely to be involved. Cortical recruitment of LL5s depends on phosphatidylinositol 3, 4, 5-trisphosphate (PIP3), to which they bind through their pleckstrin homology domain (Astro et al., 2014; Lansbergen et al., 2006; Paranavitane et al., 2003) and on activated integrins (Hotta et al., 2010). Liprin-α1 was also functionally connected to integrins and integ-

rin-dependent cell spreading and migration (Asperti et al., 2009; Asperti et al., 2010; Astro et al., 2010; Astro et al., 2014), but the biochemical connection has not been clarified.

Importantly, in spite of the link to integrins, the complexes of liprins, LL5s and ELKS do not colocalize with focal adhesions but rather accumulate around them, through a mechanism that is currently unknown. Our imaging work showed that ELKS clusters are preferentially excluded from the cortical sites occupied by actin stress fibers (Chapter 7) and do not require actin for their targeting to the plasma membrane, suggesting that their membrane binding depends on some transmembrane proteins or lipids. Although not directly coupled to actin, ELKS clusters are subject to cortical flows which require actomyosin contractility (Chapter 7). The formation of ELKS clusters is governed by two processes, a relatively fast exchange with the cytosolic pool of ELKS, which occurs in the form of ELKS dimers, and the slow movement of the clusters at the cell cortex, which depends on the organization of the actin cytoskeleton.

Another interesting question concerns the interplay between the ELKS function at the cortex and its participation in the NF-κB signaling. Our proteomics searches did not yield any obvious NF-κB-related ELKS partners, likely because the signaling pathway was not activated in the cells that we have studied. We did identify CYLD, a deubiquitinating enzyme (Courtois, 2008; Harhaj and Dixit, 2012), as an ELKS binding partner, suggesting that it might play a role in removing polyubiquitin chains required for the ELKS adaptor function in NF-κB signaling (Niu et al., 2011). It would be interesting to know whether the association of ELKS with the cell cortex is altered when NF-κB is activated. The BioGFP-ELKS knock-in cells, which we have generated, will be a very useful tool to address this question. For example, one could induce genotoxic stress in these cells and investigate whether the activation of NF-κB is associated with the relocalization of ELKS, reorganization of the cortical ELKS clusters or altered constitutive secretion. One could also imagine that the assembly of certain protein complexes responsible for the NF-κB signaling occurs at the cortex. This possibility has never been properly investigated because biochemical approaches currently strongly predominate in the studies of signaling pathways, and thus the subcellular localization of the relevant signaling complexes often remains insufficiently explored.

The function of MICAL family proteins in secretion

Our searches foe ELKS partners have yielded MICAL-3 is one of the major

hits (Chapter 4), which encouraged us to explore the role of the MICAL family of flavoprotein monooxynases in secretion. We focused on MICAL-1 and MICAL-3, because these two proteins contain a C-terminal domain that can interact with Rabs (Giridharan and Caplan, 2014; Zhou et al., 2011), suggesting that these MICALs might have a general function in trafficking. Until now, the major known biochemical function of MICALs is to promote actin disassembly through site-specific oxidation of a methionine residue at the pointed end of actin (Hung et al., 2011; Hung et al., 2010). We used MICAL-1 knockout cells to investigate the distribution of Rab6-positive secretory vesicles and found that the absence of MICAL-1 resulted in an increased vesicle accumulation at the cell periphery, suggesting a secretion defect (Chapter 5). These data helped to explain the phenotype of the MICAL-1 knockout mouse, which has neurodevelopmental abnormalities due to defects in targeting of secretory vesicles containing immunoglobulin superfamily cell adhesion molecules (IgCAMs) to the membrane of neuronal growth cones (Van Battum et al., 2014). The effect of MICAL-1 on secretory trafficking seems to be primarily due to the increase in subcortical actin, suggesting that the role of MICAL-1 in this case is primarily through the control of the actin cytoskeleton.

MICAL-3 is also a potent actin disassembly factor (Chapter 5, (Giridharan et al., 2012)). However, it seems to be involved in secretion in a more intimate fashion that MICAL-1, because it interacts with ELKS and accumulates at the cortical sites where the docking of Rab6-positive secretory vesicles takes place (Chapter 4). As explained above, MICAL-3 appears to form a part of the vesicle docking machinery through its interaction with Rab8 present on the secretory vesicles. What is the function of MICAL-3 in the vesicle-docking complex? One attractive possibility is that, similar to MICAL-1, it disassembles cortical actin, which might serve as a barrier for vesicle fusion. When MICAL-3 lacking the enzymatic activity due to mutations in the monooxygenase domain is expressed in cells, it induces very stable docking of Rab6 vesicles but prevents their subsequent fusion with the plasma membrane. If this phenotype is caused by a defect in the disassembly of the cortical actin, one would imagine that it could be alleviated by pharmacological actin disassembly, by, for example, using latrunculin B. However, our attempts to prove this hypothesis experimentally have failed. It is thus possible that MICAL-3 monooxygenase promotes vesicle fusion through another mechanism. Two observations provide potential clues on what this mechanism might be. First, the enzymaticaly active MICAL-3 copre-

cipitates Rab8 less efficiently than the enzymatically dead version. Second, the enzymatically inactive MICAL-3 exchanges at the cortex much slower than the active protein. These data suggest that through its oxidative activity, MICAL-3 can promote protein turnover in the complexes in which it is engaged. It would be interesting to know whether Rab8 or other Rabs, ELKS, or perhaps even parts of MICAL-3 itself can serve as MICAL-3 oxidation substrates. The find-ing that the oxidative reaction catalyzed by MICALs is stereoselective provides a possibility to critically test this idea by reversing the modification through the overexpression of the methionine sulfoxide reductase MsrB (Hung et al., 2013; Lee et al., 2013).

Our proteomics work has identified another potentially interesting function for MICAL-3 and ELKS: a role in cytokinesis or abscission. MICAL-3, and to a lesser extent ELKS coprecipitated the components of the centralspindlin complex (Chapter 5 and 6). The interaction likely occurs through the binding of MICAL-3 to kinesin-6 MKLP1. Importantly, we found that MICAL-3 colo-calizes with centralspindlin at the central spindle and the midbody. Interestingly, another binding partner of ELKS, LL5β, coprecipitated another protein module involved in cytokinesis, a complex of kinesin-3 KIF14 and Citron kinase (Chap-ter 6, (Bassi et al., 2013; Gruneberg et al., 2006)). An attractive possibility is that the complex of ELKS, LL5β and MICAL-3 is employed in cytokinesis, where it might participate in disassembling actin structures before abscission. The link between ELKS/MICAL-3 and Rab6/Rab8 GTPases might be relevant in this context, as Rab6 and Rab8 were also implicated in cytokinesis (Fontijn et al., 2001; Hill et al., 2000; Kaplan and Reiner, 2011).We should note that we while we have observed a strong defect in vesicle fusion induced by the expression of the enzymatically inactive MICAL-3, we were un-able to detect any significant phenotypes associated with MICAL-3 depletion, neither in trafficking nor during cell division. It is possible that this was due to incomplete depletion and the remaining residual activity of the enzyme. To in-vestigate the functions of MICAL-3 during cell division it will be important to generate cells completely lacking MICAL-3. The feasibility of such experiments is greatly facilitated by the advent of the Cas9/CRISPR technology (Doudna and Charpentier, 2014).

Another interesting question concerns MICAL activation. A previous study showed that MICAL-1 is autoinhibited and can be activated by the binding of its partner plexin to its C-terminal domain (Schmidt et al., 2008). Interestingly, the C-terminal domain of MICAL-1 and MICAL-3 is also the site of MICAL interaction with the Rabs (Fukuda et al., 2008; Grigoriev et al., 2011). Since sev-eral different Rabs can bind to MICAL-1 and MICAL-3 (Chapter 5, (Fukuda et al., 2008; Weide et al., 2003)), an attractive possibility is that Rabs can use MICALs as their effectors inducing local actin assembly to promote specific trafficking steps such as vesicle fission or fusion. Interesting in this respect is the observation that the overexpresion of Rab8 can cause pronounced changes of cell morphology that could be consistent with mild actin disassembly (Peranen et al., 1996). It would be interesting to test whether the Rab8-dependent cyto-skeletal remodeling is mediated by MICAL1 and MICAL-3.

An important outstanding issue is the potential redundancy between the three MICAL family members. The phenotype of MICAL-1 mouse knockout is rather mild (Van Battum et al., 2014), suggesting that MICAL-1 has no es-sential functions in mammals. It is possible that the three mammalian MICALs can compensate for each other. In line with this view, we noticed that while the individual knockdowns of the three MICALs had no impact on cell division, a triple knockdown did induce a phenotype: cells spent much more time with a rounded up shape before spreading after mitosis and underwent intensive bleb-bing, suggesting a possible defect in the disassembly of the cortical actin layer upon mitotic exit (Chapter 5). The three MICALs might thus have a general function in regulating the thickness and the contractile properties of the actin cortex during the cell cycle.

Fishing in the ocean: challenges associated with mass spectrometry approaches to efficiently identify specific protein binding partners

A significant part of the work described in this thesis was aimed at identification of protein binding partners using mass spectrometry. Using streptavidin pull downs from HeLa or HEK293T cells overexpressing our protein of interest with a biotinylation (Bio) tag together with the biotin ligase BirA, we have successfully identified several novel, functionally important interactions, for example between VAPB and YIF1A (Chapter 3) or ELKS and MICAL-3 (Chapter 4). While this approach is very rapid and technically simple, the obvious disad-vantage is that a highly overexpressed protein can form non-physiological complexes. To overcome this problem, we have generated a

knock-in mouse where the endogenous ELKS protein was fused to the BioGFP tag. We confirmed that the BioGFP-ELKS fusion protein is fully functional during mouse devel-opment and in exocytosis (Chapter 6). We then used the tag to perform pull downs from BioGFP-ELKS expressing cells. The results were somewhat disap-pointing because the known binding partners of ELKS were detected only with a low level of confidence, and only a few potentially interesting novel candidates were found (Chapter 6). Follow-up studies with these candidates will need to be performed in order to find out whether they are specific.

One of the problems with this type of experiments is the unspecific enrichment in the bait pull downs of certain types of proteins such as RNA-binding proteins or cytoskeletal adaptors, which obscure the specific hits that might be present in the pull down. Typically, these unspecific interactors can be recognized by their frequent occurrence in affinity purifications of different unrelated proteins and excluded from the analysis even if they show up as a specific hit in a particular pulldown (Chapter 2, {Mellacheruvu, 2013 #1762}). In some cases, multistep purification of the bait protein might help to enrich for specific binding partners. However, we do not expect this approach to be suitable for revealing additional ELKS partners because ELKS is part of membrane bound, poorly soluble complexes which are likely to be lost if a multistep procedure is applied. We conclude that rapid enrichment for potential partners using protein overexpression followed by careful case-by-case analysis might remain to be the most effective strategy to reveal the relevant protein interaction networks of membrane-associated adaptor proteins such as ELKS.

Concluding remarks

In this thesis, we have described new molecular mechanisms involved in specific trafficking steps of the secretory pathway. We have generated a knockout and a knock-in mouse model to study the function of the cortical adaptor ELKS, a molecule involved in exocytosis, cytoskeletal organization and signaling. Using proteomics and advanced imaging approaches applied to cells and tissues derived from these genetically modified mice, we obtained new insights in the mechanisms underlying secretory vesicle delivery and the organization of cortical cellular structures. The tools and methodological approaches generated in the course of our work will be useful for future research on the mechanisms of mouse development, cell migration and secretion.

References

Akhmanova, A., C.C. Hoogenraad, K. Drabek, T. Stepanova, B. Dortland, T. Verkerk, W. Vermeulen, B.M. Burgering, C.I. De Zeeuw, F. Grosveld, and N. Galjart. 2001. Clasps are CLIP-115 and -170 associating proteins involved in the regional regulation of microtubule dynamics in motile fibroblasts. *Cell*. 104:923-35.

Asperti, C., V. Astro, A. Totaro, S. Paris, and I. de Curtis. 2009. Liprin-alpha1 promotes cell spreading on the extracellular matrix by affecting the distribution of activated integrins. *J Cell Sci*. 122:3225-32.

Asperti, C., E. Pettinato, and I. de Curtis. 2010. Liprin-alpha1 affects the distribution of low-affinity beta1 integrins and stabilizes their permanence at the cell surface. *Exp Cell Res*. 316:915-26.

Astro, V., C. Asperti, G. Cangi, C. Doglioni, and I. de Curtis. 2010. Liprin-alpha1 regulates breast cancer cell invasion by affecting cell motility, invadopodia and extracellular matrix degradation. *Oncogene*.

Astro, V., S. Chiaretti, E. Magistrati, M. Fivaz, and I. de Curtis. 2014. Liprin-alpha1, ERC1 and LL5 define polarized and dynamic structures that are implicated in cell migration. *J Cell Sci*. 127:3862-76.

Bassi, Z.I., M. Audusseau, M.G. Riparbelli, G. Callaini, and P.P. D'Avino. 2013. Citron kinase controls a molecular network required for midbody formation in cytokinesis. *Proc Natl Acad Sci U S A*. 110:9782-7.

Basu, S., S. Sladecek, Y.V.I. Martinez de la Pena, M. Akaaboune, I. Smal, K. Martin, N. Galjart, and H.R. Brenner. 2015. CLASP2-dependent microtubule capture at the neuromuscular junction membrane requires LL5beta and actin for focal delivery of acetylcholine receptor vesicles. *Mol Biol Cell*.

Chen, H.J., G. Anagnostou, A. Chai, J. Withers, A. Morris, J. Adhikaree, G. Pennetta, and J.S. de Belleroche. 2010. Characterization of the properties of a novel mutation in VAPB in familial amyotrophic lateral sclerosis. *J Biol Chem*. 285:40266-81.

Courtois, G. 2008. Tumor suppressor CYLD: negative regulation of NF-kappaB signaling and more. *Cell Mol Life Sci*. 65:1123-32.

Dai, Y., H. Taru, S.L. Deken, B. Grill, B. Ackley, M.L. Nonet, and Y. Jin. 2006. SYD-2 Liprin-alpha organizes presynaptic active zone formation through ELKS. *Nat Neurosci*. 9:1479-1487.

Das, A., and W. Guo. 2011. Rabs and the exocyst in ciliogenesis, tubulogenesis and beyond. *Trends Cell Biol*. 21:383-6.

Doudna, J.A., and E. Charpentier. 2014. Genome editing. The new frontier of genome engineering with CRISPR-Cas9. *Science*. 346:1258096.

Drabek, K., M. van Ham, T. Stepanova, K. Draegestein, R. van Horssen, C.L. Sayas, A. Akhmanova, T. Ten Hagen, R. Smits, R. Fodde, F. Grosveld, and N. Galjart. 2006. Role of CLASP2 in microtubule stabilization and the regulation of persistent motility. *Curr Biol*. 16:2259-64.

Fontijn, R.D., B. Goud, A. Echard, F. Jollivet, J. van Marle, H. Pannekoek, and A.J. Horrevoets. 2001. The human kinesin-like protein RB6K is under tight cell cycle control and is essential for cytokinesis. *Mol Cell Biol*. 21:2944-55.

Fouquet, W., D. Owald, C. Wichmann, S. Mertel, H. Depner, M. Dyba, S. Hallermann, R.J. Kittel, S. Eimer, and S.J. Sigrist. 2009. Maturation of active zone assembly by Drosophila Bruchpilot. *J Cell Biol*. 186:129-45.

Fukuda, M., E. Kanno, K. Ishibashi, and T. Itoh. 2008. Large scale screening for novel rab effectors reveals unexpected broad Rab binding specificity. *Mol Cell Proteomics*. 7:1031-42.

Galvez-Santisteban, M., A.E. Rodriguez-Fraticelli, D.M. Bryant, S. Vergarajauregui, T. Yasuda, I. Banon-Rodriguez, I. Bernascone, A. Datta, N. Spivak, K. Young, C.L. Slim, P.R. Brakeman, M. Fukuda, K.E. Mostov, and F. Martin-Belmonte. 2012. Synaptotagmin-like proteins control the formation of a single apical membrane domain in epithelial cells. *Nat Cell Biol*. 14:838-49.

Gershoni-Emek, N., M. Chein, S. Gluska, and E. Perlson. 2015. Amyotrophic lateral sclerosis as a spatiotemporal mislocalization disease: location, location, location. *Int Rev Cell Mol Biol*. 315:23-71.

Giridharan, S.S., and S. Caplan. 2014. MICAL-family proteins: Complex regulators of the actin cytoskeleton. *Antioxid Redox Signal*. 20:2059-73.

Giridharan, S.S., J.L. Rohn, N. Naslavsky, and S. Caplan. 2012. Differential regulation of actin microfilaments by human MICAL proteins. *J Cell Sci*. 125:614-24.

Gomi, H., S. Mizutani, K. Kasai, S. Itohara, and T. Izumi. 2005. Granuphilin molecularly docks insulin granules to the fusion machinery. *J Cell Biol*. 171:99-109.

Grigoriev, I., D. Splinter, N. Keijzer, P.S. Wulf, J. Demmers, T. Ohtsuka, M. Modesti, I.V. Maly, F. Grosveld, C.C. Hoogenraad, and A. Akhmanova. 2007. Rab6 regulates transport and targeting of exocytotic carriers. *Dev Cell*. 13:305-14.

Grigoriev, I., K.L. Yu, E. Martinez-Sanchez, A. Serra-Marques, I. Smal, E. Meijering, J. Demmers, J. Peranen, R.J. Pasterkamp, P. van der Sluijs, C.C. Hoogenraad, and

A. Akhmanova. 2011. Rab6, Rab8, and MICAL3 Cooperate in Controlling Docking and Fusion of Exocytotic Carriers. *Curr Biol*. 21:967-74.

Gruneberg, U., R. Neef, X. Li, E.H. Chan, R.B. Chalamalasetty, E.A. Nigg, and F.A. Barr. 2006. KIF14 and citron kinase act together to promote efficient cytokinesis. *J Cell Biol*. 172:363-72.

Guo, W., D. Roth, C. Walch-Solimena, and P. Novick. 1999. The exocyst is an effector for Sec4p, targeting secretory vesicles to sites of exocytosis. *EMBO J*. 18:1071-80.

Hallermann, S., R.J. Kittel, C. Wichmann, A. Weyhersmuller, W. Fouquet, S. Mertel, D. Owald, S. Eimer, H. Depner, M. Schwarzel, S.J. Sigrist, and M. Heckmann. 2010. Naked dense bodies provoke depression. *J Neurosci*. 30:14340-5.

Harhaj, E.W., and V.M. Dixit. 2012. Regulation of NF-kappaB by deubiquitinases. *Immunol Rev*. 246:107-24.

Hetz, C., E. Chevet, and H.P. Harding. 2013. Targeting the unfolded protein response in disease. *Nat Rev Drug Discov*. 12:703-19.

Hill, E., M. Clarke, and F.A. Barr. 2000. The Rab6-binding kinesin, Rab6-KIFL, is required for cytokinesis. *Embo J*. 19:5711-9.

Hotta, A., T. Kawakatsu, T. Nakatani, T. Sato, C. Matsui, T. Sukezane, T. Akagi, T. Hamaji, I. Grigoriev, A. Akhmanova, Y. Takai, and Y. Mimori-Kiyosue. 2010. Laminin-based cell adhesion anchors microtubule plus ends to the epithelial cell basal cortex through LL5alpha/beta. *J Cell Biol*. 189:901-17.

Hung, R.J., C.W. Pak, and J.R. Terman. 2011. Direct redox regulation of F-actin assembly and disassembly by Mical. *Science*. 334:1710-3.

Hung, R.J., C.S. Spaeth, H.G. Yesilyurt, and J.R. Terman. 2013. SelR reverses Mical-mediated oxidation of actin to regulate F-actin dynamics. *Nat Cell Biol*. 15:1445-54.

Hung, R.J., U. Yazdani, J. Yoon, H. Wu, T. Yang, N. Gupta, Z. Huang, W.J. van Berkel, and J.R. Terman. 2010. Mical links semaphorins to F-actin disassembly. *Nature*. 463:823-7.

Kaeser, P.S., L. Deng, A.E. Chavez, X. Liu, P.E. Castillo, and T.C. Sudhof. 2009. ELKS2alpha/CAST deletion selectively increases neurotransmitter release at inhibitory synapses. *Neuron*. 64:227-39.

Kaplan, A., and O. Reiner. 2011. Linking cytoplasmic dynein and transport of Rab8 vesicles to the midbody during cytokinesis by the doublecortin domain-containing 5 protein. *J Cell Sci*. 124:3989-4000.

Kasai, K., T. Fujita, H. Gomi, and T. Izumi. 2008. Docking is not a prerequisite but a

temporal constraint for fusion of secretory granules. *Traffic*. 9:1191-203.

Kittel, R.J., C. Wichmann, T.M. Rasse, W. Fouquet, M. Schmidt, A. Schmid, D.A. Wagh, C. Pawlu, R.R. Kellner, K.I. Willig, S.W. Hell, E. Buchner, M. Heckmann, and S.J. Sigrist. 2006. Bruchpilot promotes active zone assembly, Ca2+ channel clustering, and vesicle release. *Science*. 312:1051-4.

Kittelmann, M., J. Hegermann, A. Goncharov, H. Taru, M.H. Ellisman, J.E. Richmond, Y. Jin, and S. Eimer. 2013. Liprin-alpha/SYD-2 determines the size of dense projections in presynaptic active zones in C. elegans. *J Cell Biol*. 203:849-63.

Ko, J., M. Na, S. Kim, J.R. Lee, and E. Kim. 2003. Interaction of the ERC family of RIM-binding proteins with the liprin-alpha family of multidomain proteins. *J Biol Chem*. 278:42377-85.

Kuijpers, M., V. van Dis, E.D. Haasdijk, M. Harterink, K. Vocking, J.A. Post, W. Scheper, C.C. Hoogenraad, and D. Jaarsma. 2013a. Amyotrophic lateral sclerosis (ALS)-associated VAPB-P56S inclusions represent an ER quality control compartment. *Acta Neuropathol Commun*. 1:24.

Kuijpers, M., K.L. Yu, E. Teuling, A. Akhmanova, D. Jaarsma, and C.C. Hoogenraad. 2013b. The ALS8 protein VAPB interacts with the ER-Golgi recycling protein YIF1A and regulates membrane delivery into dendrites. *EMBO J*. 32:2056-72.

Kypta, R.M., H. Su, and L.F. Reichardt. 1996. Association between a transmembrane protein tyrosine phosphatase and the cadherin-catenin complex. *J Cell Biol*. 134:1519-29.

Lansbergen, G., I. Grigoriev, Y. Mimori-Kiyosue, T. Ohtsuka, S. Higa, I. Kitajima, J. Demmers, N. Galjart, A.B. Houtsmuller, F. Grosveld, and A. Akhmanova. 2006. CLASPs attach microtubule plus ends to the cell cortex through a complex with LL5beta. *Dev Cell*. 11:21-32.

Lee, B.C., Z. Peterfi, F.W. Hoffmann, R.E. Moore, A. Kaya, A. Avanesov, L. Tarrago, Y. Zhou, E. Weerapana, D.E. Fomenko, P.R. Hoffmann, and V.N. Gladyshev. 2013. MsrB1 and MICALs regulate actin assembly and macrophage function via reversible stereoselective methionine oxidation. *Mol Cell*. 51:397-404.

Lev, S., D. Ben Halevy, D. Peretti, and N. Dahan. 2008. The VAP protein family: from cellular functions to motor neuron disease. *Trends Cell Biol*. 18:282-90.

Liu, C., L.S. Bickford, R.G. Held, H. Nyitrai, T.C. Sudhof, and P.S. Kaeser. 2014. The active zone protein family ELKS supports Ca2+ influx at nerve terminals of inhibitory hippocampal neurons. *J Neurosci*. 34:12289-303.

Matern, H., X. Yang, E. Andrulis, R. Sternglanz, H.H. Trepte, and D. Gallwitz. 2000. A novel Golgi membrane protein is part of a GTPase-binding protein complex

involved in vesicle targeting. *EMBO J*. 19:4485-92.

Mercado, G., P. Valdes, and C. Hetz. 2013. An ERcentric view of Parkinson's disease. *Trends Mol Med*. 19:165-75.

Mikitova, V., and T.P. Levine. 2012. Analysis of the key elements of FFAT-like motifs identifies new proteins that potentially bind VAP on the ER, including two AKAPs and FAPP2. *PLoS One*. 7:e30455.

Monier, S., F. Jollivet, I. Janoueix-Lerosey, L. Johannes, and B. Goud. 2002. Characterization of novel Rab6-interacting proteins involved in endosome-to-TGN transport. *Traffic*. 3:289-97.

Moustaqim-Barrette, A., Y.Q. Lin, S. Pradhan, G.G. Neely, H.J. Bellen, and H. Tsuda. 2014. The amyotrophic lateral sclerosis 8 protein, VAP, is required for ER protein quality control. *Hum Mol Genet*. 23:1975-89.

Nakaya, Y., E.W. Sukowati, and G. Sheng. 2013. Epiblast integrity requires CLASP and Dystroglycan-mediated microtubule anchoring to the basal cortex. *J Cell Biol*. 202:637-51.

Nishimura, A.L., M. Mitne-Neto, H.C. Silva, A. Richieri-Costa, S. Middleton, D. Cascio, F. Kok, J.R. Oliveira, T. Gillingwater, J. Webb, P. Skehel, and M. Zatz. 2004. A mutation in the vesicle-trafficking protein VAPB causes late-onset spinal muscular atrophy and amyotrophic lateral sclerosis. *Am J Hum Genet*. 75:822-31.

Niu, J., Y. Shi, K. Iwai, and Z.H. Wu. 2011. LUBAC regulates NF-kappaB activation upon genotoxic stress by promoting linear ubiquitination of NEMO. *EMBO J*. 30:3741-53.

Ohara-Imaizumi, M., T. Ohtsuka, S. Matsushima, Y. Akimoto, C. Nishiwaki, Y. Nakamichi, T. Kikuta, S. Nagai, H. Kawakami, T. Watanabe, and S. Nagamatsu. 2005. ELKS, a protein structurally related to the active zone-associated protein CAST, is expressed in pancreatic beta cells and functions in insulin exocytosis: interaction of ELKS with exocytotic machinery analyzed by total internal reflection fluorescence microscopy. *Mol Biol Cell*. 16:3289-300.

Paranavitane, V., W.J. Coadwell, A. Eguinoa, P.T. Hawkins, and L. Stephens. 2003. LL-5beta is a phosphatidylinositol (3,4,5)-trisphosphate sensor that can bind the cytoskeletal adaptor, gamma-filamin. *J Biol Chem*. 278:1328-35.

Peranen, J., P. Auvinen, H. Virta, R. Wepf, and K. Simons. 1996. Rab8 promotes polarized membrane transport through reorganization of actin and microtubules in fibroblasts. *J Cell Biol*. 135:153-67.

Proszynski, T.J., and J.R. Sanes. 2013. Amotl2 interacts with LL5beta, localizes to

podosomes and regulates postsynaptic differentiation in muscle. *J Cell Sci*. 126:2225-35.

Rocha, N., C. Kuijl, R. van der Kant, L. Janssen, D. Houben, H. Janssen, W. Zwart, and J. Neefjes. 2009. Cholesterol sensor ORP1L contacts the ER protein VAP to control Rab7-RILP-p150 Glued and late endosome positioning. *J Cell Biol*. 185:1209-25.

Schmidt, E.F., S.O. Shim, and S.M. Strittmatter. 2008. Release of MICAL autoinhibition by semaphorin-plexin signaling promotes interaction with collapsin response mediator protein. *J Neurosci*. 28:2287-97.

Spangler, S.A., S.K. Schmitz, J.T. Kevenaar, E. de Graaff, H. de Wit, J. Demmers, R.F. Toonen, and C.C. Hoogenraad. 2013. Liprin-alpha2 promotes the presynaptic recruitment and turnover of RIM1/CASK to facilitate synaptic transmission. *J Cell Biol*. 201:915-28.

Stehbens, S.J., M. Paszek, H. Pemble, A. Ettinger, S. Gierke, and T. Wittmann. 2014. CLASPs link focal-adhesion-associated microtubule capture to localized exocytosis and adhesion site turnover. *Nat Cell Biol*. 16:561-73.

Stoica, R., K.J. De Vos, S. Paillusson, S. Mueller, R.M. Sancho, K.F. Lau, G. Vizcay-Barrena, W.L. Lin, Y.F. Xu, J. Lewis, D.W. Dickson, L. Petrucelli, J.C. Mitchell, C.E. Shaw, and C.C. Miller. 2014. ER-mitochondria associations are regulated by the VAPB-PTPIP51 interaction and are disrupted by ALS/FTD-associated TDP-43. *Nat Commun*. 5:3996.

Stryker, E., and K.G. Johnson. 2007. LAR, liprin alpha and the regulation of active zone morphogenesis. *J Cell Sci*. 120:3723-8.

Sudhof, T.C., and J.E. Rothman. 2009. Membrane fusion: grappling with SNARE and SM proteins. *Science*. 323:474-7.

Tsuda, H., S.M. Han, Y. Yang, C. Tong, Y.Q. Lin, K. Mohan, C. Haueter, A. Zoghbi, Y. Harati, J. Kwan, M.A. Miller, and H.J. Bellen. 2008. The amyotrophic lateral sclerosis 8 protein VAPB is cleaved, secreted, and acts as a ligand for Eph receptors. *Cell*. 133:963-77.

Van Battum, E.Y., R.A. Gunput, S. Lemstra, E.J. Groen, K.L. Yu, Y. Adolfs, Y. Zhou, C.C. Hoogenraad, Y. Yoshida, M. Schachner, A. Akhmanova, and R.J. Pasterkamp. 2014. The intracellular redox protein MICAL-1 regulates the development of hippocampal mossy fibre connections. *Nat Commun*. 5:4317.

van Blitterswijk, M., M.A. van Es, M. Koppers, W. van Rheenen, J. Medic, H.J. Schelhaas, A.J. van der Kooi, M. de Visser, J.H. Veldink, and L.H. van den Berg. 2012. VAPB and C9orf72 mutations in 1 familial amyotrophic lateral sclerosis

patient. *Neurobiol Aging*. 33:2950 e1-4.

van der Vaart, B., W.E. van Riel, H. Doodhi, J.T. Kevenaar, E.A. Katrukha, L. Gumy, B.P. Bouchet, I. Grigoriev, S.A. Spangler, K.L. Yu, P.S. Wulf, J. Wu, G. Lansbergen, E.Y. van Battum, R.J. Pasterkamp, Y. Mimori-Kiyosue, J. Demmers, N. Olieric, I.V. Maly, C.C. Hoogenraad, and A. Akhmanova. 2013. CFEOM1-associated kinesin KIF21A is a cortical microtubule growth inhibitor. *Dev Cell*. 27:145-60.

Wagh, D.A., T.M. Rasse, E. Asan, A. Hofbauer, I. Schwenkert, H. Durrbeck, S. Buchner, M.C. Dabauvalle, M. Schmidt, G. Qin, C. Wichmann, R. Kittel, S.J. Sigrist, and E. Buchner. 2006. Bruchpilot, a protein with homology to ELKS/CAST, is required for structural integrity and function of synaptic active zones in Drosophila. *Neuron*. 49:833-44.

Wang, Y., X. Liu, T. Biederer, and T.C. Sudhof. 2002. A family of RIM-binding proteins regulated by alternative splicing: Implications for the genesis of synaptic active zones. *Proc Natl Acad Sci U S A*. 99:14464-9.

Wang, Z., and D.C. Thurmond. 2009. Mechanisms of biphasic insulin-granule exocytosis - roles of the cytoskeleton, small GTPases and SNARE proteins. *J Cell Sci*. 122:893-903.

Weide, T., J. Teuber, M. Bayer, and A. Barnekow. 2003. MICAL-1 isoforms, novel rab1 interacting proteins. *Biochem Biophys Res Commun*. 306:79-86.

Yoshida, Y., K. Suzuki, A. Yamamoto, N. Sakai, M. Bando, K. Tanimoto, Y. Yamaguchi, T. Sakaguchi, H. Akhter, G. Fujii, S. Yoshimura, S. Ogata, M. Sohda, Y. Misumi, and N. Nakamura. 2008. YIPF5 and YIF1A recycle between the ER and the Golgi apparatus and are involved in the maintenance of the Golgi structure. *Exp Cell Res*. 314:3427-43.

Zhou, Y., R.A. Gunput, Y. Adolfs, and R.J. Pasterkamp. 2011. MICALs in control of the cytoskeleton, exocytosis, and cell death. *Cell Mol Life Sci*. 31:3603-15.

Summary

Intracellular membrane trafficking is an essential cellular process that involves cooperation of many factors such as scaffolding proteins, GTPases and SNAREs. These proteins work together to ensure proper delivery of different membrane-enclosed cargoes to specific cellular destinations. In this thesis, we have combined diverse biochemical and molecular genetics approaches to get a better insight in the regulation of intracellular trafficking.

In the Introduction, we review the existing literature describing the function of ELKS, an evolutionarily conserved coiled coil protein with a scaffolding function. We discuss the role of this protein in microtubule organization and constitutive secretion, in synaptic function in neurons, in regulated secretion in pancreatic β cells and mast cells, and its potential involvement in human disease.

In the experimental part of this thesis, we have extensively used affinity purification in combination with mass spectrometry to identify novel binding partners of several proteins involved in different steps of membrane trafficking pathways. In Chapter 2, we discussed the methodology of protein partner identification using microtubule plus-end tracking proteins (+TIPs) as an example. In Chapter 3, we focused on the interaction of two components of the early steps of the secretory pathway, YIF1A and VAPB, a candidate gene for amyotrophic lateral sclerosis (ALS). We characterized the interaction between these two proteins by biochemical and cytological approaches and showed that both of them are essential for ER-to-Golgi transport and intracellular membrane trafficking in dendrites. We showed that the ALS-associated mutation of VAPB, P56S, leads to the formation of protein aggregates that can sequester YIF1A. The mis-localization of the VAPB-YIF1A complex might be a cause for pathology in ALS.

In Chapter 4, we look at the last step of constitutive exocytosis, which involves ELKS, Rab6 and Rab8. We observed colocalization of Rab6, a marker for exo-

cytotic vesicles, with Rab8, a Rab GTPase previously implicated in secretion. The depletion of ELKS leads to the accumulation of Rab6 vesicles, showing that ELKS regulates the fusion of these vesicles with the plasma membrane. We performed pull-down assays using ELKS as bait and found MICAL-3, a flavoprotein monooxygenase that binds to Rab8. A dominant negative mutant of MICAL-3 promotes Rab6 vesicle docking but strongly delays vesicle fusion with the plasma membrane. We propose that through its monooxygenase activity, MICAL-3 can participate in remodeling of the vesicle-docking complex and enable fusion. These data show how two Rab GTPases, a cortical protein ELKS and an oxidative enzyme work together to regulate the fusion of exocytotic vesicles.

In Chapter 5, we gained a better understanding of the function of MICAL family proteins. We showed that MICAL-1 is an essential regulator of actin filaments and the absence of MICAL-1 leads to a defect in the distribution of exocytotic vesicles in mouse embryonic fibroblasts. We also performed a mass spectrometry-based search for binding partners of MICAL-3, identified MKLP1 and Ankyrin-G as two potential interacting partners of MICAL-3 and confirmed their interactions using biochemical and cell biological tools. We proposed a role of MICAL-3 in cytokinesis through cooperation with MKLP1.

The function of ELKS took the stage in the last part of this thesis. In Chapter 6, we reported the generation of ELKS knockout and BioGFP-ELKS knock-in mice. We used a genetic strategy which allowed us to generate BioGFP-ELKS knock-in allele by Cre-mediated recombination of the ELKS knockout allele. We observed that homozygous ELKS knockout mice die during embryonic development, but that this phenotype was efficiently rescued in the BioGFP-ELKS knock-in mice. Culturing of the homozygous ELKS knockout cells confirmed the important role of ELKS in exocytosis: ELKS knockout cells displayed strong accumulation of Rab6 vesicles, a phenotype that could be rescued by converting the knockout allele to BioGFP-ELKS knock-in. Surprisingly, we found that ELKS knockout cells migrated faster compared to the cells where the ELKS function was restored. The localization of BioGFP-ELKS in cells and tissues matched nicely that of the endogenous untagged protein. We also extensively analyzed the ELKS interactome by pulling down biotinylated and GFP-tagged ELKS proteins, expressed at endogenous levels; this analysis provided us

with an overview of ELKS binding partners. Taken together, we showed that the knockout and BioGFP-ELKS knockin mice can be used to study ELKS function, biochemistry and localization.

In Chapter 7, we highlight the importance of cortical localization of ELKS in different non-neuronal cells. We found that the recruitment of ELKS to cortical sites that are in close vicinity of focal adhesions depends on scaffolding proteins liprin-α1 and liprin-β1. We observed that ELKS affects the distribution of ACF7/MACF1 and has a mild effect on the liprins and LL5β. Using the BioGFP-ELKS knock-in cells, we studied the dynamics of ELKS using fluorescence recovery after photobleaching (FRAP). We concluded that the cortical ELKS forms dimers which exchange with the cytoplasmic pool. The dynamics of cortical ELKS-positive structures is complex and regulated by actomyosin-dependent flows. Live imaging analysis on murine pancreatic islets isolated from BioGFP-ELKS mice confirmed the cortical localization of ELKS in β cells. ELKS marks the docking sites of insulin granules and has a different turnover rate during glucose stimulated insulin release. We proposed that this dynamic distribution of ELKS might serve to regulate the docking and fusion of insulin granules.

In Chapter 8, we discuss the experimental data described in Chapters 3 to 7 and provide an overview of potential directions for future research.

Samenvatting

Intracellulair membraan transport is een essentieel cellulair proces dat tot stand komt door de coöperatie van vele factoren zoals verbindingseiwitten (scaffolding eiwitten), GTPases and SNAREs. Deze eiwitten werken samen om er voor te zorgen dat membraan omhulde cargo bij de juiste cellulaire locatie aan komt. In dit proefschrift hebben we gebruik gemaakt van diverse biochemische en moleculair genetische technieken om een beter inzicht te krijgen in de regulatie van intracellulair transport.

In de inleiding geven we een overzicht van de op dit moment bekende literatuur die de functie beschrijft van ELKS, een evolutionair geconserveerd coiled-coil eiwit die een scaffolding functie verleent. We bespreken de rol van het eiwit in de organisatie van microtubuli en constitutieve secretie, in het licht van de synaptische functie in neuronen, in de gereguleerde secretie in pancreatische β-cellen en mastocyten en de mogelijke betrokkenheid van het eiwit bij humane ziektes.

In het experimentele deel van dit proefschrift, hebben we veel gebruik gemaakt van affiniteits purificatie in combinatie met massa spectrometrie om nieuwe bindingspartners te identificeren van verscheidene eiwitten die betrokken zijn in verschillende stappen in membraan transportwegen. In hoofdstuk 2 bespreken we de methodologie om eiwit bindingspartners te identificeren met microtubuli plus-einde bindende eiwitten (+TIPs) als voorbeeld. In hoofdstuk 3 richten we ons op de interactie van twee componenten die betrokken zijn bij de vroege stappen van de secretie route, YIF1A en VAPB, een kandidaat gen voor de ontwikkeling van amyotrofische laterale sclerose (ALS). Wij hebben de interactie tussen deze twee eiwitten gekarakteriseerd via biochemische en cytologische benaderingen en laten zien dat beide eiwitten essentieel zijn voor ER-naar-Golgi transport en intracellulair transport in dendrieten. We laten zien dat de ALS-geassocieerde mutatie in VAPB, P56S, zorgt voor de forming van

eiwit aggregaten die YIF1A kunnen onttrekken van het cellulaire milieu. Deze misplaatsing van het VAPB-YIF1A complex zou de oorzaak kunnen zijn van de pathologie gezien bij ALS.

In hoofdstuk 4 bespreken we vindingen die betrekking hebben op de laatste stap van constitutieve exocytose, waar ELKS, Rab6 en Rab8 betrokken zijn. We zien colocalisatie van Rab6, een marker van exocytotische blaasjes, met Rab8, een Rab GTPase eerder geïmpliceerd in secretie. Depletie van ELKS leidt tot de accumulatie van Rab6 blaasjes, wat laat zien dat ELKS betrokken is bij de fusie van blaasjes met de plasma membraan. We hebben pull-down assays gedaan met ELKS en vonden MICAL-3, een flavomonooxygenase eiwit die bindt aan Rab8. Een dominant negatieve mutant van MICAL-3 stimuleert de hechting van Rab6 positieve blaasjes aan deplasma membraan, maar vertraagt sterk de fusie van het blaasje met de membraan. Wij denken dat door zijn monooxygenase activiteit, MICAL-3 helpt bij het remodelleren van het blaasje geassocieerde hechtingscomplex en daarmee fusie bewerkstelligt. Deze data laten zien hoe twee Rab GTPases, het corticale eiwit ELKS en een oxidatief enzym samen werken bij de regulatie van de fusie van exocytotische blaasjes.

In hoofdstuk 5 laten we data zien die onze kennis over de functie van eiwitten in de MICAL familie verder helpt. We laten zien dat MICAL-1 een essentiële regulator is van actine filamenten en de afwezigheid van MICAL-1 leidt tot een defect in de distributie van exocytotische blaasjes in muizen embryonische fibroblasten. We hebben ook een massa spectrometrische screen gedaan voor bindingspartners van MICAL-3 waar we hebben gevonden dat MKLP1 en ANK3 twee mogelijke interactie partners zijn van MICAL-3. Deze interacties waren bevestigt via biochemische en cel biologische middelen. We stellen voor dat MICAL-3 een rol heeft tijdens cytokinese door samenwerking met MKLP1.

De functie van ELKS wordt behandeld in het laatste deel van dit proefschrift. In hoofdstuk 6 beschrijven we de generatie van een ELKS knock-out en BioGFP-ELKS knock-in muizen. We hebben een genetische strategie gebruikt welke ons in staat stelde om een BioGFP-ELKS knock-in allel te maken door Cre-gemedieerde recombinatie van het ELKS knock-out allel. We observeerden dat homozygote ELKS knock-out muizen sterven gedurende embryonische ontwikkeling, maar dat dit fenotype werd omgedraaid in de BioGFP-ELKS

knock-in. Experimenten met homozygote ELKS knock-out cellen bevestigde de belangrijke rol van ELKS in exocytose: deze cellen laten een sterke accumulatie van Rab6 positieve blaasjes zien. Dit fenotype werd terug gedraaid door de conversie van het knock-out allel naar de BioGFP-ELKS knock-in. Heel onverwacht vonden wij dat ELKS knock-out cellen sneller migreerden dan cellen waar de ELKS functie was hersteld. De localisatie van BioGFP-ELKS in cellen en weefsels kwam goed overeen met die van het endogene, niet gelabelde eiwit. We hebben ook het ELKS interactoom uitvoerig geanalyseerd door pull-down van gebiotinyleerd en GFP gelabeld ELKS, die tot expressie waren gebracht op endogeen niveau. Deze analyse gaf ons een overzicht van ELKS bindingspartners. Bij elkaar hebben we laten zien dat de knock-out en de BioGFP-ELKS knock-in muizen gebruikt kunnen worden voor de studie van de functie, biochemie en de localisatie van ELKS.

In hoofdstuk 7 belichten we het belang van een corticale localistie van ELKS in verschillende non-neuronale cellen. We vonden dat de aantrekking van ELKS naar corticale locaties die zich dicht bevinden bij focale adhesies afhankelijk is van de scaffolding eiwitten liprin-α1 en liprin-β1. We zagen dat ELKS effect had op de distributie van ACF7/MACF1 en dat het een mild effect had op de liprins en LL5β. We hebben de dynamica van ELKS bestudeerd in de BioGFP-ELKS knock-in cellen door middel van *fluorescence recovery after photobleaching* (FRAP). We concluderen dat corticaal ELKS een dimeer vormt en uitwisselt met de cytoplasmatische pool. De dynamica van corticaal ELKS is complex en gereguleerd door actomyosin-afhankelijke stromingen. Live imaging analyse op eilandjes van Langerhans geïsoleerd uit alvleesklier van BioGFP-ELKS muizen bevestigde de corticale localisatie van ELKS in β-cellen. ELKS markeert de hechtingsplaatsen van insuline granules en heeft een andere turnover rate gedurende glucose-gestimuleerde insuline secretie. We stellen voor dat deze dynamische distributie van ELKS kan helpen bij de hechting en fusie van insuline granules.

Hoofdstuk 8 bevat een discussie over de experimentele data die beschreven is in hoofdstuk 3 tot 7 en geeft een overzicht van mogelijke richtingen van toekomstig onderzoek.

About the author

Ká Lou (Carol) Yu (余加璐) was born on 14 October 1981 in Macau S.A.R., China. In 1999, she pursued her university studies in Taiwan, majoring in Life Science at National Yang Ming University. After finishing her bachelor degree in 2004, Carol worked as a research technician at Dr. Tai Huang Huang's structural biology laboratory in the Biomedical Sciences Institute of Academia Sinica, Taiwan. With her interest in Neuroscience, she was awarded the Excellence scholarship of Utrecht University in 2005 to pursue her master degree in Neuroscience & Cognition in the Netherlands. She finished her two internships in Rudolf Magnus Institute of Neuroscience and Department of Neuroscience in Erasmus Medical Center respectively. Working with Dr. Martien J. Kas, she investigated the complex nature of locomotion by studying the motor activity levels, synchronous hind limb movement and neuro-anatomical differences in spinal motor neurons of different inbred mice. After that, she joined Dr. Dick Jaarsma and Dr. Casper Hoogenraad's groups and characterized the molecular interactions of vesicle-associated membrane protein (VAMP) associated protein B (VAPB) with its interacting partners, successfully verified and mapped the interaction of VAPB with Yip1-interacting factor homologue A (YIF1A). In November 2007, Carol became interested in dissecting the molecular mechanism of intracellular trafficking and started working with Dr. Anna Akhmanova at the Department of Cell Biology in Erasmus Medical Center, she then moved with the Akhmanova's group in November 2011 and continued her work in Utrecht University. The achievement of her research project is summarized in this thesis.

Curriculum Vitae

PERSONAL INFORMATION:

Name:	Ká Lou (Carol) Yu
E-mail address:	k.l.yu@uu.nl/carolklyu@gmail.com
Nationality:	Portugal

EDUCATION:

2011-2015	Phd candidate	Division of Cell Biology, Dept. of Biology, Utrecht University, the Netherlands (The Akhmanova lab moved from Erasmus MC to Utrecht University)
2007-2011	Phd candidate	Dept. of Cell Biology, Erasmus Medical Center, Rotterdam, the Netherlands.
2005-2009	M. S.	Neuroscience and Cognition Master programme (ECN tract), Utrecht University, the Netherlands.
2000–2004	B. S.	Faculty of Life Sciences, National Yang Ming University (N. Y. M. U.), Taiwan R. O. C.
1993-1999	Diploma	Sacred Heart Canossian College, English Section, Macau.

RESEARCH EXPERIENCE:

Nov. 2007-Mar. 2015	Prof. Dr. Anna Akhmanova's group, Dept. of Biology, Faculty of Science, Utrecht University & Dept. of Cell Biology, Erasmus Medical Center, Rotterdam. PhD project: The role of ELKS protein in linking NF-kappaB activation to cortical cytoskeletal organization.
Mar. 2007-Oct. 2007	Dr. Dick Jaarsma and Dr. Casper C. Hoogenraad's group, Dept. of Neuroscience, Erasmus Medical Center, Rotterdam. Internship: Characterization of VAPB associated proteins involved in motor neuron diseases.
Feb. 2006-Jan. 2007	Dr. Martien J. H. Kas's group, Behavioural and Genomics Section, Dept. of Pharmacology and Anatomy, Rudolf Magnus Institute of Neuroscience, Utrecht. Internship: Developmental and quantitative characterization of a recently identified gene for the expression of motor activity levels in mice.
Aug., 2004-Jul., 2005	Dr. Tai-Huang Huang's Laboratory, Institute of Biomedical Sciences, Academia Sinica, Taiwan R. O. C. i) Mutagenesis Studies of the heparin binding specificity of HDGF hath domain ii) Studies on the mechanism of dimer-monomer transition of HDGF hath domain
Jul., 2002-Jul., 2004	Dr. Jing-Jer Lin's Yeast Laboratory, N. Y. M. U., Taiwan R. O. C. Undergraduate thesis: Investigation of genes that are synthetic lethal to *cdc13-1*
Feb.,2001-Jun., 2002	Dr. Gwo-Jen Liaw's Drosophila Laboratory, N. Y. M. U., Taiwan R. O. C.

EXTRACURRICULAR ACTIVITIES:

Jan. 2014-Dec. 2014	Utrecht University ambassador of the Postdoc Career Development Initiative.
Jun., 2012-Oct. 2013	Lab manager of the Akhmanova laboratory, Dept. of Biology, Utrecht University.
Sept, 2008-Jun., 2009	Organization committee, 17th MGC PhD workshop, Cologne, Germany.

TEACHINGS:

2012	Supervision of a 2nd year master student on a short-term research project.
2011	Supervision of two high school students on lab techniques and research, Junior Science Program, Erasmus Medical Center, the Netherlands.
2010	Supervision of a 1st year master student on a lab rotation project, under Molecular Medicine Master program, MGC, Erasmus Medical Center, the Netherlands.

QUALIFICATIONS:

2012	Passed in het Staatsexamen Nederlands Als Tweede Taal, programma I (the State examination 'Dutch As Second Language, Program I'), the Netherlands.
2008	Passed in radioactive protection course level 5B (Stralingsbescherming deskundigheidsniveau 5B), Erasmus Medical Center, Rotterdam, the Netherlands.
2007	Passed in the international course on laboratory animal science (Level C, FELASA requirements; Artikel 9), Utrecht University, the Netherlands.

SCIENTIFIC MEETINGS ATTENDED:

Sept., 2013	Dutch meeting on Cellular and Molecular Biophysics 2012, Veldhoven, the Netherlands.
Mar., 2013	Phd retreat 2013, Institute of Biomembrane, Utrecht University.
Oct., 2012	Day of the Institute of Biomembrane Graduate Students and IB conference on Biomembrane, Utrecht University.
Sept., 2012	Dutch meeting on Cellular and Molecular Biophysics 2012, Veldhoven, the Netherlands.
Dec., 2011	Poster presentation, 51th American Society of Cell Biology annual meeting, Denver, U.S.A.
Nov., 2011	Oral presentation, day of the Institute of Biomembrane (IB) Graduate Students and IB conference on Biomembrane, Utrecht University.
Oct., 2011	Poster presentation, Dutch meeting on Cellular and Molecular Biophysics 2011, Veldhoven, the Netherlands.
Dec., 2010	Poster presentation, 50th American Society of Cell Biology annual meeting, Philadelphia, U.S.A.
Dec., 2010	Poster presentation, Cytoskeleton, Motors and Membrane Trafficking retreat, Philadelphia, U.S.A.
Oct., 2010	Oral presentation, workshop on Mechanisms of Cytoskeleton Dynamics and Intracellular Trafficking, Warsaw, Poland.

Jun., 2010	Oral presentation, 17th MGC PhD workshop, Cologne, Germany.
Nov., 2009	Oral presentation, 1st Intercity Young Scientist meeting, Heemskerk, the Netherlands.
Jun., 2009	Poster presentation, 16th MGC PhD workshop, Brussels, Belgium.
Jun., 2008	Poster presentation, 15th MGC PhD workshop, Heidelberg, Germany.

COURSES ATTENDED:

2013	Academic Writing and Presenting, the Netherlands Proteomics Center, Utrecht University, the Netherlands.
2012	PCDI (Postdoc Career Development Initiative) Postdoc Retreat 2012 (Your PhD as a Stepping Stone to Success), Kapellerput – Heeze, the Netherlands.
2011	Workshop on Photoshop and Illustrator CS5 for PhD students and other researchers, Erasmus Medical Center, the Netherlands.
2011	Workshop on InDesign CS5 for PhD students and other researchers, Erasmus Medical Center, the Netherlands.
2009	In Vivo Imaging 'From Molecular to Organism', Erasmus Medical Center, the Netherlands.
2009	Molecular and Cell Biology, Erasmus Medical Center, the Netherlands.

2008	Radioactive Protection Course Level 5B (Stralingsbescherming deskundigheidsniveau 5B), Erasmus Medical Center, the Netherlands.
2007	Safe laboratory Techniques, Erasmus Medical Center, the Netherlands.
2007	Reading and Discussing Literatures, Erasmus Medical Center, the Netherlands.

List of publications

van Battum E.Y., Gunput R. F., Lemstra S., Groen E. J. N., **Yu K. L.**, Adolfs Y., Zhou Y., Hoo-genraad C. C., Yoshida Y., Schachner M., Akhmanova A. and Pasterkamp R. J. (2014). The intracel-lular redox protein MICAL-1 regulates the development of hippocampal mossy fiber connections.
Nature Communications 5:4317. DOI: 10.1038/ncomms5317.

van der Vaart B., van Riel W. E., Doodhi H., Kevenaar J. T., Katrukha E. A., Gumy L., Bouchet B. P., Grigoriev I., Spangler S. A., **Yu K. L.**, Wulf P. S., Wu J., Lansbergen G., van Battum E. Y., Pasterkamp R. J., Mimori-Kiyosue Y., Demmers J., Olieric N., Maly I. V., Hoogenraad C. C., Akhmanova A. (2013). CFEOM1-associated kinesin KIF21A is a cortical microtubule growth inhibitor.
Developmental Cell 27(2):145-160.

Kuijpers M., **Yu K. L.**, Teuling E., Akhmanova A., Jaarsma D. and Hoogenraad C. C. (2013) The ALS8 protein VAPB interacts with the ER-Golgi recycling protein YIF1A and regulates membrane delivery into dendrites.
EMBO Journal 32(14):2056-2072.

Yu K. L.*, Grigoriev I.*, Martinez-Sanchez E.*, Serra-Marques A., Smal I., Meijering E., Demmers J., Peränen J., Pasterkamp R. J., van der Sluijs P., Hoogenraad C. C., Akhmanova A. (2011) Rab6, Rab8, and MICAL3 cooperate in controlling docking and fusion of exocytotic carriers.
Current Biology 7; 21(11):967-974. (* Equal contribution)

Yu K. L., Keijzer N., Hoogenraad C. C., Akhmanova A. (2011) Isolation of novel +TIPs and their binding partners using affinity purification techniques.
Methods in Molecular Biology 777; 293-316.

Splinter D., Tanenbaum M. E., Lindqvist A., Jaarsma D., Flotho A., **Yu K. L.**, Grigoriev I., Engelsma D., Haasdijk E. D., Keijzer N., Demmers J., Fornerod M., Melchior F., Hoogenraad C. C., Medema R. H., Akhmanova A. (2010) Bicaudal D2, dynein and kinesin-1 asscoiate with nucle-ar pore complexes and regulate centrosome and nuclear positioning during mitotic entry.
PLoS Biology 8(4):e1000350.

de Mooij-van Malsen J. G., **Yu K. L.**, Veldman H., Oppelaar H., van den Berg L. H., Olivier B., Kas M. J. (2009) Variations in ventral root axon morphology and locomotor behavior components across different inbred strains of mice.
Neuroscience 164(4):1477-1483.

Acknowledgements

Finally here comes to the most essential part of my thesis. Over the last couple of years during my PhD, I have been very lucky to get support from many colleagues and friends to reach this far.

First of all, I would like to give my promotor Anna a big thank you. Anna, thank you for giving me the chance to work at your group. You have been the most important person to support and guide me unconditionally at all the crossroads I came across over the last seven years. Your critical thinking and perseverance in science has shown me a good example. As a good scientist, you are always available to discuss ideas and experiments at any time. You have paved the way to dive into the understanding of ELKS. I won't forget the old times when you were pipetting on the bench at Ee1075. Of course, there are also many unforgettable memories we shared in Utrecht, especially the moving, they will remain for the rest of my life. You have helped me to find my way when I got lost, especially for the delivery of this thesis, and it would never be possible to have this complete thesis without your enormous help.

Secondly, I am also grateful for Casper. Casper, thanks for allowing me to work in your lab. I had a great time with the entire Hoogenraad lab at the Erasmus. Through you, I came to start doing molecular neuroscience work on the YIF1A project as well as to know Anna's work. The interview at your office 8 years ago is still fresh in my mind, what would I be doing in short term and long term for the coming 10 years? You also asked critical questions on my projects at different meetings, which helped me to steer the way. I enjoyed the chats we had on the train while we were on the way back to Rotterdam. Thank you for being part of the reading committee.

I thank the members of my reading committee, Prof. Sander van den Heuvel, Prof Gijsje Koenderink, Prof. Jeroen Pasterkamp and Prof. Willem Stoorvogel for making your time to read the thesis.

Next, I would like to thank Dick, who has been supportive with the histology work in this thesis. Dick, thank you for being so kind all the time when I first started my master internship in Erasmus, having a desk behind you in your office, you were always so generous to share your espresso, appelflappen and

muffins when I was working with you. I enjoyed your jokes too.

Esther, I would like to show my gratitude on behalf of my mice. You have given me help and suggestions with the transfer of my mice and the moving of my bench from Erasmus MC to Utrecht in summer and autumn 2011. I still remember the day when you came to help me moving, I filled every inch of your car with all the polyester boxes. Without your patience and help, the moving, DEC protocols and all the issues with my mice in Utrecht would not be easy.

Lukas, I thank you for giving us a lot of constructive suggestions on our experimental approach to ELKS dynamics, your passion for science impresses me, your scientific thinking and overview on a project opened my eyes during our meetings. Thank you for giving your time to look at my live imaging data.

The Akhmanova lab has been dynamic over the years. I have encountered many good labmates. Ilya, thanks for imaging my boyfriend MICAL-3 live under the microscope back in Erasmus and showing me DIC and TIRF in Utrecht. Daniel, Susana and Babet, you all have been very helpful when I got started in Ee1063, thank you for being understanding when I put a lot of notes in the lab. Daniel, you are always a calm and smiling person, who helps a lot to make a good at-mosphere in the lab. Susana, it is amazing how much you travel besides working during the night shifts, I really admire you. Thanks for sharing your big house and Figo with which I spent during the Christmas 2007. Babet, we had a great time doing ES cells targeting together, it was memorable and my pleasure to share your daily work every now and then. You were focused to develop western blots every day, I recall. It was also unforgettable to travel with you to the ASCB, when we were delayed at Schiphol. Rick and Wim, it was great to know you too. Kris, you brought extra fun to the lab, your green eyes are really catchy. Renu, you are a special friend, my great company on the trains during rainy days and snowy days, we walked pass the windy corner in front of R'dam CS hundreds of time together. A lot of good prizza time or Chinese meals in the evenings. We even took the wrong trains and went all the way to Den Haag without knowing, but it doesn't matter as we made each other the best company. Kai & Shasha, the masters of molecular cloning and Asian stews, thanks for helping out with the in vitro assay of MICAL-3, all the best for the dream lab in China. Andrea, it was great to hear

your passion for SNARES, kinesins, vesicle docking and fusion, good luck with the post-doc life. Ben, you are always helpful with different constructs for live imaging that I benefited from, but you stick to the rules of your cell culture kingdom. Gert-Jan, thanks for pointing me to the pancreatic islet field. Ivar, it was great to have you as a student for 8 weeks, you are the best. Qingyang, you have given us an enormous help with mass spectrometry data analysis days and nights, thanks a lot. Jingchao, we shared some funny conversations on Chinese politics, culture and history, our exchange program of lunch boxes also worked out fantastically. Hari, I cannot forget the meter-high fire at Renu's kitchen, that marked the peak of that evening, you are a talented cook. Besides, we shared a lot of evening meals at the UMC canteen with interesting life philosophy sessions. Smiriti, you are a kind colleague, thanks for showing me the complicated FOM and SRM ordering systems. Helma, thanks for taking over the lab ordering. Hope to talk to you more. Amol, you are the precious friend to me at work and outside work, you will be my transparent wing, I look forward to fullfil our Euromast challenge this June. Ruddi, Maud, Chao, Ankit, the new blood of the Akhmanova lab, I wish I would have time to know you guys better. All in all, all the best to you all in career and life. Visitors of the lab over the years: Maga, Jesper, Ashwani, it was great to know you, I enjoyed all the chats with you. Franco, thanks for your company over 9 hours of no-tulip cycling trip last spring.

Besides the Akhmanova lab, all the lab members of the Hoogenraad lab are also equally contributing a lot to the great time I had. Eva, you have always been open to me, teaching me science and being a friend to me when I moved to Rotterdam. The swimming evening was really unforgettable; it was the first 3000 meters I ever made in the Netherlands. Phebe and Nanda, you are always kind and patient to help me find my way when I started as a Master student. Samantha, thanks for inviting me to your parties and drinks. Max, thanks for picking up my rabbit serum on Christmas eve. Myrrhe, it was fun to teach you scientific terms in Chinese. Marijn, thanks for putting the YIF1A story further, your tips on thesis printing were appreciated. Mariella, Joanna and Petra, thanks for sharing the discoveries/frustrations of those days. Marina, thanks for your VHH nanobodies and the discussion on troubleshooting. Corette and Hai Yin, thanks for the scientific discussions and giving a try to the hippocampal slices on your setup, I hope you might still be interested later. Anael, thanks for giving

help with superresolution, your images are beautiful. Josta, thanks for sharing the drugs and shRNAs. Lena, thanks for the tour in the histology lab. I also thank Robert, Karin, Laura, Martin, Kah Wai, Marta, Catia, Sam, Ines, Riccardo, Dieudonnée, Bas, Bjorn and all the new members that I do not list here for the coffee chats and for making a positive atmosphere at the department.

To my external collaborators in Utrecht: Peter and Emma, thanks for helping us with the MICAL-3 project. Jeroen, you have been very kind to share your reagents with us, this has incredibly helped to speed up our MICAL-3 paper. Yeping and Eljo, it was great to communicate with you. Harm and Maarten, thanks for collaborating with us on all the mass spectrometry experiments, which added new information to our understanding of ELKS and the secretory ma-chinery. Femke, you gave me so much help last year on the islets part, hope you are doing great in Switzerland. My collaborators in Erasmus: Elize, thanks for your patience in teaching me about histology work. Martine and Siska, you are great mentors on ES cells targeting. Jeroen, thank you for producing all the good mass spectrometry data.

A big thank you to all animal care-takers in Erasmus MC and GDL of Utrecht University. Alex, John and Robbert, thanks for your help with the DEC protocols and blastocyst injections at Erasmus. Willeke, Ajit, Annemieke, Manu, Wendy, Kiki, Sharmayne, you all have contributed greatly to the maintenance of my mice, thanks for your time and patience.

I also thank the friendly neighbours in Kruytgebouw: Paul's lab (Paul, Sabrina, Raimond, Marta, Rachid), Sander's lab (Sander, Inge, Suzan, Suzanne, Vincent, Mike and Selma), Lucy & Mark from QVQ; Bart, Rachid and Vincent, you guys always gave me good suggestions when I had problems with ordering. At the purchasing department, Guno and Cora, thank you for your efficient solutions with difficult orders.

I have precious memories at the Erasmus MC: Thank to Dies, Martine, Siska, Noorie, Gijs, Linda, Erik, Luna, Cristina, I really miss our lunches. Niels, Jeffrey, Anna Pereira, Frank, Michael, Widia, Soraya, Liu, Lisa, Robbert, Yadi, Marjon, Anne, Lalini, Ilona, Gert, Suzanne, Wengyee, Joost, Toroti, Kerstin, Jessica, Catherine, Thomas, Rick, Tao, Jun & Peng, Xiao, Tianna, Sahar,

Francesca, Stefen, From Ee1067, Mark, Oscar, Mannis & Carla, Fan & Bei, and those not mentioned particularly, thanks for all your input and kindness.

Mijn paranimfen, Eugene and Silvia, thank you for willing to stand by me at my defense. Eugene, the master of counting, thank you for all your help and collaboration on the ELKS project, you have learnt me a lot about live imaging on TIRF, and you have been extremely helpful with the analysis. Silvia, my one-month housemate, thanks to SSH for our terrifying summer stay at Parnassos, we started our great friendship. Thanks for your mental support, you are very different from me, and I learn a lot from you.

I thank my friends and teachers for their support: Class LS93, JJ Lab and THH Lab in Taiwan. David, Aunt Emily, Yeh's family, cousin Agnes who helped me with the moving to the Netherlands, Sandy, Homao & TingShuo and Andy, your friendship had made my life a lot easier at the beginning of my life in the Netherlands. Eszter and Eneda, I cherish our friendship over the years, all the gatherings we had over the years are so precious to me, let's go to the Dom Tower soon. Xin, Maciek & Nori, Dima & Alexandra, Oleg, Lupe, Ruben, Julius & Sandra, Sarah, Suzanne & Michele, Sophie, Caroline, Kei & Douwe, Andrea & Irina, Lorenzo, Dana & Florian, Ludvik & Jin, Fr. Avin, Fr. Jan and Fr. Ben, Vincent & Ivy, Irene, Agnes, Floris & Ton, little angels: Lily, Arianne, Alma, Elian & Nonoko, you have become my extended families, we share together both the joy and sadness coming across. People who relieve my homesickness, Ying, TsungWai & Carmen, KC, you have been a great company at seasonal dim sum lunches. KC for sharing your PhD in R'dam and postdoc experience in Singapore. At the same time, I would like to thank the LXH lab and Acne lab in Singapore for their welcoming support. Stijn and Miyata for your advices over practical issues in Singapore. Alessia, I look forward to our future trips. Ute, my jogging mate, I miss our time along de Maas. Special thanks to Chris for revealing your exciting MBA life, helping out with my move back to R'dam, the translation of the Dutch summary. Petra, thank you for your help with the layout of the thesis. Fanny and Nesrin, you both are amazing, my fault or your fault, do we care about the frozen dessert! We had a terrific time. Vera, my dear friend who showed me clubbing in R'dam, my teacher for my first ice-skating experience, my heroine for repairing my bike and teaching me to do all kinds of DIY work. ChingYu and SziChieh, PohSien, YingHui, hope to see you soon after a

long time, enjoy staying around in Europe, good luck with the career. Gabriella, Lucia, YuTing, ChingFen, YuHui, Angel, Caroline, 永歆, 永芬for sharing your exciting life on the other side of the world. My childhood friends Sunny and Amanda, you always cheer me up when I go back to Macau. Sr. Josephine So for your big smile and hugs at our gatherings. Till here, I might not be able to address everyone I should have mentioned, dear friends and colleagues; you are all in the big picture of my life in the Netherlands.

Lastly, I would like to extend my thanks to my parents who always support my decisions and stay awake to have the after-midnight Skype calls with me. I thank all my family members who think of me from time to time.

Cheers,
Carol加璐